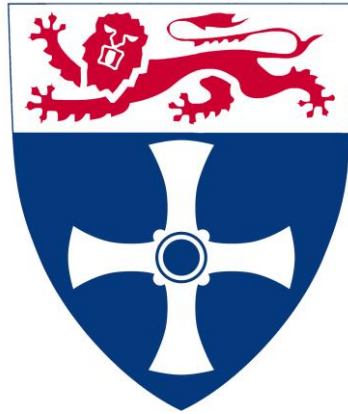


Advanced Performance Prediction Tools for the Analysis of Rotating Electrical Machines



Philip Alexander Hargreaves

Thesis Submitted for the degree of Engineering Doctorate

Department of Electrical, Electronic and Computer Engineering
Newcastle University

In collaboration with General Electric Power Conversion

©2012

COMMERCIAL IN CONFIDENCE

Abstract

This thesis seeks to advance the design tools for electrical generators. It aims to undertake an electrical generator's design, using the Finite Element method within a defined time frame. The thesis looks at the history of generator design systems and outlines the parameters a designer must predict. These parameters are then duly calculated using various finite element methods.

The thesis introduces a Pseudo Rotating Superposition system, which allows large quantities of data to be found from single static finite element simulations. Initially the system is used to predict machine saturation curves, and it is later expanded to predict the transient performance of generators. The full load performance of generators is found using a novel multivariable clustered optimisation routine. An extension using a rotating finite element solver, with pseudo rotating superposition, is then demonstrated. This creates a method which allows voltage harmonics to be quickly, accurately and validly predicted. Finally a study of iron loss is undertaken and using the above method it is shown that iron loss can be validly calculated using the quicker Radial/Tangential reference frame, rather than a slower Major/Minor frame.

A collection of 48 manufactured machines are used throughout as a test group for the created methods. Results from design calculations are compared to both factory test results and to the predictions from an existing customised in house design software tool. The methods within this thesis are shown to be over 35% more accurate in the majority of cases. The whole suite of methods created can automatically calculate results for any given machine in less than 1 hour.

The computer macros described in this thesis and the comparison with existing design methods and test were all made by the Author.

Acknowledgements

Firstly I would like to thank the backers of this research - the Engineering and Physical Sciences Research Council, my Industrial sponsor GE Energy and The Engineering Doctorate scheme at Newcastle University. Without them this work would never have taken place.

I'd like to thank my industrial supervisor Ross Hall. I first met him when he supervised my 2nd year Lab sessions and now 8 years on he's still supervising albeit as my Boss! Thank you for head hunting me into the company and for pursuing an industrial purpose for this work. I'd also like to thank all the employees at GE who I've hassled for information or have taken the time to help me over the years.

As my academic supervisor Barrie Mecrow deserves the most thanks. Constantly patient and always tactful in pointing out the flaws in my incoherent babble. Our Friday phone calls have been the highlight of my work week. Furthermore Barrie deserves a medal for reading the early drafts of this thesis, as it is safe to say that I am not a literary scholar. For this and many more things Thank you Barrie.

This work is the culmination of two decades of education and I cannot thank enough the teachers and mentors who have inspired and encouraged me on this journey. These include Miss Pretty and Mrs Fuller my maths teachers, Mr Archer and Mr Haworth from the Physics Department and Mr Collins my technology teacher. Additionally I cannot imagine myself being at this point without the excellent machines lectures given by both Barrie Mecrow and Alan Jack.

Finally I'd just like to say "It's about bloody time!"

Principal List of Abbreviations and Symbols

B	Magnetic Flux Density
H	Magnetic Field Strength
H_c	coercive force
μ	Permeability
J	Current Density
A	Vector Potential
E	Back EMF or Electric Field Strength
P	Permeance
F	MMF
V	Terminal voltage
I_f	Field current
I_a	Armature current
X_{ad}	Armature direct axis reactance
X_l	Leakage reactance
X_{lew}	End winding leakage reactance
X_f	Field winding reactance
X_{kd}	Damper cage reactance
R_f	Field winding resistance
R_{kd}	Damper cage resistance
R_a	Armature Resistance
W	Wieseman Coefficient
L_{a_eff}	Effective Axial Length
$T'_d/\tau'_d/t'_d$	Transient D axis reactance
$T''_d/\tau''_d/t''_d$	Subtransient D axis reactance
$T'_d/\tau'_d/t'_d$	Transient D axis time constant
$T''_d/\tau''_d/t''_d$	Subtransient D axis time constant
PF	Power factor
θ	Power factor angle
l_a	Axial Length
N_d	Number of radial ventilation ducts
w_d	Axial width of ventilation ducts

<i>ZPF/zpf</i>	Zero Power Factor (Saturation Curve)
<i>SCC/scc</i>	Short Circuit (Saturation Curve)
<i>OCC/occ</i>	Open Circuit (Saturation Curve)
<i>3phaseSS</i>	Three phase short circuit from open circuit
FE	Finite Element
T.H.D.	Total Harmonic Distortion
T.I.F.	Telephonic Interference Factor
T.H.F.	Telephonic Harmonic Factor
CAD	Computer Aided Design
GUI	Graphical User Interface
PRS	Pseudo Rotating Superposition
RPRS	Rotating Pseudo Rotating Superposition

Index

Abstract	iii
Acknowledgements	iv
Principal List of Abbreviations and Symbols	v
Index	vii
List of Figures	xi
Chapter 1. Introduction	1
1.1. The Company	1
1.2. Aims and Objectives	5
1.3. Contributions to Knowledge	6
1.4. Chapter Outline	7
1.5. Published work	9
Chapter 2. Overview of Design Systems for Generators	10
2.1. Genesis	10
2.2. Trend Sheets	12
2.3. General Electric's Machines	13
2.3.1. Design Variable Parameters.....	15
2.4. Analytical Design Systems.....	18
2.4.1. Electronic Design System - EDS.....	18
2.4.2. Speed Lab	21
2.5. Finite Element Method	22
2.5.1. History	22
2.5.2. Equations	22
2.5.3. Finite Element Design Systems	24
2.5.4. Finite Element Systems	25
2.6. Integrated Design Systems	27
2.7. Chapter Summary	28
Chapter 3. Initial Design Characterisation.....	30
3.1. Introduction	30
3.2. Methodology	31
3.2.1. Magnetic Coupling	31
3.2.2. Pseudo Rotating Superposition.....	31

3.2.3. Open Circuit Curve (OCC)	33
3.2.4. Sustained Short Circuit curve (SCC)	36
3.2.5. Zero power factor curve (ZPF)	38
3.3. Further Calculations and Considerations	40
3.3.1. Effective Axial Length	40
3.3.2. B-H curve Dilution	44
3.3.3. End winding Leakage	48
3.3.4. Initial Field Current Calculation using Carters Coefficient	51
3.3.5. Conductor Placement and Insulation	53
3.3.6. Mesh Size	55
3.3.7. Finite Element Machine Construction	61
3.4. Results and Discussion	61
3.4.1. Open Circuit Curve	62
3.4.2. Sustained Short Circuit Curve (SCC)	64
3.4.3. Zero Power Factor Saturation Curve (ZPF)	65
3.4.4. Leakage Paths	66
3.4.5. Calculation Speed	67
3.5. Chapter Summary	68
Chapter 4. Calculation of Transient Parameters	70
4.1. Introduction	70
4.2. Standstill Frequency Analysis	70
4.2.1. Analysis System	71
4.2.2. Simulation	72
4.2.3. Limitations	85
4.3. Equivalent Circuit	86
4.3.1. Leakage reactance - X_l	87
4.3.2. Field reactance - X_f	88
4.3.3. Wieseman Coefficients	90
4.3.4. Transient Time constant - $T'd$	91
4.3.5. Subtransient Parameters	94
4.3.6. Calculation Speed	105
4.4. Results	105
4.5. Chapter Summary	109
Chapter 5. Full Load Operating Point Prediction	111

5.1. Introduction	111
5.2. Potier's Method.....	112
5.2.1. Potier Reactance	112
5.2.2. Full Load Calculation	113
5.3. Direct Full Load Calculation Using Finite Element.....	116
5.4. Finite Element Static Analysis Using Multivariable Curve Fitting	116
5.4.1. Surface fitting and Solution Identification.....	117
5.4.2. End Winding Inductance	120
5.4.3. Cluster Analysis vs. Matrix analysis.....	121
5.4.4. Program Flow	123
5.5. Results	124
5.6. Chapter Summary	128
Chapter 6. Prediction of Waveform Harmonics	130
6.1. Analytical method	130
6.1.1. Flux Density Waves Due to Stator and Rotor Permeance Variations	130
6.1.2. Limitations of Analytical Methods	132
6.2. Proposed Method of Predicting The Open Circuit Waveform.....	133
6.2.1. Rotating Pseudo Rotating Superposition (RPRS).....	135
6.2.2. Comparison With Measurement	139
6.3. Influence Of The Field Current Source	142
6.3.1. Effect Of Exciter Harmonics Upon Field Excitation.....	143
6.4. Voltage Distortion Parameters	145
6.5. Comparison Of Total Harmonic Distortion.....	147
6.6. The Effect of Damper Bars within Synchronous Machines.....	149
6.7. Automated Damper Bar Optimisation.....	152
6.8. Chapter Summary.....	154
Chapter 7. Iron Loss Calculation	156
7.1. Abstract	156
7.2. Introduction	156
7.3. Continuous time and Discrete time.	157
7.4. Orthogonal Components.....	158
7.5. Alternative Calculations	161
7.6. Summary of Methods	162
7.7. Use of Pseudo Rotating Superposition (PRS).....	162

7.8. Determination of Constants	164
7.9. The metre cube	167
7.10. The machine	169
7.11. Comparison To Test Results	170
7.12. Chapter Summary	173
Chapter 8. Conclusions	174
8.1. Summary of Errors	175
8.2. Contributions to Knowledge	176
8.3. Limitations.....	177
8.3.1. Programming Limitations	177
8.3.2. Fundamental Limitations	178
8.4. Further work	180
Appendix Index	I
A. Open Circuit Voltage Results - 1 pu	II
B. Open Circuit Voltage Results - 0.5 pu	III
C. Short Circuit Current Results	IV
D. Zero Power Factor Results	V
E. Calculation of the End Winding Length	VI
F. Calculation of R^2	VIII
G. Frequency to Time Domain Transform.....	IX
H. Graphical User Interface	XII
I. Transferring Impedances across an Ideal transformer	XVIII
J. T.H.F. and T.I.F. Weighting Factors	XIX
References	XXIII

List of Figures

Figure 1 - Various General Electric generators including open and closed frame designs, stator and rotor detail	2
Figure 2 - Standardised construction methods: Left: Rotor lamination stacking on a mandrel; Right: Direct rotor field winding construction.	3
Figure 3 - Flow chart showing simple product flow through the company	5
Figure 4 - Left: Jedlik's Dynamo Right: Faraday's Disc	10
Figure 5 - Left: Hippolyte Pixii's Generator Right: Haselwander's Generator	12
Figure 6 - An example of a Trend sheet created from observed data	13
Figure 7 - Photographs of wound field synchronous generator laminations: Left - 4 pole rotor lamination from the A183 range (1.15m rotor diameter). Right - segmental stator laminations from 2 different generators, (outside diameter 1.6 m and 1.83m)	16
Figure 8 - Diagram showing the critical dimensions used to define laminations	17
Figure 9 - Coils at various stage of construction:	18
Figure 10 - An EDS command window screenshot showing a list of variables.	20
Figure 11 - PRS and standard FE method diagrams	33
Figure 12 - Open circuit phasor diagram	34
Figure 13 - A typical open circuit, short circuit and zero power factor saturation curve chart.	34
Figure 14 - Open circuit line voltages at a single excitation level. Each point represents a calculated value. All the points are calculated using data from a single static FE simulation	35
Figure 15 - A Finite Element plot of a generator under Open circuit simulation. [Scale for current density, J is in A/m^2]	35
Figure 16 - Short circuit phasor diagram	37
Figure 17 - Rotor & Stator linkage envisaged as a transformer	37
Figure 18 - Finite element plot of a generator under stator excitation [Scale for current density, J is in A/m^2]	38
Figure 19 - Zero power factor phasor diagram	39
Figure 20 - Finite element plot of a generator under zero power factor simulation [Scale for current density, J is in A/m^2]	39

Figure 21 - Axial 2D FE simulation at peak flux density showing stator, rotor, endplates and the shaft.	41
Figure 22 - Diagram showing the positioning of 2D axial (left) and radial (right) slices on a 3D model	42
Figure 23 - Diagram showing boundary conditions.....	42
Figure 24 - Graph showing axial length scaling factors for several machines	43
Figure 25 - Graph showing Additional Axial length for several machine in terms of radial Air gap Length	43
Figure 26 – Photograph of Machine Radial Ventilation Ducts.....	47
Figure 27 – Graph of an example B-H curve before and after dilution by 0.82	48
Figure 28 – BH curve Packing factors for a range of machines	48
Figure 29 - Diagram showing the cylindrical nature of the assumed stator-rotor configuration and the area used in calculation for calculating the initial field current	52
Figure 30 - Finite Element simulations showing coils modelled with and without insulation.....	54
Figure 31 - A cross section of an example coil side showing the individual rectangular copper strands with enamelled insulation	54
Figure 32 - Diagrams showing increasing mesh quality from coarsest in the top left to finest in the bottom right.....	56
Figure 33 - Table of solution speed.....	56
Figure 34 - Graph Showing Relative Solution Times.....	57
Figure 35 - Increasing air gap mesh densities.....	58
Figure 36 - Over stretched elements resulting in a poor quality mesh.....	59
Figure 37 - Voltage Harmonics.....	59
Figure 38 - Torque Harmonics.....	60
Figure 39 - Graph showing the phantom 8th harmonic created by a coarse mesh	61
Figure 40 - Open circuit saturation curve results showing both signed and absolute results. Red tails show extent of results spread and black box is the mean \pm one standard deviation	63
Figure 41 - Open circuit saturation curve results showing both signed and absolute results. Red tails show extent of results spread and black box is the mean \pm one standard deviation	64

Figure 42 - Sustained Short Circuit curve results showing both signed and absolute results. Red tails show extent of results spread and black box is the mean \pm one standard deviation	65
Figure 43 - Zero power factor Saturation Curve results showing both signed and absolute results. Red tails show extent of results spread and black box is the mean \pm one standard deviation	67
Figure 44 - Comparison of three identical test machines.....	67
Figure 45 - Flow Chart showing the operating sequence and software packages for open circuit saturation curve (OCC), sustained short circuit curve (SCC) and zero power factor (ZPF) calculations.....	68
Figure 46 - Comparison table showing Mean Absolute Percentage Errors (MAPE) [45] vs. test results	69
Figure 47 - SSFR test connections.....	72
Figure 48 - Photo of Saxi Batuque.....	73
Figure 49 - $Z_d(s)$ for the 17.5MVA test generator	74
Figure 50 - $sG(s)$ for the 17.5MVA test generator.....	74
Figure 51 - $Z_{afo}(s)$ for the 17.5MVA test generator	75
Figure 52 - $Z_q(s)$ for Saxi Batuque- a 17.5MVA generator	75
Figure 53 - A series of flux plots when excited by D axis current at increasing frequencies	78
Figure 54 - A series of flux plots when excited by D axis current at increasing frequencies	79
Figure 55 - D and Q axis Equivalent Circuits of increasing magnitude	81
Figure 56 - AC flux plot at 0.001Hz	82
Figure 57 - AC flux plot at 900Hz	82
Figure 58 - Magnitude of $Z_d(s)$ with and without damper bars. With damper bars in blue. Without damper bars in Green	83
Figure 59 - Magnitude of $L_d(s)$ with and without damper bars. With damper bars in blue. Without damper bars in Green	83
Figure 60 - Magnitude of $G_s(s)$ with and without damper bars. With damper bars in blue. Without damper bars in Green	84
Figure 61 - Magnitude of $Z_{afo}(s)$ with and without damper bars. With damper bars in blue. Without damper bars in Green	84
Figure 62 - Table showing a comparison between SSFR results and factory design results for a 17.5MVA generator	85

Figure 63 - The equivalent circuit of a synchronous generator	87
Figure 64 - Leakage Flux Simulation.....	88
Figure 65 - Field Winding Reactance Simulation.....	89
Figure 66 - Chart showing an example of stator and rotor excitation air gap flux densities with the first Fourier harmonic added.....	91
Figure 67 - Diagram showing the position of the Mean Turn Length for a single pole .	93
Figure 68 - Photo of the field winding being added to a 10 pole rotor body of similar rotor construction to Saxi	94
Figure 69 - A simulated example of a short circuit current plot showing subtransient distortion with $X''_d/X''_q = 2$	97
Figure 70 - An Example of slot ripple causing distortion in a short circuit.....	97
Figure 71 - A simplified single phase of a 3 Phase short circuit test.	98
Figure 72 - Correctly Identified data : Red = input data, Blue circles = chosen maxima, Green circles = chosen minima	99
Figure 73 - Factory Test results for a 17.5MVA Generator. Key: Pink = Input data, Red = DC Curve	101
Figure 74 - Maxima in the subtransient region of the test - Key: Pink = input data, Blue = Polynomial curve fit, Green = Existing company software curve fit	102
Figure 75 - Minima in the subtransient region of the test - Key: Pink = input data, Blue = Polynomial curve fit, Green = Existing company software curve fit	103
Figure 76 - Flow Chart Showing the sequence of calculation of transient parameters.	105
Figure 77 - Table showing Mean Absolute Percentage Errors (MAPE)[45] for the transient parameters	108
Figure 78 - Graph of X'_d errors for 9 machines.....	108
Figure 79 - Graph of t'_d errors for 9 machines.....	108
Figure 80 - Graph of X''_d errors for 9 machines	109
Figure 81 - Graph of t''_d errors for 9 machines	109
Figure 82- Synchronous Machine Phasor Diagram (not to scale)	111
Figure 83 - Saturation curves showing the Potier Triangle	113
Figure 84 - Saturated voltage vector found from the Potier Reactance	114
Figure 85 - Transposing of E to the Power Factor angle	115
Figure 86 - Torque and Voltage Simultaneous plots with the closest simulation highlighted. Figure contains raw simulation data hence the highlighted point is not the exact load case required showing the need for interpolation via curve fitting.	119

Figure 87 - Polynomial curve fits - Key: Magenta = Curve Fit, Blue = Raw Input data from FE	120
Figure 88 - Phasor Diagram showing the additional End winding Reactance. (not to scale)	121
Figure 89- 3D Mesh surface plots showing a good initial guess with reducing concentric clusters.....	122
Figure 90- 3D Mesh surface plots showing an average initial guess with reducing concentric off centre clusters	123
Figure 91- 3D Mesh surface plots showing a poor initial guess resulting in a second large cluster before reducing concentric clusters	123
Figure 92 - Flow Chart detailing the sequence implemented when calculating the full load operating point using clusters.....	124
Figure 93 - Table showing Full Load EDS Results and Factory Test results and % errors	126
Figure 94 - Summary Table Comparing Full Load simulation results to factory test results	126
Figure 95 - Full Load simulation Percentage errors. Red tails show extent of results spread and black box is the mean \pm one standard deviation	127
Figure 96 - Table Comparing Averaging FE Potier and cluster method predictions results to factory test results.....	127
Figure 97 - Full Load simulation Percentage errors and average FE Potier and clusters method prediction. Red tails show extent of results spread and black box is the mean \pm one standard deviation.....	128
Figure 98 - MMF shapes in the interpolar regions.....	133
Figure 99 : A Laminated four pole 15MVA Synchronous generator rotor showing: A - Damper bar placement on the pole face B - Open and Closed Damper bar slots .	134
Figure 100 : A FE plot of a four pole generator showing flux density (Bmod) and flux lines	135
Figure 101 : PRS and standard FE method diagrams	137
Figure 102 - A series of diagrams showing the effective movement of the rotor during RPRS in a 5 steps per slot system	138
Figure 103 - Diagram showing the order that data must be arranged in a five steps per slot system.....	139
Figure 104 : Harmonic content of a four pole 8.8MVA synchronous generator.	140
Figure 105 : Graph of Field Current within FE simulation.....	141

Figure 106: Graph of Field Current within FE simulation.....	142
Figure 107 - Graph of field current using a constant current source	142
Figure 108 : Topological Diagram of the excitation system on a typical synchronous generator.....	144
Figure 109 : 18 pulse exciter voltage waveform over 1 period.....	144
Figure 110 : Field Current harmonics due to machine exciter and rotating rectifier diodes.	145
Figure 111 : Comparison of the Total Harmonic Distortion of several generators	148
Figure 112 : Table showing Mean average percentile error (MAPE) vs. Test Results for 3 differing methods	148
Figure 113 : The Effect of varying Damper bar pitch and offset upon the T.H.D. of a machine.	151
Figure 114 : The Effect of varying pole shoe width and Damper Bar Offset upon the T.H.D. of Saxi Batuque.....	152
Figure 115- Flux graphs showing a 2D flux vector decomposed into Cartesian charts for both a point in the tooth and a point in the coreback of a machine. [All units in Tesla].....	160
Figure 116- A diagrammatic representation of potential calculation axes	161
Figure 117 - A rotationally symmetrical mesh allows solution over a single slot to yield full machine data	163
Figure 118 - A non-rotationally symmetric mesh.	164
Figure 119 - Detail of the conductor mesh showing non-rotational uniformity	164
Figure 120 - Four Variable Curve fit for M400-50 grade material.....	166
Figure 121 - Three Variable Curve fit for M400-50 grade material	166
Figure 122 - R squared Value Comparison for 3 and 4 variable curve fit.	167
Figure 123 - Calculated Constant Values.....	167
Figure 124 - Diagram showing the rotation of the 1m ³ test sample.....	168
Figure 125 - Calculated losses in the 1m ³ using different orthogonal components.....	168
Figure 126 - Table showing the calculated loss in a 17.5MW machine using various methods.	170
Figure 127 - Diagram showing the individual elemental percentage differences between the Radial/Tangential and the Major/Minor loop methods.	170
Figure 128 - Comparison of Test Results and Predictions.....	171
Figure 129- Several multi-megawatt generators at various stages of construction	172

Figure 130 - Table showing a summary of errors for the created FE methods and the existing EDS system	175
Figure 131 - A Solid pole rotor. Note the positioning of the pole face bolts.....	182
Figure 132 - Chart showing how flow of the GUI.....	XII
Figure 133 - Single Machine Screen	XIII
Figure 134 - Batch Machine Screen.....	XIV
Figure 135 - Vary Machine Screen	XV
Figure 136 - Solve Status Screen	XVI
Figure 137 - Individual Machine Results Screen.....	XVII

Chapter 1. Introduction

Electrical machines have been part of the industrial landscape for over a century. Initially academic novelties, converting chemical pile battery power to movement, the field rapidly grew as it was discovered that the process was bi-directional and electricity could be generated easily. Although the main commercial use of the generated power was initially lighting circuits, in 2008 65-70% of electricity usage in the EU is used to power motors [1]. Adding to this the fact that the vast majority of the 19.47 TWh [2] global annual electricity production is generated through rotating machines, the scope and field of electrical machines is massive. Following research into peak oil [3] and the realisation that nuclear power will not be 'too cheap to meter' [4], electricity utility companies, governments and the public at large have become aware of the demand for energy and cost of efficient power generation. As a result electrical machine manufacturers have had an even greater desire to create more accurate performance prediction models, to allow products to be manufactured to higher standard at lower cost, and ultimately to allow products to be perceived as 'green' by the public and market.

1.1. The Company

This research has been carried out in conjunction with General Electric Ltd and consequently must be of relevance to their specific products. General Electric are a world leader within power engineering specifically within the multi-megawatt region. They produce whole system solutions including motor generator, converter and control systems The business is focused upon delivering the highest quality products for any power conversion need.

Within electrical machines General Electric produce permanent magnet, induction and wound field synchronous generators and motors which range from tens of kVA to 100s of MVA. Specifically this thesis focuses on machines in the range of 5 to 30 MVA. The major use of General Electric's generators is within backup and islanded generation, with the offshore and remote onshore oil and gas industries, as well as marine and naval sectors, forming major customers. The generators are also used as more conventional backup generators, for example at large electrical power stations which require standby

power in the event of grid failure. The business also has significant interest in the renewable energy sector, including hydro electric and large wind turbine generators. Figure 1 shows several General Electric generators, including open and closed frame designs. This research focuses on synchronous generators as this is one of the core products constructed in the UK. It is aimed that the methods and systems developed within the work can be easily modified for other machine types.

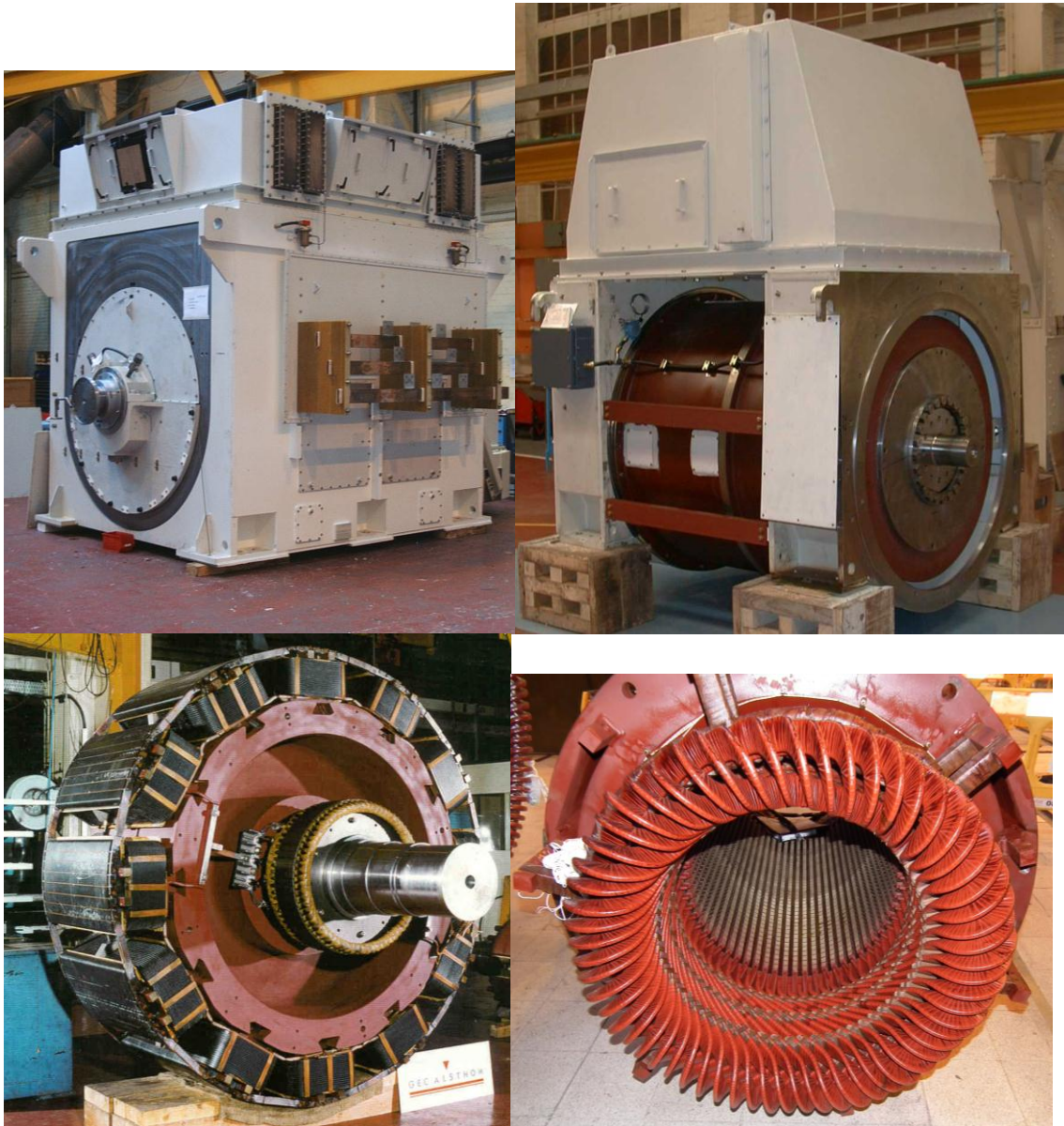


Figure 1 - Various General Electric generators including open and closed frame designs, stator and rotor detail

Wound field synchronous generators are a mature technology which has been manufactured for over 100 years: consequently the standard construction elements of the machines are well known. The stator frame sizes used by General Electric are fixed,

with the number of teeth and slot dimensions forming the main variables that change in the stator lamination profile. The rotors are all of a common topology, with all 4 pole generators made using cruciform laminations which have 4 core bars used to clamp the core together. This standardisation across the range of generators is of primary importance to the financial side of the business. Using a standard design approach allows the construction methods to be standardised, even though every generator has an element of customisation. For example, all low pole number rotors have the field winding wound directly onto the core (Figure 2) and all stators laminations are stacked onto a mandrel (Figure 2). By having standardised the designs and construction methods cost can more easily be removed from the products and hence the generators produced at a more competitive price and/or a greater margin. These standard construction methods allow design features to be common throughout the whole range and hence investigating the cost saving of a single generator feature can potentially save large amounts of money.

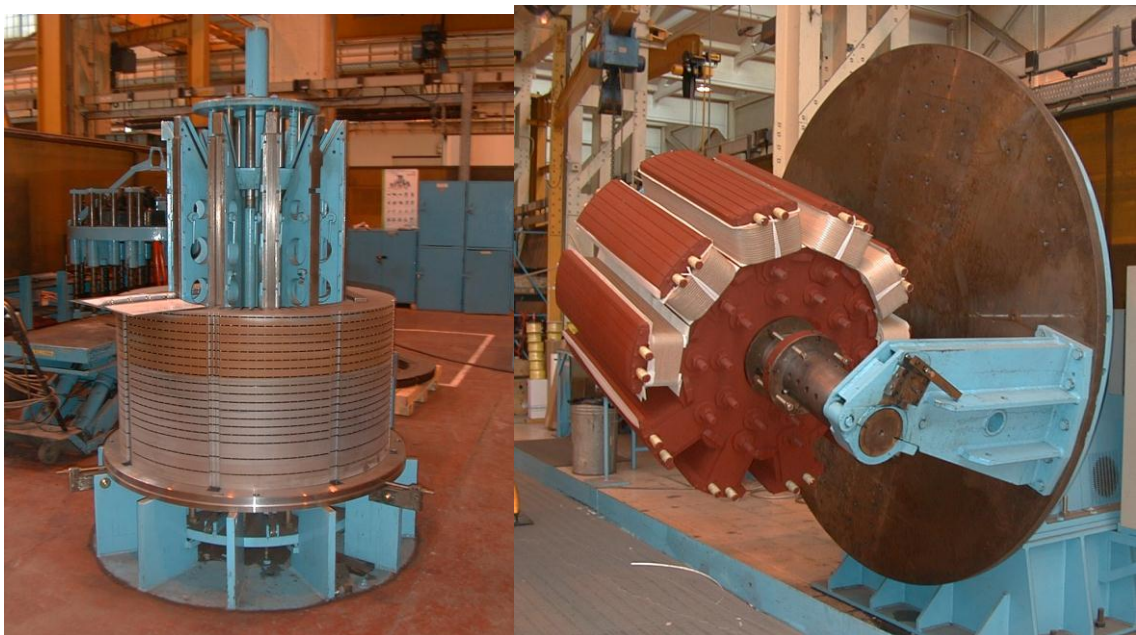


Figure 2 - Standardised construction methods: Left: Rotor lamination stacking on a mandrel; Right: Direct rotor field winding construction.

Any design feature changes have to be checked, generally via simulation, to understand the full implications of the modification. For example, changing the pole shoe shape to save material will change the open circuit voltage waveform, which will change the harmonic output of the machine. Hence a rapid prediction tool is needed so the designer can quickly make these decisions in an informed manner. Any new tool must create

more accurate predictions, which in turn creates several benefits for the company. With the more accurate predictions of machine performance, design engineers are able to reduce parameter tolerances, allowing future machines to be designed within tighter bounds. This will in turn create cost saving in two ways:

1. If a machine's performance is more accurately predicted then designers need to be less cautious and hence less material will be required when machines are manufactured.
2. If a machine prediction has been initially poor and specifications have not been met, modification of the machine must be carried out at the company's expense, or the customer must be compensated for a design concession.

Any prediction tool is likely to be used in two places within the business's product flow. Looking at Figure 3, a tendering tool is initially needed to produce an outline design quickly: a more detailed design engineering process is then required after the order has been approved. The outline tendering design forms the basis for a cost estimate and hence this design eventually ends up determining part of the gross margin. At this point the design needs to be produced rapidly to allow the sales team to rapidly capitalise upon the market. The design also needs to be fairly accurate to allow a competitive tender. Material cost estimates are based upon estimated quantities of materials and predictions of future prices; hence they have a margin for error and a period of validity. If the order is confirmed a secondary design process confirms the initial tender and refines the design to the exact set of material parts that are ordered - the Bill of Materials. Several more design iterations are often simulated at this point to hone the design to the most cost efficient design which meets the specification. This engineering process is primarily concerned with accuracy as there is less of a time constraint.

These two engineering processes have 2 diametrically opposite constraints - Accuracy and Time. A design system must therefore be a balance between the two, so that the system can be used in both processes and hence minimise engineering time and consequently cost.

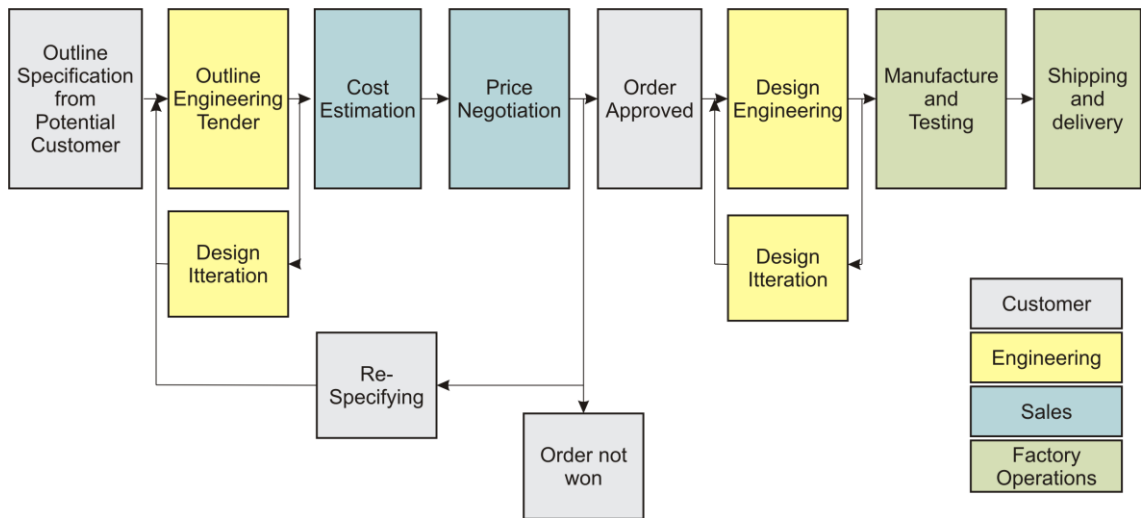


Figure 3 - Flow chart showing simple product flow through the company

1.2. Aims and Objectives

Ultimately this work simply sets out to answer the question 'Can a better design system be created?' This fundamental question rests upon the interpretation of the word 'better'. As previously discussed, the tendering engineer requires a fast answer and the design engineer requires an accurate answer, whereas the company simply wants a single system which will save money. As a result the single aim has been broken down into several objectives which in turn have sought to broaden the knowledge horizon:

- Seek out the prevalent design systems in current use and determine the merits and limitations of each.
- Form an outline list of the required parameters that an electromagnetic design tool must calculate.
- Create a design tool using appropriate novel methods which will be accurate enough and fast enough for both outline tendering and final design.
- Objectively determine the performance of a new design tool against existing systems.

- Determine the contribution of rotor damper bars within synchronous generators and to comment upon their ideal positioning for reduction of voltage harmonics.
- Investigate iron loss calculation methods within finite element analysis and systematically determine a method which is both academically valid and relevant in an industrial environment.
- Create a method for calculation of full load operating point that does not rely upon a dynamic rotating finite element simulation.

1.3. Contributions to Knowledge

This thesis has advanced knowledge in two significant areas. Firstly the introduction of novel modelling techniques and integration of methods to make a finite element based design program feasible. These methods include:

- The use of a method called Pseudo Rotating Superposition which uses static models to minimise simulation times when calculating waveform fundamentals.
- A secondary Rotating Pseudo Rotating Superposition method is created that solves using a rotating solver over 1 stator slot in order to calculate higher order harmonics including those influenced by induced damper bar and field winding currents.
- In complement to the radial slice simulations, axial simulations are used to calculate effective axial lengths.
- Within the software selective static boundary condition placement combined with rotating simulations has allowed rapid compound methods to give transient parameters.
- Integration of end winding calculations, B-H Dilution and several curve fitting techniques reduce solution time and improve accuracy.

Secondly, from the application of the above methods knowledge is gained. This includes:

- The positioning of individual conductors within simulated slots is insignificant allowing the use of a single homogenous region when using FE simulations.
- The effective axial length is found to be a function of the radial air gap to account for axial flux fringing at the air gap.
- To minimise voltage distortion the placement of damper bars should be at the same pitch as stator teeth. The rotor pole width should be an integer number of stator slots wide when flux fringing is accounted for. Shaping of the pole face will create additional fringing complicating results.
- Rotating rectifiers which are used by the field excitation system of a synchronous generator add negligible ripple to the field current.
- Iron Loss calculated with FE is dependant upon the correct choice of axes. The Cartesian coordinate plane should not be used but the choice of a Radial/Tangential reference frame plane gives comparable results to using Major/Minor Loops. The Radial/Tangential frame also gives a significant reduction in calculation time.
- The stamping of laminations and mechanical handling creates significant loss often greater than the error associated with the method of loss calculation. This extra loss is often accounted for by use of a single design factor found for this size of synchronous machine to be 1.71.

Additionally A large selection of different machines are simulated and compared to their factory test results. This broad comparison serves as a important validation of the methods created.

1.4. Chapter Outline

Chapter 2 sets out the history of design systems for electrical generators. How the pioneers of machine design used trial and error, coupled with experimentation, to create the first machines is discussed before describing how the use of trend sheets facilitated rapid development into larger machines. The use of integrated analytical design systems is discussed, along with the limitation of magnetic saturation. It is shown how the introduction of faster computing power has allowed the use of finite elements to become

the preferred design system. The chapter finishes by outlining the specific parameters a design system must calculate to meet the needs of design engineers.

Chapter 3 looks at characterising the initial design. Open circuit, short circuit and zero power factor saturation curves are calculated. Additional correction calculations for factors such as effective axial length, end winding leakage and specific machine design features are also discussed before predictions for 48 unique machines are compared to both an analytical design tool and factory test results.

Chapter 4 attends to the transient parameters of synchronous generator performance. Here the transient and subtransient axis reactance and time constant parameters are calculated and again compared to test results and analytical predictions. Similarly Chapter 5 predicts the full load operating point of the synchronous generators using both a standard method, calculated using Chapter 3 results, and a method using only static finite element results and simultaneous curve fitting with multi parameter optimisation. These two sets of results are compared to the company's design predictions and factory test results.

A novel method of predicting open circuit voltage harmonics quickly using finite element method is demonstrated in Chapter 6. The method is compared to an analytical method and a standard finite element method before a discussion of its overall accuracy. Some conclusions are drawn concerning the optimal positioning of damper bars to reduce open circuit distortion.

Chapter 7 concerns the calculation of iron loss. Several methods are compared and one is selected which gives is the optimal balance of accuracy and calculation time. Results are calculated for several machines before a discussion of the overall accuracy of the iron loss calculation is analysed, concluding with an engineering design solution.

Finally within Chapter 8 conclusions as to the overall accuracy and reliability of the work and to whether the objectives set out have been met are drawn. Some extensions to this work are then suggested.

1.5. Published work

- P. Hargreaves, B. Mecrow, and R. Hall, "Open circuit voltage distortion in salient pole synchronous generators with damper windings," *5th IET International Conference on Power Electronics, Machines and Drives (PEMD 2010)*, 2010, pp. MO431-MO431
- P Hargreaves, B. Mecrow, R. Hall, "Calculation of Iron Loss in Electrical Generators Using Finite Element Analysis", *2011 IEEE International Electric Machines & Drives Conference (IEMDC)*, DOI: 10.1109/IEMDC.2011.5994805
Publication Year: 2011 , Page(s): 1368 - 1373
- P Hargreaves, B. Mecrow, R. Hall, "Calculation of Iron Loss in Electrical Generators Using Finite Element Analysis", *IEEE Industrial Applications Society Transactions*. [Accepted and approved by the society and awaiting publication in a queue]

Chapter 2. Overview of Design Systems for Generators

2.1. Genesis

The first electrical generator was created in the late 1820s by Ányos Jedlik. The machine, which he called his '*lightning-magnetic self-rotor,*' is a basic dynamo (Figure 4). It was created as an investigation into magnetic fluxes and, although unpatented, Jedlik unknowingly had created the first self excited generator, which relied upon residual magnetism. Jedlik's achievement has largely been overlooked in favour of the famous Michael Faraday's Disc of 1831 (Figure 4). This homopolar generator, made from a copper disk rotating in a horseshoe magnet, relies upon the charge separation which results from the Lorentz force on the free charges in the disk. The motion is rotational and the field is axial, so the electromotive force is radial. Homopolar generators can create high current levels due to their low internal resistance but only at a low voltage, with the major limitation of the system being the brush contacts on the fastest part of the spinning disk.

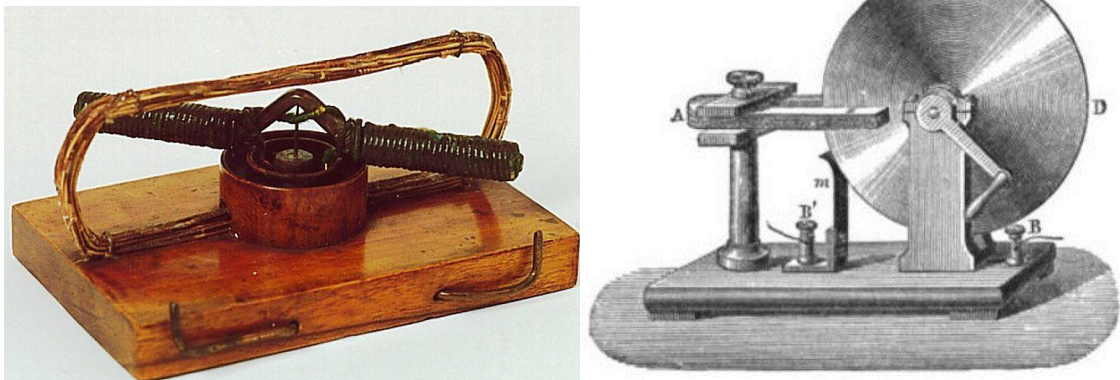


Figure 4 - Left: Jedlik's Dynamo Right: Faraday's Disc

Over the next half century many machines were developed: 1832 saw the first dynamo created by Hippolyte Pixii (Figure 5), followed by machines from Pacinotti, Whetstone and Siemens in the 1860s. These machines were all air cored, as the foundations of magnetic theory weren't fully understood. The first machine used to generate power on an industrial level was made by Zénobe Gramme in 1871 and used a large iron hoop as a flux directing core, vastly improving efficiency. All these early machines were DC machines with commutators. DC was the most prevalent form of electricity because of

large chemical laboratory piles (batteries) and the majority of loads were DC (i.e. filamentary lighting and motors). The next step in machine development came in the 1880s and sparked the war of the currents. The availability of hydroelectricity in large quantities, especially at Niagara Falls, introduced the necessity of transmitting power over larger distances. The three phase alternating current system, backed by Tesla and Westinghouse, triumphed over the 3 level direct current system used by Edison. This is mainly thanks to the electrical efficiency and material economy of transmission at higher voltages. This eventual triumph in the late 1890s was only possible thanks to work carried out by Tesla and independently by Galileo Ferraris into rotating magnetic fields. The work culminated in the first synchronous AC generator made by Friedrich August Haselwander in 1887 (Figure 5). By the turn of the century AC systems had been recognised as the better technology, although DC transmission and distribution were still in wide usage but the war was all but over.

All the early machine designs were developed by scientists with only the latter developments coming into the newly developing commercial electrical engineering sector. Designs were very much ad hoc - many of the earliest designs were experiments that had yielded some good results and were simply made slightly larger in the hope of generating power at a useful level. It could be argued the early design system was simply trial and improvement. Machines were built and if they generated an acceptable level of power the design was built multiple times as required. Machines were designed in this manner because they were the forefront of technology and so experience was negligible and material science was still developing. A trial and improvement design system requires many prototypes and consequently takes time and money to reach an optimised product. If the rate of knowledge or technology growth is more rapid than the prototyping process then trial and improvement will never reach an optimised solution.

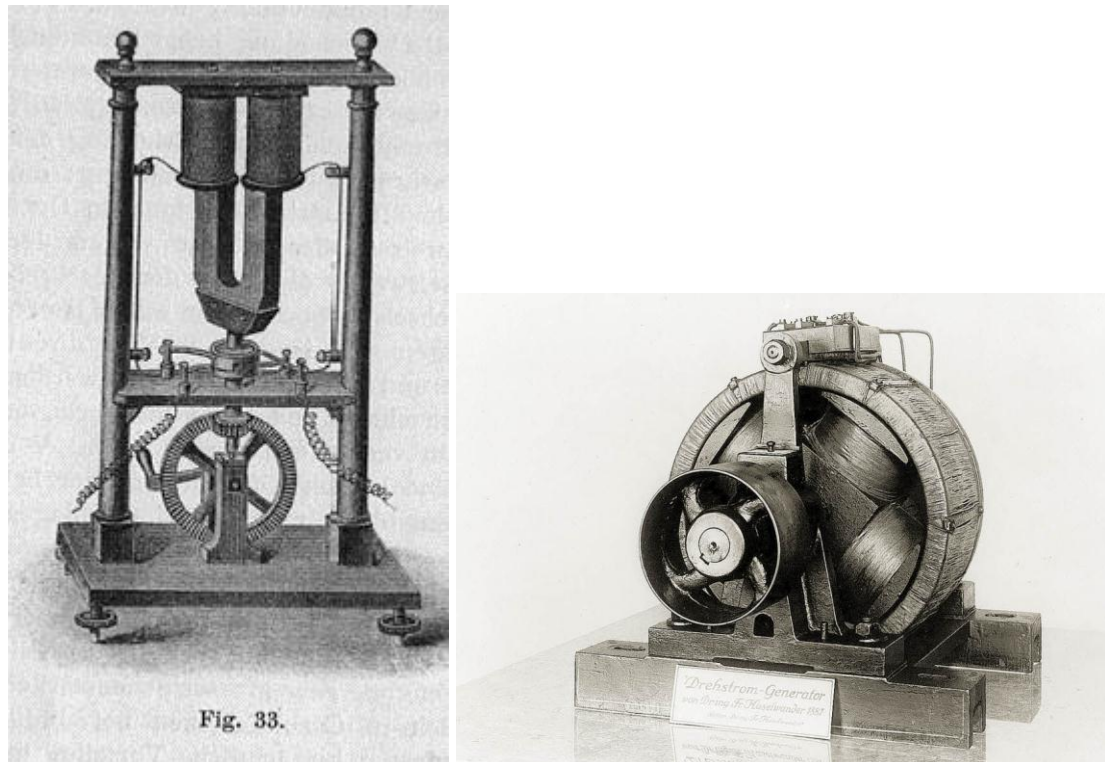


Figure 5 - Left: Hippolyte Pixii's Generator Right: Haselwander's Generator

2.2. Trend Sheets

The natural extension to trial and improvement methods is trend sheets. These sheets are typically graphs detailing the variation of one parameter against another, for example frame size against output power. Initially the sheets were created from the direct measurement of machine sizes and ratings, which allowed an expansion of knowledge. As time progressed so did the theoretical background, allowing the first steps into true scientific prediction of machine rating without having to create a prototype. Trend sheets then started to be used as a design tool to take away the effort of having to complete complicated mathematical equations.

Figure 6 shows an example trend sheet which was used when designing large hydroelectric turbines [5]. Hydroelectric turbines revolving at a lower speed tend to have high pole numbers and large air gap diameters hence the construction topology merits its own set of trend charts. Here 40 generators have been constructed and the reactances mapped against pole pitch allowing designers to quickly predict trends for future generators.

The removal of the prototyping stage occurred because the machine sizes increased and prototypes became very expensive and so typically a first of type with a higher margin for error is made which can at least be sold. The loss of prototyping also indicated that

the technology was entering a mature stage. During the mature stage products have incremental increases in performance instead of large step changes. Incremental changes are usually attributed to material science development and large step changes that happen during early machine development are typically attributed to topology changes.

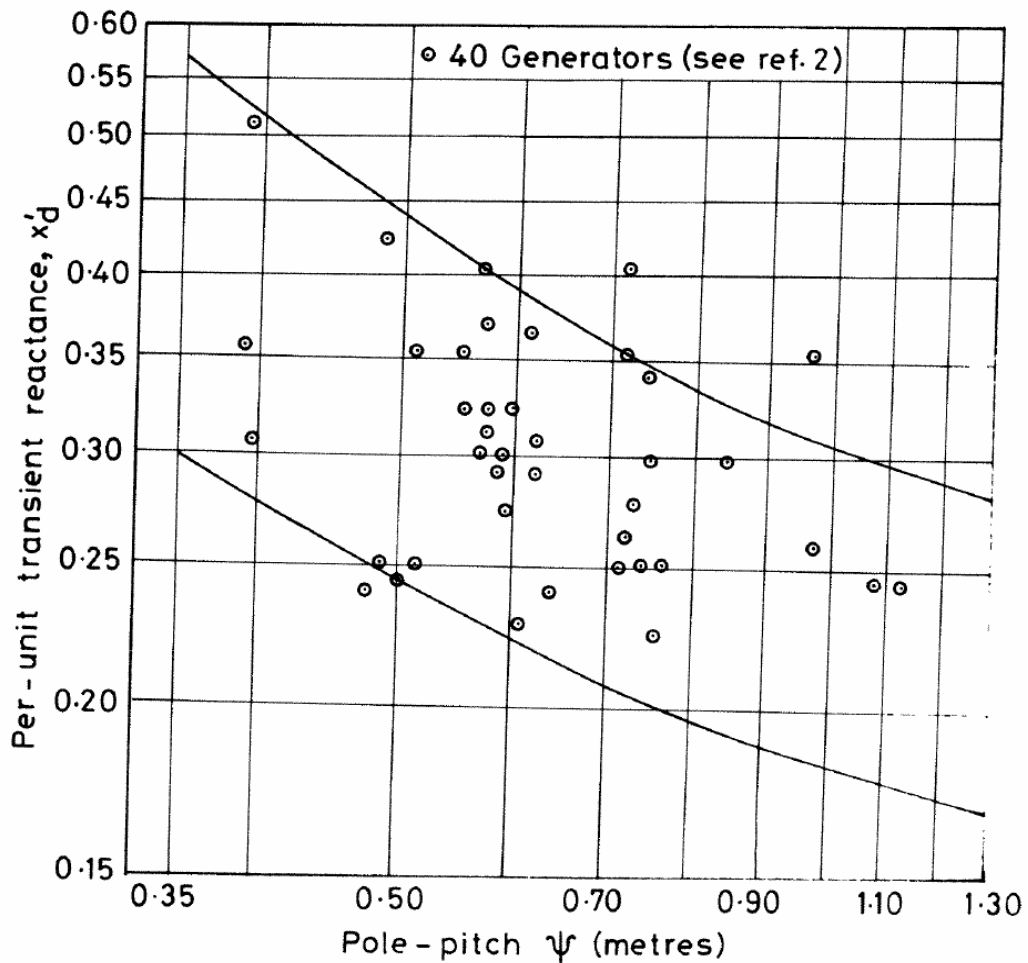


FIG. 1-4. Maximum and minimum values of transient reactance as a function of pole-pitch.

Figure 6 - An example of a Trend sheet created from observed data [5]

2.3. General Electric's Machines

Synchronous generators built by General Electric are specified by a list of parametric variables. These variables are the core inputs an engineer can change when designing a generator. Looking specifically at the electrical design the variables fit into various groups which include:

- Dimensions
- Materials
- Windings
- Additional Properties

Within the dimensions category there are many lengths, most of which are directly defining the laminations, as pictured in Figure 7 and Figure 8. Additionally lengths define axial lengths, compression plate thickness, bolt threads and other minor dimensions.

Materials are assigned by an in house numbering systems where all references fall in the format MMxxxx. MM stands for magnetic material and xxxx is a 4 digit reference to a standard. A database lists the properties to the relevant ISO, IEEE, EN and BS standards, allowing the whole company to have an easy reference from purchasing to construction. The database includes structural, electrical and magnetic properties. The use of a single numbering system is highly controllable, allows a high level of standardisation and, in the event of any documentation (such as drawings) becoming available to competitors it adds an additional layer of security. Example numbers include:

- Standard lamination materials are MM4445, MM4470 and MM4472 - 0.5mm 350 or 400 grade
- Standard Mild Steel - MM4301 to MM4306
- High Strength Steel, MM4316 to MM4318
- Copper MM9322
- Permanent Magnets MM7380 to MM7422

Winding data mainly concerns the type and form of the winding. Example parameters include whether the winding is a multi-layer lap wound diamond coil, a race track coil or a multiple tier coil. Additionally the number of slots, the pitch and distribution and the number of turns, including any parallel conductor strands and/or any parallel circuits, must be specified. The thickness of the insulation and corona shield is also defined.

Additional parameters concern the peripheral electrical systems, such as the exciter and terminal connections. Also customers may require specific monitoring, such as temperature or vibration sensors, to be fitted.

2.3.1. Design Variable Parameters

Of the parameters above the designer only has certain ones which he can vary. Product standardisation to reduce costs has fixed some manufacturing tools, such as the dies used to press the laminations. This means that certain dimensions are not changeable until a die reaches the end of its life and a new die is ordered. This may take many years, depending upon the frequency of use. Hence the designer must work within standard frame sizes. For example, for 4 pole generators these include 1.18, 1.32, 1.45, 1.60 and 1.83m stator outside diameters

A compound die is used for stator dies, so that 3 sides are cut by 1 die and the inner bore and slots are notched by a separate changeable tool. Therefore the designer can change the length of the air gap, the number and dimensions of the slots. The axial length of the machine can easily be changed by stacking more laminations. On the rotor the die is also fixed and very little can be changed. A single tool creates each rotor size so the designer can only change the axial length for the majority of machines. The exception to this rule is, of course, when a new die is made.

On large machines with higher voltages the positioning of the coils in the slot is crucial to guarantee a set thickness of insulation. For this reason the machines are not mush wound. All conductors are pre-taped with insulation before the whole coil is manually wound with a secondary main wall insulation. Finally, corona shield tape is applied to end windings. This whole process is time consuming and labour intensive but guarantees quality for machines which may have a life span of 25 or more years. Conveniently, it allows the design engineer full control of the winding type, pitch, distribution and connection. Figure 9 shows coils at various stages of construction, showing the stages of insulation winding.

The material used can be changed by the designer. For example different stator laminations steels can be specified to control loss and increase machine efficiency. A thinner, lower loss grade of steel will have a lower iron loss, but will cost more to purchase. The thinner laminations will also take longer to stack, further adding to the cost. Consequently a compromise is usually adopted, with the majority of machines

using cheaper magnetic steels, incurring a small loss in efficiency. Higher frequency machines may warrant a better grade of steel.

Finally, additional machine variables may occasionally be modified by the designer. For example, when choosing a primary field exciter for the rotor, a whole raft of parameters are factored in but the effect upon the main machine design is insignificant. The most significant example of a peripheral effect is when a larger than normal shaft mounted fan is requested for extra cooling in high ambient conditions. This will create additional drag, reducing efficiency, but the end windings may also need to be shaped to give extra clearance. The extra clearance will call for more winding copper and hence the machine resistance will be slightly affected.



Figure 7 - Photographs of wound field synchronous generator laminations: Left - 4 pole rotor lamination from the A183 range (1.15m rotor diameter). Right - segmental stator laminations from 2 different generators, (outside diameter 1.6 m and 1.83m)

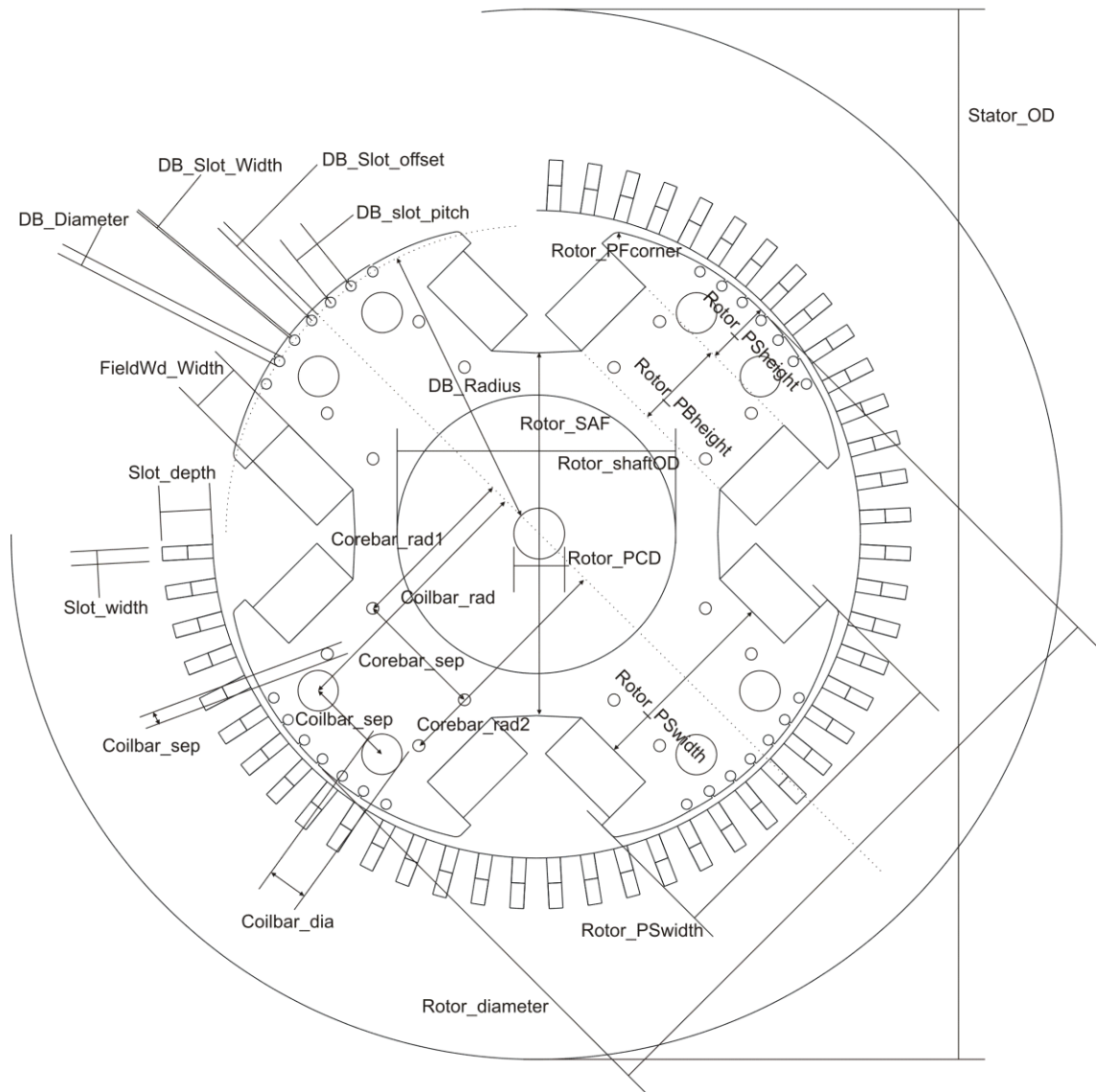


Figure 8 - Diagram showing the critical dimensions used to define laminations



Figure 9 - Coils at various stage of construction:

Top Left: Individually insulated conductor strands wound round a former and temporarily held by ties before being pulled into the desired diamond shape.

Top Right: Pulled diamond coils with their first layers of end winding and main wall insulation.

Bottom Left: Second layer of Insulation applied to the main wall.

Bottom Right: End winding corona shield applied and further main wall insulation.

2.4. Analytical Design Systems

2.4.1. Electronic Design System - EDS

General Electric's in-house design software, known as the Electronic Design System or more commonly EDS, is a computerised series of design equations and trend sheets that have been customised specifically for the company's product range. The system originated as the machines research division realised in the early 1980s that computers could be used to simplify the manual design process. Initially taking over 20 minutes to calculate a single design, EDS now provides results in a matter of seconds. Modules have been written for several machine types, such as permanent magnet and induction machines, but EDS's main application is wound field synchronous machines. Within these machine types additional modules calculate parameters, ranging from basic

electrical parameters through to thermal models and basic stress analysis, outputting values required for tendering, such as mass of copper and iron. The system also estimates noise levels, harmonics content and can create manufacturing drawings as well as an outline bill of materials. Although many of these features have been superseded (such as the structural calculations, which are no longer used) the majority of the electrical design tools are the company's primary design system. EDS also has a design database attached and hence it is also used as a backup catalogue for the last 20 years of designs. This catalogue allows rapid designing of machines, as often large quantities of a design can be copied from a previous design. EDS is also used to analyse factory test results, allowing a direct comparison to be drawn within the environment. Having test results and predictions side by side has allowed the programmers to add many constants which adjust theory to match practise. Often colloquially referred to as 'fiddle factors', many of these constants are not documented and are empirically tested. For example, in a module which calculates the additional axial length due to flux fringing the final line of code reads (in English):

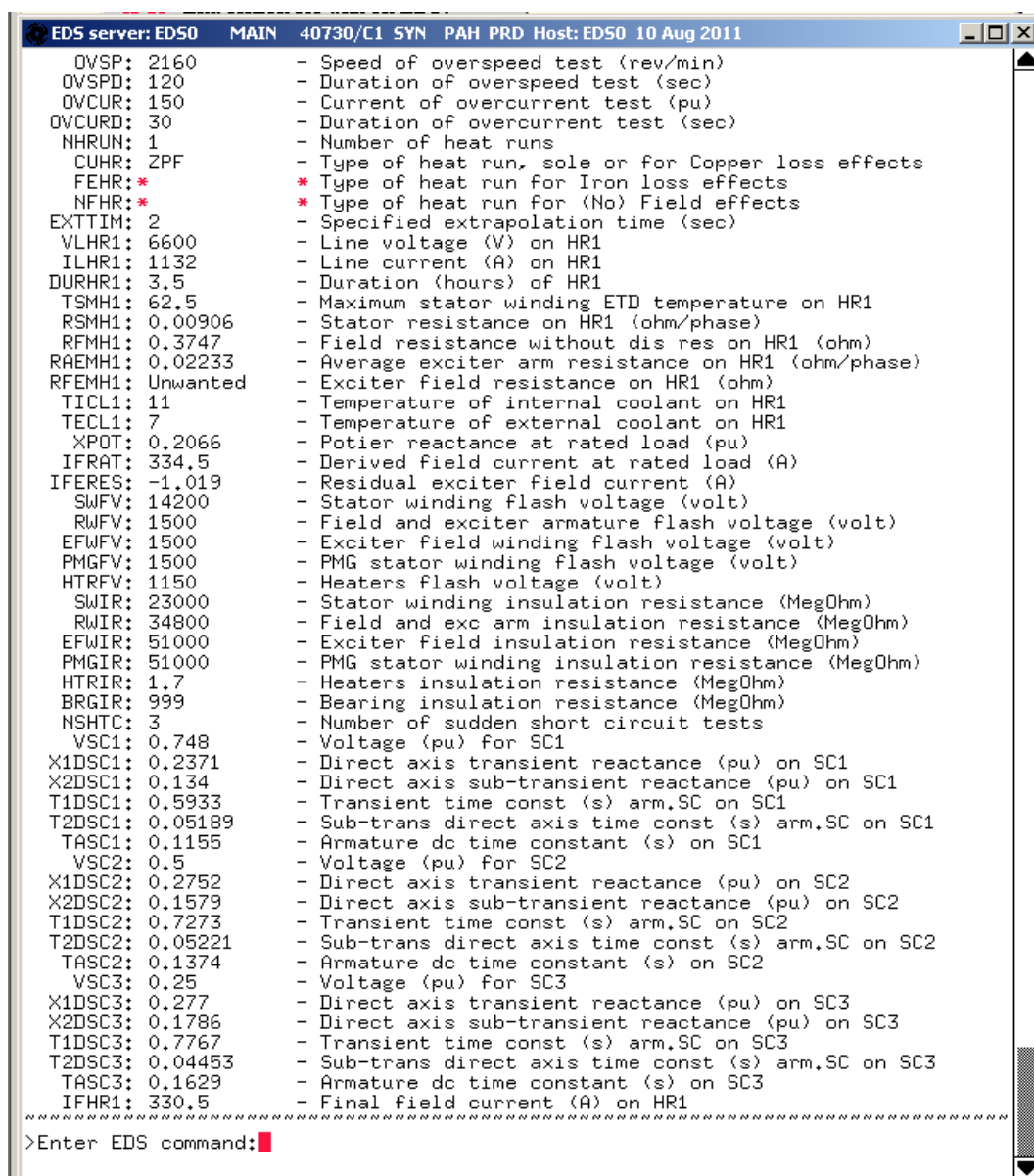
```
IF fringe length is greater than 0.0254; fringe length equals 0.0254
```

On the surface this is inconsequential, but realising that 0.0254 is a 'metric' inch highlights the fact EDS was coded in metric units from imperial data, giving many imperial conversions throughout. Additionally, simply limiting the length to an inch is poor engineering as it does not pay any attention to the machine dimensions e.g. on a small machine an inch may be valid, but on a 100MVA turbo generator an inch is likely to be too small.

The factors are also used to help EDS when machines are especially saturated. EDS would be almost perfectly accurate if all machine materials were linear but as the steel saturates EDS struggles with accuracy. With highly saturated machines engineers have learnt to add a higher margin for error on top of any built-in factors to guarantee meeting specifications. The fiddle factors have made EDS very accurate when within the narrow limits of standard designs, however as EDS is pushed into new machine types or less standard modules, such as permanent magnet machines, the constants are inadequate and hence results are less reliable.

EDS's main strength is its accuracy with core products, due to over 30 man years of development, but the main failure is the when designs fall outside previous experience and EDS fails.

The EDS the system is text based and hence all data is input parametrically using abbreviated names. The interface is command line based (Figure 10) and consequently data can be slow to input. Training takes a long time as abbreviated names are indecipherable without help, and the lack of a graphical user interface makes the whole experience daunting for new staff. The final 'nail in the coffin' for EDS is the lack of staff who are able to program it. The original research team have now retired and there are very few electromagnetic machine engineers who are fluent in FORTRAN 77 code. Hence EDS is an excellent application specific software, but of limited use with new or highly saturated machines.



```

EDS server: ED50  MAIN 40730/C1 SYN PAH PRD Host: ED50 10 Aug 2011
OVSP: 2160 - Speed of overspeed test (rev/min)
OVSPD: 120 - Duration of overspeed test (sec)
OVCUR: 150 - Current of overcurrent test (pu)
OVCURD: 30 - Duration of overcurrent test (sec)
NHRUN: 1 - Number of heat runs
CUHR: ZPF - Type of heat run, sole or for Copper loss effects
FEHR:* * Type of heat run for Iron loss effects
NFHR:* * Type of heat run for (No) Field effects
EXTTIM: 2 - Specified extrapolation time (sec)
VLHR1: 6600 - Line voltage (V) on HR1
ILHR1: 1132 - Line current (A) on HR1
DURHR1: 3,5 - Duration (hours) of HR1
TSMH1: 62,5 - Maximum stator winding ETD temperature on HR1
RSMH1: 0.00906 - Stator resistance on HR1 (ohm/phase)
RFMH1: 0.3747 - Field resistance without dis res on HR1 (ohm)
RAEMH1: 0.02233 - Average exciter arm resistance on HR1 (ohm/phase)
RFEMH1: Unwanted - Exciter field resistance on HR1 (ohm)
TICL1: 11 - Temperature of internal coolant on HR1
TECL1: 7 - Temperature of external coolant on HR1
XPOT: 0.2066 - Potier reactance at rated load (pu)
IFRAT: 334,5 - Derived field current at rated load (A)
IFERES: -1,019 - Residual exciter field current (A)
SWFV: 14200 - Stator winding flash voltage (volt)
RWFV: 1500 - Field and exciter armature flash voltage (volt)
EFWFV: 1500 - Exciter field winding flash voltage (volt)
PMGFV: 1500 - PMG stator winding flash voltage (volt)
HTRFV: 1150 - Heaters flash voltage (volt)
SWIR: 23000 - Stator winding insulation resistance (MegOhm)
RWIR: 34800 - Field and exc arm insulation resistance (MegOhm)
EFWIR: 51000 - Exciter field insulation resistance (MegOhm)
PMGIR: 51000 - PMG stator winding insulation resistance (MegOhm)
HTRIR: 1,7 - Heaters insulation resistance (MegOhm)
BRGIR: 999 - Bearing insulation resistance (MegOhm)
NSHTC: 3 - Number of sudden short circuit tests
VSC1: 0,748 - Voltage (pu) for SC1
X1DSC1: 0.2371 - Direct axis transient reactance (pu) on SC1
X2DSC1: 0,134 - Direct axis sub-transient reactance (pu) on SC1
T1DSC1: 0,5933 - Transient time const (s) arm.SC on SC1
T2DSC1: 0.05189 - Sub-trans direct axis time const (s) arm.SC on SC1
TASC1: 0,1155 - Armature dc time constant (s) on SC1
VSC2: 0,5 - Voltage (pu) for SC2
X1DSC2: 0,2752 - Direct axis transient reactance (pu) on SC2
X2DSC2: 0,1579 - Direct axis sub-transient reactance (pu) on SC2
T1DSC2: 0,7273 - Transient time const (s) arm.SC on SC2
T2DSC2: 0,05221 - Sub-trans direct axis time const (s) arm.SC on SC2
TASC2: 0,1374 - Armature dc time constant (s) on SC2
VSC3: 0,25 - Voltage (pu) for SC3
X1DSC3: 0,277 - Direct axis transient reactance (pu) on SC3
X2DSC3: 0,1786 - Direct axis sub-transient reactance (pu) on SC3
T1DSC3: 0,7767 - Transient time const (s) arm.SC on SC3
T2DSC3: 0,04453 - Sub-trans direct axis time const (s) arm.SC on SC3
TASC3: 0,1629 - Armature dc time constant (s) on SC3
IFHR1: 330,5 - Final field current (A) on HR1
*****
>Enter EDS command:

```

Figure 10 - An EDS command window screenshot showing a list of variables.

2.4.2. Speed Lab

Speed Lab is an analytical machine design package which has been developed at the University of Glasgow. The package, which aims to be "*the most advanced CAD software for electric motors and drives*" [6], not only calculates machine performance but can be integrated with simulated power converters, allowing whole system simulation. Speed Lab allows the user to parametrically input data into the software which then predicts the system performance, based upon classical and published algorithms, so the results can be independently verified. A 2 dimensional 'cross-section editor' motor view is shown and hence varying dimensions is more instinctive than just standard text entry. Speed Lab is quick - calculating over 500 parameters in around 2 seconds. With the addition of scripting, Speed Lab can vary parameters and save months of manual optimisation.

Speed Lab has two major limitations - saturation and results feedback. The system has built-in material templates and specific material data can be input, but it only calculates saturation values at certain points within the machine and hence relies on certain assumptions such as radial flux or average flux density levels in regions. This simplistic approach is quick but can cause problems. For example, when the machine hits high saturation levels, such as when highly fluxed or during three phase short circuits. Speed Lab has automated output to finite element packages and even an integrated finite element add on, but these are intended as a final design proofing check - not as a design tool.

The Speed Lab designers have taken the approach that they will stick to classical equations and consequently the software has across the board performance, but not specific customisation. This means that if the machine designed isn't vastly different to the standard designs used in classical derivations the calculations will be accurate. However, creating a less standard design, for example inserting tooth vents or creating unique slot shapes, will cause inaccuracies to increase.

2.5. Finite Element Method

2.5.1. History

The Finite Element Method is a numerical analysis technique based upon a system of differential equations, designed to find approximate solutions to problems. The creation of the Finite Element Method is accredited to Richard Courant [7] who, in an expansion to a 1942 address to the American Mathematical Society, spoke about how variational methods, used by Lord Rayleigh, could be used in a wider scope. Using a set of two dimensional triangles, he termed 'elements', a series of piecewise linear approximations were carried out to solve the problem and the Finite Element Method was created. This mathematical work was built upon over the next few decades by such names as J Synge [8] and R Duffin [9], but didn't find a suitable audience until the advent of more advanced computing systems.

Several authors expanded the mathematical methods into various scientific and engineering disciplines, but within electromagnetism it wasn't until 1968-69 that the first true electromagnetic engineering works were published in concurrent works by Ahmed & Dlay [10]; Arlett, Bahrani & Zienkiewicz [11] and P Silvester [12]. Of these authors it is Silvester who has been credited with having the first real electromagnetic engineering application paper, and therefore could be given the title Father of the Electromagnetic Finite Element Method.

The Finite element method has grown over the past 40 years, with several thousand papers, journals and books dedicated to its study. The main facilitator in finite elements growth has been the increase in processing power. As Moore's Law [13] continues to predict performance increases, computers allow engineers to create more and more accurate models within simulations and gain solutions in more and more rapid times. This increased speed and accuracy is allowing Finite Elements to become the prevalent design tool for both final machine simulation and for cost estimation via tendering. It is now routinely used for even initial machine design characterisation.

2.5.2. Equations

This thesis is mainly concerned with electromagnetics, whose basis within the finite element method originates from the low frequency limits of Maxwell's Equations [14]:

Current density and Field strength are associated by Ampère's circuital law:

$$\nabla \times H = J \quad \dots(2.1) \text{ in vector representation}$$

Similarly the Maxwell–Faraday equation (Faraday's law of induction) defines electric field strength (E) and magnetic flux density (B):

$$\nabla \times E = -\frac{\partial B}{\partial t} \quad \dots(2.2)$$

Gauss's law for magnetism is defined giving B zero divergence:

$$\nabla \cdot B = 0 \quad \dots(2.3)$$

B and H are linked by the permeability where H_c is the coercive force of any extant permanent magnetic materials:

$$B = \mu(H - H_c) \quad \dots(2.4)$$

Whilst J and E are linked by the electrical conductivity:

$$J = \sigma E \quad \dots(2.5)$$

It is also useful to specify the magnetic vector potential, A :

$$B = \nabla \times A \quad \dots(2.6)$$

Static finite element models have time invariant magnetic fields and are defined by a non-linear Poisson equation. Vector potential is usually used for magnetic field analysis, as scalar potential cannot include current as the source of the fields.

Substituting (2.6) in (2.4) gives:

$$H = \frac{1}{\mu} \nabla \times A - H_c \quad \dots(2.7)$$

Substituting (2.7) in (2.1) gives:

$$\nabla \times \left(\frac{1}{\mu} \nabla \times A - H_c \right) = J \quad \dots(2.8)$$

With a time varying FE solver transient eddy currents solutions must be included. This modifies equation (2.8), which becomes:

$$\nabla \times \left(\frac{1}{\mu} \nabla \times A - H_c \right) = J - \sigma \frac{\partial A}{\partial t} \quad \dots(2.9)$$

where $\sigma \frac{\partial A}{\partial t}$ is indicative of any induced currents and J is any specified currents through either fixed current values or varying driving circuits in a circuit editor. Time varying transient solvers include rotating motion, linear motion and static electrically transient models.

2.5.3. Finite Element Design Systems

Modern Finite Element packages are normally based around a Computer Aided Design (CAD) user interface with several different solver modules used to process the data before the CAD interface is used to post process results. The usual method for using an FE system is to start by drawing the machine in either 2 or 3 dimensions. The user next specifies the driving source for the simulation by typically specifying any coils or boundary conditions or, in the case of static non time varying models, fixed potentials. The user must also define the material properties, normally by importing material BH curve data, and setting conductivities from a library or manually. Once the model is built the user sets the solver type and simulation parameters. This includes setting linear or non-linear solutions, the size of time steps for transient models, any geometric movements and any specific variables that need to be logged. Next a meshing process is undertaken. This is when the model is divided into a series of triangular or quadrilateral elements in the 2D sense, or tetrahedral, prismatic or cuboidal in 3D. Often this is fully automated within the FE package, with the user specifying options such as a maximum element size or number of elements in a region. The final step is to initiate the solver to find a solution. Some solvers are programmed to multi thread, taking advantage of extra

processing power, whilst other software houses have preferred to program 1 thread per solution, allowing many solutions to be found on a single computer at once. The solution can take anywhere from seconds to days, depending upon the complexity of the model and mesh.

Post processing the solution is normally undertaken within a CAD user interface, allowing objects to be selected for individual data extraction. Fields can be evaluated at points, along lines and over areas in 2D models, as well as in volumes and surfaces in 3D. These integral fields are calculated using the data stored by the solver. Additionally, data logged in circuits or mechanical values can be viewed. All the commands issued in the CAD GUI can normally be controlled using a peripheral command line or macro control code, typically in a modified coding language, which becomes specific to the individual FE package.

2.5.4. Finite Element Systems

Historically many companies or universities would have their own in house FE packages which were programmed, maintained and used by the same development team. This has fallen out of favour due to the complexity of organising a user friendly interface and managing the ever growing demands of users versus the development time required. These in house programs have either been sold and developed into commercial products or simply superseded by a cheaper competitive package, developed by a market place software house.

Within the marketplace there are several companies that have FE systems. Maxwell is the electromagnetism module from the ANSYS software suite [15]. The ANSYS company formed in 1970 during the dawn of commercial FE software and has capitalised upon the market to be a multibillion dollar company. Maxwell solves in 2D and 3D for all desired solver types and uses a C derived programming language. The user interface is quick and easy to use with many built in materials and designs. Infolytica MagNet [16] uses a C based coding system similar to Maxwell, with an easy to use interface and multicore meshing system. Other than native nuances the systems are similar.

Cobham Opera Vector Fields [17], unlike previous systems, was historically programmed using a Fortran code base, so the scripting and macros are also in a modified high level Fortran derivative. This difference in code base makes the initial

training period longer as most engineers are taught C derived code at University. However, Fortran does allow the code to run faster, as Fortran is a simpler language and preferred for high power computing [18]. Opera, particularly in 2D, is designed around a command line interface, allowing powerful commands to be executed directly from the main window. Consequently the user interface is not as developed. Opera has all the required solvers, but they are all currently programmed for individual processing thread operation. Tera Analysis Quickfield [19] is another FE system with the associated solver and user interfaces. As a smaller competitor to the likes of ANSYS they claim to be more affordable. JMAG [20] is another company that specialises in finite element analysis for electromagnetic systems. The company, formed in 1983, initially focussed upon 3D modelling before creating a 2D product. Like many other solvers, JMAG can be scripted, but this time in Python, VB script or J script.

The majority of these programs allow embedding of the solver within a script inside a MATLAB or Simulink program. This allows the simulation of more complicated motor/drive systems. This integrated set up can, however, be slow as for every time step MATLAB will have to call the FE solver.

Many of these FE systems have scripted front end macros that will automatically draw, simulate and evaluate designs using parametric input values. For example, Infolytica has Motorsolve, JMAG use Motor Bench and Cobham have Optimizer. ANSYS has DesignXplorer, which varies a user's design to find variations. Each one of the holistic packages has many of the same features, taking parametric data to draw specific machines within certain bounds. The packages then often set up standard rotating simulations to determine charts for parameters such as cogging torque, open circuit voltage, inductances and losses. Some of the packages, such as Motor Bench, can also be programmed to do some basic structural analysis. These packages are excellent outline design tools, but have several fundamental limitations.

1. Limited user data input. As these design tools are programmed for generalised designs, if the simulated machine does not fall within the standard design template then either the machine cannot be simulated or an approximation must be accommodated. For example, Motor Solve has modules for Brushless DC, Induction and Switched reluctance machines but as yet does not accommodate

wound field synchronous machines - a major limitation for a generator manufacturer.

2. Limited Parameter Output - The systems are set to give typical charts that are desired by engineers, such as Current, Back-EMF, Torque or Flux Linkage plots, however analysis of these is often not incorporated, or the correct charts are not even produced. For example a torque chart is normally produced, but the cogging torque must often be manually calculated. Specific parameters, such as transient or subtransient reactances, which are mainly specific to synchronous generators, are not even calculated.
3. Lack of Manufactured Machine Feedback - The biggest limitation of any integrated system that is developed for general usage is that when it is used in a specific setting the accuracy must invariably drop and the benefits of using a FE system are lost. The feedback from specific manufactured cases could be appended to create a customised system, but this must be done for every machine case and is not economic or possible for a commercial software development house, who often do not have access to this commercially sensitive data.

2.6. Integrated Design Systems

The company desires a proven integrated design system. This will allow the user to have 'sit and go' functionality without having to learn many systems. The user is removed from the internal calculations, so there is a lower chance of making calculation errors or typographical mistakes. Although this process in effect de-skills the end user and creates a 'black box' that calculates a solution, it does provide a high level of transparency and accountability once the system has been proven.

Consequently, a specification has been formed that defines a desirable design package:

- It must have an easy to use graphical user interface
- It must be validated against existing test results
- It must be more accurate than any existing design system
- The user must be removed from the calculations

2.7. Chapter Summary

The development of design tools started with experimental trial and improvement, which expanded through into trend sheets to allow rapid scaling of designs. As knowledge increased analytical models were created, using what are now considered the classical machine equations. These models allowed designs to be more accurately predicted and hence, as machines matured, the need to prototype was removed through both the prohibitive cost and the incremental nature of development. Before cheap, quick computing was available these analytical models were again developed into trend sheets, so tendering engineers could estimate costs without having to expend effort in slowly calculating a whole design. As computing power increased the analytical models were implemented and hence calculated designs very rapidly, but the systems still suffered from fundamental problems - poor calculation of leakage field paths and saturation levels, as well as the inability to quickly adapt to new machine types, such as permanent magnet generators. Modern finite element analysis solves all of these problems and should give accurate machine predictions, but at the expense of time. Even with the addition of multiple processing and clever pre and post processing software routines, finite element analysis struggles to be fast enough for a design tool. Additionally, even if an existing FE system is quick enough, it does not produce the correct set of parameters required by the tendering engineers.

Consequently there is scope for a piece of work to occupy this region in-between slow finite element models with high accuracy and fast, but less accurate, analytical models. This middle ground is perfect for primary tendering design and even for secondary final design in standard machines that are inside the companies experience and hence do not need the third detailed finite element design stage. The work must create methods that:

- are more accurate than analytical design
- are faster than a standard finite element simulation
- are consistent at getting the same solution
- provide the desired parameters that the engineers require

More specifically a maximum time limit of 1 hour to complete all calculations is a reasonable target. Although this cannot be described as 'fast' it is a maximum and many

individual part calculations should be completed in less than this time. Also when the analytical methods were first computerised into full design packages they took many minutes to calculate and only through 30 years of PC development have the calculations been reduced to seconds. It is reasonable to assume that the same computing acceleration will continue reducing the hour marker sizeably.

The specific electrical parameters that the engineers require are:

- Open circuit, short circuit and zero power factor saturation curves, including field current for 1 pu operating points
- Field current for 1 pu full load operating point.
- Direct axis reactance, transient reactance and subtransient reactance
- Total Harmonic Distortion, Telephonic Interference Factor and Telephonic Harmonic Factor.
- Iron Loss

Chapter 3. Initial Design Characterisation

3.1. Introduction

Traditionally, manufacturers of large rotating electrical machines have used analytical methods to predict performance. This was chiefly due to the limited availability of finite element packages and computers with suitable processing power. Over the past twenty years or so there has been a substantial increase in the number of commercially available electromagnetic Finite Element (FE) packages. This along with the development of high performance computers has now allowed electrical machine manufacturers the opportunity to develop new performance prediction packages that make use of FE methods for improved performance prediction, and hence a more optimum machine, with the key objective being cost reduction.

Finite element methods should potentially be more accurate than analytical based methods as a result of better prediction of field paths; in particular leakage paths and saturation. The major restraint of FE methods is computation time; a typical 2D rotating solver solution with an average mesh distribution and suitable time step may take several hours to complete.

This Chapter specifically focuses on the prediction of initial design variables. These initial characteristics, often referred to as the saturation curves, are the open circuit, short circuit and zero power factor saturation curves. They are one of the standard set of charts that customers request during the tendering stage of any project and they are also created during standard factory testing. To accurately predict the saturation curves several additional analytical and FE factors need also to be calculated. These factors, such as effective axial length or end winding leakage reactance are not specifically requested by the customer and often they cannot be found by testing but are essential in the accurate calculation of saturation curves.

3.2. Methodology

3.2.1. Magnetic Coupling

Figure 11A shows the cross section of a four pole geometry constructed in an electromagnetic FE package [21] with stator excitation. The voltage induced in a conductor is equal to the time (or position for a given speed) derivative of the flux linking that conductor:

$$v = \frac{d\phi}{dt} \quad (3.1)$$

The magnetostatic solver calculates vector potential, A_z , (essentially flux linkage per turn per unit length) in a conductor relative to the boundary conditions on the machine ($A=0$). The flux linkage is calculated by multiplying the Average Vector Potential (AVP) in a conductor by its axial length and turn number. The average vector potential in a 2D FE simulation is calculated by integrating over a region and dividing by that region's area.

$$\phi = AVP \times l_a \times turns = \frac{\iint A d(\text{Area})}{\text{Area}} \times l_a \times turns \quad (3.2)$$

3.2.2. Pseudo Rotating Superposition

Producing a voltage waveform using a rotating solver with a satisfactory resolution requires a number of solutions at a number of positions over a single rotation of the machine. The required time step is inversely proportional to the resolution required. If high frequency slotting harmonics are required the total solve time can be significant due to the high resolution and resulting low time step.

The Pseudo Rotating Superposition method (PRS) method developed by the author uses a single solution of a magnetostatic solver to achieve the same waveform made up of all the harmonics up to the $n/2$ th harmonic where n is the number of slots per pole. This use of a static solver removes the need for a time consuming rotating solution.

The effect of moving the rotor can be achieved in a static simulation by calculating flux linkages using different conductor regions. In a normal rotating FE simulation the average vector potentials in the conductors comprising a stator phase are summed up to

calculate the flux linkage. The rotor is then moved before the solution for the next step is calculated. In the new solution the same conductors are used to calculate that phases flux linkage. This process is repeated for every time step requiring 1 solution for each time step - a slow process. Using a static simulation the process starts in the same manor, a solution is formed and the conductors of a phase are summed to extract the flux linkage. Then rather than moving the rotor, the reference point for the conductors is shifted meaning the conductors extracted for summation have moved by a slot. This could be imagined as rotating the stator as it has periodic symmetry of 1 slot. Since the geometry has not changed there is no need to solve the FE solution again hence only a single static FE solution is required.

This is best demonstrated using diagrams; Figure 11B and Figure 11C show the rotor in two different positions - the rotor has rotated 1 stator slot width (6 degrees) anticlockwise. The highlighted conductors in B and C have the same average vector potential as their respective conductors in the other machine (i.e. average vector potential in conductor B1 = average vector potential in conductor C1 e.t.c.). This is clearly visible by looking at the relative position of the conductors to the rotor. Since machines A and B have a shared geometry i.e. the rotor has not moved so only a single solution is required to extract all the data for both positions A and B.

Converting to using a single static simulation means that equation (3.1) is modified to become a function of the number of slots, equation (3.3). Only a single solution is required where one solution per slot was used before. Hence this use of Pseudo Rotating Superposition will on average make the calculation for a geometry with thirty slots per pole pair around thirty times quicker.

$$v = \frac{d\phi}{dt}$$

$$v = \frac{d(AVP) \times la \times turns}{1} \quad (3.3)$$

$$f \times Slots$$

$$v = (AVP_{topofslotconductor} - AVP_{bottomofslotconductor}) \times la \times turns \times f \times Slots$$

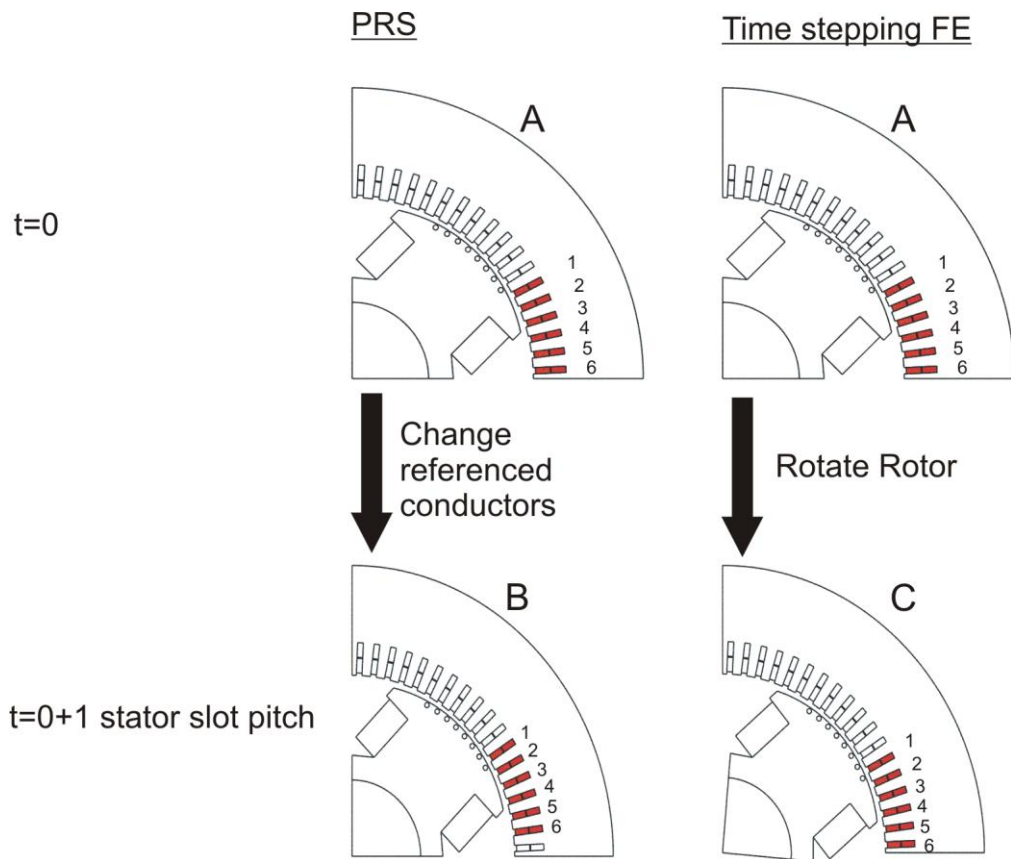


Figure 11 - PRS and standard FE method diagrams

3.2.3. Open Circuit Curve (OCC)

Figure 12 shows the voltage/current phasor diagram of an open circuit synchronous machine. It shows that to attain an open circuit curve field excitation has to be placed in the geometric d-axis. On a salient pole wound field synchronous generator this is simply energising the field as the coil is wound around the poles which are centred on the d-axis. The extracted average vector potentials are processed using the described PRS method and the voltage waveform established as shown in Figure 14. A Fourier transform is used to find the fundamental magnitude of r.m.s. line voltage allowing it to be plotted against the field current. Several different field excitation levels are required to create a single open circuit curve as shown in Figure 13. Therefore for the open circuit curve shown 10 individual static simulations were carried out each with a different level of field current. Figure 15 shows a screen capture of a generator under open circuit analysis. Only the field winding has any current present as shown by the strong positive (magenta) and negative (blue) coloured current density regions. Additionally Flux lines have been plotted showing the strong d axis flux and the small

quantity of flux which is leaking across the interpolar region on the rotor and therefore not linking any of the stator coils.

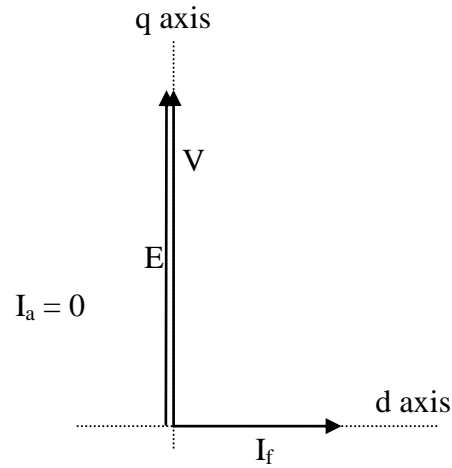


Figure 12 - Open circuit phasor diagram

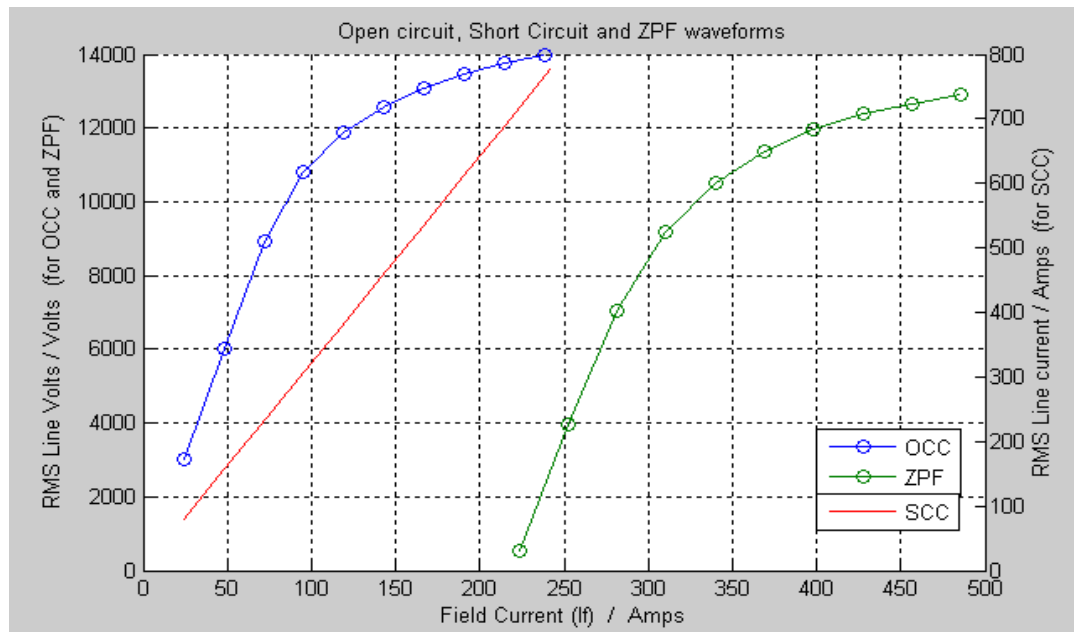


Figure 13 - A typical open circuit, short circuit and zero power factor saturation curve chart.

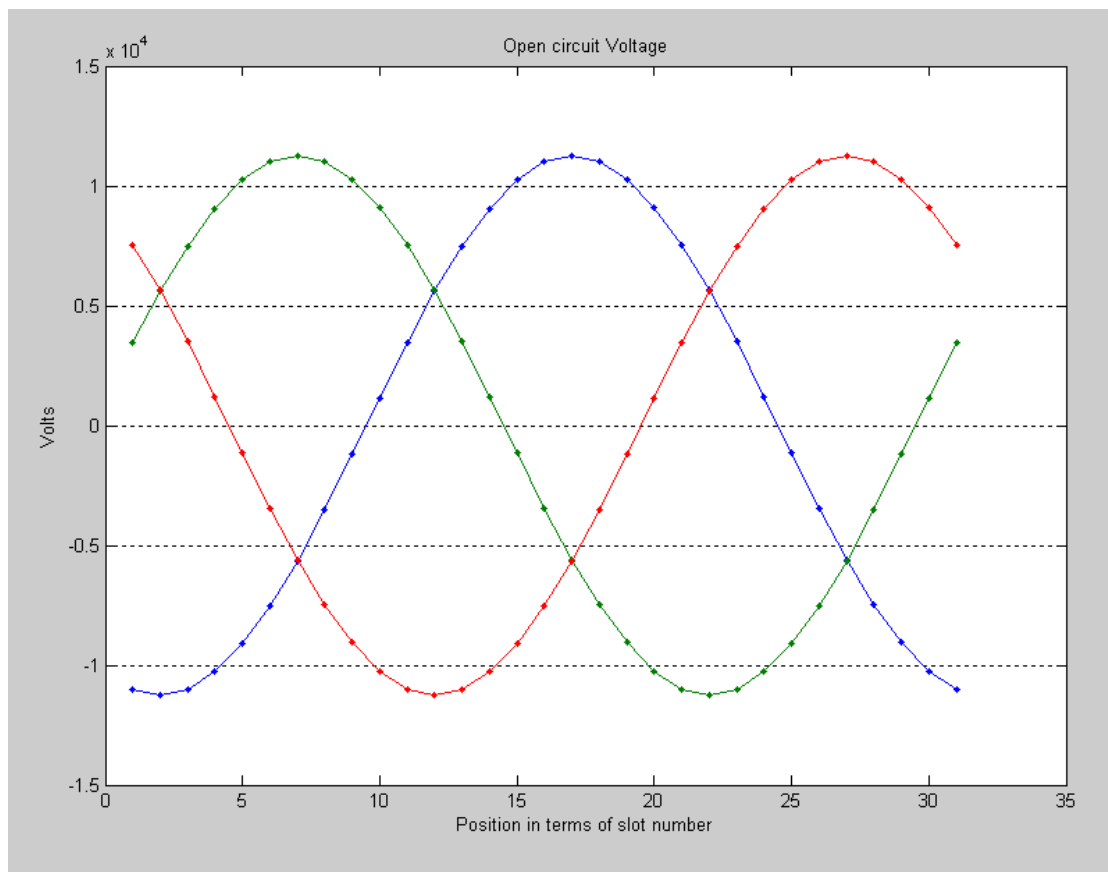


Figure 14 - Open circuit line voltages at a single excitation level. Each point represents a calculated value. All the points are calculated using data from a single static FE simulation

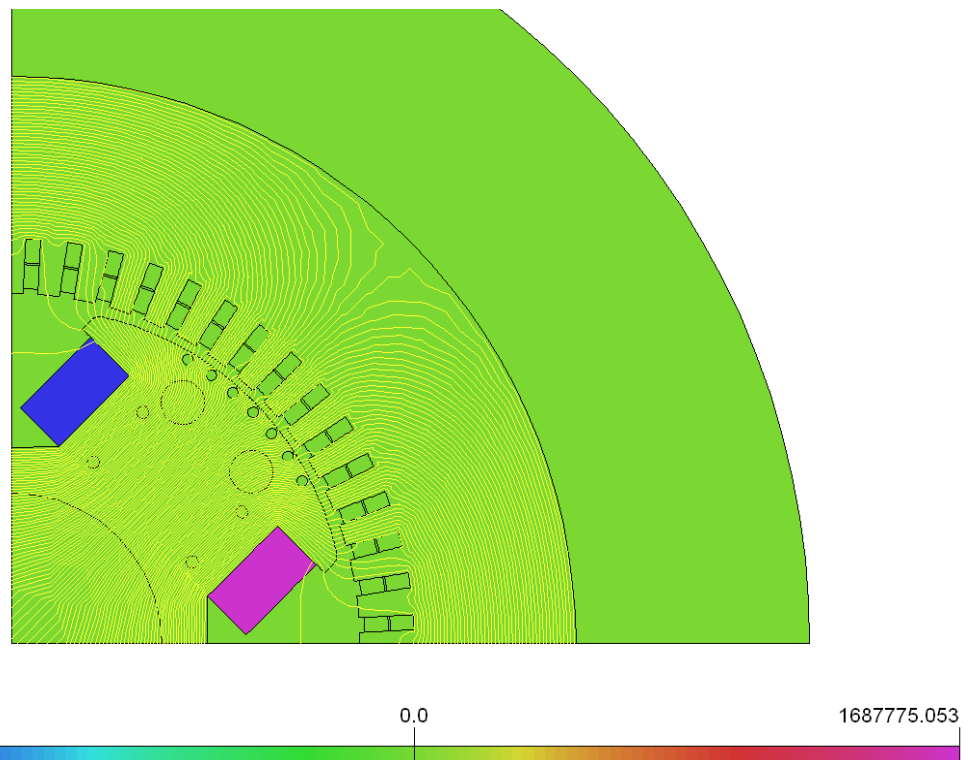


Figure 15 - A Finite Element plot of a generator under Open circuit simulation. [Scale for current density, J is in A/m^2]

3.2.4. Sustained Short Circuit curve (SCC)

Figure 16 shows a phasor diagram of a sustained short circuit. Envisaging the machine as a transformer as in Figure 17 it can be seen that during a sustained short the rotor produces an MMF equal to the stator MMF minus a component of MMF associated with the stator leakage. This aforementioned MMF is the net MMF in the air gap thus the flux level in the machine is low. The low flux level means that the system is in the linear region of the BH curves so only a single static solution is required.

The stator winding is excited with typically 0.2 p.u. rated stator current to achieve a representative saturation level. Using PRS, the line voltage is calculated and compared to the open circuit saturation curve which is calculate above. The voltage has an associated field current (I_f), hence the I_f to armature current (I_a) relationship of a sustained short circuit curve is formed. This relationship of I_a/I_f is the gradient of the short circuit saturation curve.

A 2D solver is used so the end winding component of the stator leakage is not included. Therefore for a fixed stator current this increased reactance would result in a larger line voltage. The end winding reactance is calculated later in Equation 3.25 and the field current is scaled proportionally. A sustained short circuit is essentially a zero power factor case pertaining to d axis current flow i.e. the zero power factor case with zero terminal volts. Figure 18 shows a finite element plot of a generator being simulated. The simulation is not as short circuit would be in reality as the field winding current density is zero - only the stator is being excited. The stator conductors are all carrying current in a three phase set. The outer 2 phases with high current levels shown by the blue and magenta create a strong d axis flux. The central phase which has yellow current densities (slightly positive) would be zero if the generator did not have a short pitched winding. The short pitched winding means that to correctly apply d axis stator current Clarke (and where necessary Park) [22] transforms are used.

Using this stator excitation there is potential to create phase belt harmonics which could potentially skew the results. However as the machines have a distributed winding with several slots per pole the magnitude of this will be small. Additionally in this instance only the fundamental is being inspected to a higher order harmonic will be of little significance.

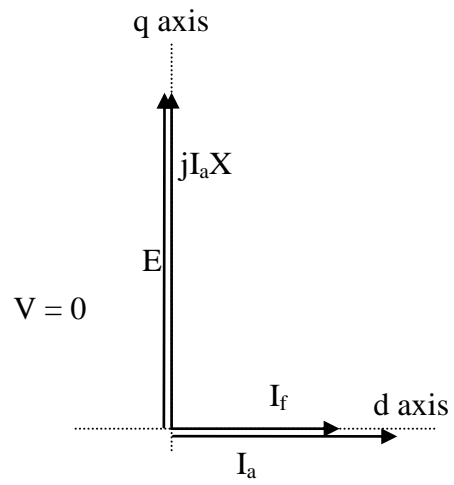


Figure 16 - Short circuit phasor diagram

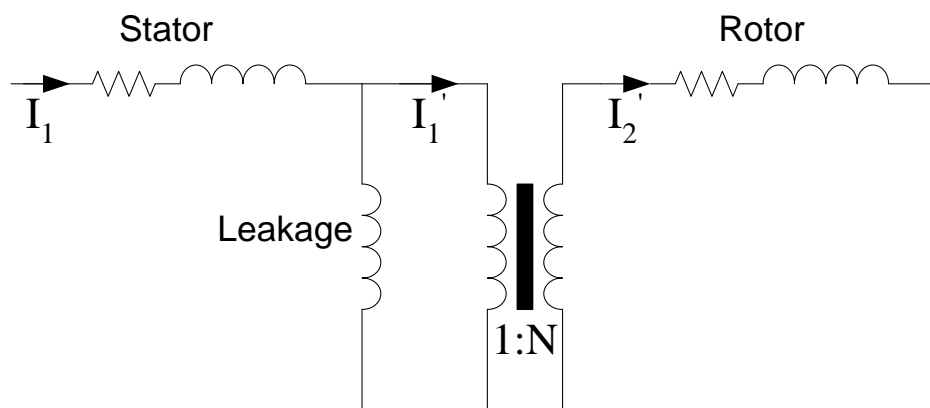


Figure 17 - Rotor & Stator linkage envisaged as a transformer

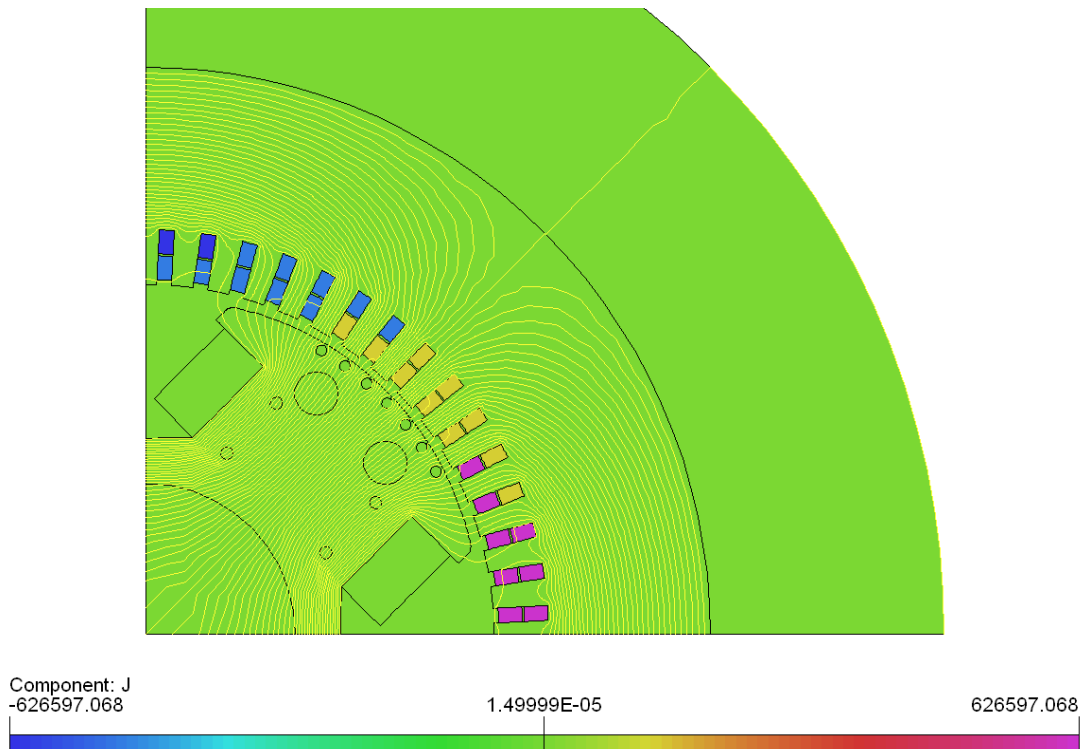


Figure 18 - Finite element plot of a generator under stator excitation [Scale for current density, J is in A/m^2]

3.2.5. Zero power factor curve (ZPF)

Figure 19 shows the generator operating under zero power factor conditions. Under zero power factor conditions the aim is to run the machine with a power factor equal to zero which equates to connecting the machine to another generator excited to have a high inductance. During the factory characterisation tests the machine is connected back to back with another synchronous machine and a test set which comprises of an another pair of synchronous generators separated by a differential gearbox allowing variation of load angle and hence power factor. The machine runs at rated armature current when connected to the load and hence on a real machine this test can be useful to mimic the heating the machine would experience when running under rated load conditions. This I^2R heating run is often referred to as a ZPF heat run and is used to warm the machine to rated temperature for other tests. As the load is inductive and therefore reactive power is required relatively little real power is used.

From Figure 19 it can be seen that the current is placed into the d-axis. Again this is achieved in the FE by the use of Park and Clark transforms as in the short circuit case. To create the saturation curve the field current is varied and the PRS method is applied to attain the line voltage for the various field excitation levels. A single simulation is required for each zero power factor loading case. Again the curve is adjusted to account

for the end winding leakage component. Figure 20 shows a finite element plot of the machine under zero power factor simulation. Inspection shows the rotor to have d axis excitation and the stator having currents arranged in a similar manor as the short circuit case i.e. effectively opposing the MMF from the field winding.

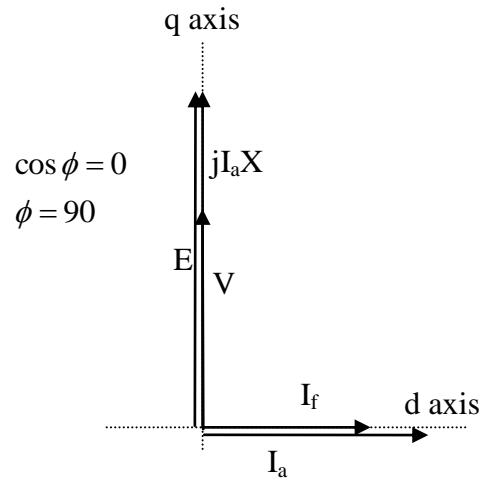


Figure 19 - Zero power factor phasor diagram

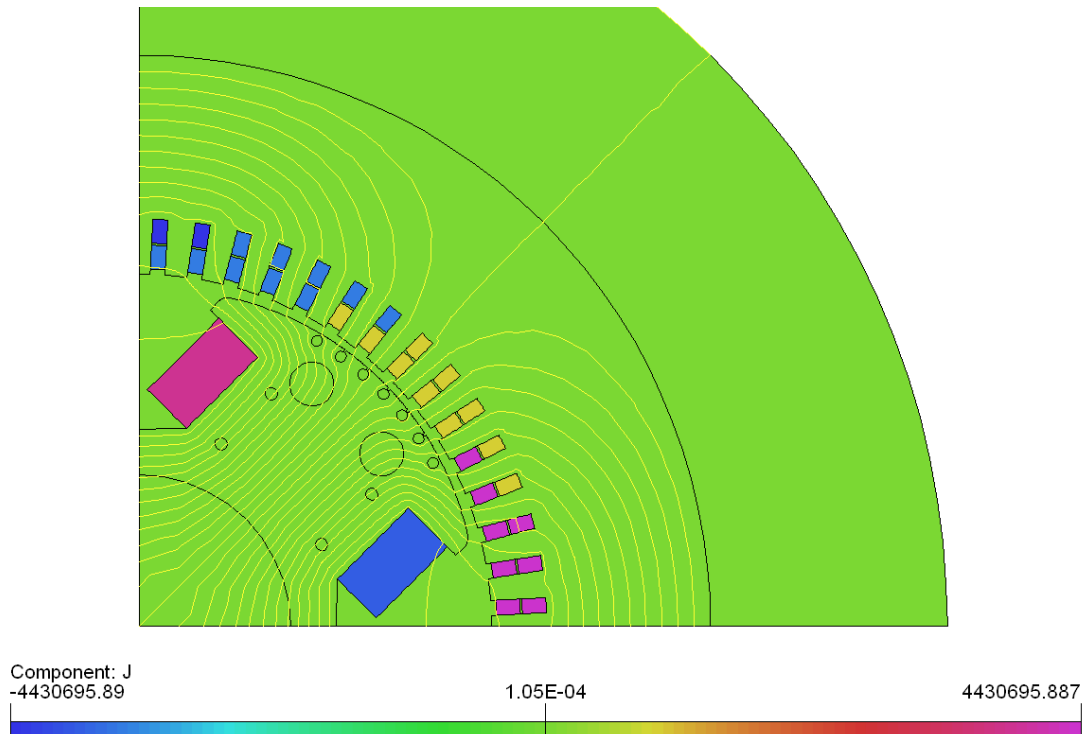


Figure 20 - Finite element plot of a generator under zero power factor simulation [Scale for current density, J is in A/m^2]

3.3. Further Calculations and Considerations

3.3.1. Effective Axial Length

To a first approximation rotating synchronous generators can be assumed to have a constant cross section, allowing finite element simulation to be calculated in two dimensions. With calculations in a two dimensional plane an axial length of the machine must be used to determine the machine performance. This length is primarily based upon the stack length of the laminations, but effects around the air gap and specific construction methods force further calculations in order to get accurate results.

Fringing around the air gap region at the end of the lamination stack increases the amount of flux that passes from the rotor to the stator. This extra flux increases the induced voltage for a given field excitation. To incorporate the extra flux into the 2D calculations the axial length is accordingly lengthened.

To do this a 2D FE simulation of the air gap axial length is modelled at a nominally fixed one metre length (Figure 21). This model created is in the axial plane rather than a more conventional radial slice (Figure 22). The 2D model contains regions to model features such as endplates, the shaft and the flux that is allowed to flow in the end region. By setting the boundary conditions to fixed potentials in the FE package flux can be forced to travel from stator to rotor. To create this the boundary conditions are shown as set in Figure 23.

To calculate how long the extra effective axial length to account for fringing is the 2D model must be compared to a 1D model of the same scenario. In a 1D model the MMF drop across the air gap can quickly be calculated. As in the FE the change in vector potential $\Delta A = 1$,

$$\text{Therefore the 1D flux density} = B_{1D} = \frac{\Delta A}{L} = \frac{1}{\left(\frac{l_a}{2}\right)} = \frac{2}{l_a} \quad (3.4)$$

Assuming all the MMF is across the air gap and the permeability of air is μ_0 the MMF required to create flux density can be found:

$$MMF_{1D} = H \cdot l_g = \frac{B_{1D} \cdot l_g}{\mu_0} \quad (3.5)$$

From the 2D FE simulation the average H field in the air gap can be found by integrating along the axial length of the model.

$$H_{airgap} = \frac{\int H \cdot dl_a}{l_a} = \int H \cdot dl_a \quad (3.6)$$

The ratio of the 1D MMF to the 2D FE MMF is the proportion by which the lamination axial length must be scaled to account for the extra axial length caused by fringing [equation (3.7)]. Typically for a machine with a large aspect ratio (axial length to radial air gap length) the extra length per end is 2.4 times the radial length of the air gap as can be seen in Figure 24 and Figure 25.

$$\text{Scaling Factor} = \frac{\text{Machine without end effect}}{\text{Machine with end effect}} = \frac{MMF_{1D}}{MMF_{FE}} = \frac{MMF_{1D}}{H_{airgap} \cdot l_g} \quad (3.7)$$

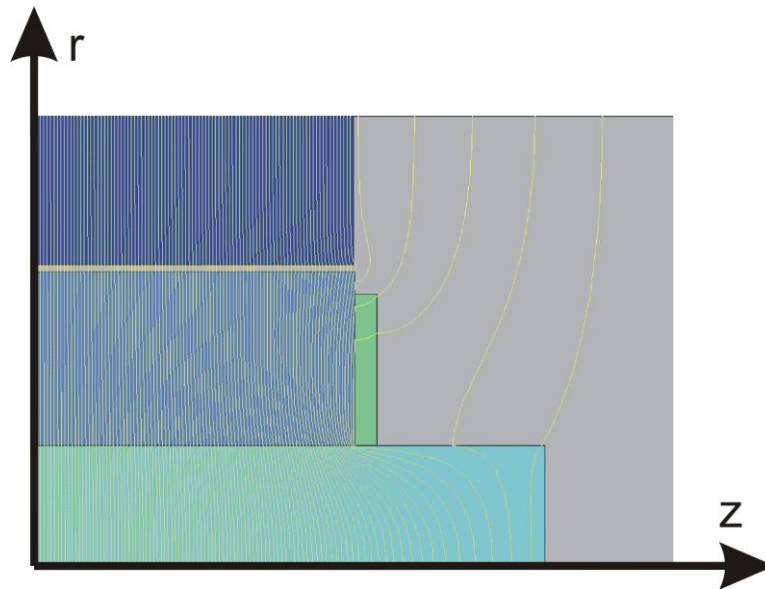


Figure 21 - Axial 2D FE simulation at peak flux density showing stator, rotor, endplates and the shaft.

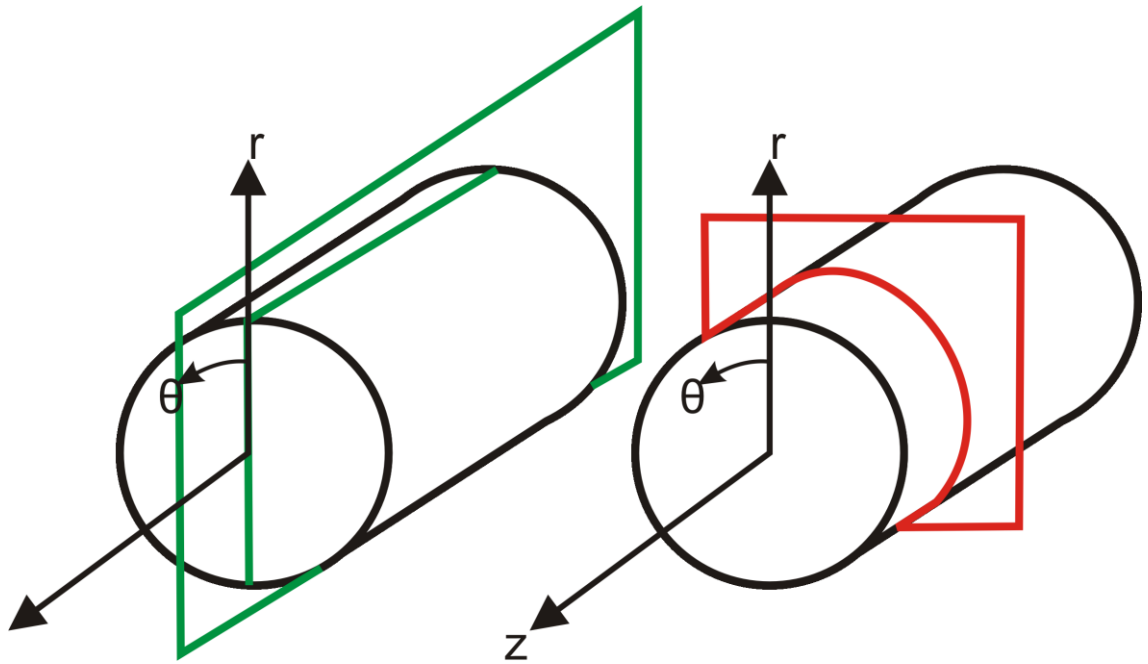


Figure 22 - Diagram showing the positioning of 2D axial (left) and radial (right) slices on a 3D model

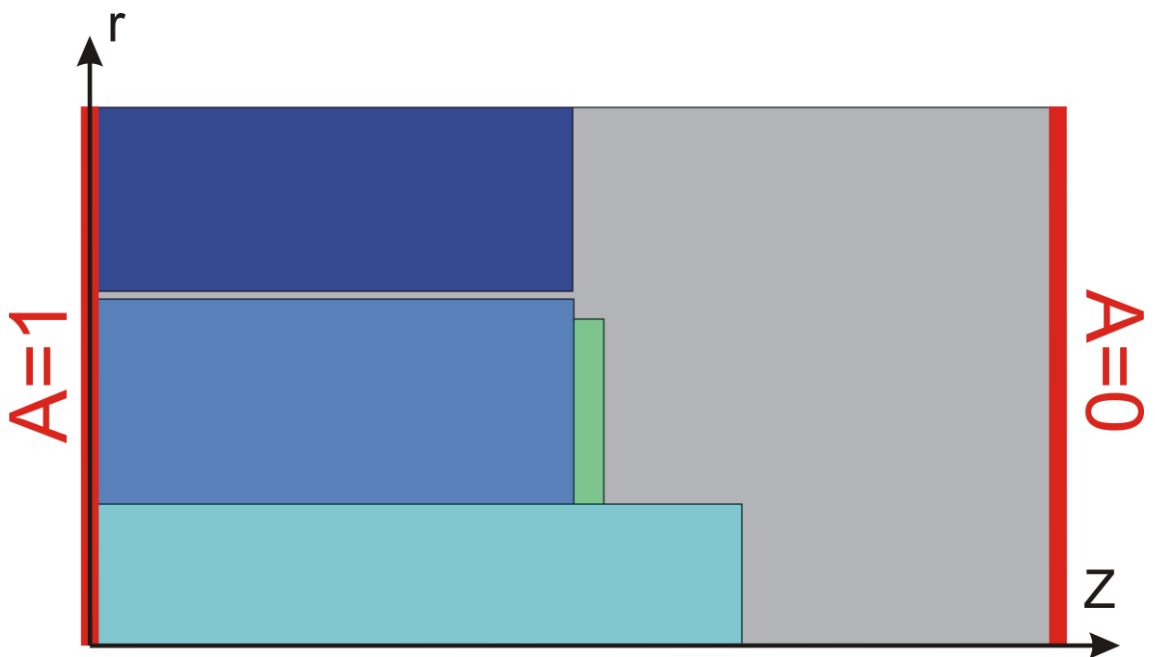


Figure 23 - Diagram showing boundary conditions

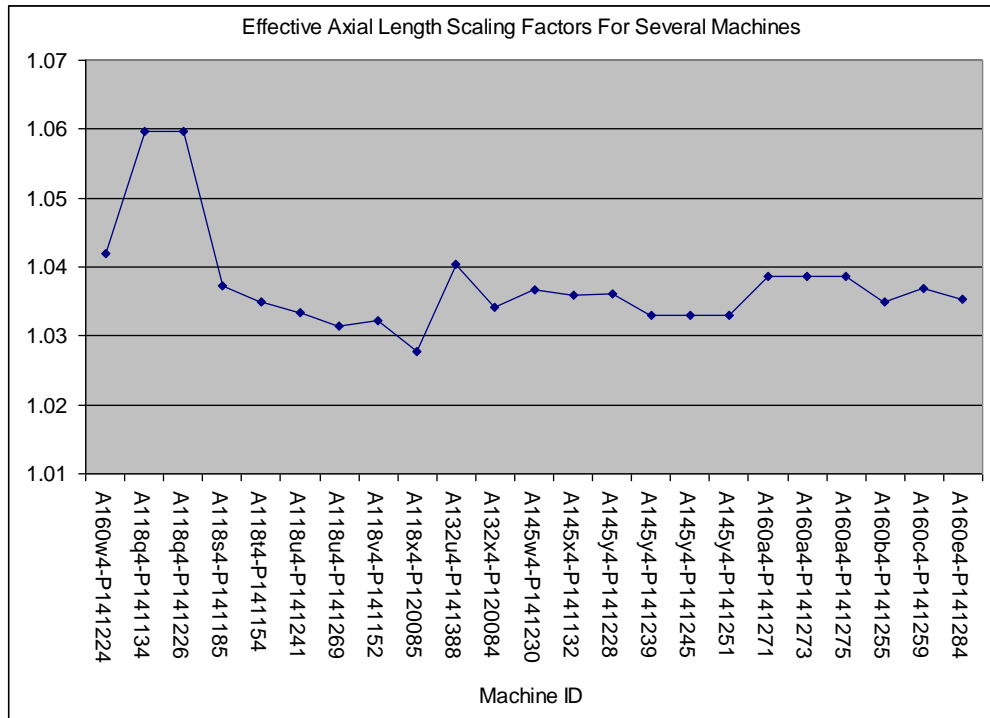


Figure 24 - Graph showing axial length scaling factors for several machines

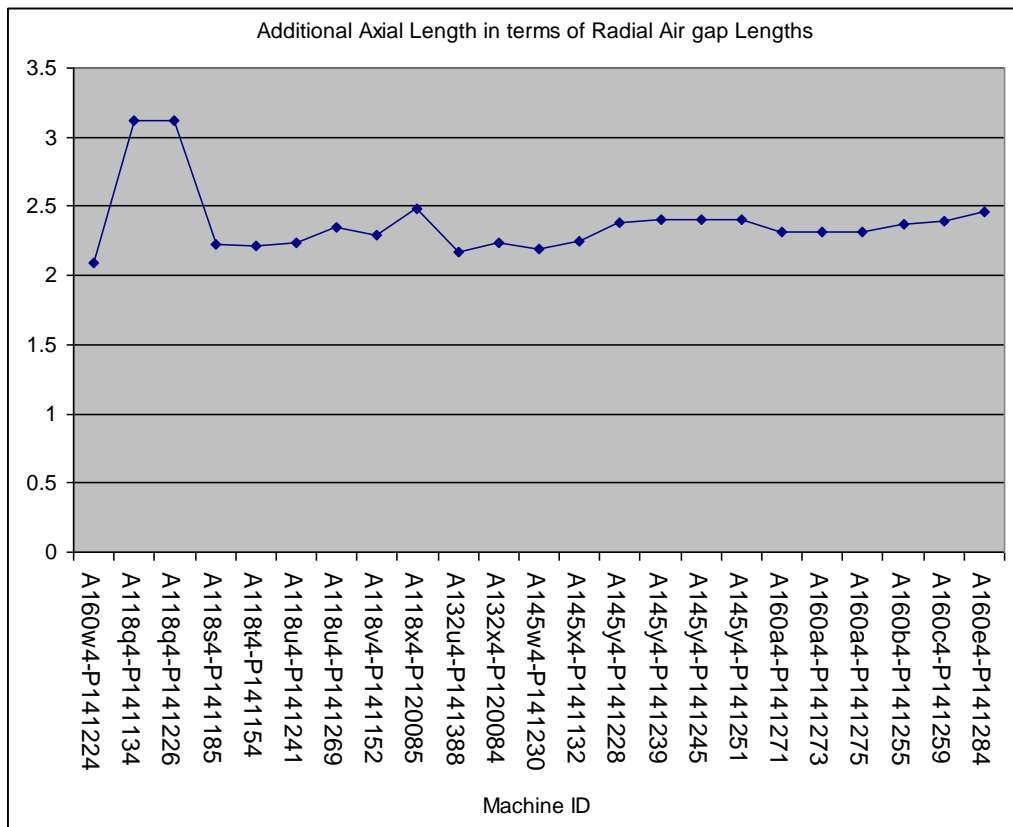


Figure 25 - Graph showing Additional Axial length for several machine in terms of radial Air gap Length

The 2 machines that have seemingly anomalous effective axial lengths are the geometrically smallest machines in the data set. The machines A118q4-P141134 and 118q4-P141226 are only 4.375 MVA and 5 MVA respectively. This in itself is not abnormal - A118t4-P141154 is only 5.3MVA but the 2 smallest machines have axial length of only 0.84 m compared to the 1.02 m of the A118t4-P141154. All of the A118 series machines have an 8mm air gap and a 32mm endplate. Consequently the shorter the machine the bigger the effect the endplate will have upon the scaling factor. In an extreme case of a very short machine the thick endplate would be responsible for creating a very large effective axial length scaling factor. In theory as the machine shrinks in length the clamping force that is required on the rotor lamination stack decreases and hence the endplate should be reduced in thickness. However as this would require a new manufacturing drawing, a new part number, a new order line and new mechanical calculations a single endplate is used for a range of machines. As a result for the shortest machines, such as 118q4-P141134 and 118q4-P141226, the end plate is thicker than required but actually cheaper!

3.3.2. B-H curve Dilution

To aid cooling many generator stators and rotors are constructed using radial ducts which are visible in Figure 26. These ducts are typically separated using small non-magnetic pins or I-beams. These spaces complicate the simplistic assumption that the machine is constant along its axial length. Also even though the lamination stacks are pressed during manufacture, air still remains between the laminations. This is chiefly due to burrs of metal and other small surface contamination obstructing the laminations and not allowing the individual laminations to be fully in contact. Furthermore the stator laminations are insulated to prevent eddy currents introducing yet more non-magnetic material. In a 2D simulation the results are calculated per unit length and as such, if the manufacturer supplied BH curves are used without modification, the FE software assumes the whole machine is solid - that is without any non-magnetic material in the stack.

To counter this problem the BH curves are diluted by a factor which makes the lamination stack less permeable thus inclusively averaging out any ducts, insulation or air. The ducts and air are included by summing up the axial length of the iron relative to the effective axial length. The duct length is known so is easily included. The insulation and trapped air which cannot be removed by the press creates a stacking factor which

has been found empirically by in house experimentation. From measurements this scaling factor is typically 0.97. The dilution factor is calculated as in equation (3.8) by a combined packing factor calculated below. Figure 27 shows a graph of BH curves before and after being diluted whilst Figure 28 has total Packing factors for a range of machines.

$$\text{Packing factor} = \frac{\text{Iron Length}}{\text{Effective Axial Length}} = \frac{0.97(l_a - N_d w_d)}{\text{Effective Axial Length}} \quad (3.8)$$

l_a - Axial Length

N_d - Number of radial ventilation ducts

w_d - Axial width of ventilation ducts

Once the Packing factor has been calculated the points of the BH curve are each transformed using the packing factor. This new diluted BH curve is the material data which is input into the final finite element simulation. To dilute the BH data it must be recognised that the packing factor is essentially a ratio of material to total length. Take the simplest case in equation (3.9).

$$B = \mu_0 \mu_r H \quad (3.9)$$

As B is made of up of 2 proportions the equation can also be written in terms of a material, M and a vacuum part:

$$B = \mu_0 H + \mu_0 M \quad (3.10)$$

Rearranging gives an equation for M

$$M = \frac{B - \mu_0 H}{\mu_0} \quad (3.11)$$

Only the material part of equation (3.10) is modified by dilution. It is diluted by the Packing Factor (PF).

$$B = \mu_0 H + \mu_0 M \cdot PF \quad (3.12)$$

Substituting (3.11) into (3.12) gives an equation which can be used to calculate the new diluted B value using the existing old B value.

$$B_{new} = \mu_0 H + \mu_0 \left(\frac{B_{old} - \mu_0 H}{\mu_0} \right) \cdot PF \quad (3.13)$$

$$B_{new} = \mu_0 H + (B_{old} - \mu_0 H) \cdot PF \quad (3.14)$$

This process can alternatively be thought of as a sum of 2 parts that make up axial length - the iron and the air. For example in a case where the axial length is 95% iron and 5% air an equation for B can be formed:

$$B_{diluted} = 0.95 \times B_{iron} + 0.05 \times B_{air} \quad (3.15)$$

Given that the 5% air is simply 100% total length minus 95% iron and that $B_{air} = \mu_0 H$ some substitutions and rearrangements can be made

$$B_{diluted} = 0.95 \times B_{iron} + (1 - 0.95) B_{air} \quad (3.16)$$

$$B_{diluted} = 0.95 \times B_{iron} + (1 - 0.95) \mu_0 H \quad (3.17)$$

$$B_{diluted} = 0.95 \times B_{iron} - 0.95 \times \mu_0 H + \mu_0 H \quad (3.18)$$

$$B_{diluted} = 0.95 \times (B_{iron} - \mu_0 H) + \mu_0 H \quad (3.19)$$

As 0.95 is simply the packing factor, PF , equation 3.19 can easily be shown to be the same as 3.14

$$B_{diluted} = PF(B_{iron} - \mu_0 H) + \mu_0 H \quad (3.20)$$

This equation can be further simplified within the FE Program by converting to the cgs unit system for the BH curve dilution and switching back to SI afterwards. This simplification occurs as within cgs as the units for flux density and magnetic field strength are Gauss and Oersted respectively and therefore $\mu_0 = 1$. Hence equation 3.14 becomes:

$$B_{new} = H + (B_{old} - H) \cdot PF \quad \text{within cgs unit system (3.22)}$$



Figure 26 – Photograph of Machine Radial Ventilation Ducts

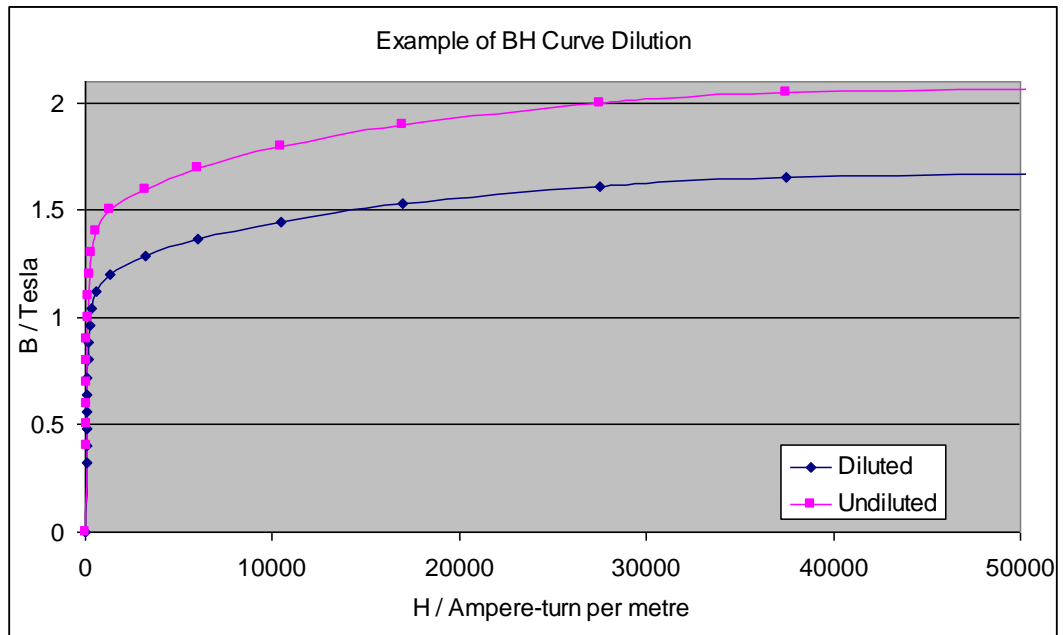


Figure 27 – Graph of an example B-H curve before and after dilution by 0.82

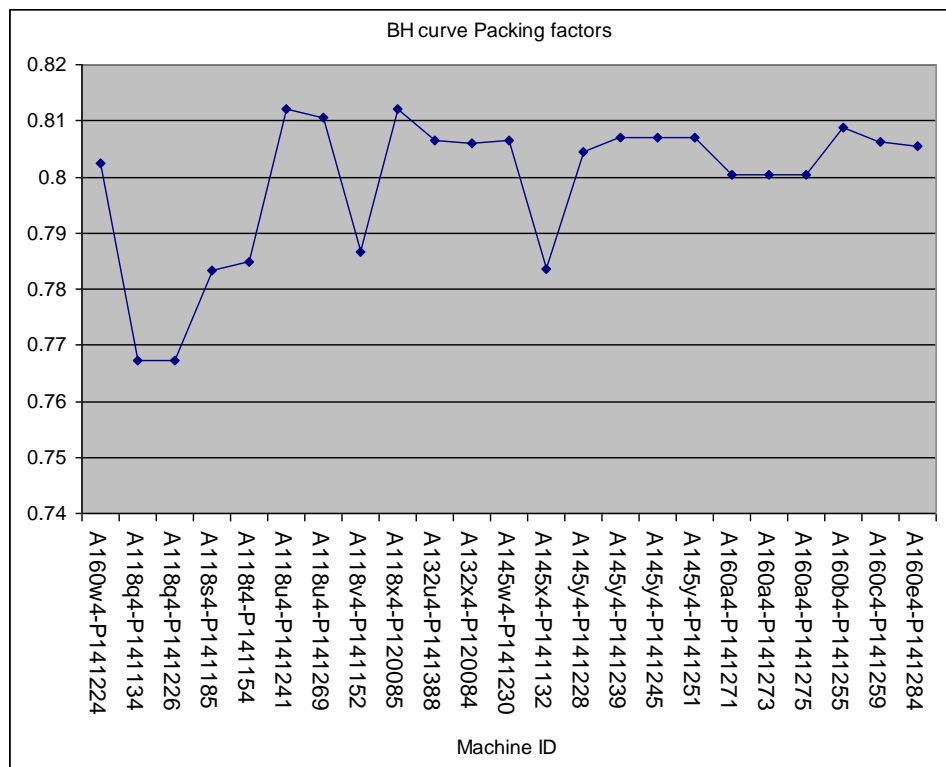


Figure 28 – BH curve Packing factors for a range of machines

3.3.3. End winding Leakage

Two dimensional FE simulations are used to reduce computation time but exclude significant 3D leakage flux paths. These however can be calculated analytically. The end winding component of stator leakage permeance is calculated as in equation (3.23):

$$\Lambda_{1e} \approx 0.42 \cdot q_1 \left(1 - \frac{2}{\pi} \frac{w_c}{l_{1e}} \right) k_{wl}^2 \quad (3.23) [23]$$

$$\text{Where } q_1 = \frac{z_1}{1p \cdot m_1} \quad (3.24) [23]$$

w_c - Conductor Width

l_{1e} - Length of a single end winding (calculated as in Appendix A)

k_{wl} - Combined winding factor i.e. $k_{p1} \times k_{d1}$

z_1 - Slots per pole per phase

p - Pole pairs

m_1 - Phases

From this permeance the per phase reactance can be calculated

$$X_{Lew} = 4 \cdot \pi \cdot \mu_0 \cdot f \cdot \frac{N_1^2 \cdot l_{1e} \cdot \Lambda_{1e}}{p \cdot q_1} \quad (3.25) [23]$$

f - Frequency

N_1 - Turns per phase

w_c - Conductor Width

The extra quantity of field current, I_f , required to drive the leakage paths can be proportionally added if the proportion of X_{Lew} to X_d is calculated. The proportion of X_{Lew} to X_d will change as X_d is dependent upon the saturation level in the machine. In the sustained short circuit curve case the machine is unsaturated hence $X_{d_unsaturated}$ must be used and is calculated using data from the saturation curves.

$$X_{d_unsat} = \frac{I_f \text{ for rated SCC current}}{I_f \text{ for rated OCC volts on the airline}} \quad (3.26)$$

At 1pu line voltage the Zero Power Factor point is usually on the knee of the saturation curve at the initial stage of saturation. This means that the actual value X_d during this period will lie somewhere between the saturated and unsaturated values of X_d . Therefore

for this reason the value of X_d used is the average of $X_{d\ sat}$ and $X_{d\ unsat}$. The saturated value of X_d is again calculated using the saturation curves:

$$X_{d\ sat} = \frac{I_f \text{ for rated SCC current}}{I_f \text{ for rated OCC volts}} \quad (3.27)$$

$$X_{d\ average} = \frac{X_{d\ sat} + X_{d\ unsat}}{2} \quad (3.28)$$

The correct value of the field current including the correction to include end winding leakage is calculated below:

$$I_{f_new} = I_{f_old} \left(1 + \frac{X_{Lew}}{X_d} \right) \quad (3.29)$$

Where $X_d = X_{d\ unsat}$ or $X_{d\ average}$

Gieras et al in [23] estimate the permeance based upon experimentation. This is the reason equation (3.23) is only an approximation and has an empirical 0.42 factor present. The permeance chosen has been calculated for high voltage double layer diamond coils of the type used in the generators constructed. By using an approximate equation there is a validity associated with the equation and consequently an associated error. Taking an average of X_{Lew} calculated for 20 generators it is found that ratio of $\frac{X_{Lew}}{X_d}$ is 0.0131. Therefore without any end winding calculation on average I_f would be 1.3% lower than desired. Assuming that there is a large $\pm 20\%$ error in the Gieras calculation the average error in the I_{f_new} due to X_{Lew} can be calculated:

Average Error in I_{f_new} due to $X_{Lew} = \text{Relative Size of } X_{Lew} \times \text{Potential Error in } X_{Lew}$

Average Error in I_{f_new} due to $X_{Lew} = 0.013 \times \pm 0.2$

Average Error in I_{f_new} due to $X_{Lew} = \pm 0.0026 = \pm 0.26\%$

As the X_{Lew} is a small fraction of the total I_{f_new} the maximum potential error carried forward into the calculation becomes a tolerable sub percentile number. Although still significant the benefit of having the added end winding calculation outweighs the potential error.

3.3.4. Initial Field Current Calculation using Carters Coefficient

Finite Element Software requires current density values to be entered into a simulation to allow flux levels to be calculated. As with creating a standard saturation curve, when a machine is under going factory tests, several different values of field current must be simulated to show the full range. A typical curve requires a minimum of 2 or 3 points within the linear region, 3 or 4 points during the elbow or knee of the saturation curve and finally another 2 or 3 points as the machine heads into saturation. Hence typically a minimum of 10 points are simulated, with more when required. Deciding the current values where these points are set is done by making an initial estimate of field current required for 1pu volts open circuit. This is done by assuming the machine to be unsaturated, making 1pu operation lie upon the airline. The assumption that all MMF is dropped across the air gap is made (i.e. the iron is perfectly permeable). Firstly working on a per pole basis the reluctance of the air gap is calculated. The Reluctance is calculated straight from the machines geometry assuming stator doesn't have any teeth and that the air gap is of a constant length. This effectively makes the rotor and stator become two concentric cylinder wedges as shown in Figure 29. Flux is assumed to travel radially therefore the area which is used in the calculation of the reluctance is the area of the rotor face.

$$\text{Rotor Face Area} = W \times L = \frac{\pi D_r}{P} Y \times l_{a_eff} \quad (3.30)$$

$$\text{Reluctance, } S = \frac{\text{Gap Length}}{\mu \times \text{Area}} = \frac{l_{g_eff} K}{\mu_0 \frac{\pi D_r}{P} Y l_{a_eff}} \quad (3.31)$$

where:

$K = \text{Carter's Coefficient [24]}$

$l_{g_eff} = \text{Radial Air gap length across the pole (geometric average)}$

$D_r = \text{Rotor Diameter}$

$Y = \text{Pole Arc [per unit]}$

P = number of poles

l_{a_eff} = Effective Axial Length

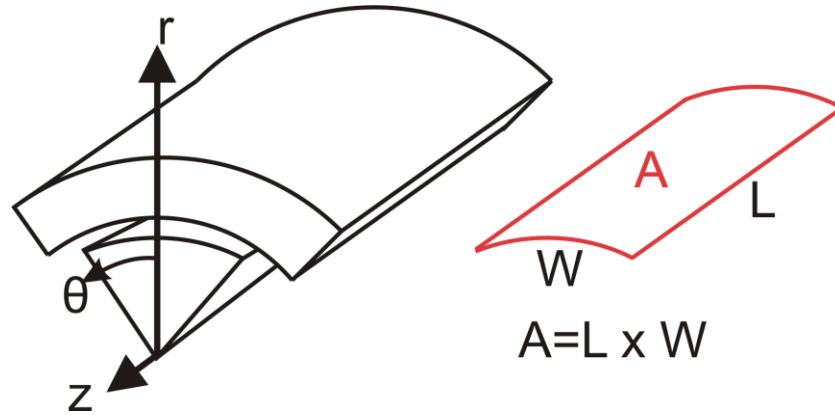


Figure 29 - Diagram showing the cylindrical nature of the assumed stator-rotor configuration and the area used in calculation for calculating the initial field current

Next given that $e = -N \frac{d\phi}{dt}$ the stator flux can be found

$$\phi = \frac{e}{\frac{2\pi}{\sqrt{2}} f \cdot N_s \cdot SPP \cdot Kp \cdot Kd} \quad (3.32)$$

where:

N_s = number of stator turns

$Kp \cdot Kd$ = Winding pitch and distribution factors

SPP = stator slots per pole per phase

Field current estimate I_{f_est} can then be calculated from the Rotor and Stator MMFs

$$MMF_{rotor} = MMF_{stator} \quad (3.33)$$

$$I_{f_est} N_r k_f = S\phi \quad (3.34)$$

$$I_{f_est} = \frac{S\phi}{N_r k_f} \quad (3.35)$$

where:

N_r = Number of Stator Turns

k_f = Fourier Factor calculated from the pole span

Once the field current for the 1pu open circuit operation is finalised the individual field current values can be decided by a linearly spaced array between 0.5 and 3 times I_{f_est} which is sufficient to cover the 3 curve regions as depicted in Figure 13.

3.3.5. Conductor Placement and Insulation

Copper conductors within electrical machines are typically insulated in several ways. Firstly the copper is manufactured with layer of insulating tape pre wound around each conductor which forms the inter-turn insulation. The individual conductors are wound into coils externally of the machine on a former before being inserted into the slots. The coils are given integrity by being manually wound by a secondary layer of insulating tape around the bundles. This tape as well as acting as insulation between the stator core and ground also gives the coil durability to cope with being inserted. In a double layer winding, which most synchronous generators possess, two separate coil sides are inserted into single slot. As slots are one of several standard sizes (due to tooling) between the two coil sides a non conductive separator is sometimes inserted to make sure the slot is fully filled and the coils do not move which would increase the chances of coil failures. Additionally as the coils are not wound directly into the slots there must be a tolerance to allow the coil to be inserted. Each one of these insulation and manufacturing processes means that less and less of the slot is actually filled with copper yet a typical finite element simulation simply fills the whole slot with copper. This difference will affect inductances due to any cross slot leakage flux paths.

To investigate this phenomena two simulations have been compared, one with a simple conductor layout and one with every strand positioned as it is within the manufactured machine (subject to tolerances) as shown in Figure 30. Figure 31 shows a cross section of a coil side highlighting the insulation applied to the copper. By setting boundaries to the finite element simulation flux can be forced across the slot and the inductance of the coil in each simulation calculated.

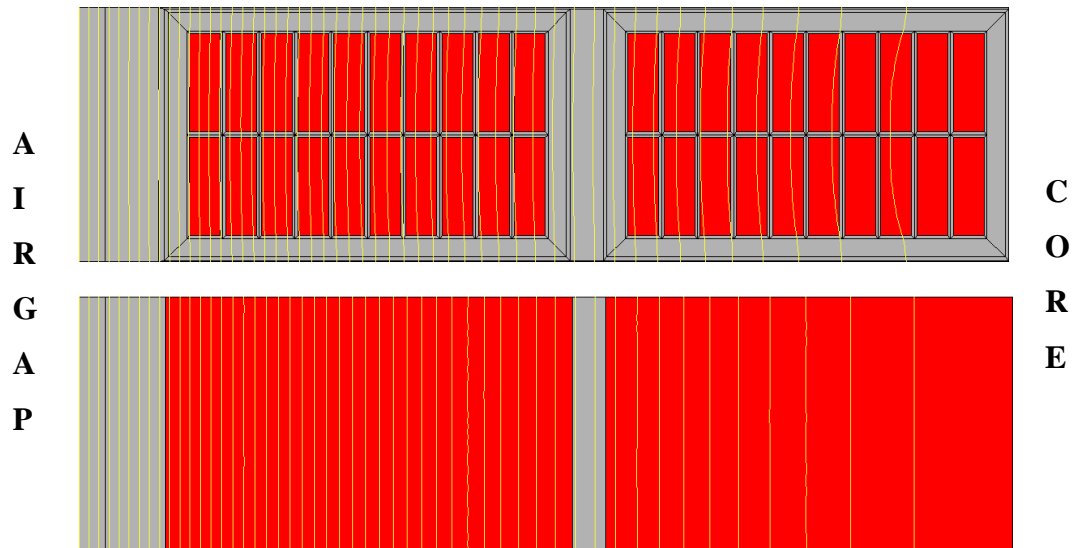


Figure 30 - Finite Element simulations showing coils modelled with and without insulation

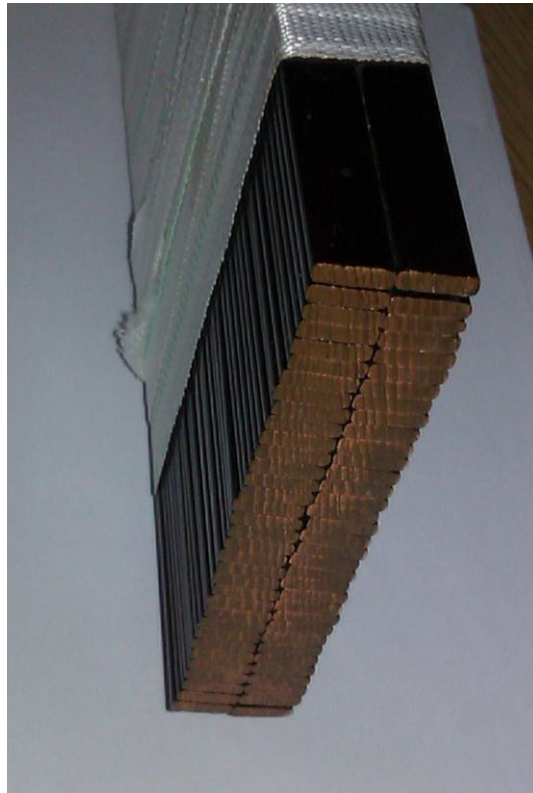


Figure 31 - A cross section of an example coil side showing the individual rectangular copper strands with enamelled insulation

The simulations yield the inductances of 2.934mH for the insulated simulation and 2.906mH for the simple uninsulated simulation. This is a difference of just 1% in the worst case scenario i.e. when the whole of the flux is crossing the slot of a machine. As in reality this cross slot flux will be a small fraction of the main flux path the difference falls into insignificance. Additionally the insulated mesh has to be much finer to allow

elements within all the created areas which results in a mesh with over double the number of elements and nodes. This larger mesh takes longer to solve but as shown doesn't give significant benefit in accuracy. As a result the uninsulated conductor model is used within the design package.

3.3.6. Mesh Size

Within a design package the balance between accuracy and speed of calculation must be decided. When using Finite Element solutions the major factor affecting speed and accuracy is the size of the mesh. The finer the mesh the higher the number of nodes and elements and more detail can be dependably extracted from a solution however the model will take longer to solve. To balance these two constraints FE designers typically force the mesh to be finest where flux is most concentrated and most active i.e. most varying. These areas invariably are the regions closest to the air gap - being the teeth, slots, pole shoe and air gap itself. To find an acceptable compromise between speed and accuracy a series of meshes of a single pole of a 4 pole generator have been constructed with increasing mesh size (Figure 32). The time for a static solution including time to create the mesh has been measured and is shown in Figure 33 and Figure 34. This simple study shows as expected that the larger the mesh the slower the solution. It also shows that there is diminishing returns heading to ever small meshes. This is because of the logistics of the finite element software. The software must check that there is a license for the solver every time a solution is requested hence an amount of time is wasted as the program searches the local area network for the license server to authenticate the action. Additionally the computer must retrieve the solver program file from the hard drive, transfer it to the RAM, run the instruction set and seek out the location of the simulation to be solved. From Figure 34 the zero element (y-axis) intercept point is around 2 or 3 seconds which is the amount of initialisation time that is required to run any simulation regardless of size.

From this study it is decided that the automatically generated simulations within the package were to have a mesh density similar to that of the 17346 element simulation. This obviously would vary depending upon machine design parameters such as number of slots but the overall solution time to simulation accuracy is deemed acceptable.

The optimum solution would be to use a meshing routine that uses adaptive meshing. Using adaptive meshing the meshing routine looks at the energy product and aims to

reduce any error by increasing the number of elements until a tolerance is reached. This is generally quicker as the routine places elements where they are needed and can significantly reduce the total number of elements. The Cobham Vector Fields Opera 2D FE software used does not have this capability which is a severe limitation of the chosen package and is further discussed in Chapter 8.

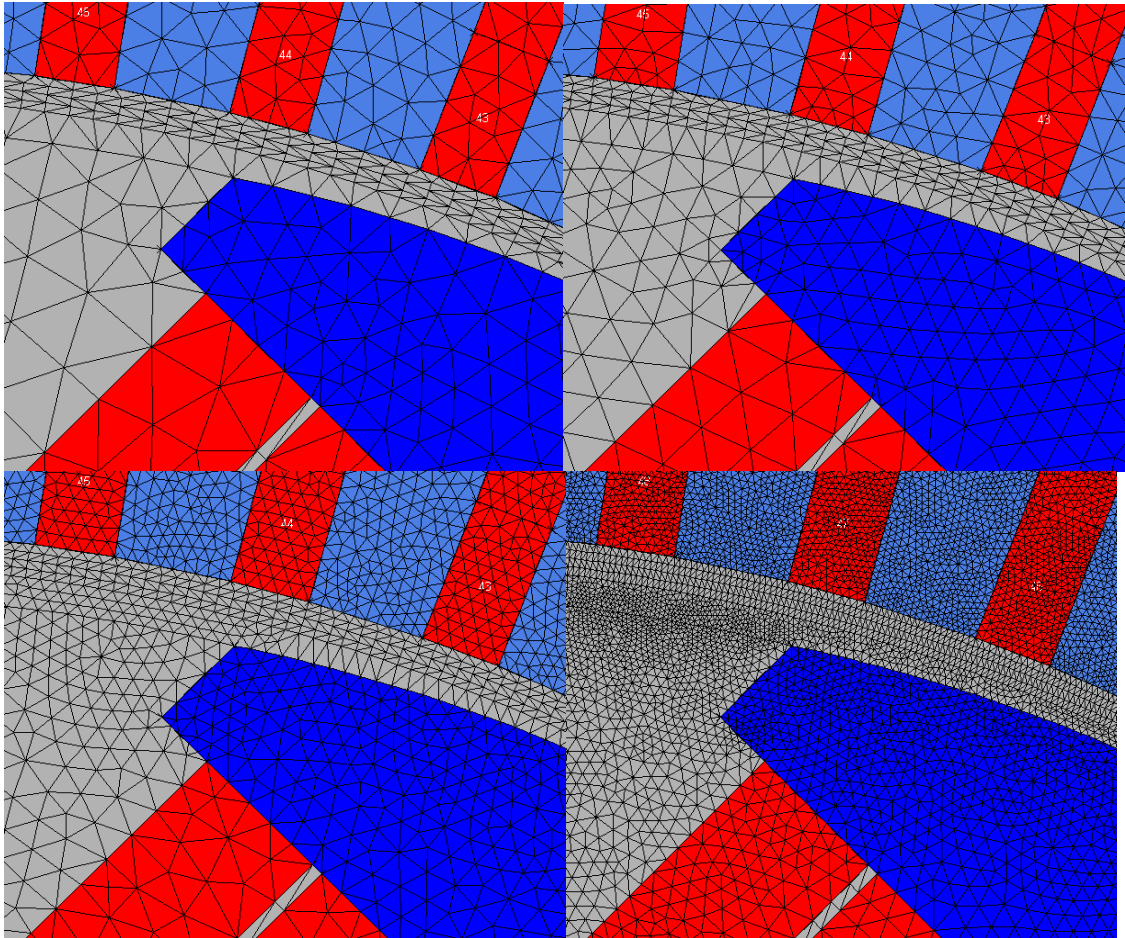


Figure 32 - Diagrams showing increasing mesh quality from coarsest in the top left to finest in the bottom right

Mesh	Elements	Time to Solve
Coarsest	5318	4.57 seconds
↓	7938	5.38 seconds
↓	17346	8.53 seconds
↓	39860	17.14 seconds
↓	66203	22.39 seconds
Finest	75452	25.42 seconds

Figure 33 - Table of solution speed

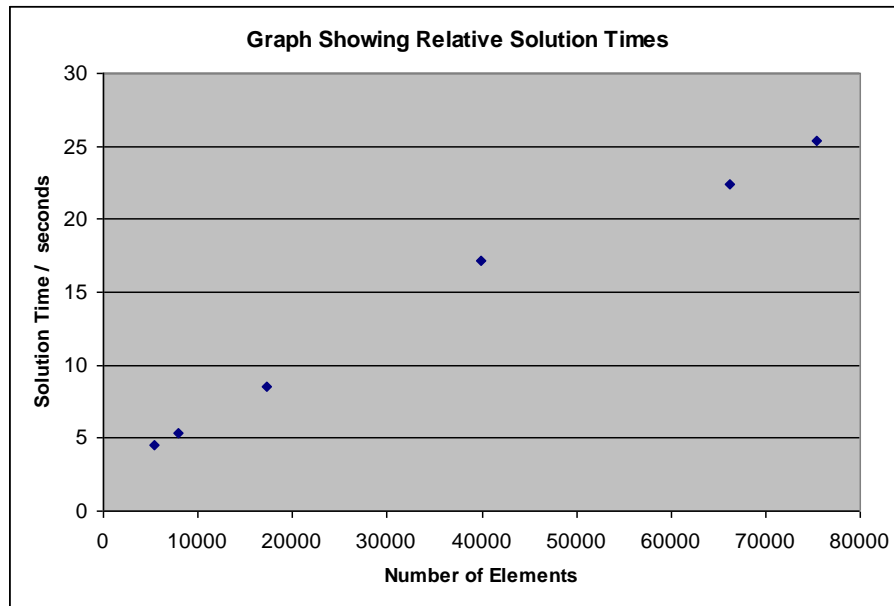


Figure 34 - Graph Showing Relative Solution Times

3.3.6.1. Meshing Nuances

The actual mesh is generated by the computer program. The mesh size is based upon specified data - either a number of elements per side or a maximum element size. The generated mesh is then used to calculate solutions. As discussed above the size or fineness of the mesh affect the solution but also the quality of the mesh can make a huge difference. It is typically assumed the mesh generator creates a regular mesh but this is not so. An excellent example of this is a machine where the cogging torque variation is being measured under open circuit conditions. The machine having 18 slots per pole pair would expect to have a 18th harmonic of torque caused by permeance variation which manifests itself as a 17th and 19th harmonic in the voltage waveform. When the initial machine simulation was created and the results analysed an additional unexpected 24th harmonic of torque was found to exist. It was speculated that this harmonic was caused by a meshing problem so a finer mesh was created Figure 35. The results for the mesh contained even worse harmonics at many different frequencies. Close inspection of the mesh found that the automatic meshing routine was struggling to create a regular mesh and over extended highly stretched elements were being created. These elements added extra harmonics and caused incorrect torque variation yet voltage harmonics remained unaffected. A final finer mesh was created which when checked had no errors and the results as shown in Figure 37 and Figure 38 confirmed the initial simulation. The 24th harmonics were later found to be caused by a badly shaped pole and poorly placed rotor compression studs.

The poor mesh is created automatically as the program works in a Cartesian plane yet rotational objects are best described in a polar plane. Poor meshes such as this one are a rare occurrences and tend to be found in higher mesh densities. A quadrilateral mesh could be generated to avoid this problem but this relies on all regions having 4 sides. This is feasible in certain machines but not in others and hence is not the universal solution. In an automated system the only method available to seek out these errors is post processing where high harmonic content is highlighted to the engineer.

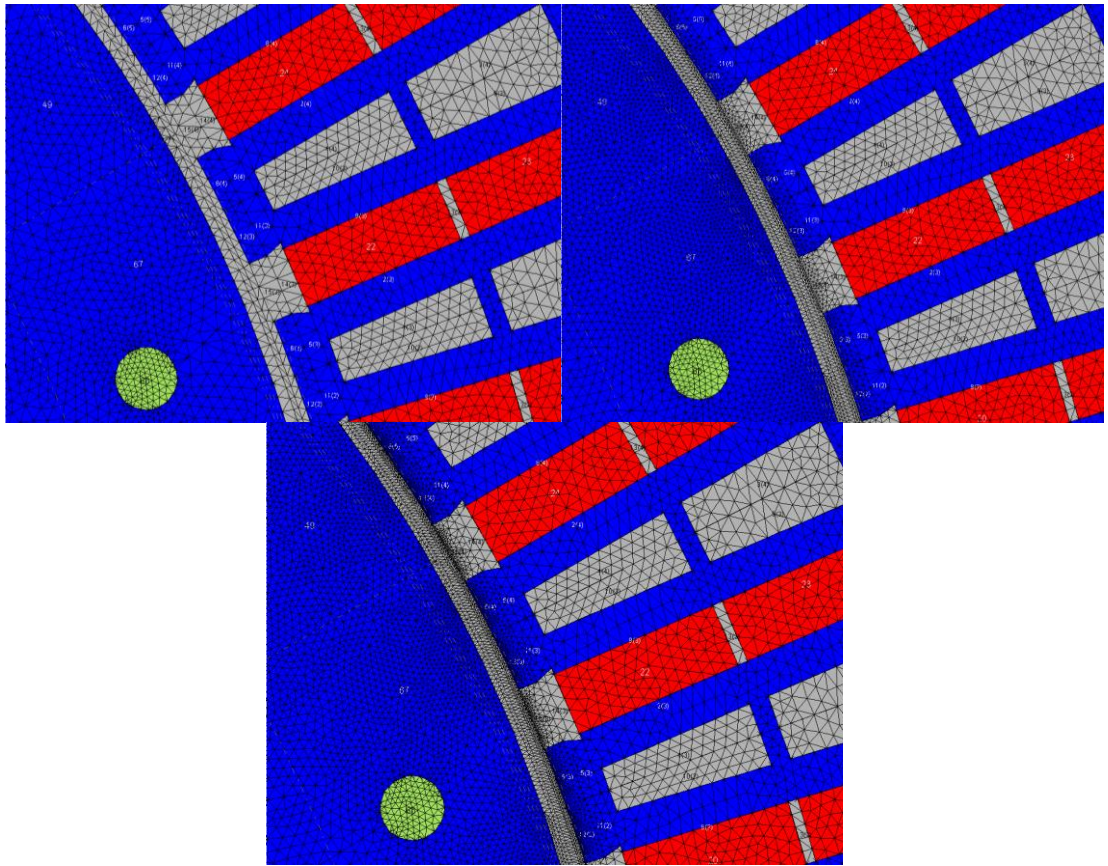


Figure 35 - Increasing air gap mesh densities

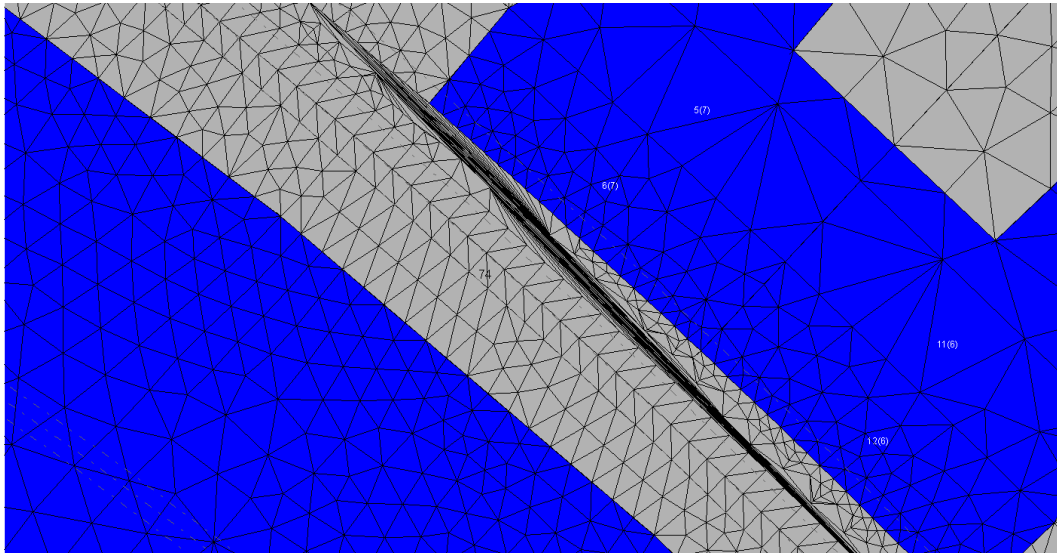


Figure 36 - Over stretched elements resulting in a poor quality mesh

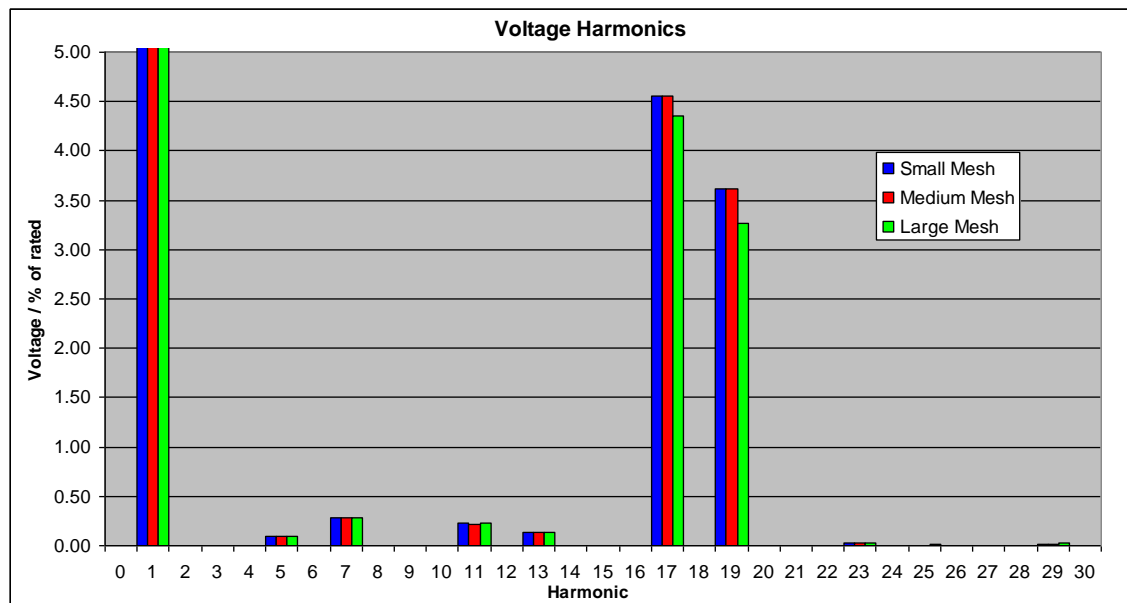


Figure 37 - Voltage Harmonics

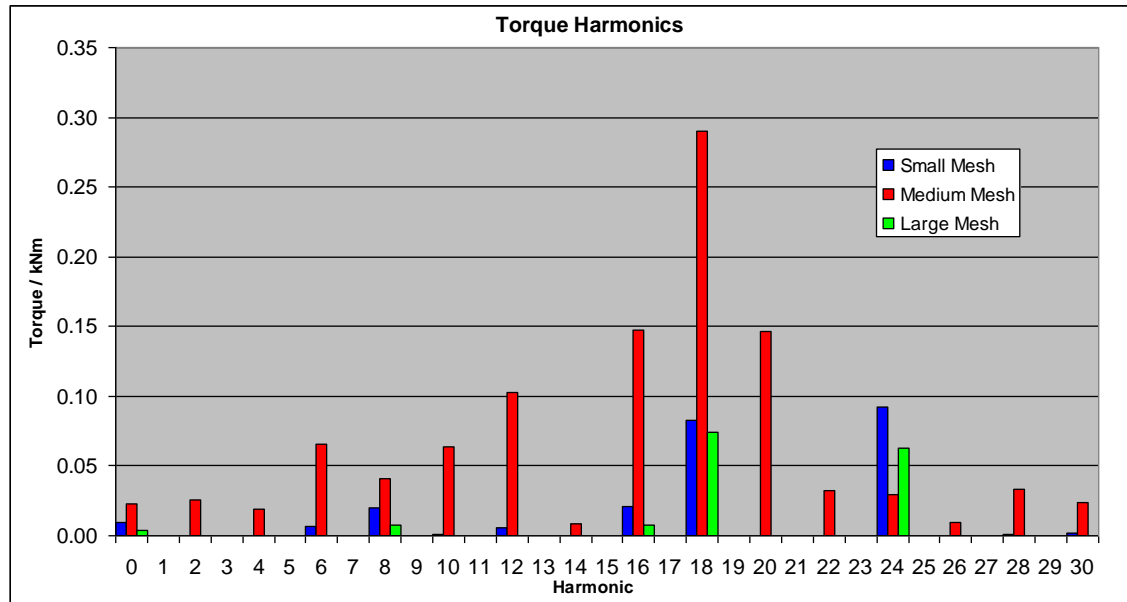


Figure 38 - Torque Harmonics

3.3.6.2. Mesh Aliasing

Aliasing is when a sets of different signals become becomes indistinguishable from each other because of the rate at which they have been sampled. The commonest place where this is noticed in on the television when striped images or clothing interferes with the resolution of the image broadcast and a moiré pattern is created. This same effect can occur in a finite element simulation when the sampling rate of air gap flux density interferes with the harmonics within the flux density waveform. This form of aliasing can lead to phantom harmonics appearing in the results. For example a simulation of a generator under load was found to have significant 6th, 8th and 12th harmonics of torque (Figure 39). The generator is question has 6 slots per pole and so the 6th and 12th harmonics can be attributed to the number of slots but the 8th cannot. The machine mesh was shown to be particularly coarse in the air gap hence a re-simulation of the machine with a finer mesh completely eliminated the 8th harmonic problem. Phantom harmonics are easily solved by having a finer mesh.

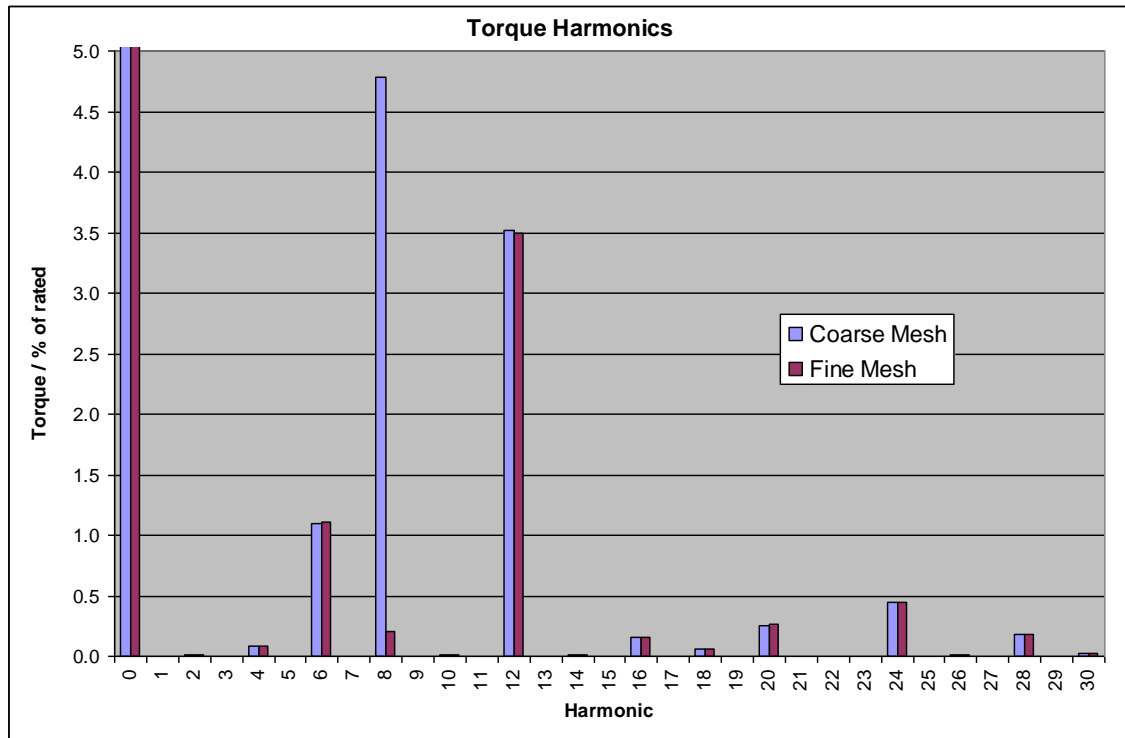


Figure 39 - Graph showing the phantom 8th harmonic created by a coarse mesh

3.3.7. Finite Element Machine Construction

To allow rapid simulation of multiple machines a parametric machine simulation package has been constructed. This takes the machine dimensions, ratings and specifications and automatically draws within the FE package the machine based upon input data. This rapid simulation routine allows the designer to quickly analyse designs without having to manually construct each model. Additionally a Graphical User Interface has been constructed around the core simulation routines meaning the end user is removed from the background calculation processes further increasing ease of use and reducing training. A more detailed account of the graphical user interface can be found in Appendix H.

3.4. Results and Discussion

The test results of forty eight previously tested machines are compared to the simulated results to allow conclusions to be drawn. The machines are all four pole wound field synchronous generators and range from 5MVA to 25MVA at a variety of medium voltages levels and frame sizes. The analytically based design package currently used in

the Engineering Design Department of the company, named EDS is used for further comparison. Results are given in terms of percentage errors and both signed and absolute values are shown.

3.4.1. Open Circuit Curve

From Figure 40 it is seen that the spread of the FE results is less than half of the EDS results. This is reflected in the narrow standard deviation blocks and shows that the FE design method gives consistent performance. The signed FE results are spread approximately equally across zero showing excellent correlation. EDS generally overestimates the required field current and has a larger spread of circa twenty percent. This reduced accuracy is a result of the inability of the analytical method to model saturation correctly. The mean absolute percentage error results show a reduction in the error of 56% down to 2.22%. A table showing full results for 1 pu Open Circuit Voltage can be found in Appendix A.

In Figure 41 the open circuit saturation curve results at 0.5pu are shown. At this field excitation the iron is unsaturated. From the signed results it is shown that the spread and the distribution of the results are comparable, being around 27% and 8.5% respectively. The mean absolute percentage error for the FE and EDS has respectively increased to 3.82% and 7.01%. A table showing full results for 0.5 pu Open Circuit Voltage can be found in Appendix B. This was unexpected as one would expect to be able to predict the air gap line quite accurately. The reason for this discrepancy is due to the residual magnetisation of the iron material during test. Typically the machine is run nominally on a zero power factor heat run before the open circuit saturation curve test is performed. After this initial excitation the rotor iron retains some magnetisation. This is clearly shown in the open circuit saturation curve produced during test that does not pass through zero. The result is that the field current prediction is too high. At low excitation levels the error is more apparent than at higher excitation. The residual magnetisation error could be corrected by several methods:

- Using statistical method by analysing the test results to date to find an average value which could be added
- Research into the cause of the residual magnetisation and develop a mathematical model allowing the residual magnetisation to be predicted.

Both of these methods would be extremely time consuming accounting for the quantity of data that would need to be analysed in an effort to make satisfactory predictions for every machine type, frame size and power rating. Furthermore, the fact the error is circa 1% of rated field current makes it justifiable that the residual magnetisation error is neglected.

The below charts show both signed and absolute results. Signed results show the spread across zero error whereas absolute results must be used to quantify average results. For example in a data set with 2 results of +10% and -10% using an average of the signed results would give zero error - clearly invalid. Whereas the absolute results would give a representative 10% average error. However looking at the spread of the same data set the signed results should be used as absolute values would misleadingly give a 0% spread.

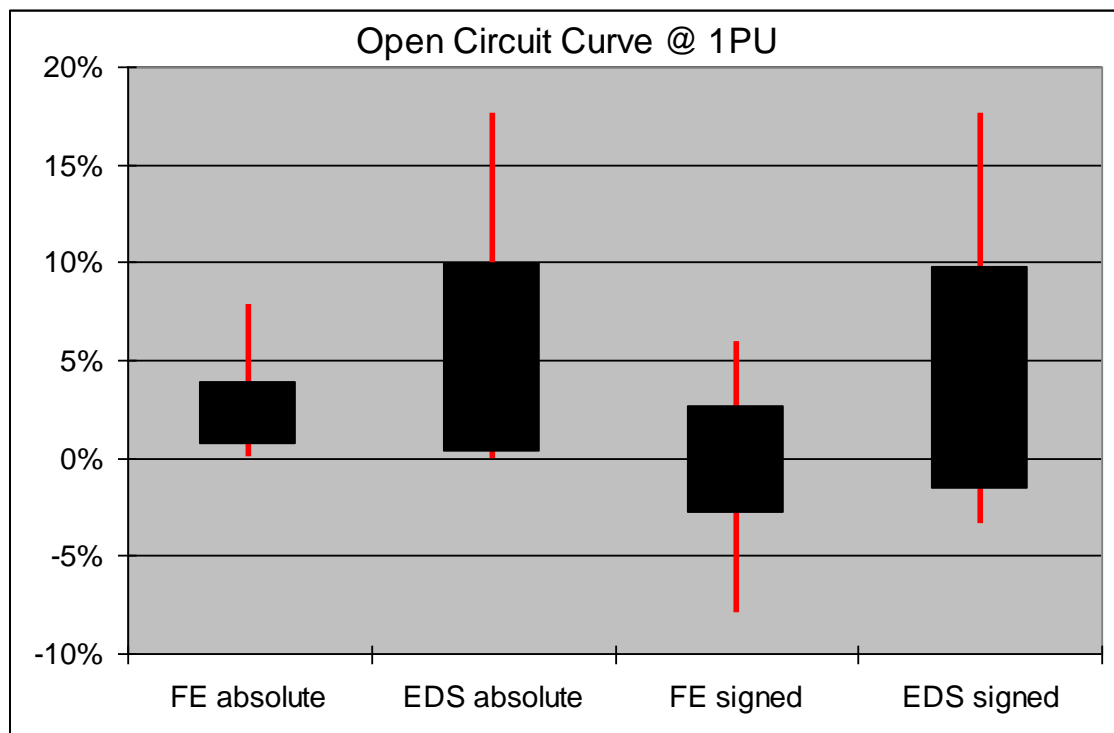


Figure 40 - Open circuit saturation curve results showing both signed and absolute results. Red tails show extent of results spread and black box is the mean \pm one standard deviation

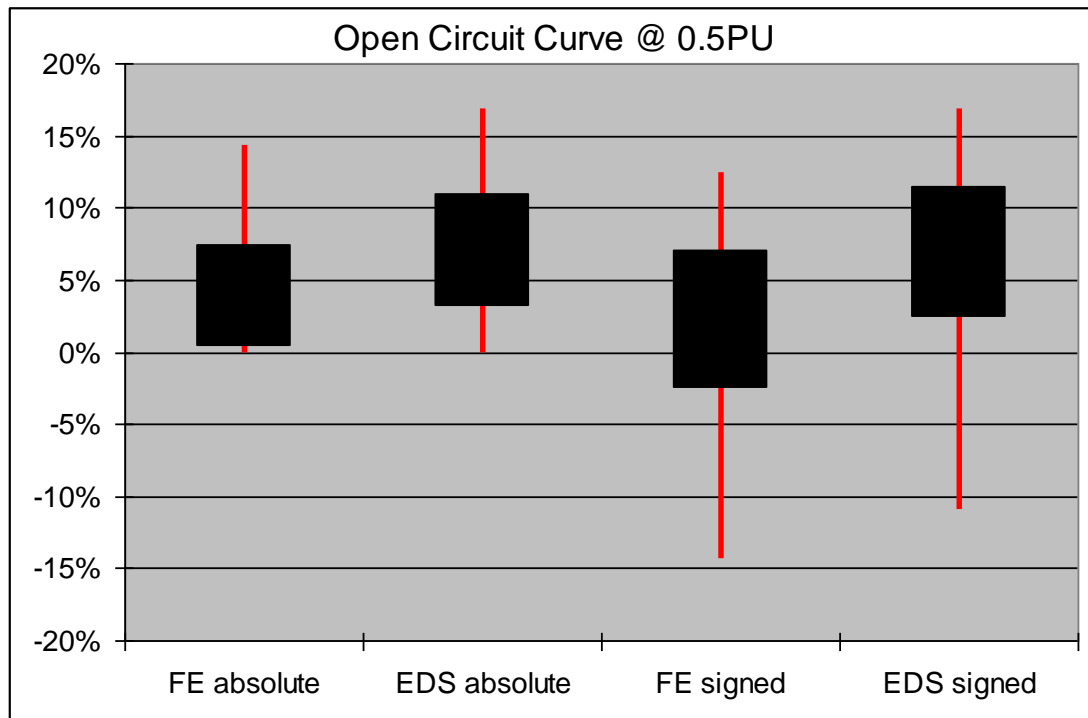


Figure 41 - Open circuit saturation curve results showing both signed and absolute results. Red tails show extent of results spread and black box is the mean \pm one standard deviation

3.4.2. Sustained Short Circuit Curve (SCC)

From Figure 42 it can be seen that FE predictions are accurate to within 4% and have a mean absolute percentage error of 1.28%. The spread of the results crosses 0% but marginally underestimates the field current. All of the EDS results are within 2.5% and have a lower mean absolute percentage error than the FE of 0.78%. The EDS results are ideally placed across 0% having an almost normal distribution in the signed results. The EDS is shown to be on average more accurate than the FE. Having less accurate prediction using FE methods is unexpected but can be attributed to the method employed. The FE method references the unsaturated part of the open circuit curve which has an inherent error due to the residual magnetisation affect. Another reason for the perceived poor prediction when compared to analytical methods can be attributed to the fact that the EDS calculation has been adjusted throughout development using test results to ensure a correct prediction of the sustained short circuit curve which is then used in reactance calculations. The sustained short circuit curve was chosen during the development of EDS as the curve to be used in benchmarking as it is unsaturated and hence EDS's method is most likely to be correct here. Again a table showing full results for sustained short circuit current at 1pu can be found in Appendix C.

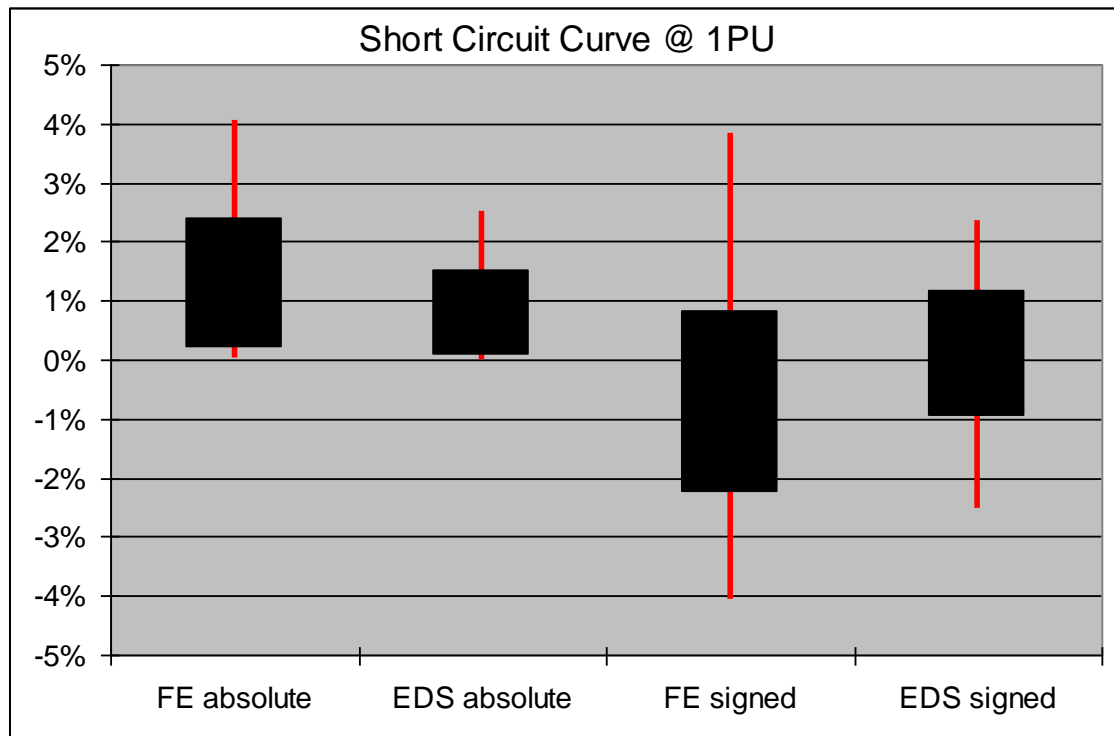


Figure 42 - Sustained Short Circuit curve results showing both signed and absolute results. Red tails show extent of results spread and black box is the mean \pm one standard deviation

3.4.3. Zero Power Factor Saturation Curve (ZPF)

From Figure 43 the spread of the FE results is approximately 15% whereas EDS has a spread of 40%. Consequently the standard deviation for EDS is twice that of FE methods. The mean absolute percentage error results of the FE method is 5.55% and EDS 8.32%. The large distribution of EDS results is not caused by anomalous readings as there are three machines with errors over 30%. Operation at zero power factor requires increased field excitation, resulting in significant saturation which alters the field distribution. It is the inability of analytical methods to predict this field distribution that results in zero power factor curve inaccuracies. The EDS program on average over predicts the field current indicating that it overestimates saturation.

The FE results have a narrow spread as a consequence of consistency in the method and accurate prediction of saturation. The spread is likely to occur mainly because of manufacturing process tolerances. For example segmental laminations must be stacked systematically to distribute any discrepancies - it would be impossible to measure every lamination's thickness. Similarly coil insulation tape and slot liners are manually applied on the end windings introducing another tolerance. This is clearly seen in a series of 3

identical machines built and tested which had a zero power factor spread of 2.63% (Figure 44). Although designs are identical results are spread due to the tolerances.

The FE results have a mean absolute percentage error of 5.55% which is a large improvement over EDS however looking at the signed results it is seen that the results show an underestimation of field current. It is highly likely this error is due to disregarded leakage paths. A table showing full results for 1pu voltage at zero power factor can be found in Appendix D.

3.4.4. Leakage Paths

Flux is driven around four distinct leakage paths:

- X_{Ls} : Stator slot leakage
- X_{Lew} : Stator end winding leakage
- X_{Lp2p} : Rotor pole end to pole end leakage
- X_{Lrs} : Rotor slot leakage

Of these four paths X_{Ls} and X_{Lrs} are modelled in the 2D simulation. X_{Lew} is accounted for using equations (3.7) to (3.12). X_{Lp2p} is currently neglected within the FE method because it assumed to be a very small effect. However as field excitation increases the rotor pole saturates and even though the leakage path is through air the flux increases. Consequently rotor pole leakage is very important. Since 3D FE models are too time consuming and as there is no 2D model that can be used to fully describe the problem it is suggested that the leakage could be modelled using analytical methods such as a modified Pohl's method [25]. A 3D model is time consuming as the third dimension very quickly adds many additional elements making simulation much slower. A 2D simulation cannot be used as the path out of 1 pole and back into another pole cannot be sliced by a 2D slice - in other words the flux follows a 3D path.

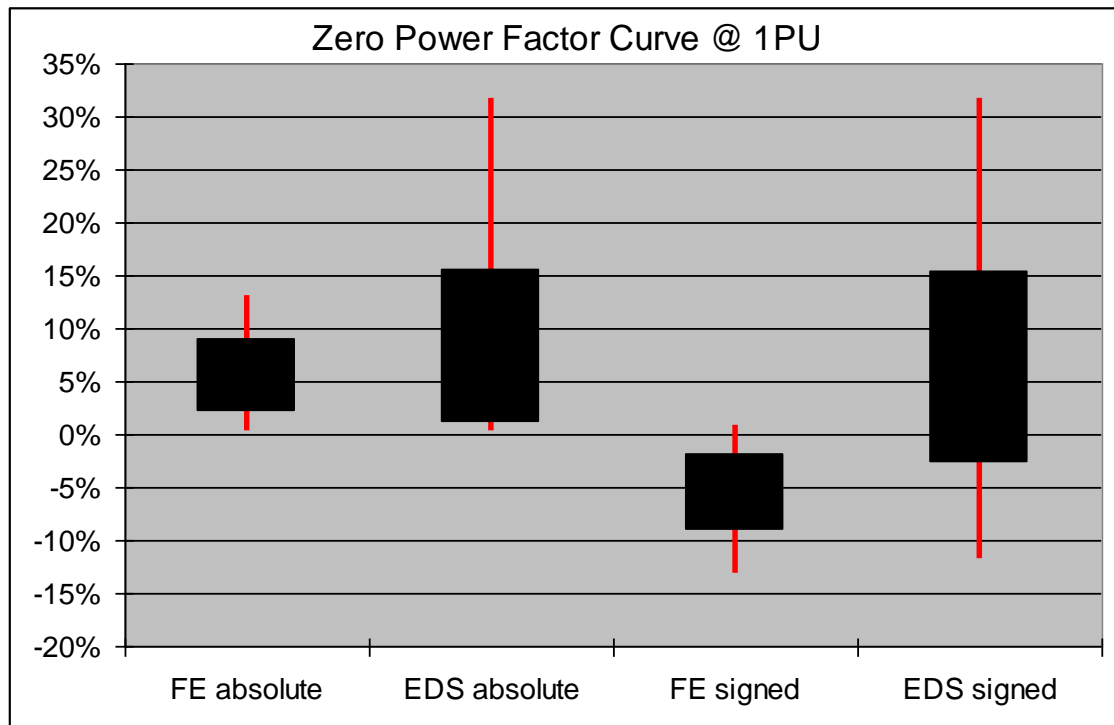


Figure 43 - Zero power factor Saturation Curve results showing both signed and absolute results. Red tails show extent of results spread and black box is the mean \pm one standard deviation

	If / Amps			
	OCC @ 1PU	OCC @ 0.5PU	SCC @ 1PU	ZPF @ 1PU
Machine 1	92.13	37.98	151	312.56
Machine 2	92.35	38.66	153	311.56
Machine 3	92.77	40.40	153	319.83
Mean	92.41	39.01	152.3	314.65
Maximum	92.77	40.40	153	319.83
Minimum	92.13	37.98	151	311.56
Spread	0.69%	6.19%	1.31%	2.63%

Figure 44 - Comparison of three identical test machines

3.4.5. Calculation Speed

All calculations were performed on a quad core Intel Xeon running at 2GHz with 8Gb of RAM. A MATLAB based script is used to control the ordering of the FE simulations and to process the data. Due to the nature of the FE solver using a single processor per solver thread parallel processing means that 'n' parallel processes can be adopted. As a rule of thumb one less solvers are used than the number of cores available. This leaves one core for background operating system processes and for extra foreground data

handling tasks. Hence with the PC in question three solver processes are run in parallel reducing computation time. Occasionally this is increased to 4 processes such as when the sustained short circuit curve is calculated. This is mainly a logistical simplification to ease coding priorities and as the sustained short circuit curve is only a single simulation taking less than 30 seconds there is only a short period with 100% PC usage [high priority processor interrupts are still valid in this period to keep system stability]. Figure 45 shows the operating sequence and which sections are calculated in each program as well as the 'n+1' processes during sustained short circuit curve calculation. With the Xeon CPU typically an open circuit saturation curve, sustained short circuit curve and zero power factor saturation chart is calculated in five minutes. This speed could be further reduced by the upgrading to a higher number of PC computing cores.

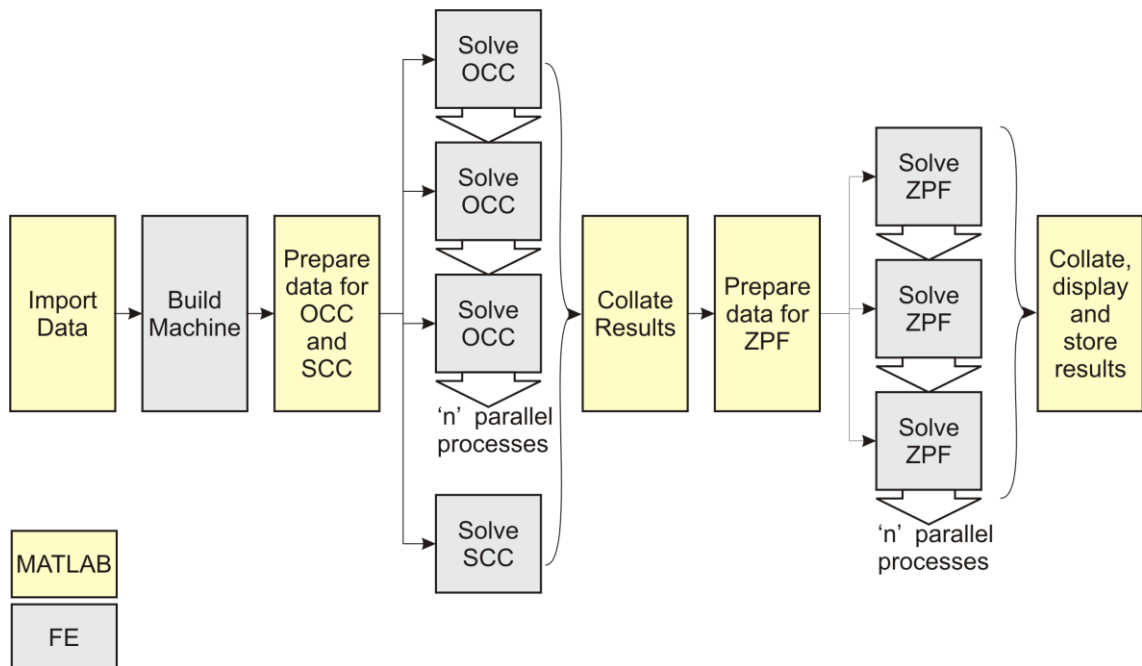


Figure 45 - Flow Chart showing the operating sequence and software packages for open circuit saturation curve (OCC), sustained short circuit curve (SCC) and zero power factor (ZPF) calculations

3.5. Chapter Summary

The FE PRS method has been shown to be more accurate than the current analytical EDS method used within the company as shown in summary table

Figure 46. On open circuit the error at rated field excitation has been reduced by 56% to 2.22% and by 54% to 3.82% at 0.5pu field current. The increased accuracy is attributed to the more accurate prediction of field leakage paths and iron saturation. The concept of residual magnetisation is the likely cause of a systematic error throughout the process

which would be particularly difficult to correct. During sustained short circuit curve conditions FE gives a worse prediction than EDS but nevertheless is still acceptable at only 1.28%. EDS has been adjusted to reduce this error so it is a somewhat unfair comparison. Again this sustained short circuit curve error can chiefly be attributed to the open circuit saturation curve residual magnetisation error.

Finally the zero power factor saturation curve shows a reduction in error of 67% but the majority of results underestimate the field current showing that a flux leakage path(s) is being incorrectly estimated or neglected. Axial rotor pole to pole end leakage and rotor end winding leakage effects are not currently included and are likely to be the source of error. These must be included using an analytical method as 3D FE would be too slow. With a calculation time of five minutes this method would be satisfactory for final design optimisation but not as an estimating tool. However with increases in computing power it may be possible to model the machine in 3D to improve the estimation of the 3D leakage paths.

	FE PRS Method MAPE	EDS Method MAPE
Open Circuit Saturation Curve @ 1pu	2.22%	5.07%
Open Circuit Saturation Curve @ 0.5pu	3.82%	7.01%
Sustained Short Circuit Curve @ 1pu	1.28%	0.78%
Zero Power Factor @ 1pu	5.55%	8.32%

Figure 46 - Comparison table showing Mean Absolute Percentage Errors (MAPE) [45] vs. test results

Chapter 4. Calculation of Transient Parameters

4.1. Introduction

Synchronous generators often operate under conditions where they can be subject to sudden and large changes in load through normal load cycling or through outside intervention, such as line faults. These changes affect the stability of the generator and the grid as a whole. To mitigate the adverse consequences caused by grid failure and out of specification operation, the majority of customers require generators that can be analysed in load flow and transient stability software analysis packages. These packages require a standard set of input parameters, which govern the stability of the machine and therefore any design tool created must be able to reliably and accurately predict these values. The parameters that are typically required are transient and subtransient reactances, X'_d , X''_d as well as the associated time constants - T'_d , T''_d . This section of work looks at how the transient parameters have been calculated, compares the accuracy of existing design methods to the system employed, and finishes with some conclusions.

4.2. Standstill Frequency Analysis

Many authors have used standstill frequency response (SSFR) testing to calculate parameters for synchronous generators [26][27][28]. This testing method is typically used to analyse electrical machines in situ within installations as it does not require the machine to be attached to a dedicated testing motor which is required for sustained three phase short circuit testing. The SSFR method involves connecting a variable frequency supply to the generator across two phases and then across the field winding and measuring various input and output voltages and currents to allow transfer functions to be created and parameters determined via curve fitting representative functions determined from equivalent circuits. Alternating current solvers exist within Finite Element analysis packages and can easily be programmed to produce the same testing environment produced using a SSFR test and hence the test can be used as a design tool to allow designers access to predicted data.

4.2.1. Analysis System

During the tests the machine is connected in several setups, as shown in Figure 47. Firstly the rotor is aligned so that the D axis (i.e. pole centre) lies normal to the C phase and the tests completed in each of the setups. Then the rotor is moved 90 electrical degrees to allow the tests to be completed in the Q axis. The finite element software allows multiple circuits to be monitored and logged simultaneously, allowing only 3 series of simulations to be calculated. The 3 series are both open and closed circuit field windings aligned in the D axis and closed circuit field winding aligned in the Q axis. The test requires frequency to be varied over a range of typically 6 decades from around 0.001Hz to 1kHz, with approximately 10 points per decade. This gives a total of approximately 240 individual simulations, which in total take around 40-50 minutes to simulate.

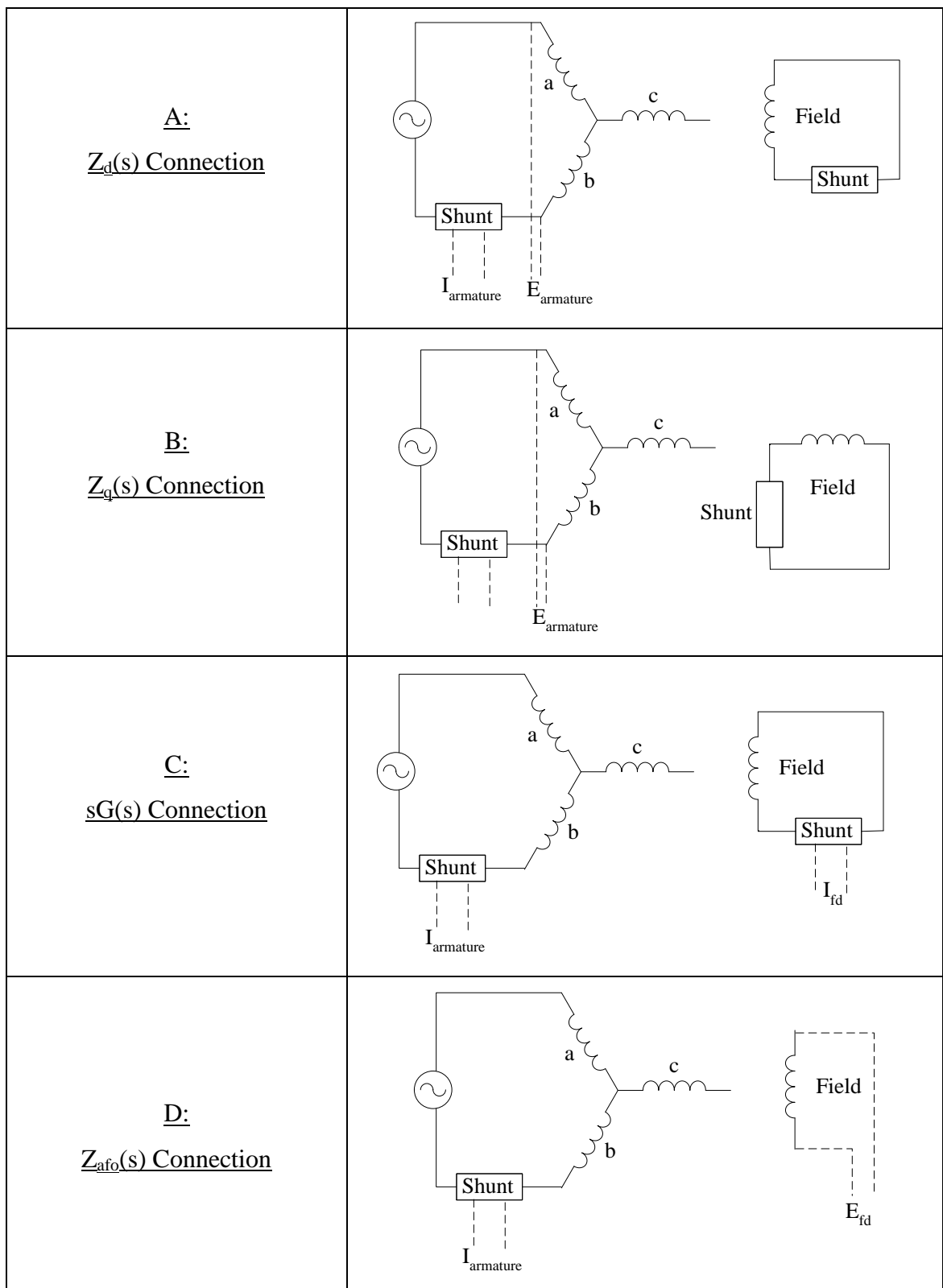


Figure 47 - SSFR test connections.

4.2.2. Simulation

To test the practicality of this system a single 17.5MVA generator has been simulated. The machine, which has the project number A145y4-P141239, is often simply referred

to as 'Saxi' after 'Saxi Batuque'. Saxi Batuque is the name of the floating production, storage and offloading (FPSO) ship that the generator was designed to power. The machine is a 4 salient pole, wound field synchronous generator with damper bars. The machine has both laminated rotor and stator and has a rated speed of 1800rpm. Saxi is used as the primary source of electrical power on board the ship and is a classic example of islanded power generation. This machine has been chosen to simulate as it is a highly fluxed machine i.e. the machine is running in the more saturated regions of the B-H curve. This non-linear region of the curve makes predictions much more difficult to achieve and usually forces design engineers to add an extra margin of error. A picture of Saxi is shown in Figure 48.



Figure 48 - Photo of Saxi Batuque

The machine has been simulated as connected in Figure 47, and the 4 transfer functions generated below:

$$Z_d(s) = \frac{E_{armatur}(s)}{I_{armatur}(s)} \dots (4.1)$$

$$sG(s) = \frac{I_{fd}(s)}{I_{armatur}(s)} \dots(4.2)$$

$$Z_{af0}(s) = \frac{E_{fd}(s)}{I_{armatur}(s)} \dots(4.3)$$

$$Z_q(s) = \frac{E_{armature}(s)}{I_{armature}(s)} \dots(4.4)$$

The first 3 are completed with alignment in the D axis and the final equation with Q axis rotor alignment. The test is normally excited with a low level of excitation. These 4 functions are complex equations and hence have both magnitude and phase, which are graphed below in Figure 49, Figure 50, Figure 51 and Figure 52.

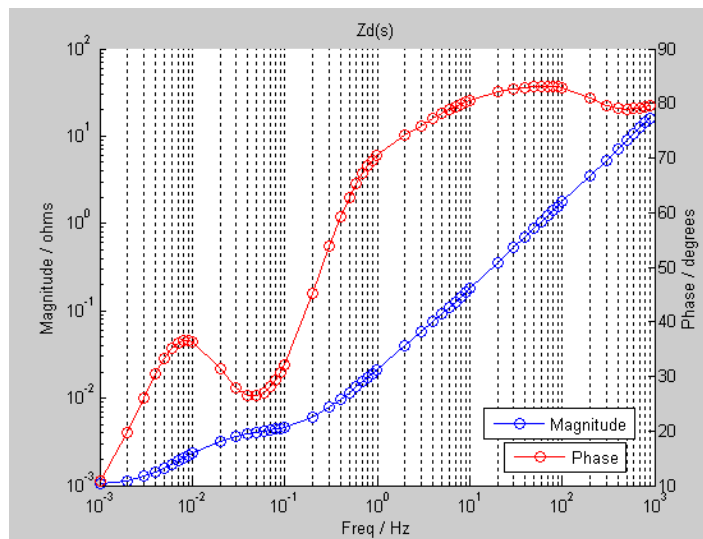


Figure 49 - $Z_d(s)$ for the 17.5MVA test generator

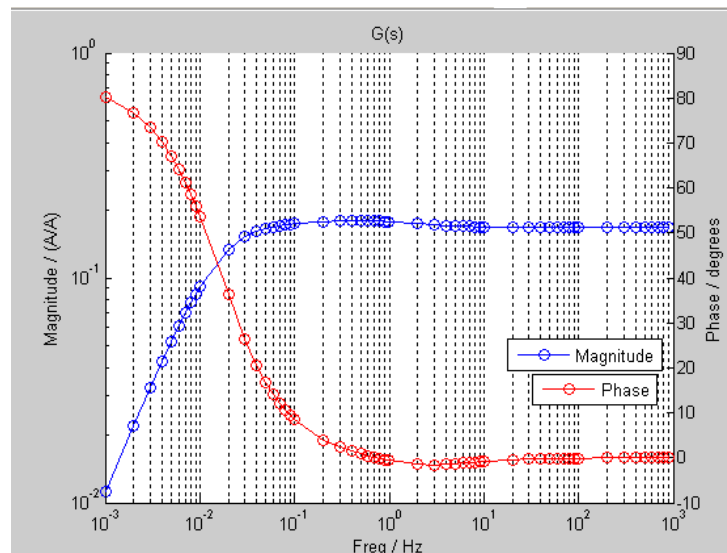
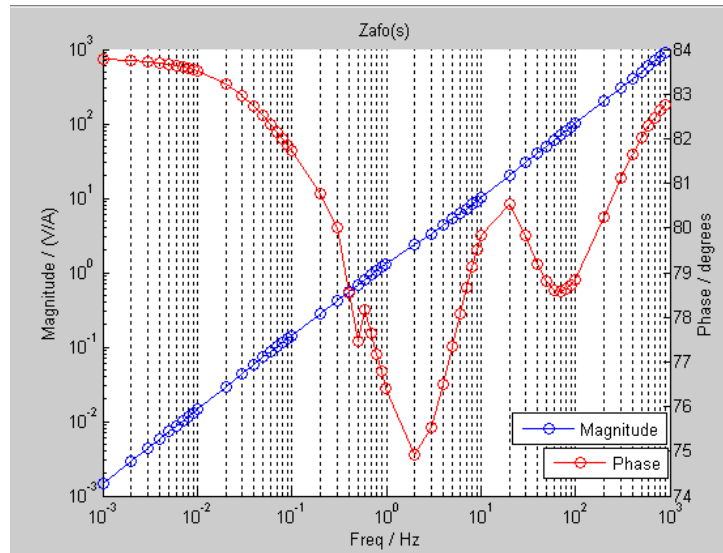
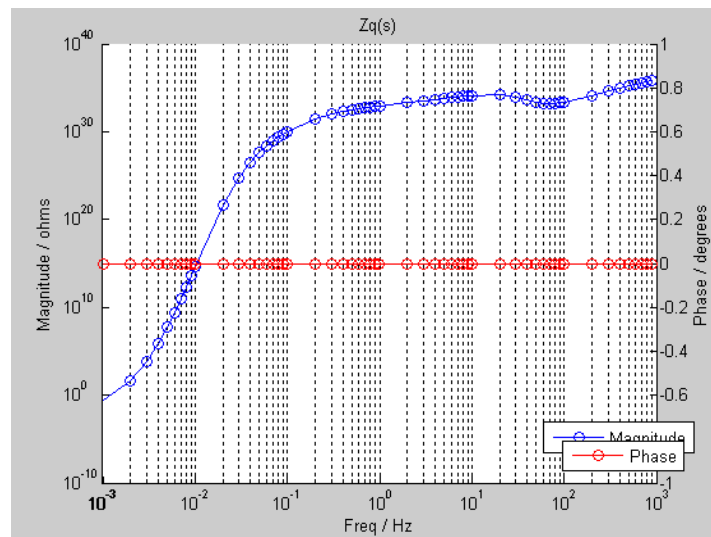


Figure 50 - $sG(s)$ for the 17.5MVA test generator

Figure 51 - $Z_{afi}(s)$ for the 17.5MVA test generatorFigure 52 - $Z_q(s)$ for Saxe Batuque- a 17.5MVA generator

The armature resistance can be extracted directly from the data without the need to curve fit. As the impedance to DC current is naturally the armature resistance R_a , the low frequency limit of Z_d provides a quick calculation of R_a as shown in equation (4.5)

$$R_a = \frac{1}{2} \left\{ \lim_{s \rightarrow 0} [Z_d(s)] \right\} \quad \dots (4.5)$$

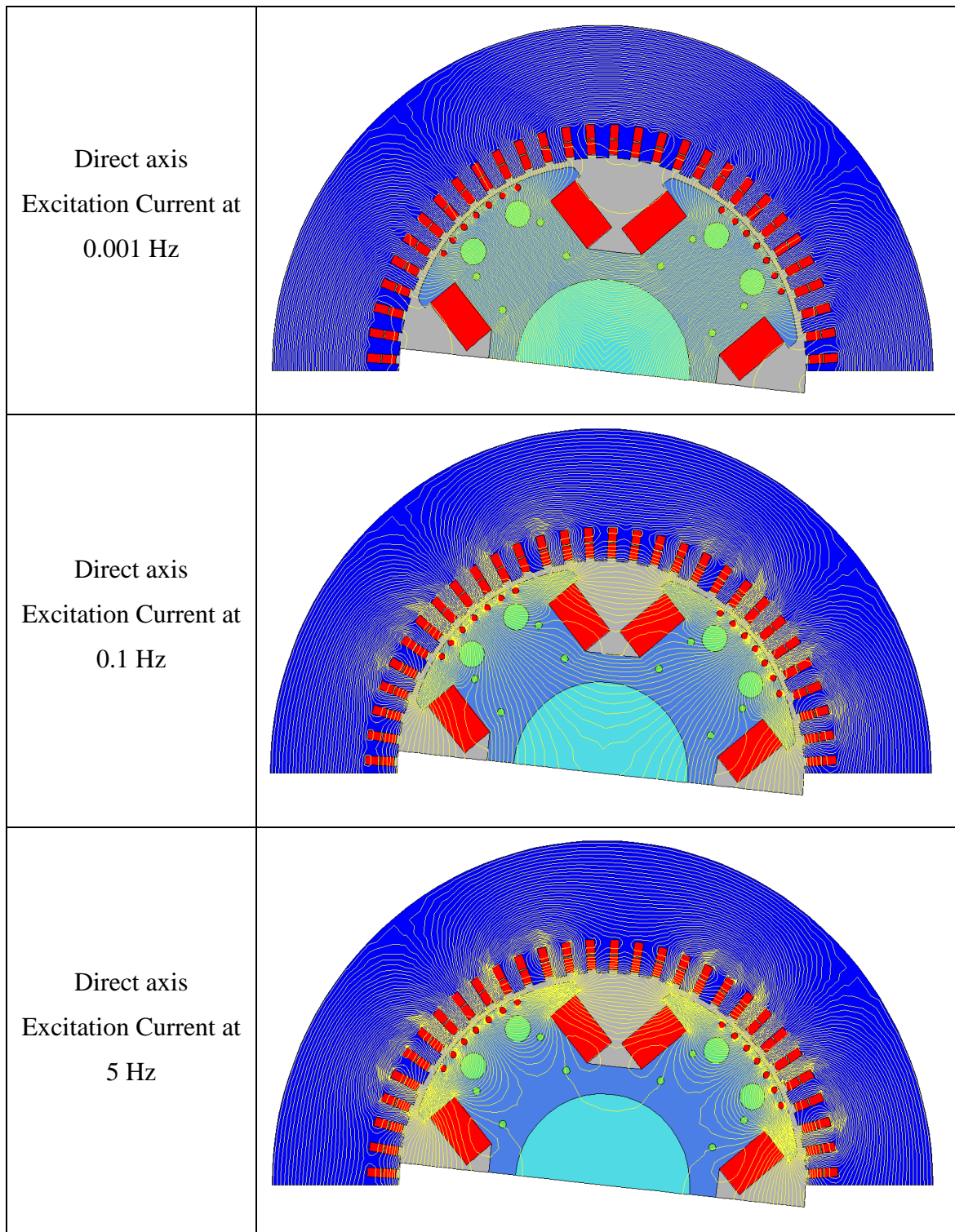
With the removal of the armature resistance the direct axis inductance can be plotted directly.

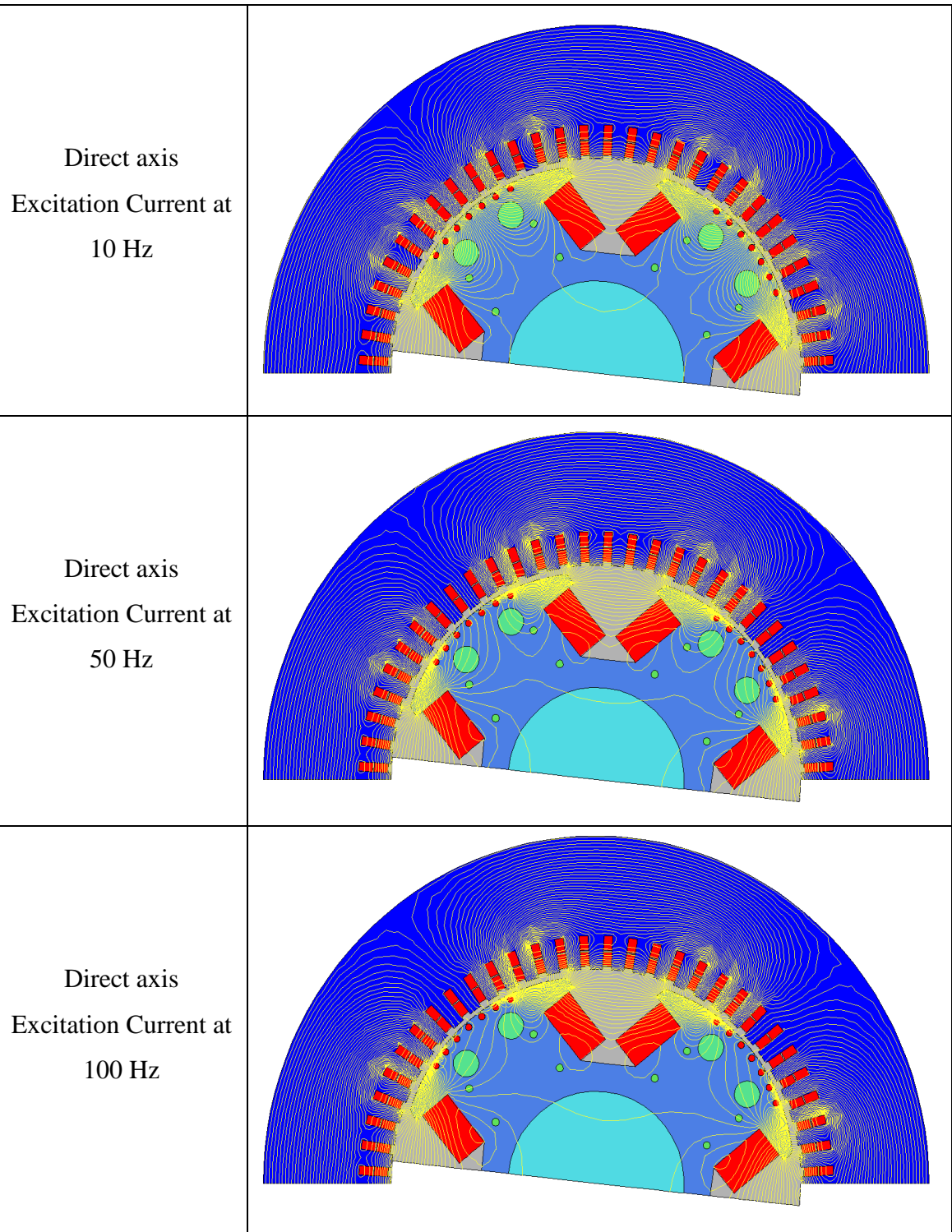
$$L_d(s) = \frac{Z_d(s) - R_a}{s} \quad \dots (4.6)$$

Similarly the machine can be viewed as a transformer and the field to armature turns ratio can be calculated using another limit.

$$N_{af}(0) = \frac{1}{sL_{ad}(0)} \left\{ \lim_{s \rightarrow 0} [Z_{af0}(s)] \right\} \quad \dots (4.7)$$

where $L_{ad}(0)$ is the low frequency limit of $L_d(s)$ minus the manufacture supplied stator leakage inductance.





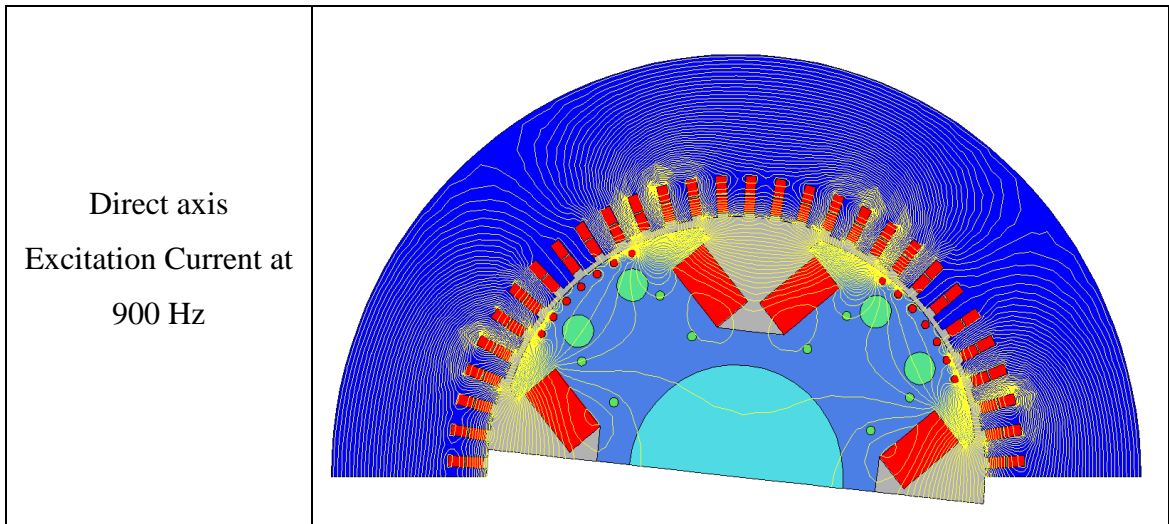
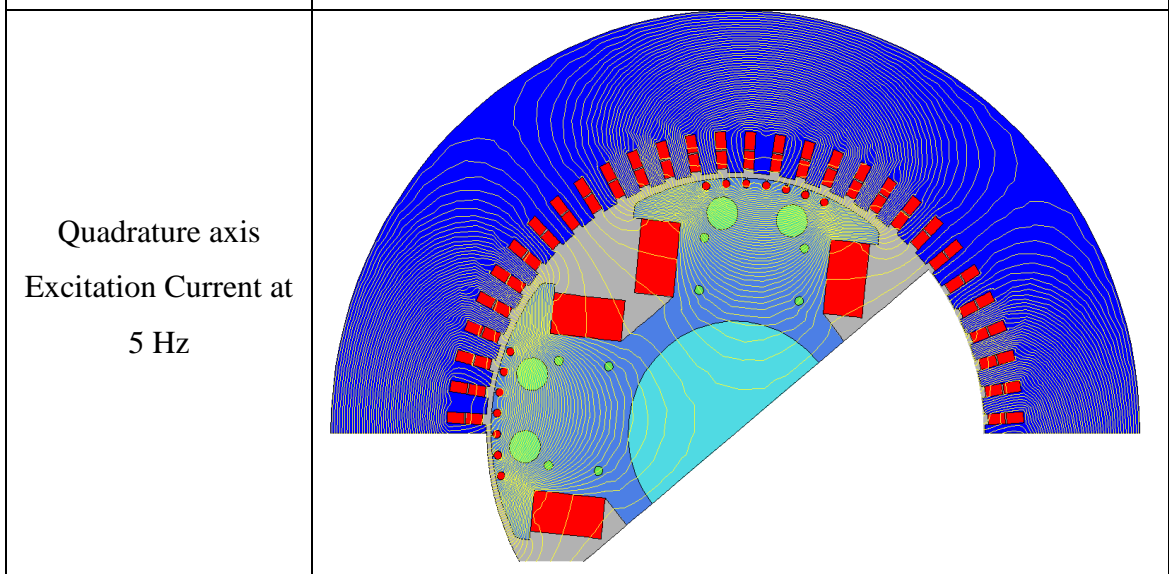
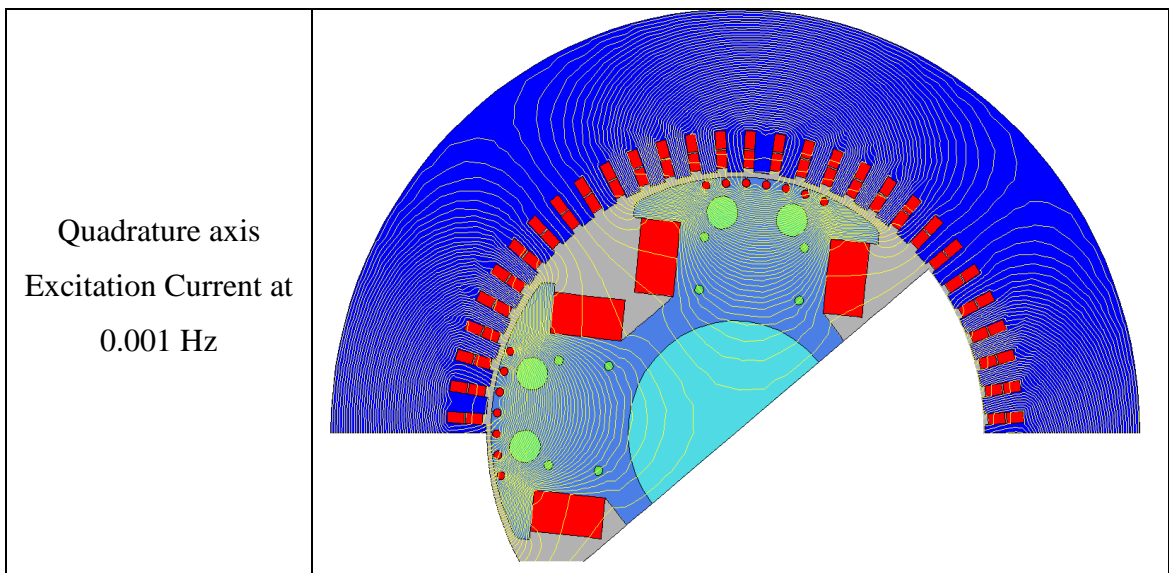


Figure 53 - A series of flux plots when excited by D axis current at increasing frequencies



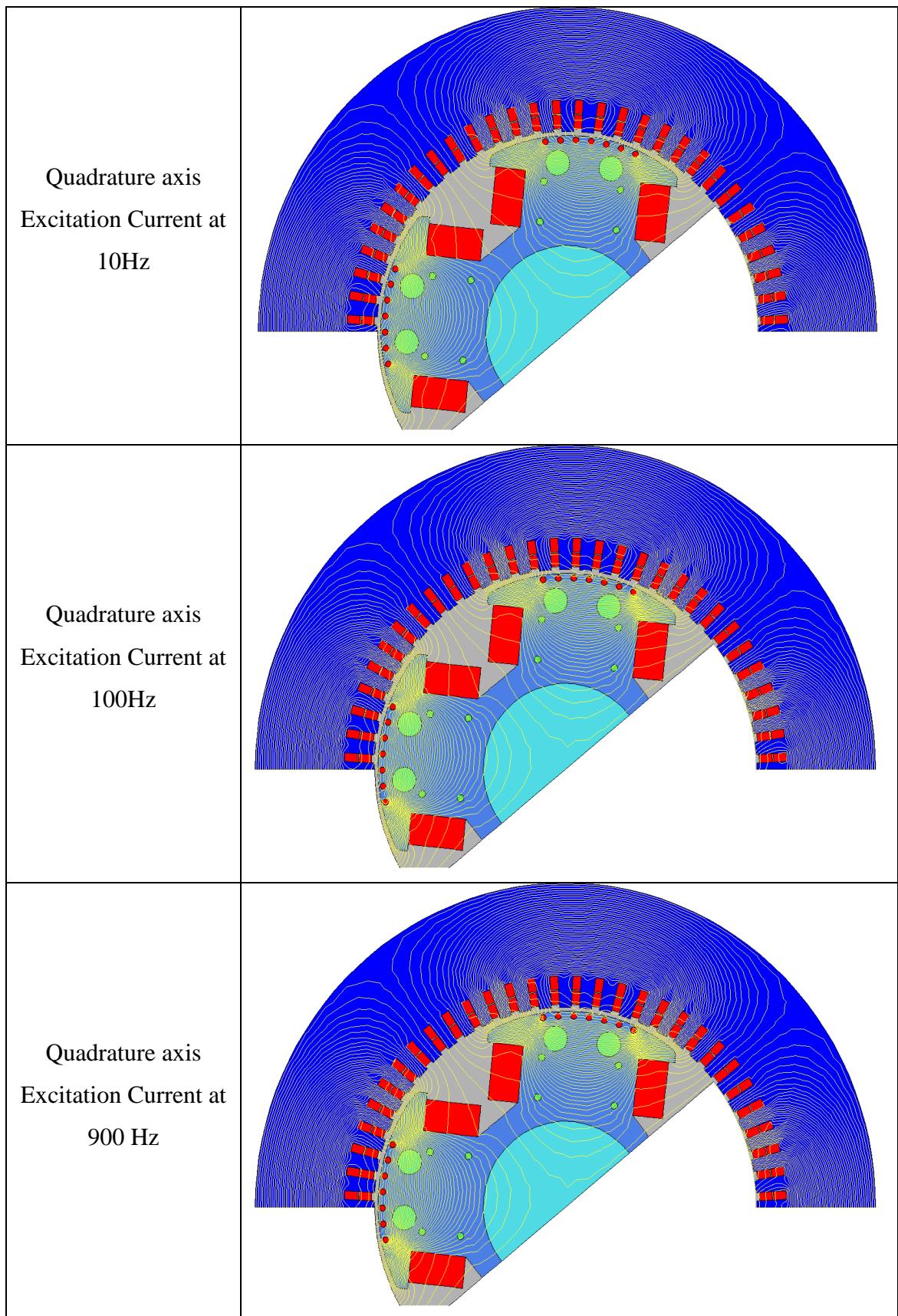


Figure 54 - A series of flux plots when excited by D axis current at increasing frequencies

4.2.2.1. Equivalent Circuits & Transfer Function Selection

Once the calculations have been completed the equivalent circuit must be decided upon. The machine is typically represented by 2 circuits: one for the q axis and one for the d axis. The order of the circuit used depends upon the type of machine being tested - simple machines require lower order networks, whilst machines with complicated topologies need larger models. The main factor affecting the complexity is the presence of rotor and stator components affected by AC fields - any closed loop into which current can be induced. Hence components such as damper bars, field windings stator windings, solid rotor poles, structural core bars and rotor casings are typical reasons for higher order circuits. Figure 55 shows D and Q axis equivalent circuits of increasing magnitude. In the synchronous machine analysed the machine has a single layer damper cage and a field winding and the lowest order model is adequate to analyse the machine (row A in Figure 55).

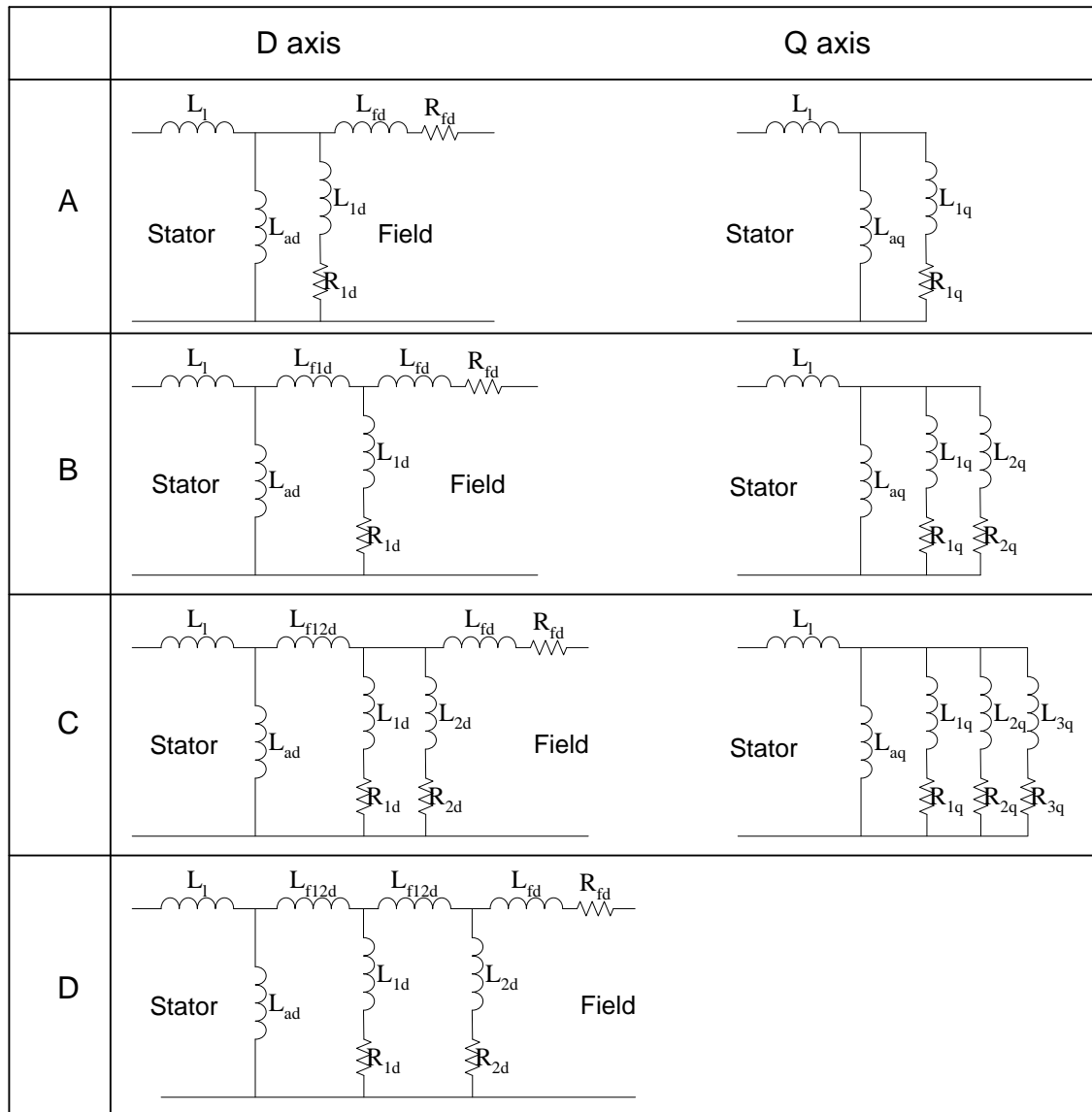


Figure 55 - D and Q axis Equivalent Circuits of increasing magnitude

Once the data is collected the order of the model dictates the transfer function used to curve fit the simulation. The transfer functions take the general form of equation (4.8)

$$f(s) = \frac{k(0)(1 + sT_1)(1 + sT_3)\dots(1 + sT_{2n-1})}{(1 + sT_2)(1 + sT_4)\dots(1 + sT_{2n})} \quad \dots (4.8)$$

4.2.2.2. Effect of the Damper bars

Flux plots in Figure 56 and Figure 57 clearly show the effect of the damper cage. The flux at low frequency is virtually DC and does not induce any current in the damper

cage: consequently the cage is very passive and does not actively alter the flux lines other than through the permeance variation. As the frequency increases the cage is more actively coupled to the stator windings and induction increases. The current flow creates its own field which opposes the main path and, as the flux plot shows, the cage acts as a very effective block, stopping the majority of pole body flux, reducing field winding linkage and leaving leakage across the inter polar air gap region. The 17.5MVA machine was simulated with and without the damper cage, so the effect can be seen in the frequency plots shown in Figure 58, Figure 59, Figure 60 and Figure 61. On the left hand low frequency side of the charts there is little or no deviation between the 2 simulations. As the frequency increases, typically around 1Hz, the charts diverge and the simulations with damper bars show increased attenuation in all plots.

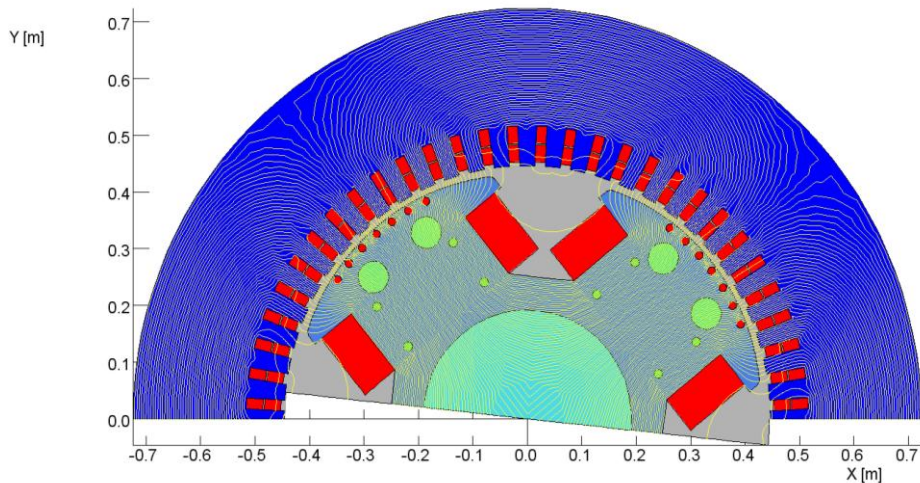


Figure 56 - AC flux plot at 0.001Hz

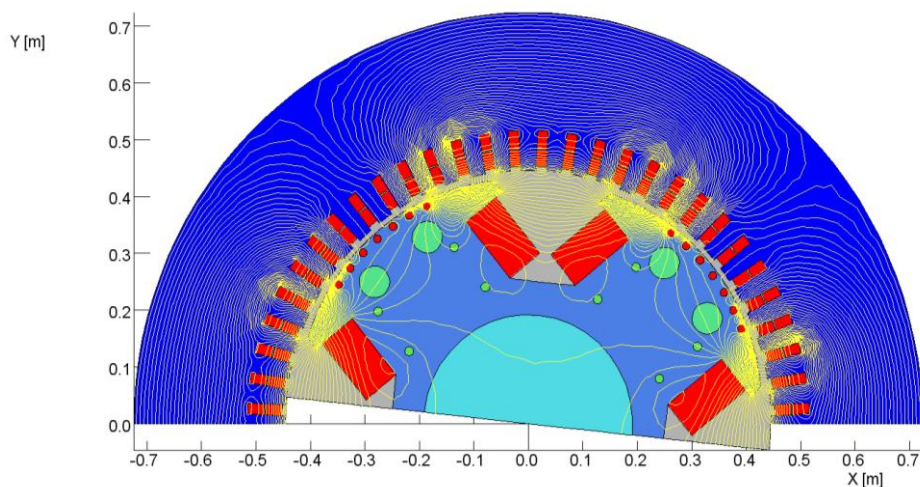


Figure 57 - AC flux plot at 900Hz

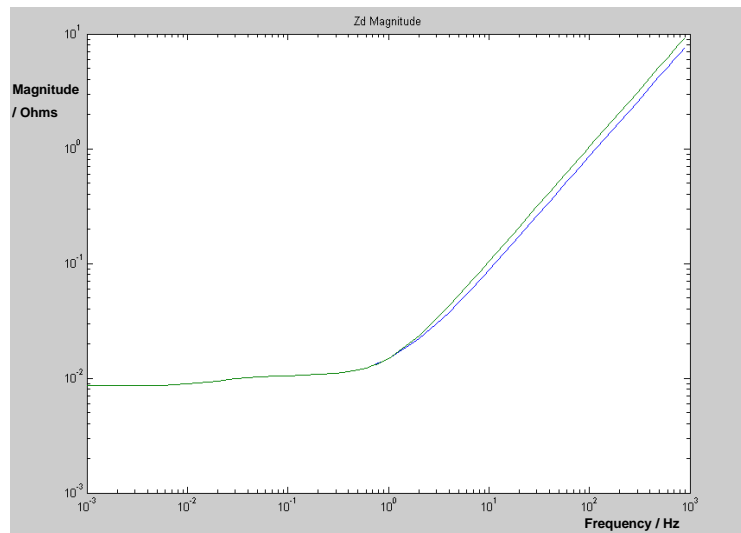


Figure 58 - Magnitude of $Z_d(s)$ with and without damper bars. With damper bars in blue. Without damper bars in Green

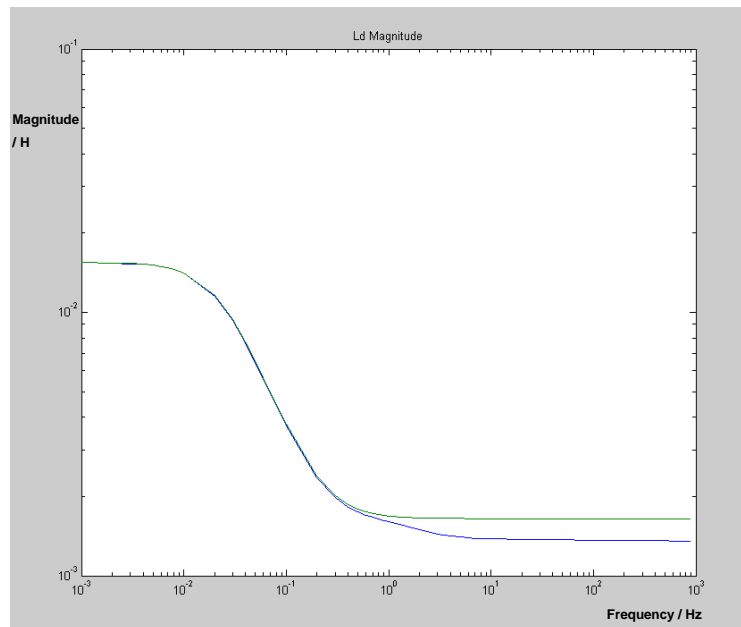


Figure 59 - Magnitude of $L_d(s)$ with and without damper bars. With damper bars in blue. Without damper bars in Green

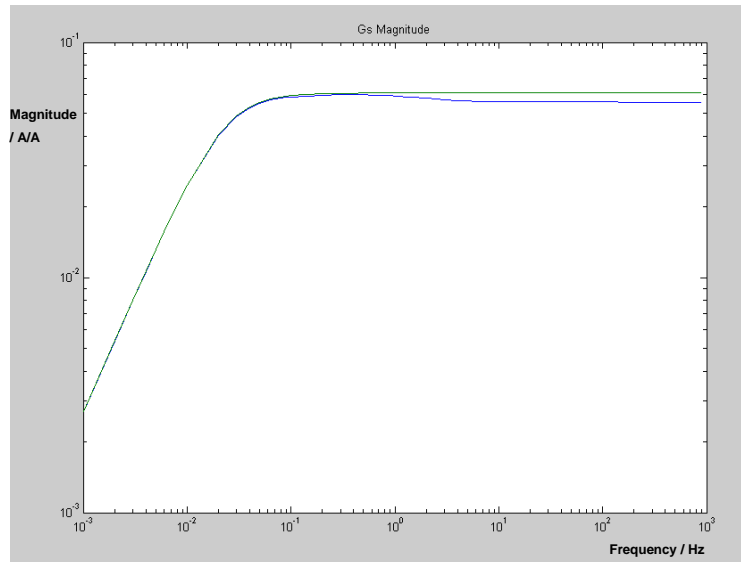


Figure 60 - Magnitude of $G_s(s)$ with and without damper bars. With damper bars in blue. Without damper bars in Green

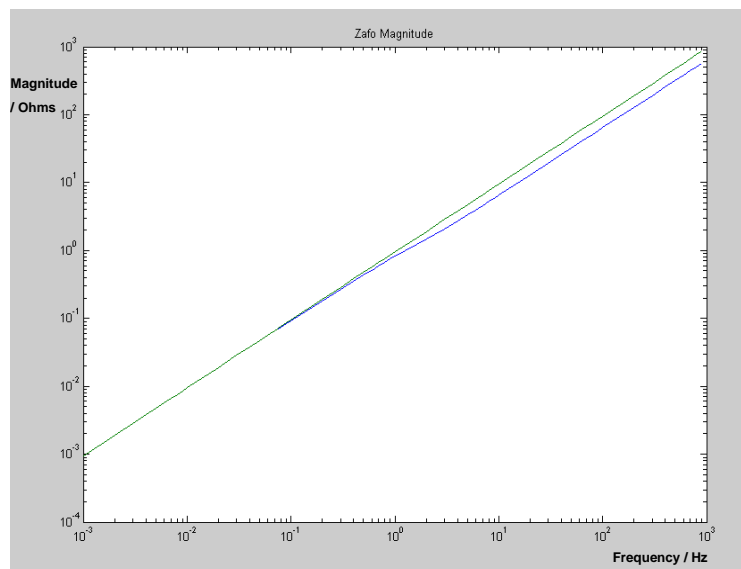


Figure 61 - Magnitude of $Z_{af0}(s)$ with and without damper bars. With damper bars in blue. Without damper bars in Green

4.2.2.3. Calculated results

For the curve fitting and the calculations the following results have been found and are compared to the design program used to originally design the machine. The curve fitting is calculated, based upon the characteristic equation in section 4.2.2.1. With the characteristic equation the constants are varied until the coefficient of determination (R^2) is as close to 1 as possible. To quickly vary the parameters a genetic algorithm is used within MATLAB. The genetic algorithm relies upon the fitness function giving an output of 0 with a perfect fit. The fitness function output must also be positive. Therefore the output R^2 is modified to be a suitable output from the fitness function:

$$\text{Fitness Function Output} = |1 - R^2| \quad \dots (4.9)$$

	EDS Design Calculation	SSFR FE Prediction	
L_{EW}	0.03174	0.0425	pu
L_l	0.0887	0.06062	pu
L_{ad}	2.2959	2	pu
L_{aq}	1.0974	1.0935	pu
R_a	0.00907	0.0086	ohms
R_{fd} (field referred)	0.3625	0.3671	ohms
L_{fd}	0.2018	0.1666	pu
Nafo	12.33	9.876	

Figure 62 - Table showing a comparison between SSFR results and factory design results for a 17.5MVA generator

4.2.3. Limitations

The system generates results for several of the desired parameters and can be very accurate in calculating easily obtainable parameters, such as the resistances. The system's main limitation is apparent when the reality of the parameters determined is examined. The choice of equivalent circuit and hence the order of transfer function used in the curve fitting exercise finds many terms which, although similar, are not the same as the standard terms which customers require. Test standard IEEE STD 115-1995 aptly summarises the issue:

"Thus T1 would be considered representative of T'q, and T4 to be representative of T'q0, and so on. Such time constants ... may be reasonably close in value.... but they are not identical.

...

The direct axes transfer functions expressions are not identical in time constant values to those developed in section 11 from various short circuit or voltage recovery tests such as T'd, T''d, T'do etc"

This insurmountable problem, coupled with fact that the system isn't particularly fast, simply makes the process, although potentially ideal, in reality incapable of finding the desired solution. The system must simulate a large range of frequencies - 0.001 to 900Hz for multiple test configurations and hence a large number of simulations are generated. In the test case these took up to 50 minutes to solve. From Section 2.7 the whole prediction system is being limited to approximately 1 hour, therefore the Standstill frequency response analysis simply does not give the required parameters in the time allotted.

4.3. Equivalent Circuit

Under transient conditions synchronous generators are typically represented by an equivalent circuit derived from viewing the synchronous machine as a compound transformer. The field winding and damper cage can be viewed as secondary windings against the primary armature winding. Each transformer leg has an associated turns ratio which can be ignored if all the terms are stator referred, as in Figure 63. During transient behaviour different parts of the generator, and hence different branches of the equivalent circuit, are active depending upon the speed of the transient. During fast transients the whole circuit is active due to the theory of constant flux linkage. The theory states that the linkage of a loss-free inductive circuit, closed on itself, cannot be altered [29]. The damper cage is by its very nature a closed circuit loop, as is the field winding, which is closed through the exciter. Hence, if resistance is neglected initially, the parallel branches of the whole circuit must be used to calculate the subtransient reactance, as in equation (4.10). Fast transients decay rapidly due the resistance of the damper cage, leaving the slower transient in the main field winding due to its much larger inductance and low resistance. This shortens the equivalent circuit, removing the subtransient branch, leaving the simpler transient reactance, as in equation (4.11). Finally, when all transients have decayed the machine will remain running in the stable synchronous mode, leaving only the standard synchronous reactance branch and hence equation (4.12). Similarly, given the frequency of the machine under a transient condition, if the resistance of the various branches are known the classical short circuit time constants can be calculated from the transient and subtransient reactances as shown in equations (4.13) and (4.14). Therefore to find the desired parameters for the machine data sheet the package must first calculate: X_{ad} , X_b , X_f , X_{kd} , R_f and R_{kd}

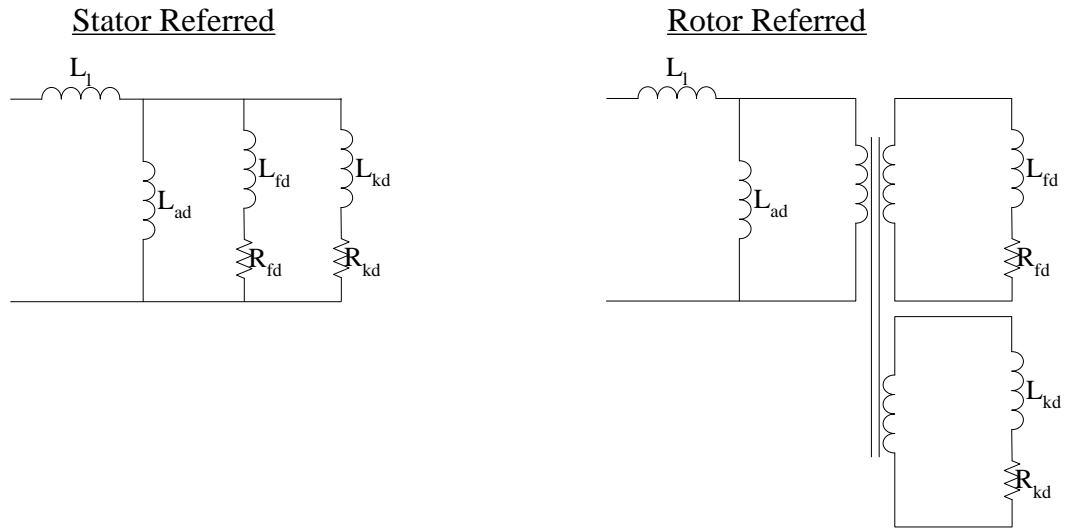


Figure 63 - The equivalent circuit of a synchronous generator

$$X''_d = \frac{X_{ad}X_fX_{kd}}{X_{ad}X_f + X_{ad}X_{kd} + X_fX_{kd}} + X_l \quad \dots(4.10)$$

$$X'_d = \frac{X_{ad}X_f}{X_f + X_{ad}} + X_l \quad \dots(4.11)$$

$$X'_d = X_{ad} + X_l \quad \dots(4.12)$$

$$T'_d = \frac{X'_d}{\omega R_f} \quad \dots(4.13)$$

$$T''_d = \frac{X''_d}{\omega R_{kd}} \quad \dots(4.14)$$

4.3.1. Leakage reactance - X_l

Firstly the leakage reactance must be calculated. Physically, this is flux that when under short circuit does not link the rotor field or damper cage. This is analogous to the flux which is skipping across the pole face of the machine and crossing the q axis of the machine. Within the FE program this can be easily achieved in a quickly solvable static model by exciting the stator conductors in the Q axis and placing tangential ($A=0$) boundaries around all rotor conductors, effectively blocking any linkage and forcing a leakage scenario. The field created can be seen in Figure 64. The extracted stator fluxes are converted into the per unit system to create a value for X_{IFE} which in turn is added to

the end winding leakage, as calculated in 3.3.3, to create the desired leakage reactance. X_l is already stator referred and so does not require transferring by a turns ratio.

$$X_l = X_{lFE} + X_{Lew} \quad \dots(4.15)$$

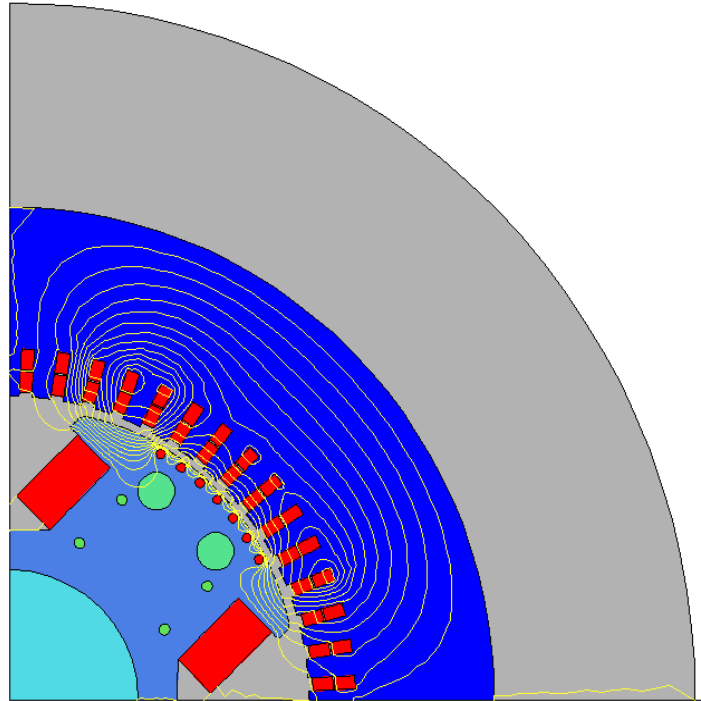


Figure 64 - Leakage Flux Simulation

4.3.2. Field reactance - X_f

The field leakage reactance is created by the flux which only links the rotor field winding and not the stator or damper cage winding. Technically a leakage inductance, the field reactance is regarded separately in the equivalent circuit, as it must be referred by a turns ratio. Consequently the field winding inductance can again be calculated by placing tangential flux boundaries around all the stator conductors and the damper cage. This pretty much limits the flux to the rotor, leaking around the inter polar region, as can be seen in Figure 65. It should be noted that although only a single pole is simulated the reactance must take to account the whole machine, which typically involves all the rotor poles being wound in series, increasing the reactance accordingly. The calculated value of reactance is rotor referred and must be referred across to the stator by the rotor/stator turns ratio squared, according to equation (4.16) The squared transformation is derived in Appendix I. As the synchronous generator is not just a simple transformer yoke, the turns ratio must be calculated to take into account not only the number of turns but the quantity of phases, the machine shape, the relative position of the phases

and any non-linking flux. Equation (4.17) describes the turns ratio used. The majority of the terms are straight forward, being direct physical properties or easily calculated. The exception is the Wieseman coefficients that are used to describe the machine's shape. These are explained more in section 4.3.3.

$$X_f^s = N_1^2 X_f^r \quad \dots(4.16)$$

$$N_1 = \sqrt{\frac{3}{2}} \frac{4}{\pi} \frac{n_s k_p k_d}{n_f} \frac{W_s}{W_r} \quad \dots(4.17)$$

where: $\sqrt{\frac{3}{2}}$ derives from the 3 phase nature of the machine

$\frac{4}{\pi}$ is as a result of Fourier analysis

n_f, n_s are the number of field and stator turns

W_s, W_r are stator and rotor Wieseman coefficients

$k_p k_d$ are pitch and distribution factors

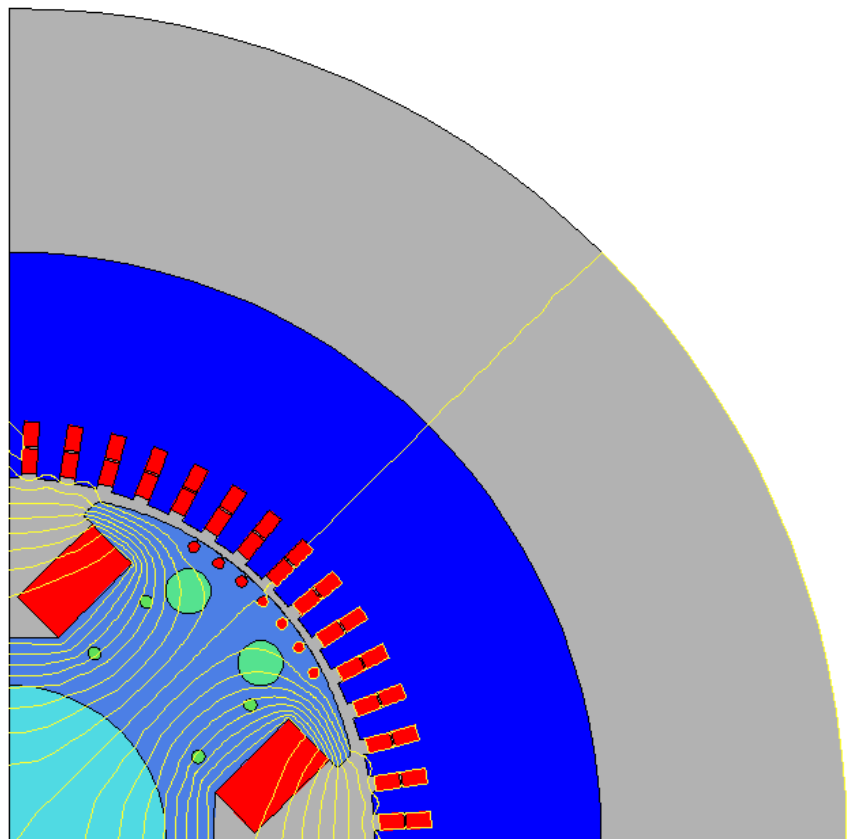


Figure 65 - Field Winding Reactance Simulation

4.3.3. Wieseman Coefficients

In 1927 Wieseman[30] used graphical means to calculate fields as an improvement upon Carters'[24] work. By using detailed flux plots a coefficient can be created which determines the relative peak of the flux density compared to a sinusoid in salient pole rotors. By using this coefficient both stator and rotor generated flux density can be compared to a sinusoid and hence a factor to account for the non sinusoidal nature of the machine air gap can be found. In the era before quick FE simulation Wieseman created various graphical plots with trend lines for different air gap size and pole pitch ratios, as well as air gap variation trends, to allow designers to quickly identify the coefficient needed for their machine. Thanks to modern computing power the method can be quickly implemented to allow a rapid calculation of the coefficient for every specific machine. Equation (4.18) shows the formula for calculation of the coefficients. Every harmonic of the Fourier will create a Wieseman coefficient but only the fundamental is required. The coefficients are calculated for both rotor and stator excitation as each excitation creates a different field distribution.

$$W = \frac{\hat{B}}{\frac{4}{\pi} \int_0^{2\pi} B(t) \sin(hwt) dwt} \quad \dots (4.18)$$

where h is the harmonic numbers 1,3,5,7 etc

B is the air gap flux density

Figure 66 shows the air gap flux density under both stator and rotor excitation, each with their own Fourier sinusoids overlaid. The peak flux densities, Fourier values and corresponding Wieseman coefficients have been calculated and are shown in the table below:

	Stator	Rotor
Peak Flux Density, \hat{B}	1.375	1.137
Fundamental Fourier Coefficient	1.178	1.027
Wieseman Coefficient, W	1.107	1.167

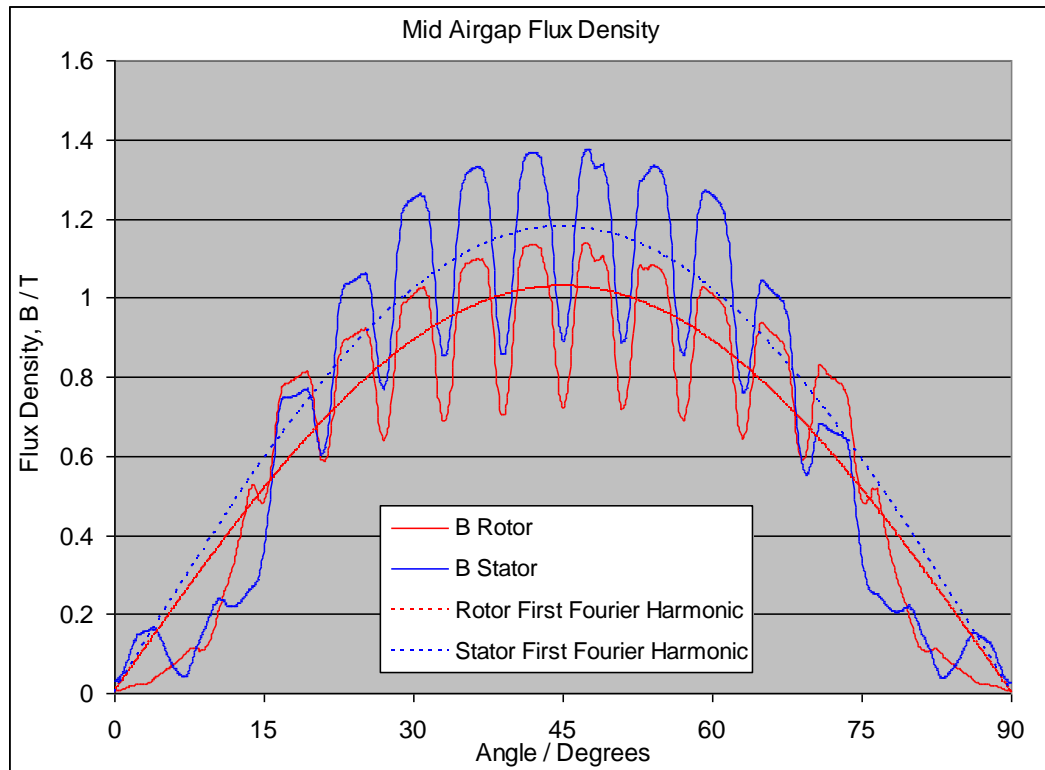


Figure 66 - Chart showing an example of stator and rotor excitation air gap flux densities with the first Fourier harmonic added

4.3.4. Transient Time constant - T'_d

To calculate the transient time Constant T'_d using equation (4.13) the field winding resistance R_f must be found. This resistance is calculated from a calculated mean length of turn, the wire dimensions and the bulk resistivity of copper. The mean length of turn assumes an average winding is in the middle of the winding area and forms a rectangular race track shape, as shown in Figure 67. This average length is not just a function of active material length and pole body width: it must also incorporate any additional overhang lengths that must be added to allow for additional rotor features. The main overhang length is caused simply by the field winding itself - as the copper is wound the additional layers stack on top, making the next coils longer. To create a high fill factor (high ratio of copper to non-copper in a region) square section copper is used, hence the winding dimensions can be easily calculated. The second additional length is the end plate or compression plate. This is typically a 50mm thick plate made from mild steel which is used to compress the stack of laminations. The plate must be used as the lamination stack alone cannot spread the load placed by the core studs used to compress the lamination stack. Hence without the endplate the laminations would splay or fan out as the distance from the stud increases. Being mild steel the endplate is magnetic,

therefore to avoid any eddy current heating loss on the pole face the endplate is slightly smaller than the rotor, as depicted in Figure 67. Once the mean length of turn is calculated the resistance can be calculated with equations from the resistivity of copper, the number of turns and the dimensions of the copper [Equations (4.19) and (4.20)]. The winding is wound directly on to the pole body (Figure 68) i.e. the coils are not wound onto a former and fitted later. This is for several reasons.

- on cruciform laminated rotors (Figure 7) there would be no possible way to fit a pre wound coil
- by winding directly on to poles the coil becomes mechanically stiffer and more durable as it is a tighter fit.
- The coils are handled less - just once during winding. Therefore there is a reduced risk of rotor coil failure.
- there is no additional stand out length required to allow the coil to be threaded onto the pole. Hence the additional cost of copper is saved.

$$MLT = 2(l_a + 2l_{ep} + 2w_f + w_{pb}) \quad \dots (4.19)$$

$$R_f = \frac{\rho \cdot MLT \cdot N_f \cdot p}{w_{fc} \cdot t_{fc}} \quad \dots (4.20)$$

where: MLT is the Mean Length of Turn

l_a and l_{ep} are the axial and end plate lengths

w_{pb} and w_f are the pole body and field winding widths

N_f is the number of field winding turns

ρ is the resistivity of copper

w_{fc} t_{fc} are the width and thickness of the field winding conductors

p is the number of series poles

The field resistance calculated is a DC resistance. This resistance is used as the field winding to a first approximation will be experiencing DC flux. The winding may

experience a slight AC field but as this is expected to be small the AC resistance has not been used. The field winding will also experience a proximity effect which increase the resistance. This effect has not been investigated and is an area where further study could be undertaken.

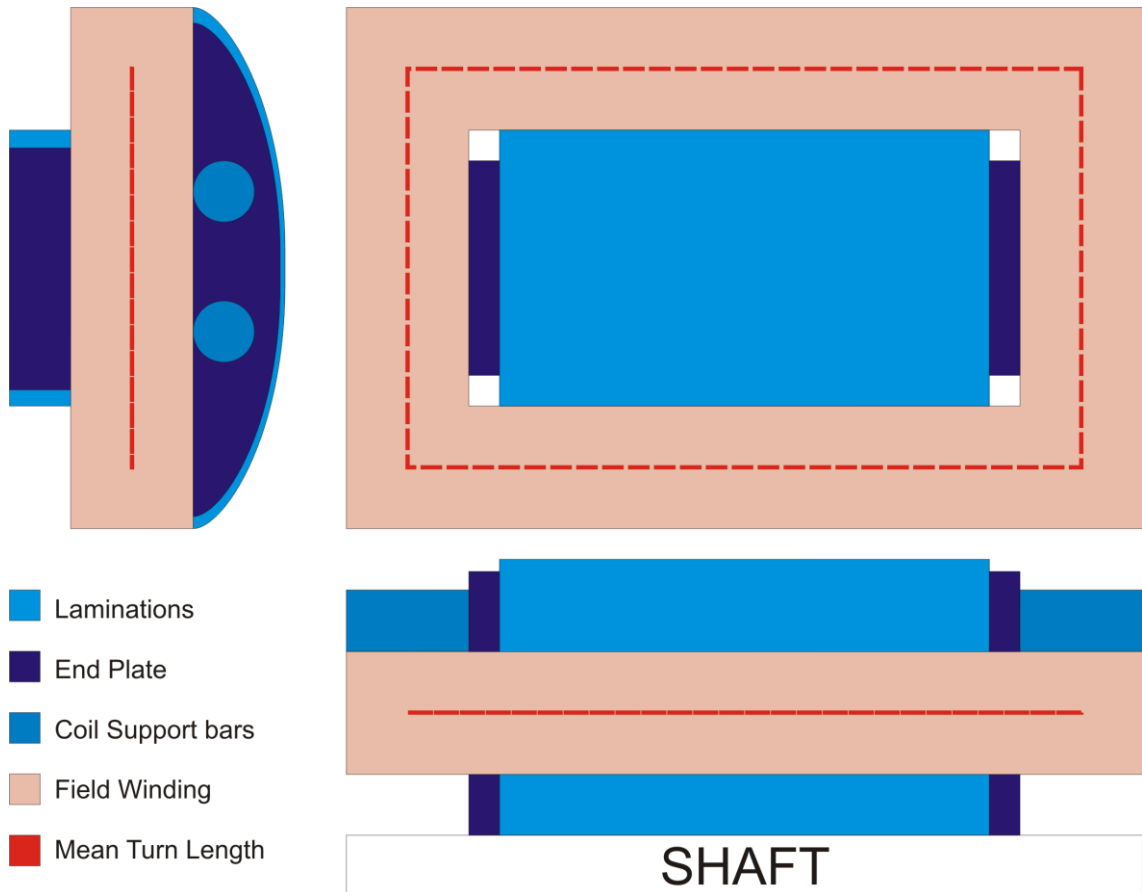


Figure 67 - Diagram showing the position of the Mean Turn Length for a single pole

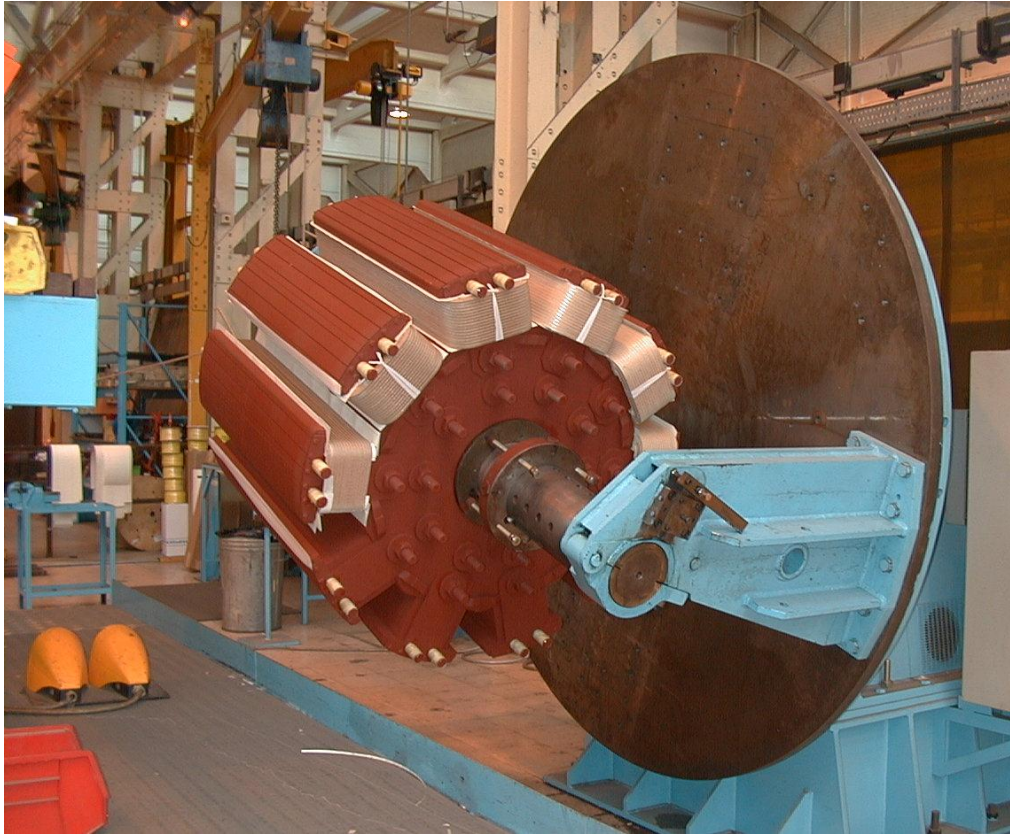


Figure 68 - Photo of the field winding being added to a 10 pole rotor body of similar rotor construction to Saxi

4.3.5. Subtransient Parameters

Similarly to the transient parameters it is possible to calculate subtransient parameters using equations (4.10) and (4.14). For this the value of the cage reactance X_{kd} must be found and it must be referred to the stator. The calculation and the referral of the reactance across the air gap begin to add significant problems because of the compound nature of the damper cage. The cage is not a simple racetrack coil like the field winding - it is several single turn coils all in parallel across the face of the pole. On some machines the cages on each pole are connected together, creating q axis damping, whilst on the majority of 4 pole machines they are left unconnected. This makes the ratio a complicated parameter to find. To avoid this issue a three phase short circuit test has been simulated within the FE. The three phase short circuit test is a standard characterisation test which can be undertaken before a machine has left the factory. The test involves spinning the generator on open circuit at rated speed using a driving motor. The test machine then has a 3 phase short circuit applied at the terminals and the driving motor is turned off. The resulting current profiles from the test machine and the initial terminal voltage are logged to create a series of envelopes from which all the desired

parameters can be found using curve fitting techniques. The test takes only a matter of seconds, with the envelopes decaying entirely within 10 seconds, however within FE due to the rapidity of changes and use of a rotating solver the simulation takes many hours and is often left overnight, allowing results to be gleaned in the morning. Additionally two poles of the machine must be simulated as the damper cage is critical in this scenario and as it differs from pole to pole the mesh must include all this data. Allowing the simulation to decay fully is not feasible for a design system - it is too slow: fortunately the subtransient parameters have a very rapid decay rate and can be found from the initial section of the simulation, so the machine need only rotate around 4 electrical cycles to allow the envelope to be identified

4.3.5.1. Curve Fitting Routine

A three phase short circuit envelope is typically represented as a cosine wave multiplied by 2 compound exponentials with an added distortive component set upon a dc offset exponential. This results in the characteristic equation (4.21)

$$I_{sc} = I_{envelope} - I_{harmonic} - I_{DC}$$

$$I_{sc} = V \left\{ \begin{array}{l} \left[\frac{1}{X_d} + \left(\frac{1}{X'_d} - \frac{1}{X_d} \right) e^{\frac{-t}{\tau'_d}} + \left(\frac{1}{X''_d} - \frac{1}{X'_d} \right) e^{\frac{-t}{\tau''_d}} \right] \cos(\omega t - \phi) \\ - \frac{1}{2} \left[\frac{1}{X''_d} - \frac{1}{X''_q} \right] e^{\frac{-t}{\tau_a}} \cos(2\omega t - \phi) \\ - \frac{1}{2} \left[\frac{1}{X'_d} - \frac{1}{X'_q} \right] e^{\frac{-t}{\tau_a}} \cos(\phi) \end{array} \right\} \dots \quad (4.21)$$

The DC component is a consequence of the initial position of the rotor relative to the stator conductors, consequently it is possible for it to be zero in a phase if the short circuit occurs at the correct time. In many synchronous generators X''_d and X''_q are similar in size due to d and q axis connected damper cages: this results in twice fundamental frequency distortion cancelling. By removing the sinusoidal terms and just looking at the envelope created by the peaks, the reactances and time constants for a machine can be found.

For test and simulation data a robust curve extraction routine has been created. Firstly to remove the time dependant cosine components the envelope of the waveform is extracted. The peaks of the waveform are first identified by a gradient change routine. This routine looks for any change in the sign on the gradient to identify a maxima or minima. Since only a change in sign is sought the true gradient need not be calculated. The denominator is a change in time which is always positive as the simulation data progresses. Therefore to save processing time the gradient can be approximated to just the numerator, as shown in equation (4.22).

$$\text{True Gradient}(n) = \frac{\text{LineA}(n+1) - \text{LineA}(n)}{\text{Time}(n+1) - \text{Time}(n)}$$

$\text{Time}(n+1) - \text{Time}(n)$ is finite and always positive hence :

$$\text{Gradient}(n) = \text{LineA}(n+1) - \text{LineA}(n) \quad \dots(4.22)$$

These identified maxima and minima form the envelope, however special cases can cause false maxima and minima to be detected:

- 1) Distortion - If X''_d is significantly different to X''_q the double frequency harmonic can cause turning points which are not the desired maxim or minima. Figure 69 shows a simulated short circuit where there is a significant difference between X''_d and X''_q . The distortion of the double frequency component gives the characteristic extra maxima and minima midway between the main envelope peaks

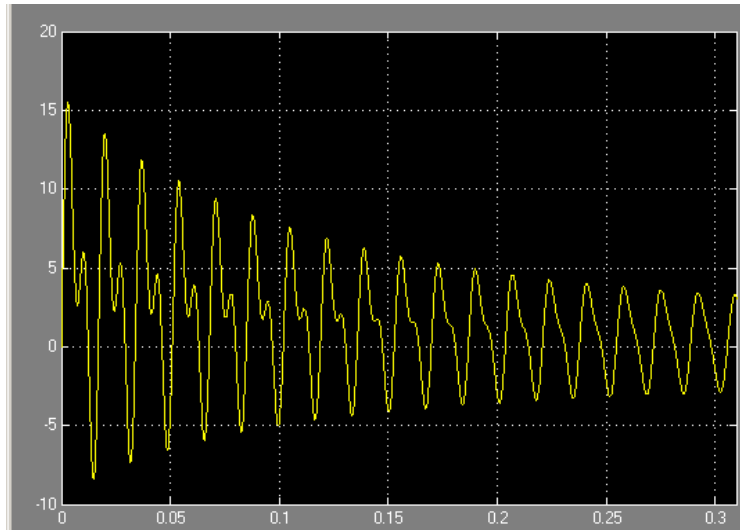


Figure 69 - A simulated example of a short circuit current plot showing subtransient distortion with $X''_d/X''_q = 2$.

X axis: Time in Seconds Y axis: Current in Amps

- 2) Harmonic content - Ripple in the waveform can be caused by the stator slots due to the change in permeance: this can cause several gradient changes on a single peak which could result in extra maximum points near to the maxima. Figure 70 shows the evidence of a slot ripple on the peak of waveform which has 3 gradient changes on 3 subsequent points (maxima - minima - maxima).

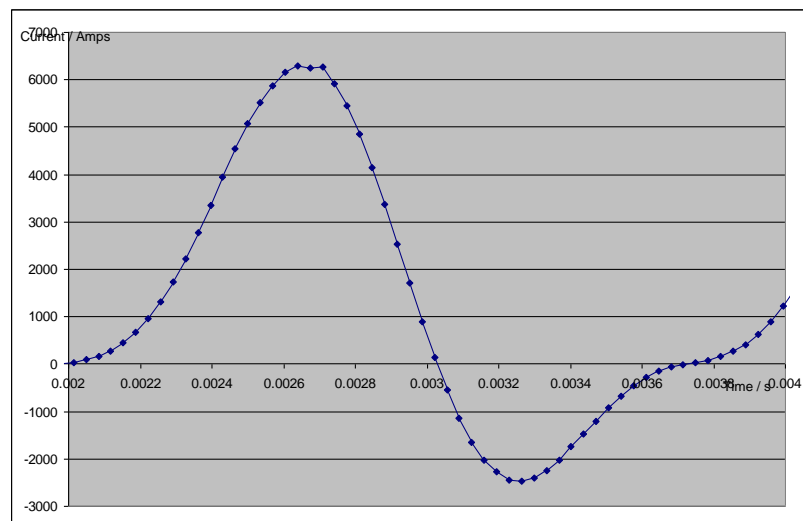


Figure 70 - An Example of slot ripple causing distortion in a short circuit

- 3) Noise, although minimal, can cause false readings, particularly at low current values, such as when a phase has a high initial DC offset and the phase current is at

a minima, resulting an actual short circuit value which is close to zero and thus is distinguishable from measurement error.

To remove anomalous readings found by a simple peak search, added functionality has been added. When a peak is found it is tested to make sure it is within the correct time frame i.e. the criteria that it must be a whole period since the previous maxima or minima (within a tolerance) must be satisfied. When the criteria is satisfied then the point is accepted as a valid maximum or minimum candidate. This will remove any points caused by distortion. Additionally the period used for the criteria must be based upon a running average since during factory tests the driving machine is switched off when the short is applied, resulting in the test machine slowing. The maxima or minima candidates are approved after they are inspected to confirm that they are the extreme value within that tolerance. If a larger point is found any additional candidates are disregarded and replaced by the new maximum.

For example:

Using the simplified example diagram below (Figure 71) several points can be observed.

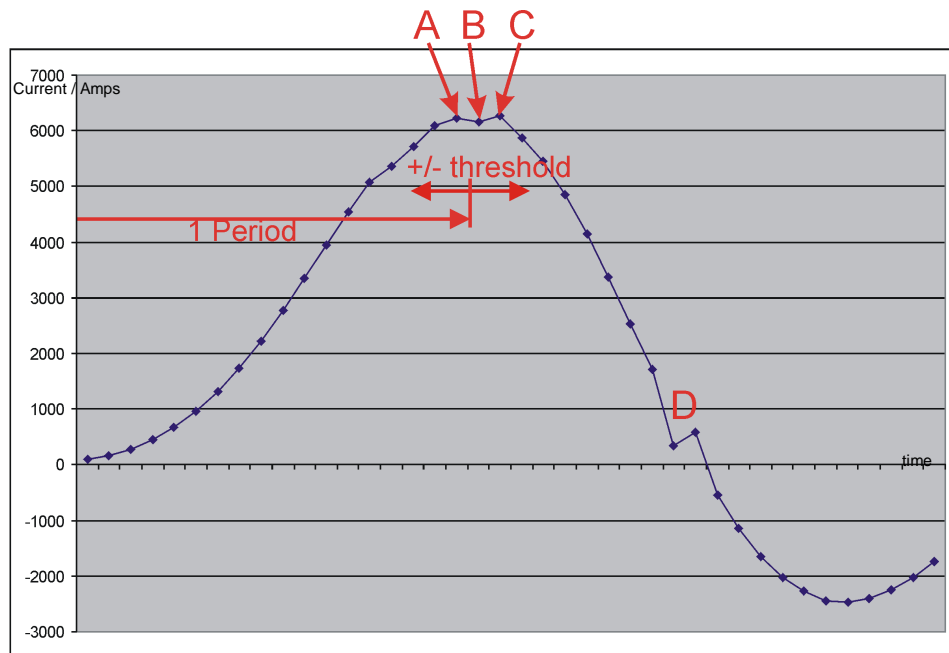


Figure 71 - A simplified single phase of a 3 Phase short circuit test.

A gradient sign change is detected at point A. It will be accepted as a valid maxima as the point falls within 1 period of the previous maxima ± 1 threshold, however it can be seen that point C is a higher maxima. The routine will then search within ± 1 threshold to find the maximum point: hence point C will be logged as the actual maxima.

Point B is a minima caused by slotting ripple: it would be rejected as the point is not a period from the previous minima. Similarly at D there are minima and maxima caused by harmonic distortion, again both of these points will be rejected as they do not pass the period criteria. Figure 72 below shows some examples of the correct sample being identified by the routine.

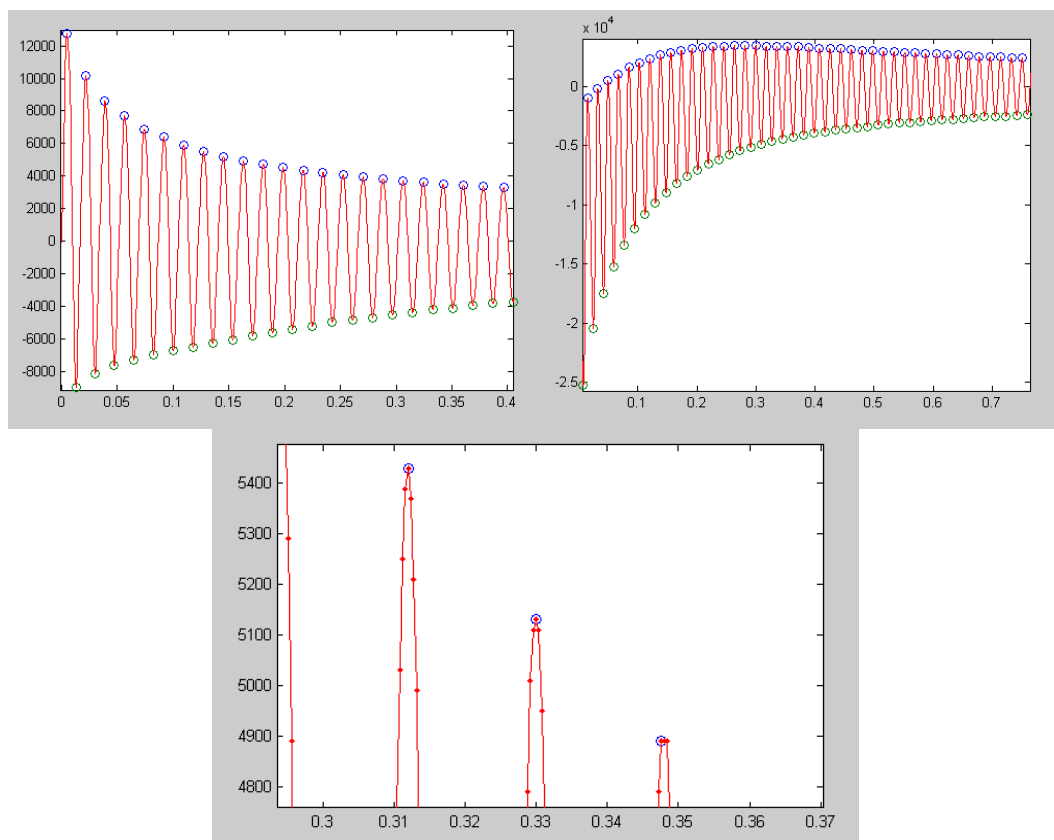


Figure 72 - Correctly Identified data : Red = input data, Blue circles = chosen maxima, Green circles = chosen minima

X axis: Time in Seconds Y axis: Current in Amps

Curve fitting

Once peaks have been identified the envelope is defined and a curve fitting routine can be used to find an equation which describes the points. A polynomial equation is found

to describe both the upper and lower envelopes. For a polynomial of power n the equations are described in equation (4.23) where A is a constant

$$\begin{aligned} P_{upp}(t) &= A_{upp0} + A_{upp1}t + A_{upp2}t^2 \dots + A_{uppn}t^n \\ P_{low}(t) &= A_{low0} + A_{low1}t + A_{low2}t^2 \dots + A_{lown}t^n \end{aligned} \quad \dots (4.23)$$

Hence the total envelope is the sum of the two individual equations:

$$P_{total}(t) = P_{upp}(t) + P_{low}(t)$$

$$P_{total}(t) = A_{upp0} + A_{low0} + (A_{upp1} + A_{low1})t + (A_{upp2} + A_{low2})t^2 \dots + (A_{lown} + A_{uppn})t^n$$

$$P_{total}(t) = A_{total0} + A_{total1}t + A_{total2}t^2 \dots + A_{totaln}t^n \quad \dots (4.24)$$

A DC decay curve can be found and is the average of the 2 envelopes and hence the symmetrical non-DC dependant curve can be found

$$P_{DC}(t) = \frac{P_{total}(t)}{2}$$

$$P_{sym}(t) = P_{upp}(t) - P_{DC}(t) = P_{upp}(t) - \frac{(P_{upp}(t) + P_{low}(t))}{2}$$

$$P_{sym}(t) = \frac{(P_{upp}(t) - P_{low}(t))}{2} \quad \dots (4.25)$$

The 3 phase short circuit factory test results for a 17.5MVA machine have been used to demonstrate the curve fitting routine. Figure 73 shows the first second of the test, following a short circuit. The routine easily identified the peaks of the waveform and then, using the chosen peaks, fits the polynomial to the chosen points. The DC offset caused by initial position is easily identified and is shown in red. Figure 74 and Figure 75 show a cropped view of the subtransient regions for each of the phases. As well as the polynomial curve fit described, the curve fit created by the company's existing software is shown. Four of the six charts show a very high correlation between

the polynomial method and the existing method. The diagrams with high correlation are phase A maxima, phase A minima, phase B maxima and phase C minima. The minima in phase B and the maxima in phase C show significant variation, specifically at $t=0$.

Looking closely at Figure 75 for the minima in phase B the polynomial is much closer to the first minima than the company's software, yet it assigns a lower significance to the second minima. The second variation occurs in the phase C maxima chart. The company's software fails completely, heading to zero instead of following the correct trend which the polynomial correctly identifies.

These differences will result in a discrepancy in calculated parameters - especially the subtransient reactance. Although only a single test is not statistically sufficient, this demonstration shows the polynomial curve fitting to be an acceptable curve fitting method. The limitation of using a curve fitting method adds an identifiable but unquantified potential source of error into any results, which is discussed more in the results section.

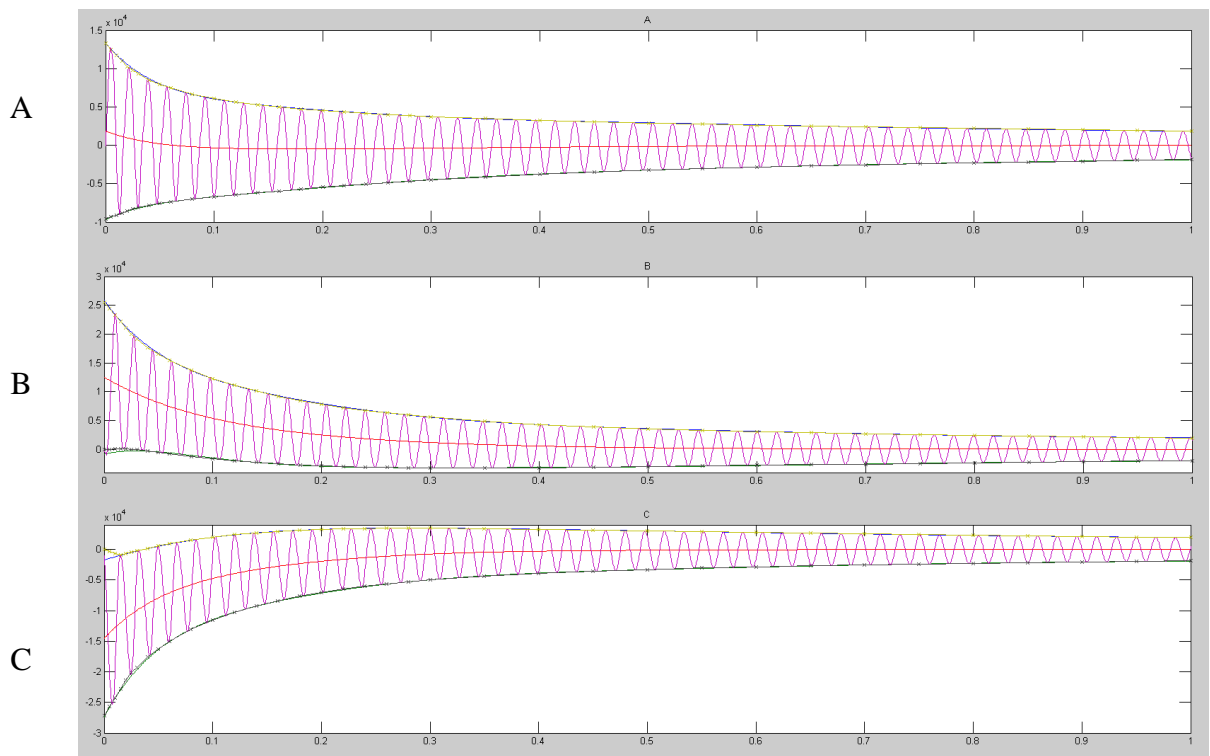


Figure 73 - Factory Test results for a 17.5MVA Generator. Key: Pink = Input data, Red = DC Curve

X axis: Time in Seconds Y axis: Current in Amps

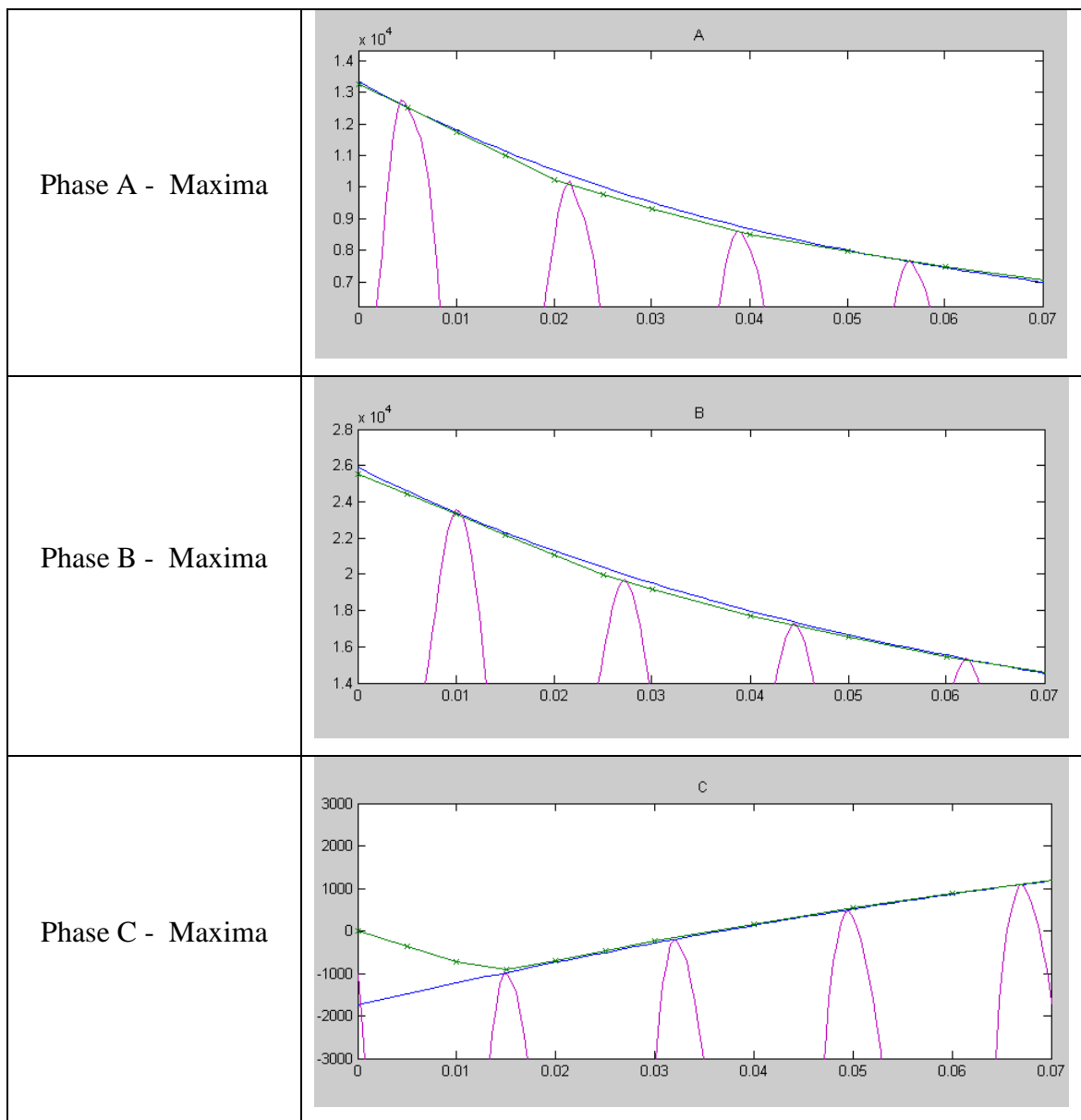


Figure 74 - Maxima in the subtransient region of the test - Key: Pink = input data, Blue = Polynomial curve fit, Green = Existing company software curve fit

Units for all For all charts X axis: Time in Seconds Y axis: Current in Amps

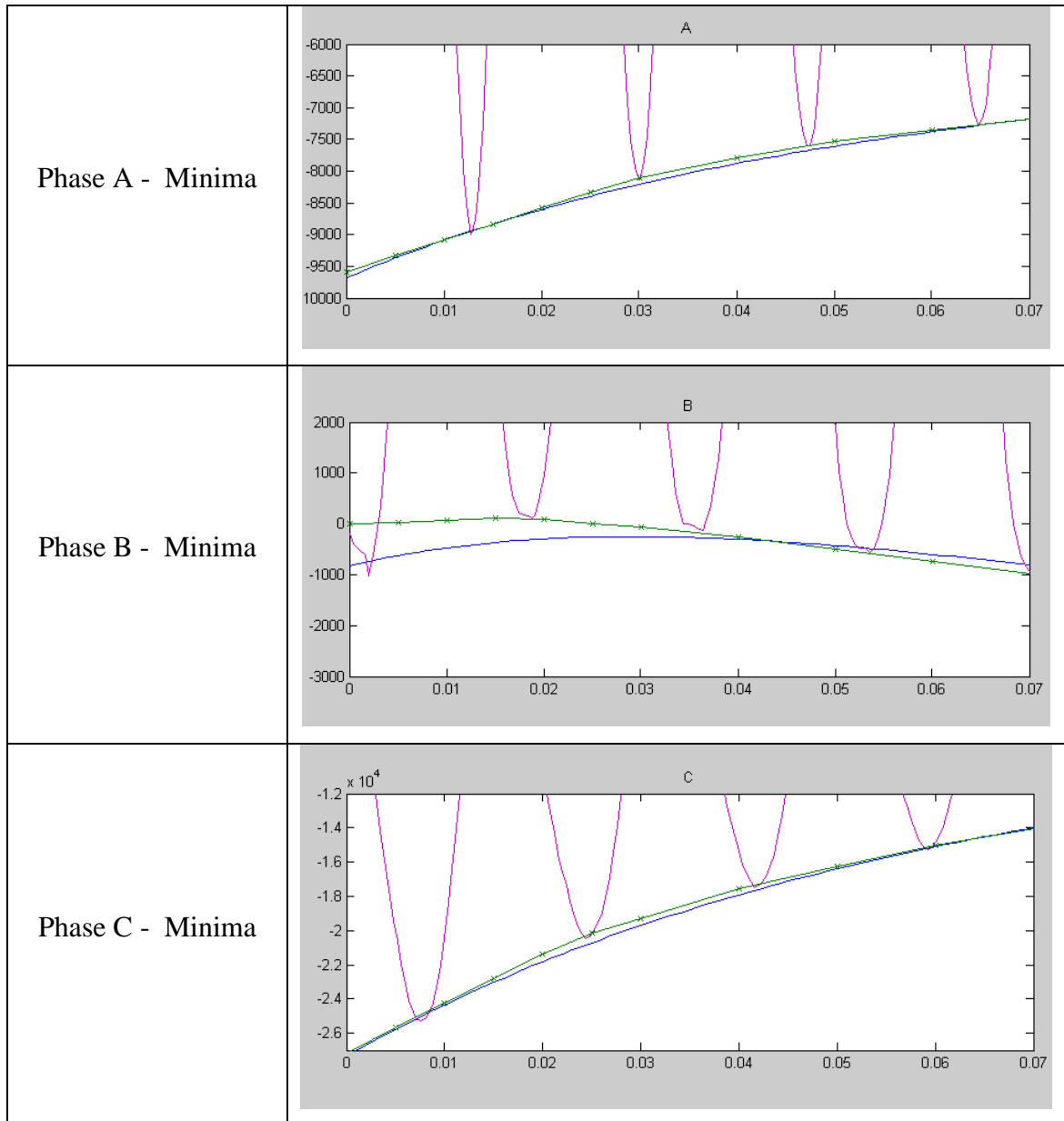


Figure 75 - Minima in the subtransient region of the test - Key: Pink = input data, Blue = Polynomial curve fit, Green = Existing company software curve fit

Units for all For all charts X axis: Time in Seconds Y axis: Current in Amps

Determination of the Subtransient Reactance - X''_d

Once the curve has been fitted it is very quick to find X''_d . Using the curve fit for the symmetrical envelope (equation (4.25)) the DC and Harmonic content of equation (4.21) can be removed, leaving equation (4.26). Additionally, if the curve fits are inspected at time = 0, several parts of the equation become zero and leave equation (4.27). Therefore the subtransient reactance can be quickly found using the point at which the symmetrical envelope intersects the y axis using equation (4.28). This is

convenient as it removes all the time dependant parts of the fit polynomial reducing it down to a single constant A_{sym0} allowing rapid calculation.

$$I_{sc} = V \left[\frac{1}{X_d} + \left(\frac{1}{X'_d} - \frac{1}{X_d} \right) e^{\frac{-t}{\tau'_d}} + \left(\frac{1}{X''_d} - \frac{1}{X'_d} \right) e^{\frac{-t}{\tau''_d}} \right] \dots \quad (4.26)$$

$$I_{sc} = \frac{V}{X''_d} \dots \quad (4.27)$$

$$X''_d = \frac{V}{I_{SC}} = \frac{E}{P_{sym}(0)} = \frac{E}{A_{sym0}} \quad \dots \quad (4.28)$$

It should be noted that to create the best results the average of all 3 phases is used to create an average X''_d , which takes into account any slight variation in the 3 phases. The exception to this averaging is if the routine detects a phase in which the result is significantly different to the other 2 phases. In this case the average of the 2 good phases is used. If all 3 phases show significant deviation then the result is flagged for further investigation. Causes of an individual anomalous phase are usually a poor set of test results, with an incorrect result at zero time. For example the sample before the short circuit is zero as the machine is open circuit. If it is included in the analysis the sign change routine may detect a maxima or minima on the second sample. This will the result in a poor polynomial curve fit.

Once X''_d is identified the subtransient time constant can be calculated by substituting all the known parameters into equation (4.26). This will leave a single exponent which is found by linearly fitting a curve to the log of the remaining envelope to find the gradient which is directly related to τ''_d as shown in equation (4.32)

$$I_{sc}(t) - \frac{V}{X_d} - V \left(\frac{1}{X'_d} - \frac{1}{X_d} \right) e^{\frac{-t}{\tau'_d}} = I_{SC_T''_d}(t) = \left(\frac{1}{X''_d} - \frac{1}{X'_d} \right) e^{\frac{-t}{\tau''_d}} \dots \quad (4.29)$$

$$\ln[I_{SC_T''_d}(t)] = \frac{-t}{\tau''_d} \ln \left(\frac{1}{X''_d} - \frac{1}{X'_d} \right) \dots \quad (4.30)$$

from $y = mx + c$:

$$m = \frac{-1}{\tau''_d} \ln \left(\frac{1}{X''_d} - \frac{1}{X'_d} \right) \dots \quad (4.31)$$

$$t''_d = \frac{-1}{m} \ln \left(\frac{1}{X''_d} - \frac{1}{X'_d} \right) \dots (4.32)$$

The short circuit test is simulated at 1 pu open circuit volts. The factory test is carried out at 0.25, 0.5, 0.75 and 1pu open circuit voltage.

4.3.6. Calculation Speed

The use of parallel processing is shown in Figure 76. The static simulations on the top row all run one after the other because in total they take about 3 minutes, whereas the rotating simulation used for the three phase short circuit takes about 20 minutes. The 3 series simulations could be paralleled, but leaving them in series leaves spare processors for other tasks. Typically the MATLAB processes are calculated in seconds, compared to the minutes used by the FE simulations. As the short circuit simulation occurs from open circuit this whole process must be calculated after the field current for 1pu open circuit operating conditions is determined in Chapter 3.

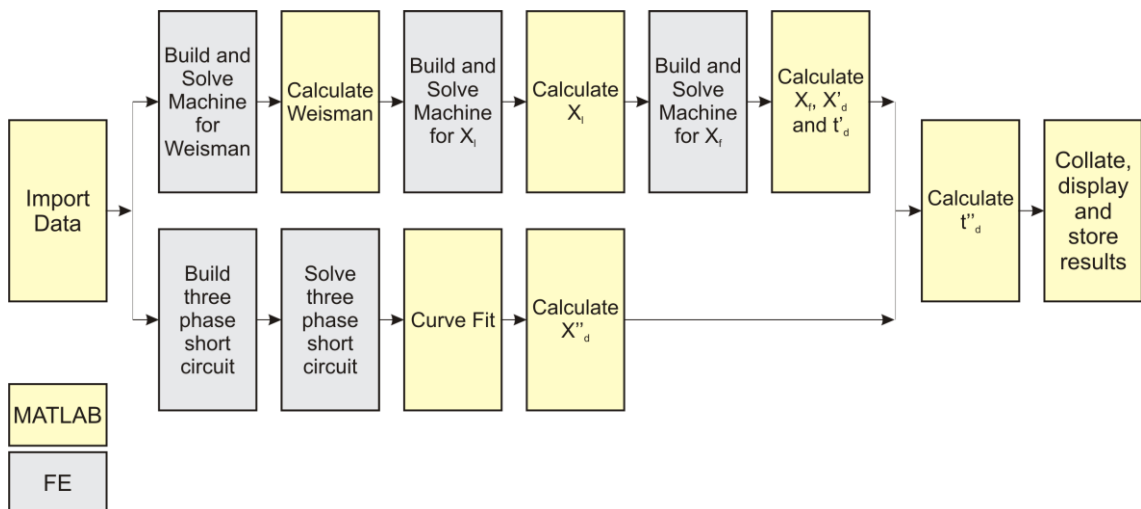


Figure 76 - Flow Chart Showing the sequence of calculation of transient parameters

4.4. Results

Of the forty eight machines used for testing in section 3.4 only nine of the customers opted to have a three phase short circuit characterisation test. This is because customers do not wish to increase capital expenditure when purchasing a machine and are content with the values of the reactances stated in the product design. Occasionally customers may conduct their own characterisation, but this is extremely rare. The customers who

opted for a test to be conducted normally did so as the machine may be in a reactance critical system or simply for insurance underwriting reasons. The nine machines have been simulated and again compared to test results and the analytical software currently used by the Engineering Design Department of the company, named EDS. Figure 77 shows the mean absolute percentage errors for the 4 main parameters and Figure 78, Figure 79, Figure 80 and Figure 81 show the individual errors for each parameter in each of the 9 machines.

The first obvious conclusion is the high level of inaccuracy: both the EDS and the FE package regularly have average errors greater than 10% and individual errors over 30% and even up to 100%. These higher errors seem concerning, but as the machine reactances are quoted with a high margin for error (typically 20-30%) this is acceptable. The FE package predicts the transient parameters more accurately than EDS in all but 1 of the cases, typically being over 10 percentage points more accurate. Errors are also all negative, with the exception of one machine, which shows a constant underestimation of the reactances. The underestimation could be in any of the individual parts used in the calculation, but due to the size it is likely that it comes from all of the parts - for example looking at the relative sizes of components X_l is typically 0.1pu and would therefore need to have about a 50% error in order to be the sole cause of a 20% error in X'_d . With X_{ad} being around 2 pu and X_f 0.2 pu an error in each of these of a smaller magnitude would cause some deviation from the test results, again accounting for some of the inaccuracies. The simulation has been conducted in a 2 dimensional sense with additional factors for the end windings and axial length as used in section 3.3 and therefore there is a likelihood that additional end winding effects that haven't been integrated are causing some additional reactance. Without running time consuming three dimensional simulations (which are not possible for a design tool) it is unlikely that a static 2D FE simulation will be able to improve without significant, case specific, analytical compensation factors. Again these case specific factors are of little use in a system which is designed to be used with multiple topologies.

The subtransient parameters have a bipolar outlook - having both the best and worst average accuracies. The subtransient reactance calculated from a three phase short circuit is very accurate with the exception of the first machine, with all the results less than 5% in error and a few machines having errors of virtually zero. The first machine

has a higher error and is the only positive result in both the EDS and FE results. This machine is a highly fluxed machine with an abnormally high tooth and core back saturation level which is being operated at an above normal loading level, hence it was for this reason the machine had a three phase short circuit test conducted. It is therefore unsurprising that the machine is significantly different. The curve fitting method used can add error to the results - for example

Figure 75 shows 2 different curve fitting routines carried out on the same test data. The method in green is arguably incorrect compared to the blue FE method which was described above, however the green method has been used to analyse the test results by the design office and consequently there is the possibility of a similar data analysis error. The error in the example shown is 3.1%, 2.6% and 0.5% in each of the respective phases and so the error is significant.

The errors in the sub-transient time constants are the worst of the set. They range from +40% to -95% and even on average are almost 50% in error. The reasons for this are twofold. Firstly the method that calculates T''_d calculates it last after all the other parameters are calculated and in the calculation it uses all the other parameters. Consequently all the errors and discrepancies in all the other parameters cascade down the chain to be shown in the final answer giving a high compound error. This is a limitation of the method: the final parameter will always have a collection of errors unless each parameter is somehow calculated in isolation. Secondly the actual values of the time constants are tiny, the values of T''_d range from 0.04 to 0.06 seconds and are extremely consistent. This means that the designers rarely look at the predicted values as they know an estimate of 0.05 will always be within 20%, with an actual error of 0.01 seconds, which is minuscule compared to the main DC time constant, which is will be in the region of 2 seconds.

The whole method takes typically 25 minutes to calculate the values. The static transient simulations take a few minutes and the Wieseman simulations take only a few seconds. However the bulk of the time is taken up by the 3 phase short circuit simulation, which is run in parallel with all the others to increase the speed of the system. This 25 minute simulation is relatively slow and consumes a sizeable proportion of the allotted 60 minutes available. It does, however, yield results that are more accurate on average than the current EDS system.

	EDS Vs Test	Package Vs Test
X'_d	27.30%	16.06%
X''_d	8.10%	2.83%
t'_d	26.49%	17.49%
t''_d	29.65%	48.69%

Figure 77 - Table showing Mean Absolute Percentage Errors (MAPE)[45] for the transient parameters

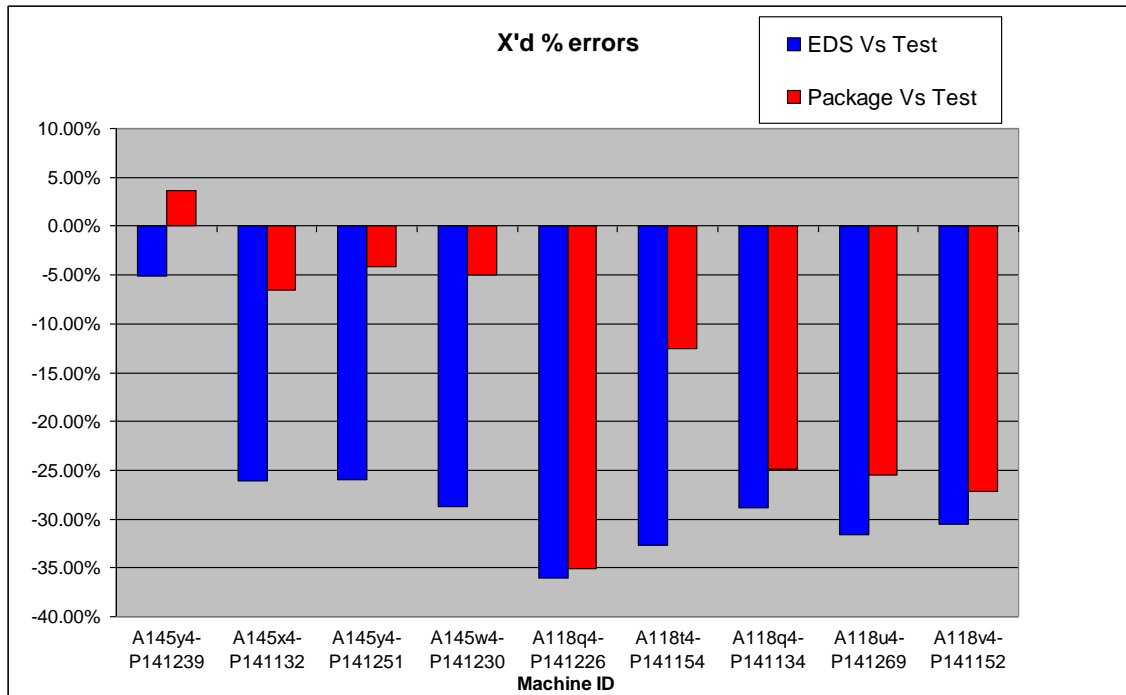


Figure 78 - Graph of X'_d errors for 9 machines

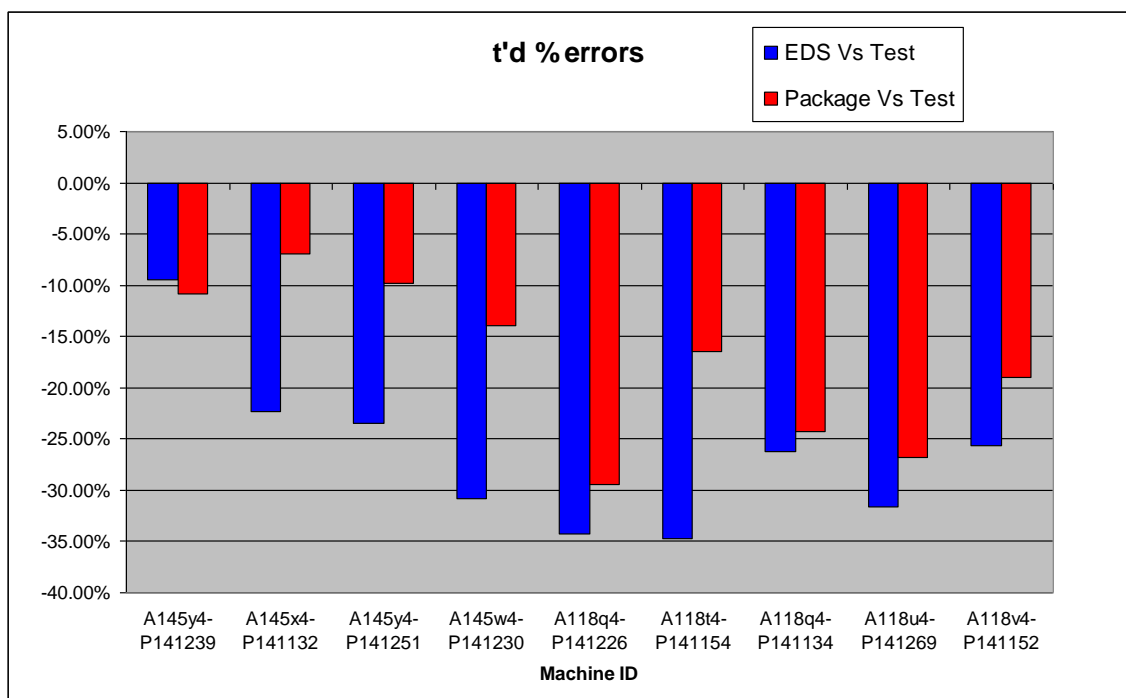


Figure 79 - Graph of t_d' errors for 9 machines

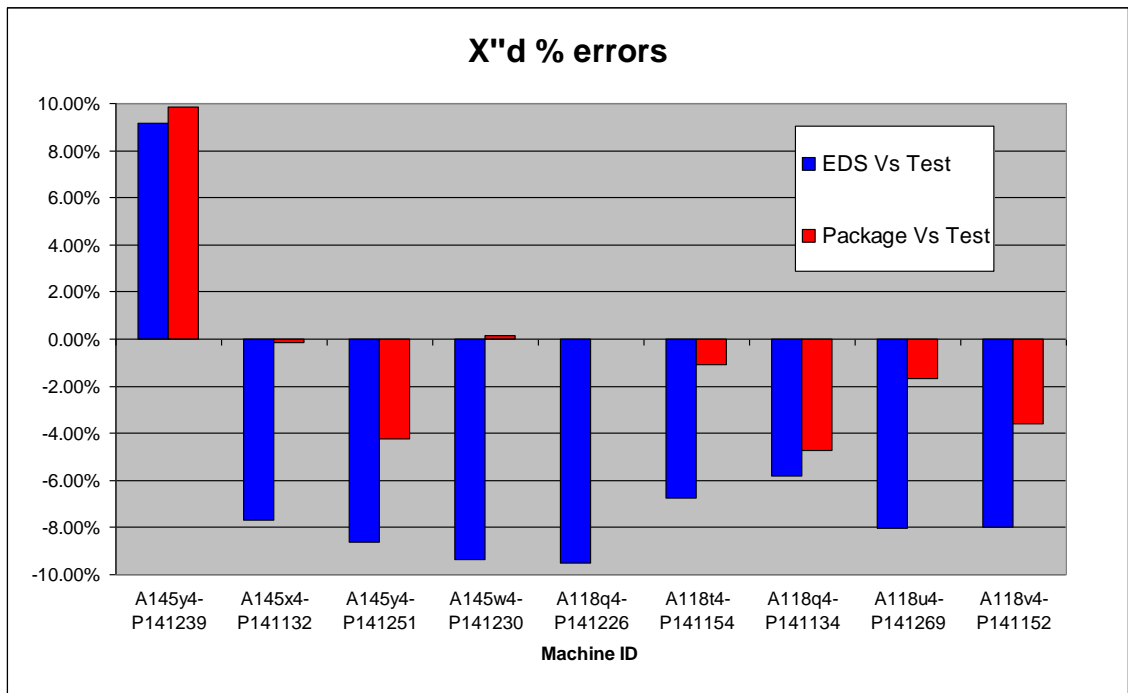


Figure 80 - Graph of X_d' errors for 9 machines

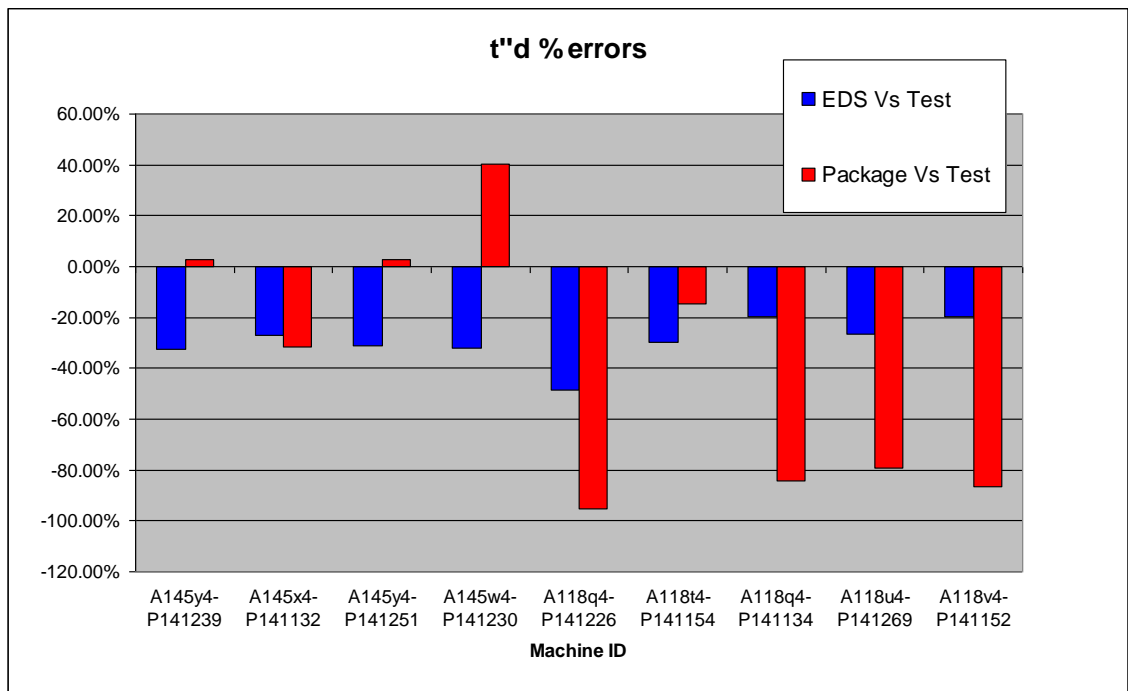


Figure 81 - Graph of t_d'' errors for 9 machines

4.5. Chapter Summary

This chapter looks at the calculation of the transient parameters for a synchronous generator. Initially standstill frequency response methods are investigated for a single generator. The results have two major limitations. Firstly the method is not particularly fast, taking around 40-50 minutes to complete the required simulations. Secondly the parameters found are only representative and, although close in value, are not identical to the desired parameters. Hence the method is simply incapable of meeting all expectations.

Next a method using the equivalent circuit for a synchronous generator is evaluated. By understanding what each individual reactance represents, X_l and X_f are calculated from individual static FE simulations with individually placed flux blocking boundaries. A turns ratio and the field resistance are likewise calculated using geometry and a Wieseman constant found again using static FE. From these values the transient parameters can be found. Due to the complicated compound cage nature of the damper cage a direct FE boundary condition method cannot be used for finding subtransient parameters. Instead they are found from the initial retardation of a three phase short circuit. An automated peak search and curve fitting routine finds the reactance from the y axis intercept. Finally the subtransient time constant is found by substituting all the known components into the characteristic equation for the three phase short circuit and evaluating it.

When compared to test results the FE simulation gives greater accuracy than the company's existing design system by a significant margin. The transient reactance and time constant are both about 10 percentage points better than EDS at around the 16% mean absolute error mark. The subtransient reactance is 3 times better than EDS at only 2.83%, but the time constant has an error of 48%. It is postulated this is because t_d'' is calculated last so the errors may be carried forward. It is also important to observe that actual values are very small (0.04 to 0.06s) and very consistent so without doing any calculations the engineer can give a guess at 0.05s with only 20% error instantly.

Chapter 5. Full Load Operating Point Prediction

5.1. Introduction

One of the critical parameters customers often requested during the tendering process is the field current required when the machine is operating at the full load operating point. This will occur at rated terminal voltage and terminal current, whilst running at the specified power factor. This point is critical as it determines the current and therefore rotor loss and the power that the excitation system must provide to the field. This in turn goes a long way towards specifying the rotating rectifier diodes, automatic voltage regulation system (AVR), exciter and the primary excitation permanent magnet machine in systems which have an integrated excitation system. In externally excited machines the maximum field current level is the primary parameter needed in determining the slip ring size. Figure 82 shows an example phasor diagram for a machine running at full load. The machine is shown overexcited, which relates to a higher field current level i.e. a worst case scenario.

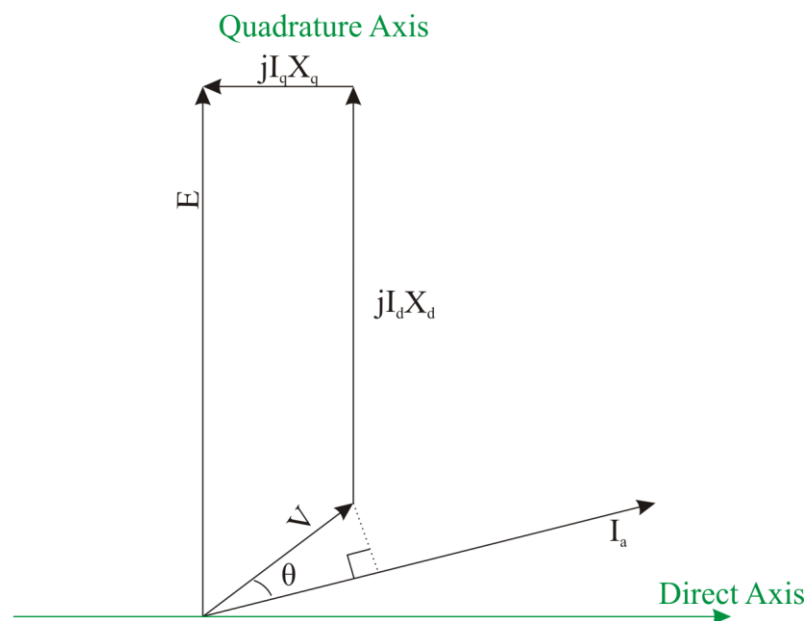


Figure 82- Synchronous Machine Phasor Diagram (not to scale)

5.2. Potier's Method

A well known method used for predicting the full load field current is the Potier method. This is commonly used when undertaking factory tests, when it is impractical or impossible to run a machine at full load within the factory. This often occurs when large machines are constructed, as it is uneconomic to maintain a prime mover capable of providing 1pu power on site, simply for testing. This mathematical method uses the open circuit and zero power factor saturation curves to estimate full load field current: hence the machine does not need to be operated at its actual full load condition. Consequently this method can be calculated in seconds from the data obtained in Chapter 3. The company's design software, EDS, also uses the Potier method to predict full load field current. The factory test prediction of full load field current is obtained using the Potier method, laid out in the relevant test standard [31].

5.2.1. Potier Reactance

The Potier reactance is a reactance which takes into account the leakage of the field winding, on load and in the over-excited region, which is used in place of the armature leakage reactance to calculate the excitation on load by means of the Potier method [32]. By using the saturation curves, the method aims to take into account the saturation and hence achieve an accurate prediction.

The first step in calculating the Potier Reactance is to obtain accurate open circuit and zero power factor saturation curves, as covered in Chapter 3. Next the Potier triangle is constructed, as in Figure 83. The triangle $b d e$ is the Potier triangle. Triangle $a f g$ represents the machine running in an unsaturated mode. Under an ideal linear case the zero power factor curve is the open circuit saturation curve, shifted bodily by the distance $o a$ and hence $c b$ (which equals $o a$) would touch both zero power factor and open circuit curves. However, as the greater total field excitation increases, the field leakage and hence pole saturation increases, making zero power factor and open circuit curves dissimilar. This results in the gap between point c and the open circuit curve. Likewise the differing curves make $d e$ slightly larger than $f g$. The Potier reactance X_p is the length $d e$ when measured in per unit terms [29][31].

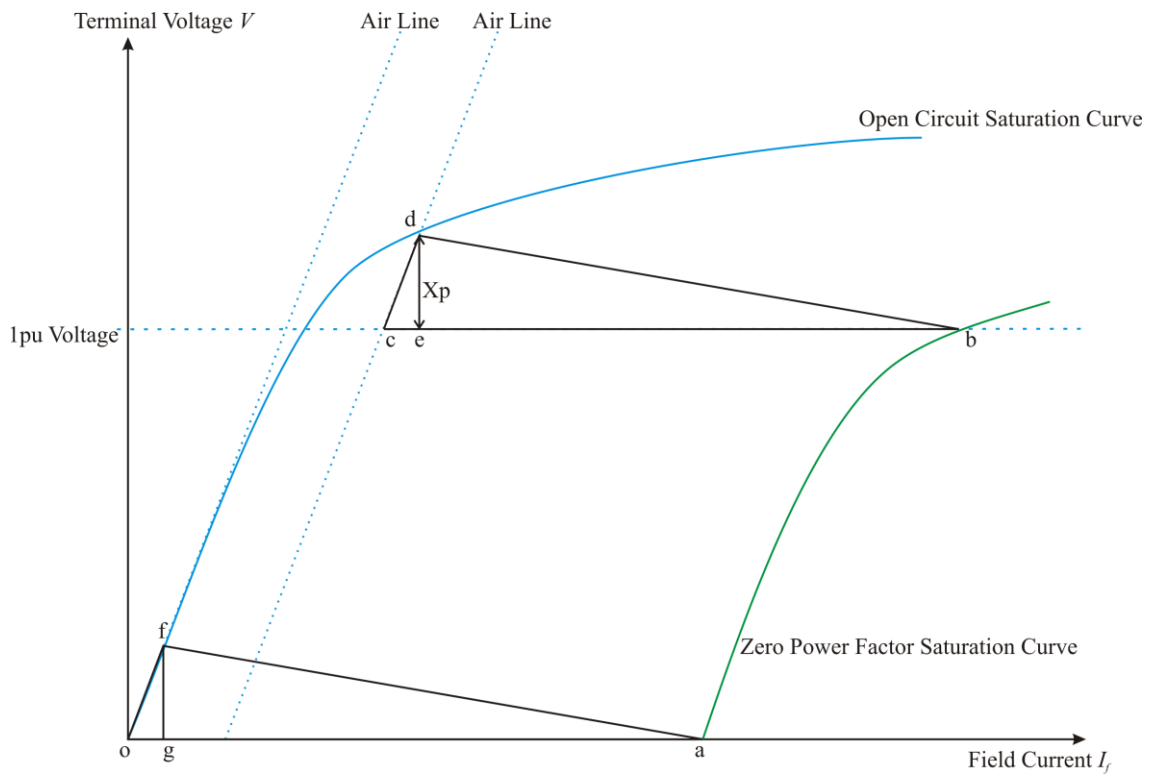


Figure 83 - Saturation curves showing the Potier Triangle

For example, using the same 17.5MVA generator used in earlier chapters, rated volts lies at 6600V and point *b* has a field current of 405A. Line *o a* is 220A long, meaning that point *c* lies at (185,6600). Transposing the airline puts point *d* at (205,7800) and hence point *e* must lie at (205,6600). Therefore equation (5.1) shows the final calculation of X_p .

$$X_p = \frac{\text{Point } d_y - \text{Point } e_y}{V_{base}} = \frac{7800 - 6600}{6600} = 0.1818 pu \dots (5.1)$$

5.2.2. Full Load Calculation

Once the Potier reactance has been calculated a sum of separate parts of the excitation is undertaken to calculate the full load operation point. Firstly the Potier reactance is used to find how much extra field current is required to counteract the field leakage. Take the phasor diagram in Figure 84. V_{sat} shows the voltage which would be expected at the terminal should there be no Potier reactance, hence finding the field current responsible

for V_{sat} will allow the direct estimation of the excitation by subtracting the saturated field current from the airline field current.

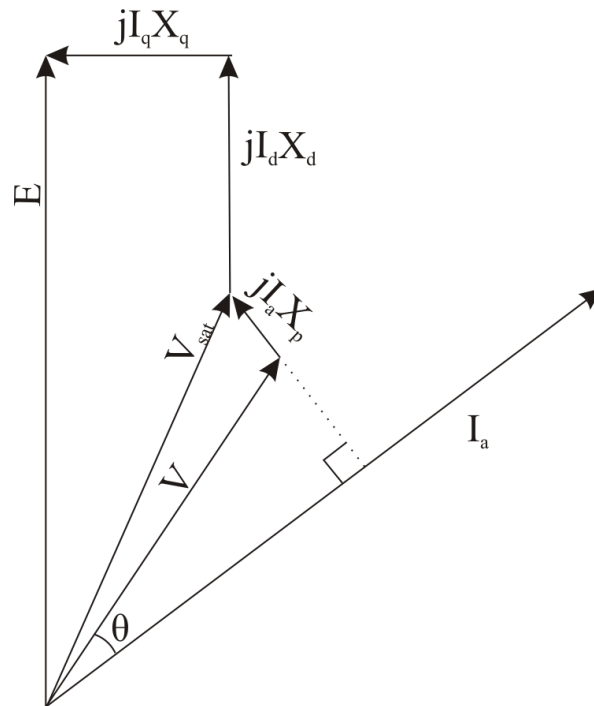


Figure 84 - Saturated voltage vector found from the Potier Reactance

In the 17.5MVA example

$$V_{sat} = V \cos(\varphi) + jV \sin(\varphi) + jI_a X_p \dots (5.2)$$

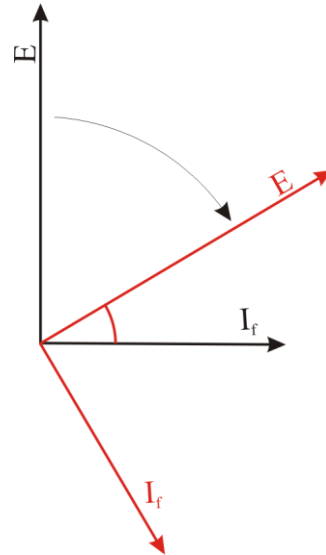
Since $V = 1\text{pu}$ & $I_a = 1\text{pu}$ and the Full Load Power Factor = 0.8

$$\begin{aligned} V_{sat} &= \cos(\cos^{-1}(PF)) + j \sin(\cos^{-1}(PF)) + jX_p \\ V_{sat} &= \cos(\cos^{-1}(0.8)) + j \sin(\cos^{-1}(0.8)) + j0.1818 \dots (5.3) \\ V_{sat} &= 1.11857 \angle 44.3 \end{aligned}$$

Tracing on the Open Circuit Curve and Open Circuit Curve airline curve at $|V_{sat}|$ the following current values are found and hence the current caused by saturation alone is found.

$$\begin{aligned} I_f \text{ for } V_{sat} &= 153\text{A} \\ I_f \text{ for } V_{sat} \text{ on the airline} &= 97\text{A} \\ \therefore I_{f_FL_Saturated} &= 153 - 97 = 56\text{A} \end{aligned}$$

The second part of the calculation involves finding the field current for an unsaturated machine, running at full load, via a superposition method. Firstly the unsaturated machine is operated at rated volts open circuit and the field current found on the air line. This E is then transposed to the power factor angle and the field current found is consequently moved and recalculated, as shown in Figure 85.



$$I_{f_new} = [\cos(\theta) + j \sin(\theta)] I_{f_old}$$

Figure 85 - Transposing of E to the Power Factor angle

To represent the 1 pu stator current at full load the field current under sustained short circuit at 1 pu is found from the short circuit saturation curve graph. This point is also the same field current level as point a in Figure 83, hence the short circuit curve is not necessary. From Figure 16 it is seen that I_f in this condition runs along the imaginary axis and hence j must be appended to accurately determine the unsaturated field current. Using the 17.5MVA example the unsaturated full load current can then be estimated as the vector sum of the unsaturated components:

$$I_{f_old} = 87A$$

$$I_{f_new} = [\cos(\cos^{-1}(0.8)) + j \sin(\cos^{-1}(0.8))] \times 87 = 69.6 + j52.2A$$

$$I_f @ 1pu \text{ Short Circuit} = 220A$$

Therefore Vector sum:

$$I_{f_FL_Unsat} = 69.6 + j52.2 + 220 = 280.9 \angle 75.7$$

Finally the sum of the saturated and unsaturated magnitudes gives the full load field current estimation according to Potier's method:

$$I_{f_FL} = I_{f_FL_Unsaturated} + I_{f_FL_Saturated} \dots (5.4)$$

For the example 17.5MVA generator $I_{f_FL} = 208.9 + 56 = 336.9A$

5.3. Direct Full Load Calculation Using Finite Element

Brandl, Reichart and Voght[33] demonstrate a method to calculate the on load performance of finite element machine by directly calculating loadings within the finite elements. This method being by very nature a direct method finds the full load operating case within a single Newton Raphson iteration and hence is very quick. However this method requires access to the FE source code to allow modification of the solver. This is clearly not possible using a commercial FE package and hence as long as the company continues to use Cobham Vector Fields Opera 2D as their standard package the Brandl, Reichart and Voght method cannot be implemented.

5.4. Finite Element Static Analysis Using Multivariable Curve Fitting

At an instant in time any electrical machine can be simulated as a static finite element simulation provided the current magnitudes are known. However, in a generator, it is often necessary to determine the excitation level and load angle for a given operating point. Figure 82 illustrates, the per-phase phasor diagram for a synchronous generator running on full load. The task is to determine the excitation current and load angle when the terminal voltage, load current and power-factor are known. This must be achieved using an iterative process, as the solution process requires the inputs to be excitation current, d-axis current and q-axis current.

The actual current level whilst running on full load is known to be 1pu and hence can be calculated from voltage and power terminal ratings, as shown in equation (5.5).

$$I = \frac{S}{V_{line}\sqrt{3}} \dots (5.5)$$

From the terminal ratings and the machine's rated speed the air gap torque on full load can also be found. This is then calculated per metre as the 2D FE package calculates a per metre value [equation (5.6)].

$$T = \frac{S \cos(\varphi)}{\omega \cdot L_{a_eff}} \dots (5.6)$$

Using the system laid out in section 3.2.2 the terminal voltage can also be monitored, allowing a series of simulations to be undertaken in which the Field excitation current and the angle between the rotor and stator d axis currents are varied. The angle between the 2 axes, named λ , is analogous to the load angle and hence the loading of the machine can be varied. This allows a spectrum of load cases to be simulated by varying the two variables and monitoring the voltage and torque. From this spectrum the Full Load operating condition, where the desired terminal voltage and torque occur, can be found.

Equation (5.7) specifies the two 2 variable functions which must be simultaneously solved to identify the desired full Load operating current, I_{f_FL}

$$\begin{aligned} V &= f(I_f, \lambda) \\ T &= f(I_f, \lambda) \dots (5.7) \end{aligned}$$

5.4.1. Surface fitting and Solution Identification

Solving the equations over a range of values creates a 3D plot of data which must be curve fitted to allow the estimation of the full load operating point. The solution will invariably lie between points and, as the solution is simultaneous, a continuous function is required for a computer to quickly create a solution using an error minimization routine. For example, take the range of data in Figure 86. The machine required a full load voltage of 6600V and a torque per unit length of 1.49×10^4 Nm/m, yet the closest simulation point (which is highlighted) at $I_f = 342.7$ and $\lambda = -50$ leaves the voltage and torque both too high at 6895V and 1.518×10^4 Nm/m. This is solved by wrapping a 2 dimensional third order polynomial regression model over each set of data such that the continuous solutions take on the form in equation (5. 8)

$$\begin{aligned}
 V &= A_1 I_f^3 + A_2 I_f^2 + A_3 I_f + A_4 \lambda^3 + A_5 \lambda^2 + A_6 \lambda + A_7 I_f^2 \lambda + A_8 I_f \lambda^2 + A_9 I_f \lambda + A_{10} \\
 T &= B_1 I_f^3 + B_2 I_f^2 + B_3 I_f + B_4 \lambda^3 + B_5 \lambda^2 + B_6 \lambda + B_7 I_f^2 \lambda + B_8 I_f \lambda^2 + B_9 I_f \lambda + B_{10} \\
 &\dots (5.8)
 \end{aligned}$$

where $A_1 \dots A_{10}$ and $B_1 \dots B_{10}$ are constants

This polynomial can be evaluated and plotted over a continuous range as is shown in Figure 87. The coefficient of determination R^2 in these two charts is 0.989 and 0.993, showing a high degree of correlation (1 being perfect correlation). The method for calculation of R^2 is shown in Appendix F. To identify the individual solution a multidimensional unconstrained non-linear minimization routine has been implemented which uses the Nelder-Mead method [34]. This finds the point at which the absolute error between the desired outputs and the calculated polynomial values is zero by modifying the 2 input variables. In this example case the solution returned is $I_f = 333.4\text{A}$ and $\lambda = -73.65$ degrees. This whole 'fit and find' routine takes less than a second to return the answer and therefore, compared to the finite element solution, becomes a negligible time drain.

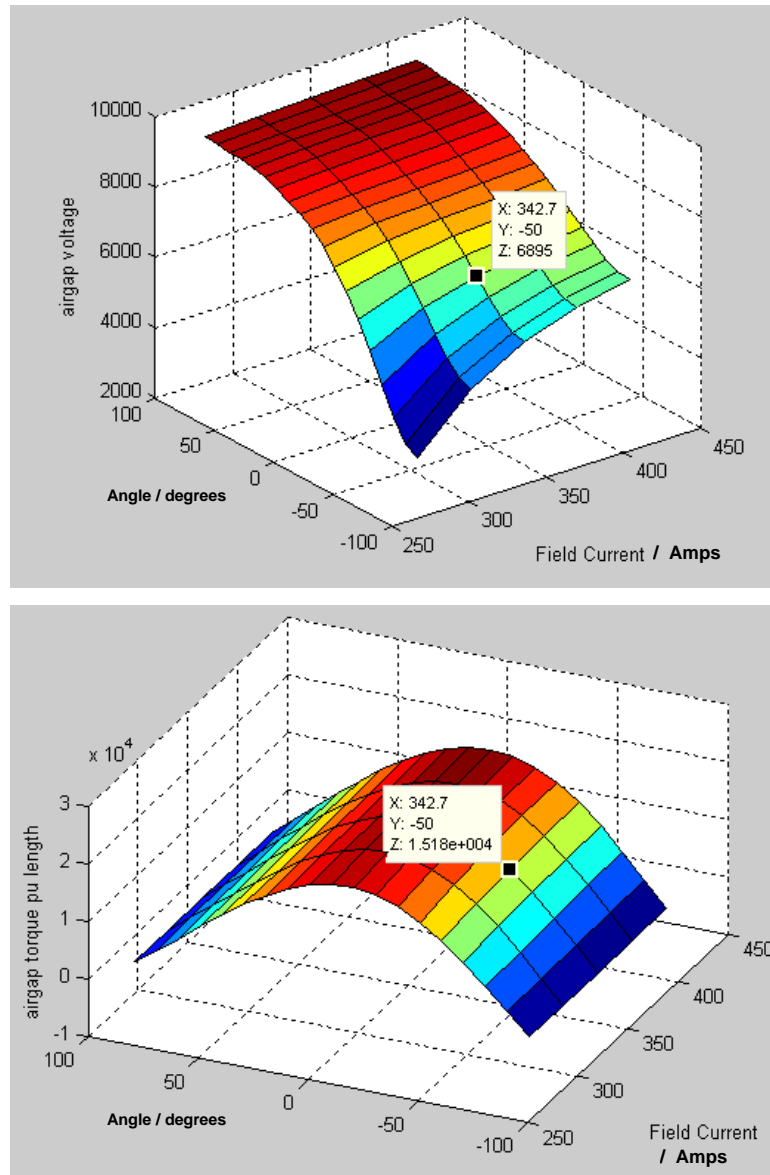


Figure 86 - Torque and Voltage Simultaneous plots with the closest simulation highlighted. Figure contains raw simulation data hence the highlighted point is not the exact load case required showing the need for interpolation via curve fitting.

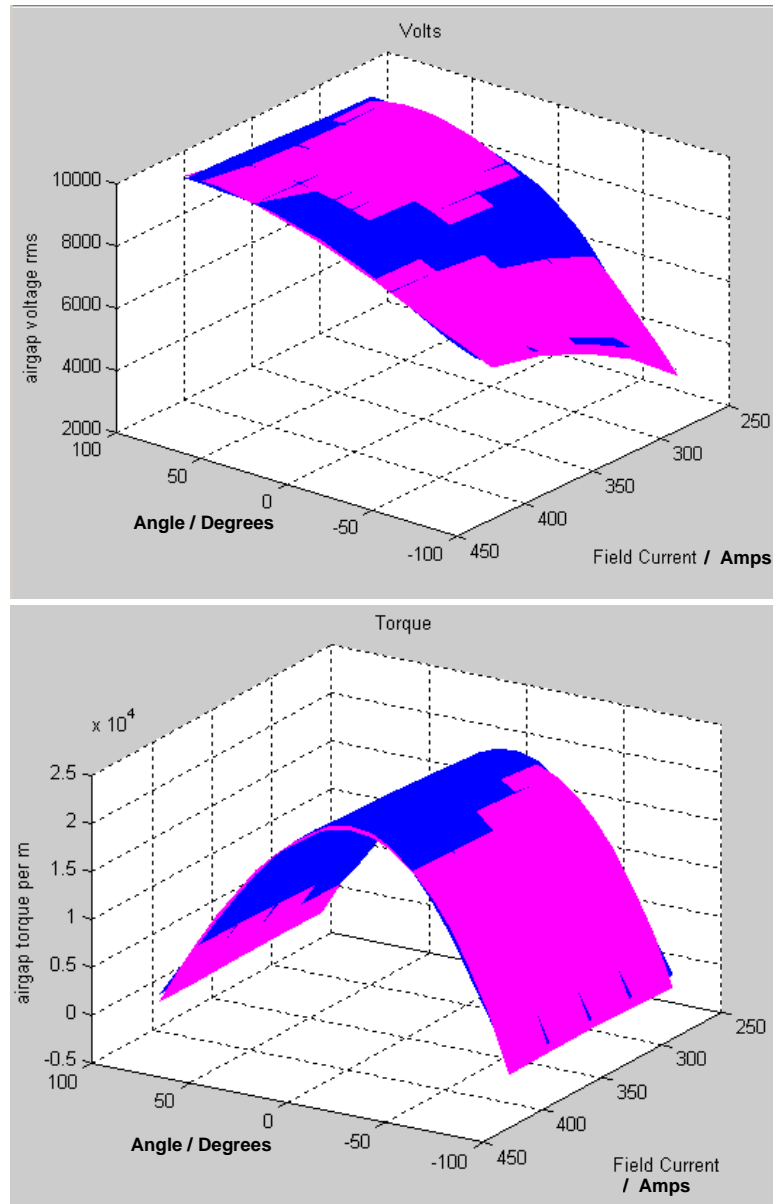


Figure 87 - Polynomial curve fits - Key: Magenta = Curve Fit, Blue = Raw Input data from FE

5.4.2. End Winding Inductance

In the actual machine the inductance of the end windings will have an effect upon the full load excitation point. The 2D FE model does not account for this vector, consequently the easiest way incorporate the vector into to the routine is to curve fit for a different voltage - one which is free of the end winding inductance. Figure 88 shows the phasor diagram for a machine on load, with the end winding reactance vector added, creating a new voltage V' , which is the desired voltage the FE must solve for.

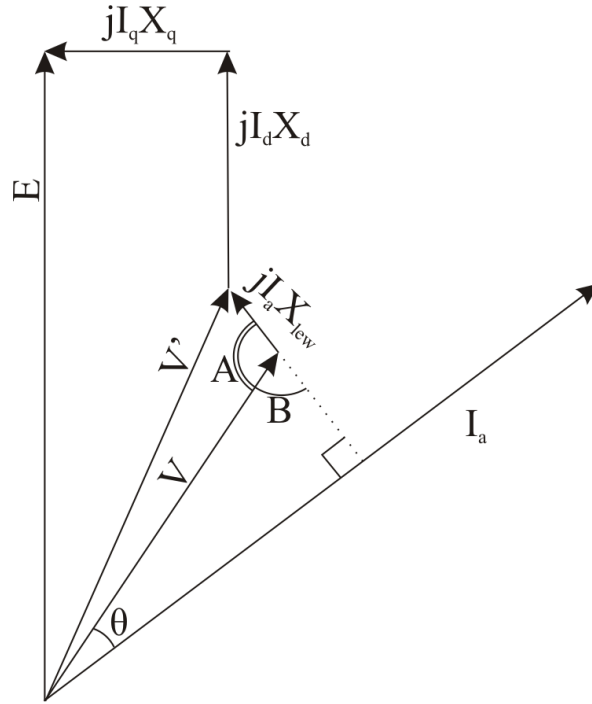


Figure 88 - Phasor Diagram showing the additional End winding Reactance. (not to scale)

Given that the angle $B = 180 - 90 - \varphi = 90 - \varphi$ and therefore angle $A = 180 - (90 - \varphi) = 90 + \varphi$, the magnitude of V' can be vectorially found using the cosine rule:

$$V' = \sqrt{V^2 + (I_a X_{lew})^2 - 2VI_a X_{lew} \cos(90 + \varphi)} \dots (5.9)$$

X_{lew} has previously been calculated in Chapter 3. As both V and I_a are 1pu and X_{lew} is expressed per unit, to reduce processor overheads, this equation can be simplified using the per unit system:

$$V' = V_{base} \sqrt{1 + X_{lew}^2 + 2X_{lew} \sin(\varphi)} \dots (5.10)$$

5.4.3. Cluster Analysis vs. Matrix analysis

Figure 86 shows the implementation of the FE solving routine using a single pass matrix solution. This means that the solver calculates a range over which it varies I_f and λ , based upon the machine's terminal data. This open loop system creates a matrix of data which is curve fitted. The system is fairly slow as every solution within the matrix is evaluated before any curve fitting is carried out. In the example I_f has 5 values

and λ has 20, so there are 100 simulations and with each one taking approximately 10 seconds it takes over 16 minutes to find a solution. This is not particularly efficient and, even after this delay, if the required solution lies in the middle of an element on the surface the solution is likely to have a significant error. Consequently a system has been created which searches for an optimal full load positioning. The system works by creating a 3x3 matrix, or cluster, centred upon an initial estimation of the full load position. The cluster is vastly oversized and if this alone were to be used the estimation would be very poor. Once the first cluster is calculated, as with a large matrix, it is surface fitted and the solution found. If the found solution lies within the initial estimate the process is repeated using a smaller cluster, centred on the new estimation. This iteration occurs 3 times, creating concentric clusters which accurately map the surface, as shown in Figure 89. On occasions where the initial estimate was poor the second iteration can form an off centre cluster, as in Figure 90, which again concentrates down to the actual solution. Figure 91 shows a worst case scenario where the initial estimate was incorrect, resulting in the cluster not forming around the desired solution. Due to the continuous nature of the surface fit an estimate is formed but, as it is outside any FE data, the routine automatically restarts, centred on the new solution, but with a large cluster. It should be noted that Figure 91 had to be created artificially by the introduction of an absolute error, as this case was not observed in any of the machines tested.

This use of clusters reduces the number of simulations to 27 and achieves a high degree of accuracy as the final solution in each case is very close to the middle of the final cluster, meaning an FE solution is almost at the full load case. This reduction to 27 solutions also reduces the time taken to a quarter - around 5 minutes from start to solution.

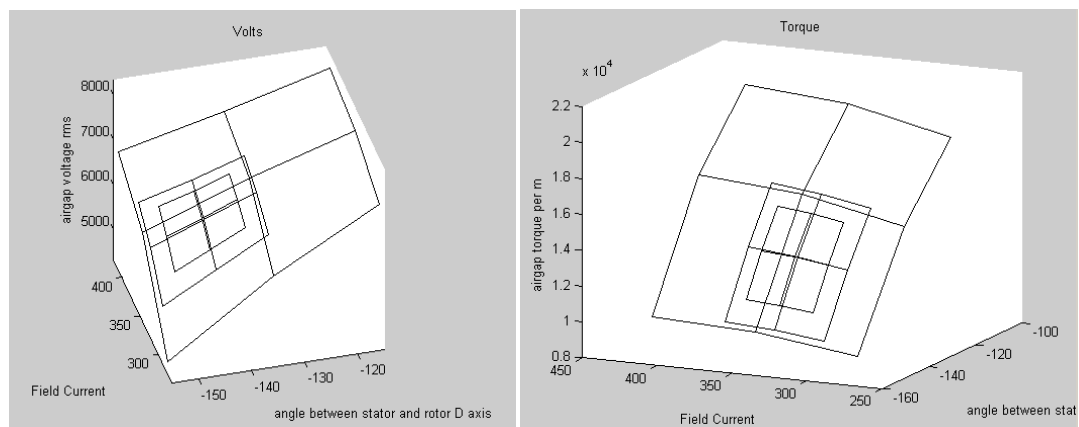


Figure 89- 3D Mesh surface plots showing a good initial guess with reducing concentric clusters

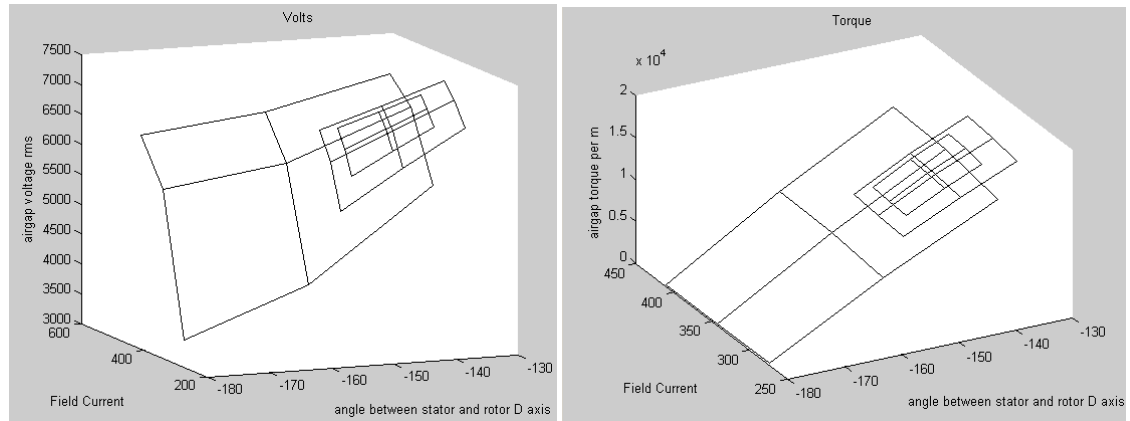


Figure 90- 3D Mesh surface plots showing an average initial guess with reducing concentric off centre clusters

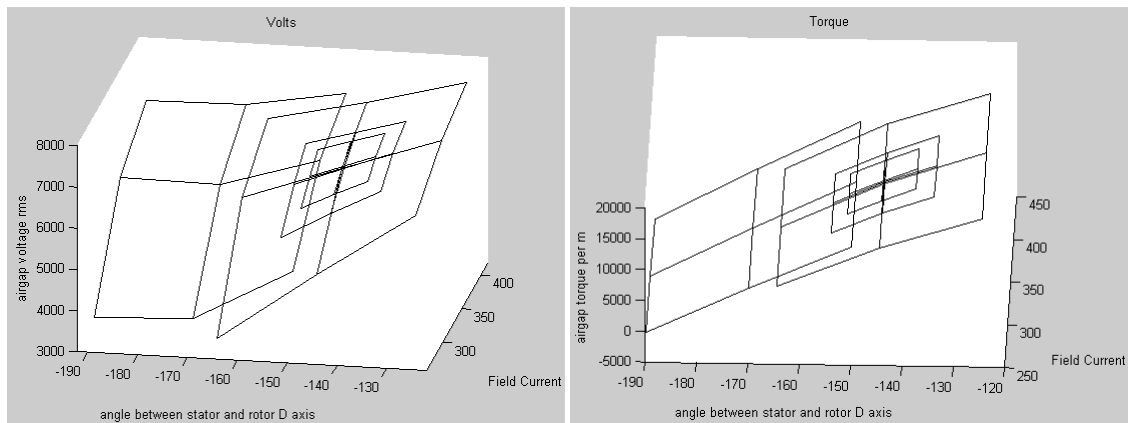


Figure 91- 3D Mesh surface plots showing a poor initial guess resulting in a second large cluster before reducing concentric clusters

5.4.4. Program Flow

Figure 92 shows the sequence in which the program flows. The majority of the processes are calculated within MATLAB, but the majority of the calculation time is taken by the FE solver, with the whole solution taking about 5 minutes, of which 95% of this is FE time. It should be noted that a substantial proportion of the time is taken by the FE solver checking the networked license file server for a valid software license. This handshake check takes about 1-2 seconds per solver call, so that around 45 seconds of the 5 minutes is a fixed delay, which could only be removed by employing a license free solver. This program flow is serial, with each of the 3x3 simulations performed one after the other. It could be coded to be solved in parallel using 'n' solvers. However this whole section is run in parallel with the transient solution in Chapter 4 and Waveform Distortion calculation which will be detailed in Chapter 6. Therefore the advantage of a serial layout has the benefit of not over committing the PC's processors. This section must be run after the initial design characterisation in Chapter 3, as not only does the

initial design section use all the processor capability, but the saturation curves are used for the initial estimate of the full load operating point.

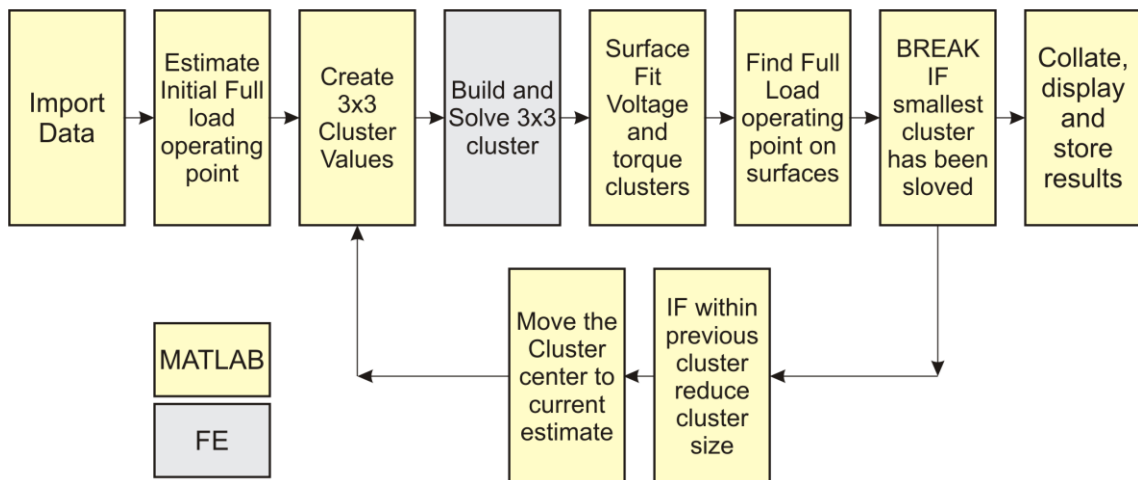


Figure 92 - Flow Chart detailing the sequence implemented when calculating the full load operating point using clusters

5.5. Results

Twenty 4 pole synchronous generators have been simulated using FE analysis and Potier methods. The simulations results have then been compared to the results calculated from the factory test results (Figure 93). The full load factory test value, as previously mentioned, is calculated using the saturation curve set as found using IEEE test Std 115 [31] and the Potier method. Figure 94 shows a numerical summary of the results, whilst Figure 95 has a graphical representation of the data spread. From Figure 95 it is immediately evident that the finite element methods are more accurate, with the clusters method having half the data distribution of EDS. Just examining the methods that use Potier's reactance, it can be hypothesised that the method with the most accurate saturation curve will create the most accurate full load predictions, since Potier's source of data is the saturations curves. Hence any errors into the methods input data will create a systematic error which cannot be eliminated. The mean absolute percentage error for EDS stands at 6.68%, where as FE using Potier is only 2.55%, a reduction in error of over 4 percentage points. Importantly the standard deviation of the data has reduced in error by 1.5% to 3.1%. This reduction in standard deviation is almost more important than a low average error as the worst case solution is much smaller. The mean error of the FE Potier results is also only 1%. This shows an accurate prediction system. The Clusters method further improves upon both EDS and FE Potier methods. The mean absolute percentage error is only 2.49% and the standard deviation has again

dropped to 2.4%, showing an even higher consistency in prediction. The mean error is slightly higher than the FE Potier prediction at 1.6%, but the reduction in the maximum negative and maximum positive errors, shown in Figure 95, clearly indicate a more accurate prediction system. From these results it is clear that the clusters method is the most accurate system, but it is also the slowest. The Potier systems have their results calculated in seconds, whereas clusters takes around 5 minutes. This delay is perfectly acceptable for the improvement compared to EDS, however the delay compared to the FE Potier method does not warrant the added delay - an extra 0.06% accuracy in the mean absolute percentage error is not significant.

Figure 96 and Figure 97 shows the results of averaging the predictions of both FE methods and comparing them to test results. As the clusters method generally slightly under predicts and the FE Potier method generally slightly over predicts this, averaging of the 2 predicted field currents reduces slightly both the mean absolute percentage error and the standard deviation, with the mean absolute percentage error dipping below 2%. Similarly the mean becomes only -0.28%, giving Figure 97 a symmetrical look. This averaged result is the best, but takes the longest to calculate, albeit only by a few seconds longer than the clusters method. It is suggested that in a design package that the average method is not given as the only prediction. Quoting the FE Potier and the clusters method results, as well as their average, will allow the design engineer the opportunity to gain further understanding of the most suitable method for a more extended set of machines. The Graphical User Interface, as programmed and described in Appendix H, automatically runs the FE Potier method and gives the user the option of whether to additionally run the clusters method. This is because, although the user may not be interested in the full load operating point, FE Potier calculation is so rapidly available that the information may as well be supplied if the saturation curves have been calculated.

Project	Field Current for Full Load / Amps				Percentage error Vs Test		
	EDS	FE Analysis		Factory Test Results	EDS	FE Analysis	
		Potier's Method	Clusters			Potier's Method	Clusters
A145y4-P141239	325.34	342.67	345.27	334.11	-2.6%	2.6%	3.3%
A145y4-P141251	316.82	339.65	343.13	357.64	-11.4%	-5.0%	-4.1%
A145x4-P141132	295.19	309.18	308.81	314.57	-6.2%	-1.7%	-1.8%
A145w4-P141230	303.48	331.06	326.84	331.32	-8.4%	-0.1%	-1.4%
A145y4-P141228	336.78	357.00	357.44	371.67	-9.4%	-3.9%	-3.8%
A145y4-P141245	311.65	342.67	345.27	337.51	-7.7%	1.5%	2.3%
A118q4-P141226	252.25	269.44	252.82	254.00	-0.7%	6.1%	-0.5%
A118t4-P141154	241.80	255.16	248.08	256.00	-5.5%	-0.3%	-3.1%
A118q4-P141134	293.92	291.66	272.57	284.90	3.2%	2.4%	-4.3%
A118u4-P141269	317.30	328.83	310.43	324.11	-2.1%	1.5%	-4.2%
A118v4-P141152	308.97	315.37	294.30	301.07	2.6%	4.7%	-2.3%
A118s4-P141185	315.91	326.35	319.96	324.27	-2.6%	0.6%	-1.3%
A118u4-P141241	250.45	261.04	248.52	258.26	-3.0%	1.1%	-3.8%
A160a4-P141271	238.47	262.11	254.45	265.71	-10.3%	-1.4%	-4.2%
A160a4-P141273	254.68	279.46	276.95	274.53	-7.2%	1.8%	0.9%
A160a4-P141275	217.96	261.28	243.48	249.14	-12.5%	4.9%	-2.3%
A160b4-P141255	235.67	276.84	264.12	260.39	-9.5%	6.3%	1.4%
A160c4-P141259	255.62	278.66	275.29	277.18	-7.8%	0.5%	-0.7%
A160e4-P141284	254.33	284.21	281.17	278.58	-8.7%	2.0%	0.9%
A160w4-P141224	267.45	296.79	295.16	304.72	-12.2%	-2.6%	-3.1%

Figure 93 - Table showing Full Load EDS Results and Factory Test results and % errors

	Percentage error in field excitation current compared to factory test results		
	EDS	FE Analysis	
		Potier Method	Clusters
Mean Absolute Percentile Error, MAPE	6.68%	2.55%	2.49%
Mean Error	-6.1%	1.0%	-1.6%
Standard Deviation	4.6%	3.1%	2.4%
Maximum Positive Error	3.2%	6.3%	3.3%
Maximum Negative Error	-12.5%	-5.0%	-4.3%

Figure 94 - Summary Table Comparing Full Load simulation results to factory test results

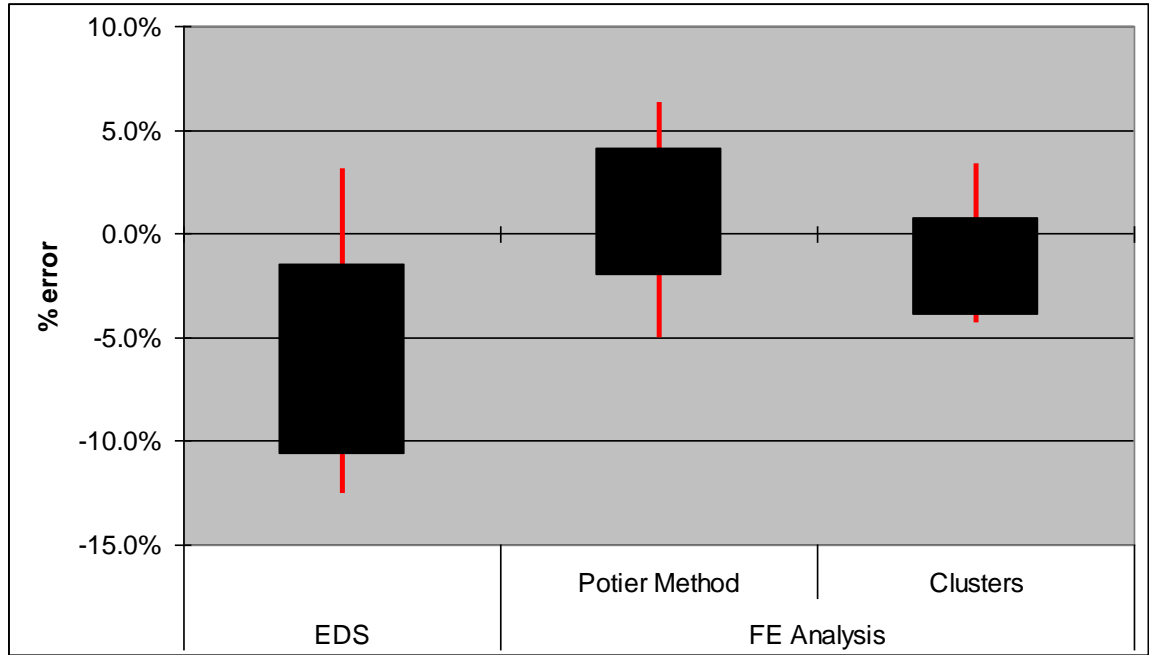


Figure 95 - Full Load simulation Percentage errors. Red tails show extent of results spread and black box is the mean \pm one standard deviation

	Averaging FE Potier and cluster method predictions
Mean Absolute Percentile Error, MAPE	1.97%
Mean Error	-0.28%
Standard Deviation	2.34%
Maximum Positive Error	3.87%
Maximum Negative Error	-4.54%

Figure 96 - Table Comparing Averaging FE Potier and cluster method predictions results to factory test results

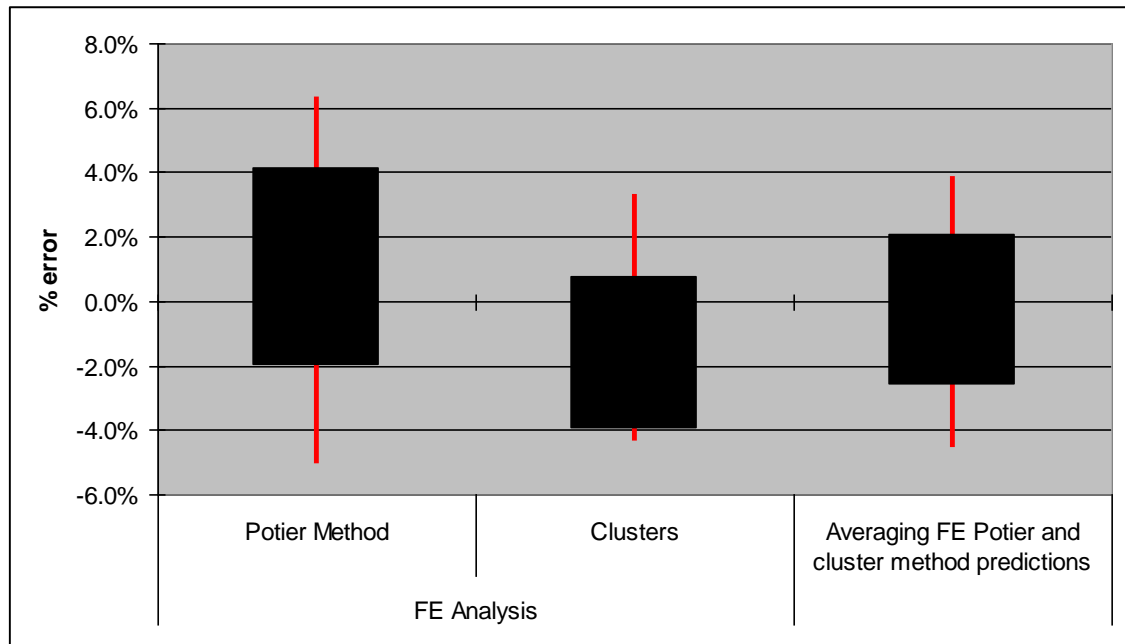


Figure 97 - Full Load simulation Percentage errors and average FE Potier and clusters method prediction. Red tails show extent of results spread and black box is the mean \pm one standard deviation

5.6. Chapter Summary

This chapter details a method used to predict the full load excitation of a synchronous generator. Firstly the Potier reactance method is evaluated, using the saturation curves calculated in Chapter 3. This method is found to have a lower error than E.D.S. as the saturation curves are more accurate. Secondly, a Finite Element method is proposed that uses static simulations. The magnitude of the field current and the position of the stator current are varied, whilst the terminal voltage and air gap torque are monitored. The PRS system, detailed in 3.2.2, is used with a single static simulation for each case. This yields a multidimensional simultaneous problem that is solved using 3 dimensional curve fitting and an unconstrained non-linear minimization routine. A smart clustering routine speeds up the process, avoiding time consuming matrix solutions. Due to the 2D FE simulations end winding inductance must be factored in by curve fitting for a different, larger, terminal voltage. The Clusters method is also shown to be more accurate than E.D.S. and marginally more accurate than the Potier method, with mean absolute percentile errors of 6.68% for E.D.S., 2.55% for Potier and 2.49% for the Cluster method. Finally averaging the Potier and Clusters methods together for the test selection of machines gives a mean absolute percentile error of only 1.97%, but crucially also gives a near perfect distribution across the zero error. The time taken for

the Potier method is insignificant - a matter of seconds, whilst the FE Clusters method takes on average about 5 minutes.

Chapter 6. Prediction of Waveform Harmonics

The harmonic content of the generated line to line open circuit voltage of large rotating synchronous generators must meet the rules set out in section one of IEC 60034 [35]. It states that all generators above 500 kW (kVA) must have a calculated total harmonic distortion (T.H.D.) of less than 5 %. To this end, careful consideration of all aspects of the electrical machine geometry is required by the design engineer, which must be complemented with accurate prediction of the T.H.D. to mitigate the necessity of requiring a design concession from the customer.

The influence of the general geometry of the machine can be predicted in a relatively straightforward manner using magnetostatic finite element methods. However, the presence of damper windings (Figure 99) introduces additional stator voltage harmonics either side of the slotting frequency. These harmonics can be substantial and require a more complex computation. There have been a series of attempts to model this effect, ranging from the purely analytical methods of [36][37][38] through to the hybrid finite element/analytical methods employed in [39][40][41]. Full transient solutions will provide the most accurate model, but have hitherto been avoided because, even in two dimensions, they are very slow and cumbersome. Here a two dimensional, finite element based, transient eddy current solution method, is used, exploiting the geometrical symmetry of the stator laminations to give a rapid solution.

6.1. Analytical method

Analytical methodology is based upon the creation of an extensive Fourier series to describe the geometry of a machine. The harmonic content of the open circuit waveform is affected by several different factors, which are typically analysed in isolation and brought together to form a holistic view.

6.1.1. Flux Density Waves Due to Stator and Rotor Permeance Variations

J H Walker [36] calculates the air gap flux waveform, Φ , by multiplying the total permeance of the air gap, P , by the rotor MMF acting upon the stator, F , As shown in equation (6.1)

$$\Phi = P \cdot F \quad \dots (6.1)$$

Where P and F are Fourier series

$$P = K_1 \sum_{v_1=1,2,3}^{\infty} \frac{1}{v_1} \varepsilon_s \sin[v_1 N_{ss} \theta]$$

$$F = K_2 \sum_{v_2=1,3,5}^{\infty} \frac{1}{v_2} \sin[v_2 N_p (\theta - \omega t)]$$

N_p = Number of pairs of rotor poles

N_{ss} = Number of stator slots

K_1, K_2, K_3 = Constant Coefficients

v_1 = Order of the harmonic in the permeance wave

v_2 = Order of the harmonic in the main rotor MMF

ε_s = ratio of r.m.s. value of permeance variation, due to the v_1 th harmonic of slot permeance, to the mean permeance of the air gap

Hence the flux at the stator bore (when simplified) becomes

$$\Phi_s = K_3 \left\{ K_2 \sum_{v_2=1,3,5}^{\infty} \frac{1}{v_2} \sin[v_2 N_p (\theta - \omega t)] + \sum_{v_1=1,3,5}^{\infty} \sum_{v_2=1,2,3}^{\infty} \frac{1}{v_2} \sin[v_2 N_p (\theta - \omega t)] \frac{1}{v_1} \varepsilon_s \sin[v_1 N_{ss} \theta] \right\}$$

The first term is at fundamental frequency and can be omitted from further analysis, whereas the second term can be resolved into forward and backward rotating waves and hence becomes:

$$\Phi_s = K_3 \sum_{v_1=1,3,5}^{\infty} \sum_{v_2=1,2,3}^{\infty} \frac{1}{v_2} \frac{1}{v_1} \varepsilon_s \left\{ \frac{1}{2} \cos[(v_1 N_{ss} - v_2 N_p) \theta + v_2 N_p \omega t] - \frac{1}{2} \cos[(v_1 N_{ss} + v_2 N_p) \theta - v_2 N_p \omega t] \right\}$$

As these 2 waveforms are at fundamental frequency relative to the stator, they will not induce any harmonics within the stator windings and will not directly cause any slot frequency harmonics within the open circuit voltage waveform. However, relative to the rotor, the harmonics are rotating and are described below. The difference in angular velocity allows current to be induced into any suitably pitched rotor winding, including damper cages and field windings.

$$\Phi_r = \frac{K_3}{2} \sum_{v_1=1,3,5}^{\infty} \sum_{v_2=1,2,3}^{\infty} \frac{1}{v_2} \frac{1}{v_1} \varepsilon_s \left\{ \cos\left[(v_1 N_{ss} - v_2 N_p)\theta + v_1 N_{ss} \omega t\right] - \cos\left[(v_1 N_{ss} + v_2 N_p)\theta - v_1 N_{ss} \omega t\right] \right\}$$

The induced currents within the damper cage hence create a flux waveform perturbation which creates a castellation upon the open circuit waveform. Walker in [36] shows how the pitch and positioning of the damper cage as well as the pole shoe can be used to minimise the open circuit distortion.

6.1.2. Limitations of Analytical Methods

Analytical methods all have one fundamental limitation. The machine is transformed into a rectilinear Fourier series and hence any diverging flux which creates tangential flux in the air gap is ignored. In other words the method assumes that all flux within the air gap is radial. For non salient pole machines this assumption is fairly accurate, but within salient pole machines there is significant flux diversion from the pole tips. The radial permeance can be accurately calculated from the geometry, however the rotor MMF is only ever an estimation, typically relying upon either an ideal square wave, simple sinusoidal fundamental, exponential or inverse square tapering off within the interpolar regions, as pictured in Figure 98. The method also assumes that machine iron is a perfect flux carrier and hence all the MMF drop is across the air gap. This is untrue, particularly if dealing with machines that have partial slot closures. For example, some of the damper bar slot closures become saturated at low excitation levels. Similarly the pole shoe arms become saturated and the flux path altered.

Analytical methods also struggle with complicated air gap shapes: for example Walker states about the effect of the pole shoe and hence air gap:

"the effect of this shaping cannot be predicted without considerable labour" [36]

and simply leaves the matter at that.

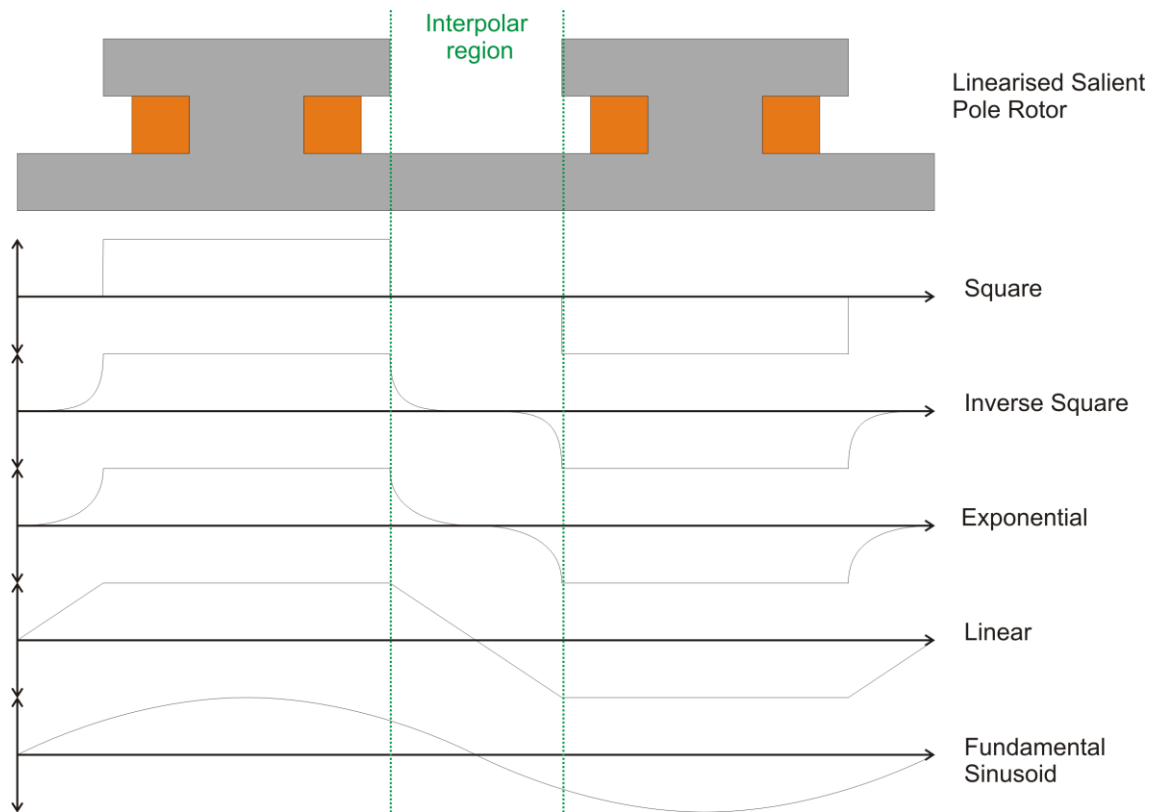


Figure 98 - MMF shapes in the interpolar regions

6.2. Proposed Method of Predicting The Open Circuit Waveform

The advantage of finite element methods for increasing the accuracy of the voltage waveform prediction has been shown in [41]. However the method is reliant on accurate prediction of damper bar currents due to the use of a static finite element solver. The method proposed in this thesis employs transient finite element methods. Time stepping methods are generally perceived to be too time consuming. For example a typical rotating model solution to analyse total harmonic distortion (T.H.D.) takes around 4 hours to solve, which is too long for most design engineers and hence is readily dismissed. However, simulation time depends principally upon two factors; mesh complexity and step size. Step size ultimately determines how far the machine will rotate between solutions and hence determines the quantity of solutions in a single revolution, which in turn determines the validity of harmonics analysed. To allow the critical analysis of high order harmonics a small time step is required: for example to reliably analyse the 150th harmonic it is suggested that at least 4 points are needed in a 150th harmonic period (i.e. double the Nyquist-Shannon sampling theorem [42]) which in a 60Hz machine would correspond to a time step of 2.777×10^{-5} seconds. For this reason time step size cannot be increased to reduce simulation time. Mesh complexity

can be reduced with the use of symmetry - only one pole pair needs be simulated, as in Figure 100, for a four pole machine with offset damper bars. A single pole cannot be simulated, as the rotor pole face damper bars are offset in opposite directions on adjacent poles - a non-symmetrical design feature incorporated to directly affect stator harmonics. End effects can generally be incorporated with lumped parameters, leaving a two dimensional model in the radial/circumferential plane.

Figure 100 shows flux in the shaft of the generator. This is to be expected as the shaft is made from steel and will conduct flux. The shaft is not laminated so this flux could cause loss but as the rotor flux is nominally DC this is unlikely.

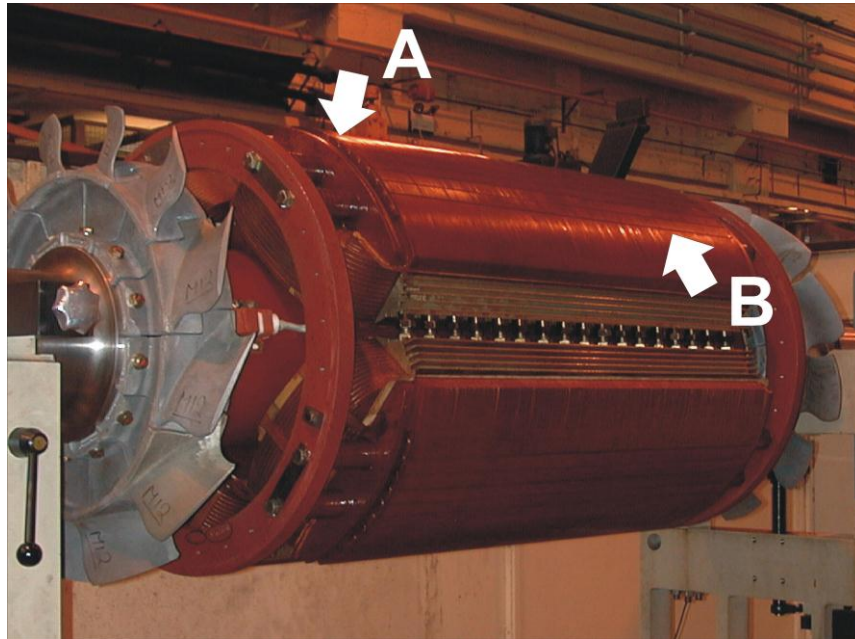


Figure 99 : A Laminated four pole 15MVA Synchronous generator rotor showing: A - Damper bar placement on the pole face B - Open and Closed Damper bar slots

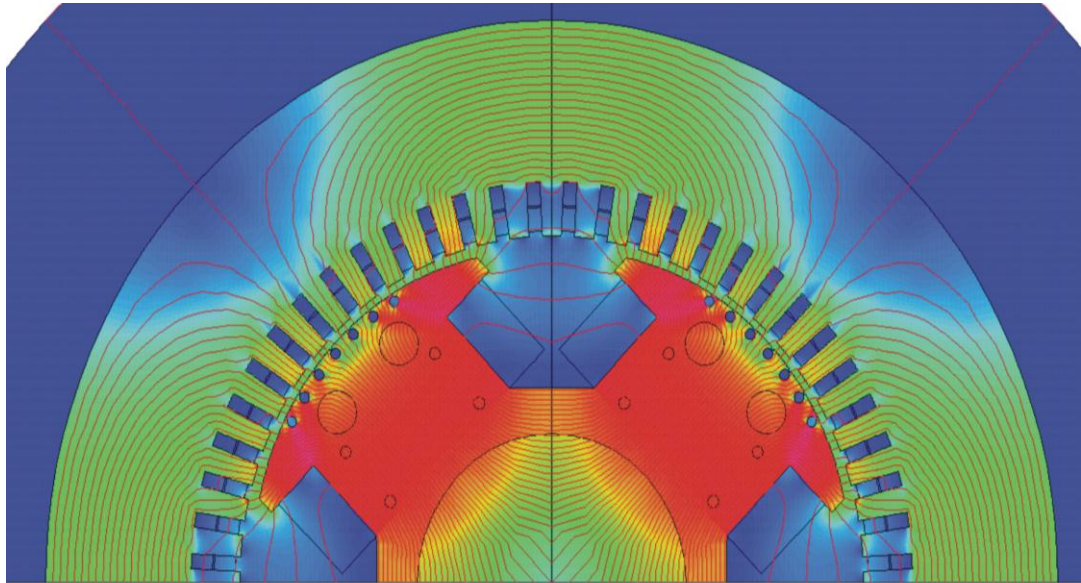


Figure 100 : A FE plot of a four pole generator showing flux density (Bmod) and flux lines

6.2.1. Rotating Pseudo Rotating Superposition (RPRS)

A unique FE solution is usually required at every position in a single rotation of a machine in order to reproduce the voltage waveform. This is time consuming and inefficient, since information can be taken from a single solution to create an adequate waveform made up of all harmonics up to the n^{th} , where n is the number of slots per pole. During a normal simulation a single winding is monitored and the rotor moved and solved at each position (Figure 101A and Figure 101B). Since FE allows Average Vector Potential (AVP) to be extracted from all conductors (not just a single winding) the same effect as moving the rotor can be achieved by simply changing the conductor used in the calculation (Figure 101C). Figure 101A and Figure 101B show the rotor in 2 different positions, yet the highlighted conductors have the same average vector potential as their respective partners in the alternative machine (i.e. conductor B1 = conductor C1 etc). Since A and C have a shared geometry, then only a single magnetostatic solution is required. Multiple solutions can be found at different rotor positions across a slot.

By calculating solutions at multiple places across a single slot (i.e. using a small time step) a waveform can be created with significant data to analyse high order harmonics.

Consider the series of diagrams in Figure 102. Pseudo rotating superposition, as described in Chapter 3, would jump directly from position A to G as the vector potential in the highlighted conductors in F and G are identical. Rotating Pseudo rotating superposition adds several steps in-between - position B, C, D and E. Each one of these

steps represents one fifth of a slot pitch step, meaning that from A to E a solution over 1 slot is required. As diagrams A & G, B & H, C & I, D & J and E & K share geometry the respectively highlighted conductors can be used to extract the vector potentials and hence flux calculated. This hence leaves the correct sequence of diagrams as A→B→C→D→E→G→H→I→J→K→L etc. Therefore, to create a full period the average vector potential data from all slots will eventually be required and can be extracted in a single pass to avoid continual inefficient reopening of solution data files. Once all the data is extracted special care must be taken to rearrange the data into the correct order. Whilst traversing the stator periphery the combined vector potentials would hence take on the order of:

slot 1 from position 1
 slot 1 from position 2
 slot 1 from position 3
 slot 1 from position 4
 slot 1 from position 5
 slot 2 from position 1
 slot 2 from position 2
 slot 2 from position 3
 slot 2 from position 4
 slot 2 from position 5
 slot 3 from position 1
 etc...

This manipulated vector potential series is illustrated in Figure 103. From the vector potential map the flux can be calculated, remembering that the pitch of each coil is now over a greater number of data values [equal to n times the pitch where n is the number of steps per slot]. Additionally, in any voltage calculations the dt must be equal to the time step to traverse from one position to the next. It is for this reason that the RPRS data combining procedure must be done in the vector potentials or fluxes, but not in voltages as the larger dt by combining several PRS voltage plots at different positions in effect masks the harmonic content. The number of steps per slot is an input variable, allowing higher order harmonics to be accurately found by simply changing one value. Five steps per slot are used in the example diagrams, but it is suggested that this may be

a little low to gain a comfortable level of accuracy in higher order harmonics. Ten steps per slot is a better choice.

Similarly to [41], in this method a reassignment of stator conductors can be undertaken to allow a no load voltage waveform to be created, using the full periodicity of a single slot pitch. Unlike [41] the method employed includes eddy current effects, dynamic field current and full interaction of all MMF sources. This Pseudo Rotating Superposition (PRS) method is solved using a non-linear solver, rotating over a single slot pitch. The model must incorporate the damper eddy currents, so in practice it must run for longer, until the initial transient has decayed. In practice the damper current time constant is very short, and decays within a rotation of one slot pitch. Consequently the model covers rotation over two slot pitches and uses the last half of the simulation results for subsequent calculation. This has allowed solutions to be found in around 10-15 minutes, which is more than acceptable to the design engineer.

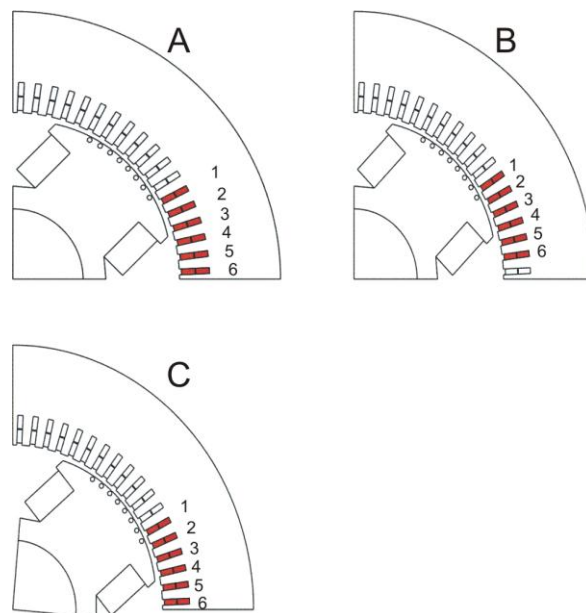
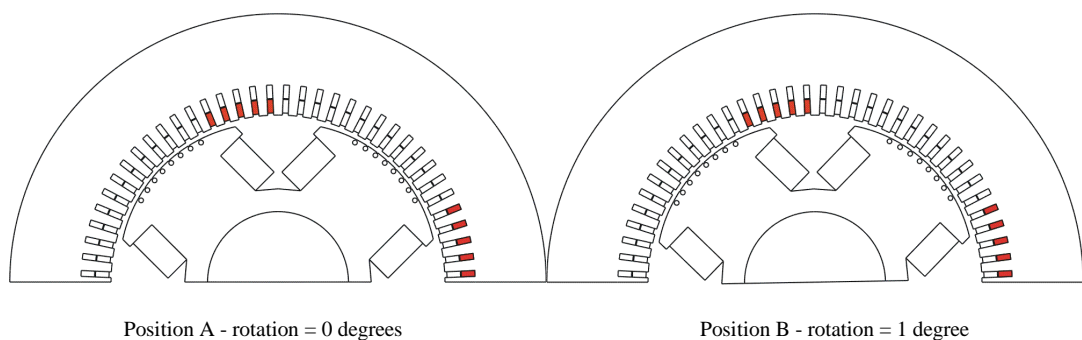


Figure 101 : PRS and standard FE method diagrams



Position A - rotation = 0 degrees

Position B - rotation = 1 degree

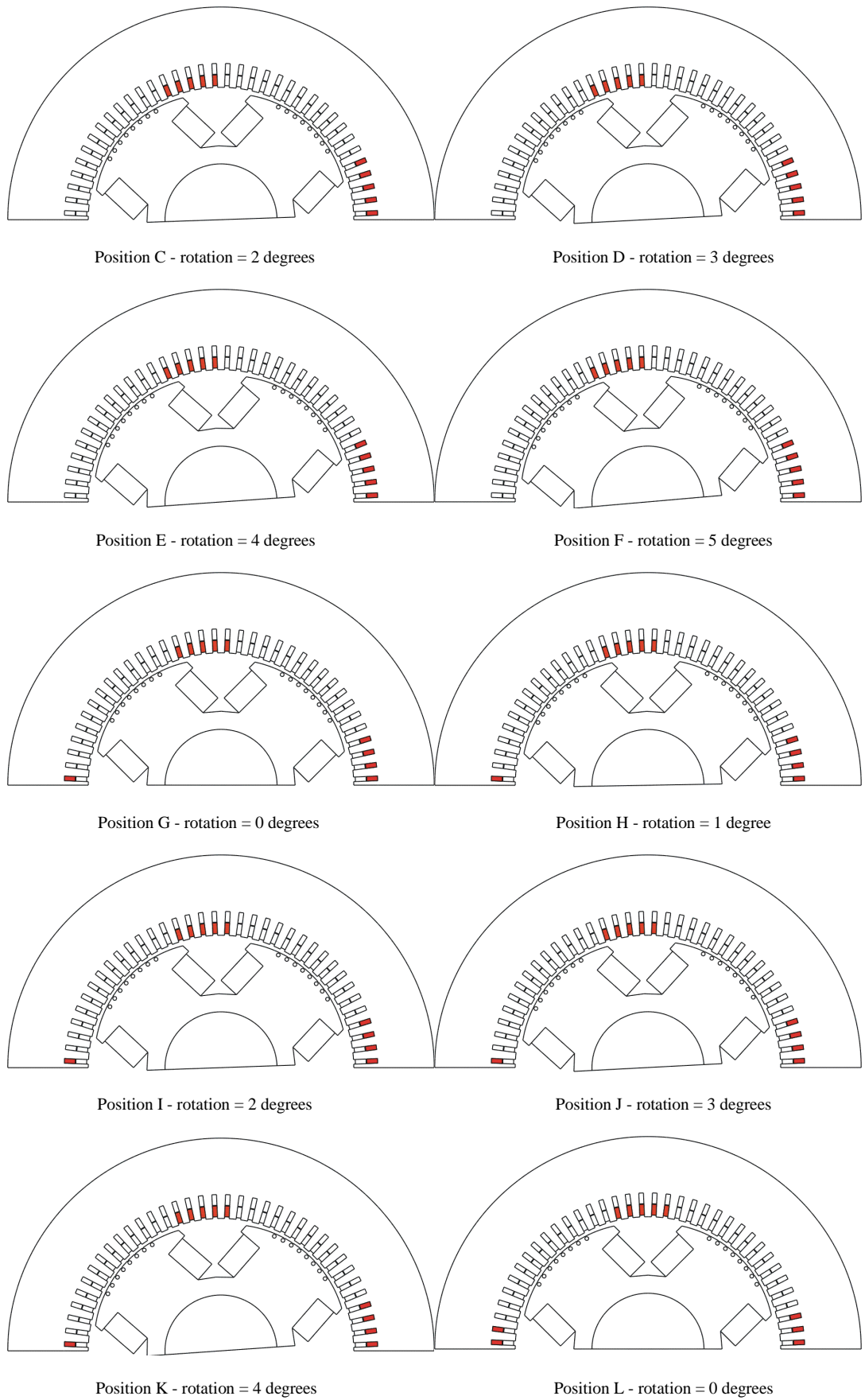
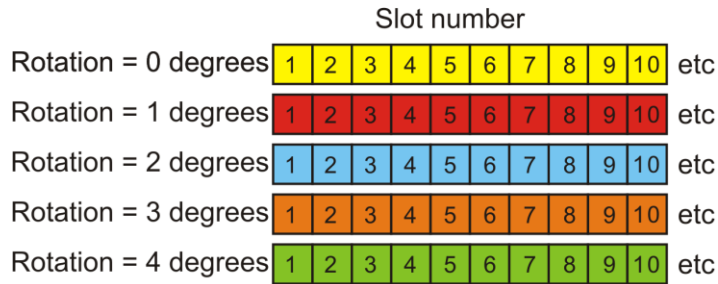


Figure 102 - A series of diagrams showing the effective movement of the rotor during RPRS in a 5 steps per slot system

Individual position average vector potentials



Combined vector potentials



Figure 103 - Diagram showing the order that data must be arranged in a five steps per slot system.

6.2.2. Comparison With Measurement

The method proposed has been compared to both a full rotating transient finite element solution and test results taken from eight machines. Figure 104 shows a comparison between measurement and simulation for a typical four pole, 8.8MVA machine. Both the new method and a full FE transient model have been compared to manufactured machine test results. The full transient solution took over six hours to solve – over 25 times longer than the proposed method. The first point to note is that all harmonics are very small – less than 0.4% of the fundamental. This in itself causes problems, because the required parameters are a small perturbation on a large signal, and are therefore prone to rounding errors. Triplen harmonics should be zero as line quantities are measured in the machine and only odd harmonics are expected as the waveform has odd quarter wave periodicity. The shape of the rotor pole within the machine creates geometrical harmonics. Although minimised by well designed, short pitched and distributed windings, these harmonics cannot be eliminated and hence the 5th, 7th, 11th and 13th harmonics are evident. These low order harmonics, resulting as a consequence of the air gap dimensions, are accurately predicted by both the proposed method and the fully rotating FE simulation when compared to the test results.

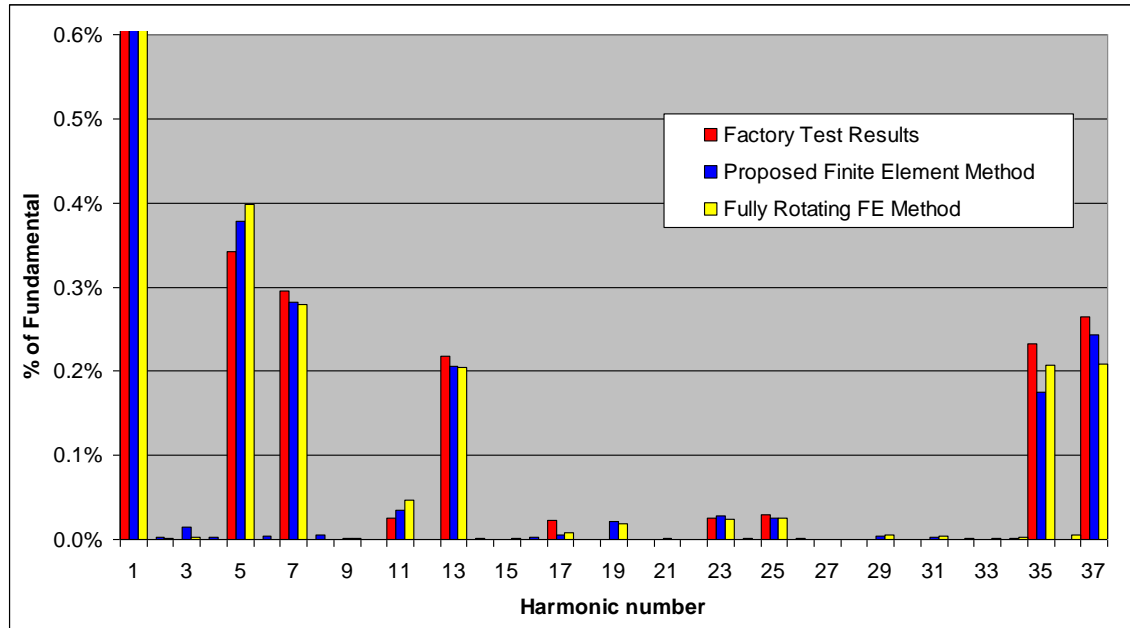


Figure 104 : Harmonic content of a four pole 8.8MVA synchronous generator.

The machine has 72 slots and, because of the 4 pole nature, the slotting harmonics are the 35th and 37th, which can be seen to be significant. These higher order slotting harmonics do show some deviation from test results. For the 35th harmonic the test results are 0.1% higher than the proposed method, with the full FE model differing from the measurement by only 0.06%.

The field current level in a generator is normally assumed to be constant, according to equation (6.2), however there are two additional sets of perturbations which make up the field winding current within the FE [equation (6.3)]. An ac perturbation, I_{ac} , in the field winding is caused by the change in permeance due to the variation in number of slots that are covered by the pole shoe and associated diverging field. This effect is well documented by [36], along with a design methodology to reduce it and consequently minimise slotting harmonics contained within the stator voltage. The finite element method is able to incorporate this by representing the field circuit with an external voltage source and series resistance. This is an expected effect the finite element correctly predicts, and is noticeable in both finite element methods. The resultant oscillation in the field current is of the order of 0.2% of the mean value and is illustrated in Figure 105.

$$I_{DC} = \frac{V_{field}}{R_{field}} \dots (6.2)$$

$$I_{FE} = I_{DC} + I_{AC} + I_{transient} \dots \quad (6.3)$$

The perturbation in the field current poses a problem for the finite element method because, unlike the damper currents, the field circuit time constant is relatively long – well beyond the time taken for the rotor to rotate through two slot pitches. The mean steady state field current, given in equation (6.2) is used as the initial value that the finite element solver assigns to the field current at $t=0$. If the actual machine has a non zero field current perturbation at this point then an initial transient occurs in the simulated field current, of maximum value 0.2A, as shown in Figure 106. Until the transient has decayed there are additional harmonics in the field current and hence the stator windings. The Fully rotating FE simulation is run over a long period of time, allowing the harmonics to decay and have minimal effect. However, the proposed method is only run over a short period of time and is influenced by this small transient. The transient could be eliminated entirely by using a less dynamic source - in the extreme a constant current source. Figure 107 shows the field current when an ideal current source is used as the electrical drive for the rotor circuit. This graph clearly has no induced currents and as such it does not simulate the field winding as it is in a real machine. Therefore an ideal current source is not used.

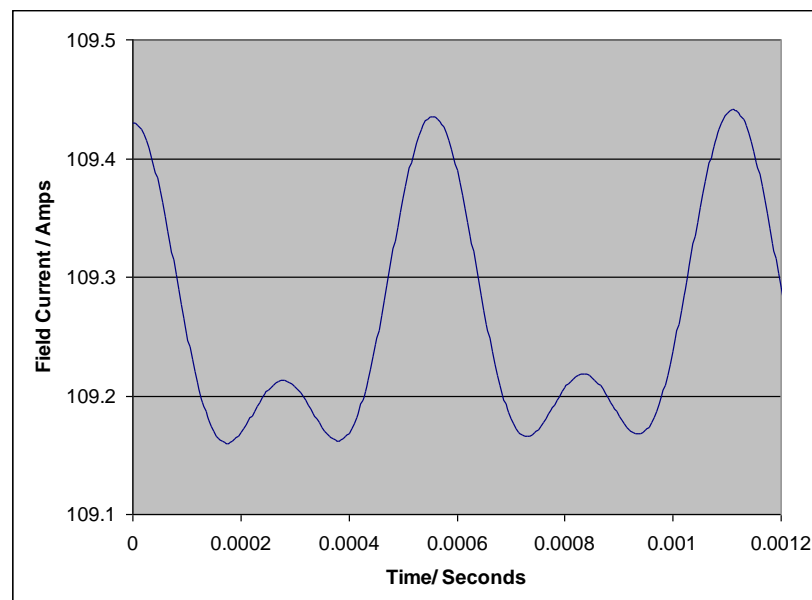


Figure 105 : Graph of Field Current within FE simulation

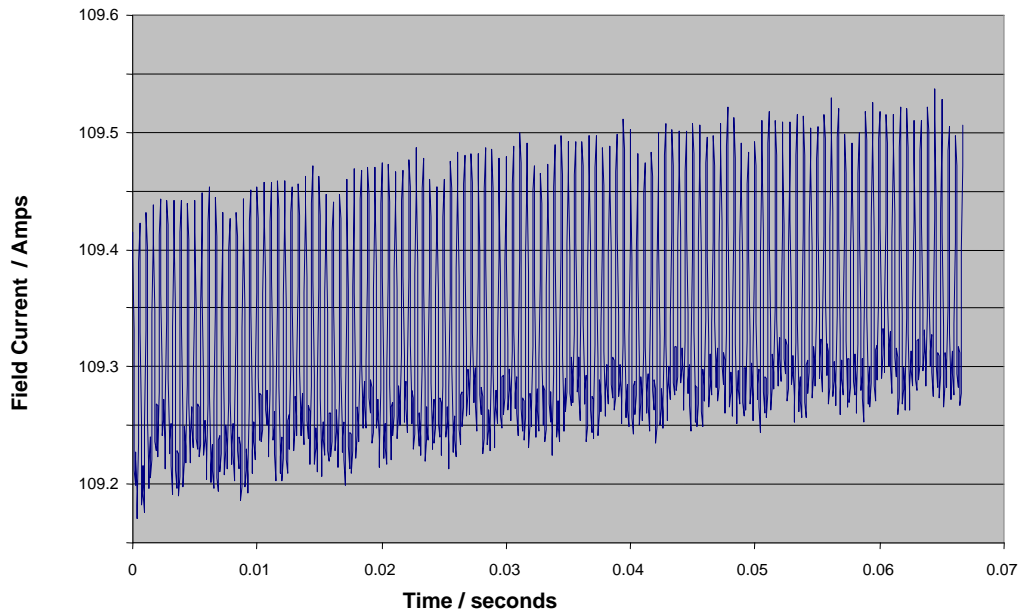


Figure 106: Graph of Field Current within FE simulation

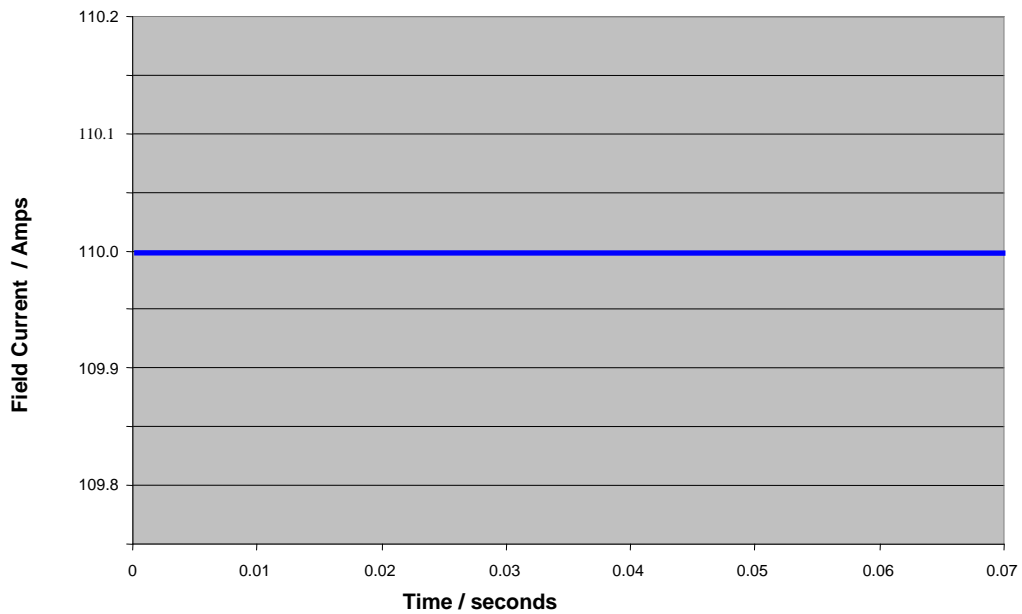


Figure 107 - Graph of field current using a constant current source

6.3. Influence Of The Field Current Source

The magnitude of the slotting harmonics was found to be significantly influenced by assumptions made when modelling the field current source. Previous publications model the field current as a fixed quantity with a perfect current source – this is shown in the previous section to be a source of error. It is suggested the deviation between test results and calculated FE results is caused by the method of modelling the field

winding. The manufactured machine, as in Figure 108, is equipped with a permanent magnet generator, an AVR, an exciter and rotating rectifiers and becomes too complicated to simulate quickly. Hence a simpler arrangement of a voltage source with a series impedance determines the dynamics of the field's response within the FE. The virtual circuit not only determines the level of the excitation but the response to perturbations caused by the slotting. Varying the impedance alters the field's LR time constant and hence changes the effects of the slotting harmonics. Experience has found that the field circuit requires external parameters, including a resistance equal to the field winding and an inductance equivalent to the summation of the exciter inductance and the field winding end winding inductance

6.3.1. Effect Of Exciter Harmonics Upon Field Excitation

Rotating rectifier diodes convert the ac excitation to a DC field current which is assumed to have no ripple, however the effect of the bridge must be acknowledged. As the main machine and the exciter have a pole number mismatch, with the exciter having three times more poles, the sinusoidal input into the rotating rectifiers is at 3 times nominal frequency, giving an 18 pulse waveform. The 18 pulse rectified voltage signal, shown in Figure 109, can be Fourier analysed as in equations (6.4) to (6.7). Each field current harmonic is then calculated using the field impedance $R_f + j\omega L_f$ in equation (6.8). The calculated field current ripple harmonics expressed as a percentage of the DC level is then charted in Figure 110.

$$V = V_{dc} + \sum_{h=1}^{\infty} [a_h \cos(h\omega t) + b_h \sin(h\omega t)] \dots (6.4)$$

$$V_{dc} = \frac{18}{2} \int_0^{\frac{\pi}{9}} \sin \left[3 \left(\omega t - \frac{5\pi}{9} \right) \right] d(\omega t) = \frac{3}{\pi} \dots (6.5)$$

$$a_h = \frac{2}{\pi} \left[\sum_{n=0}^8 \left[\int_{\frac{n\pi}{9}}^{\frac{(n+1)\pi}{9}} \sin \left[3 \left(\omega t - \frac{(n+5)\pi}{9} \right) \right] \cdot \cos(h\omega t) d(\omega t) \right] \right] \dots (6.6)$$

$$b_h = 0 \dots (6.7)$$

$$I = \sum_{h=0}^{\infty} \frac{V_h}{R_f + jh\omega L_f} \dots (6.8)$$

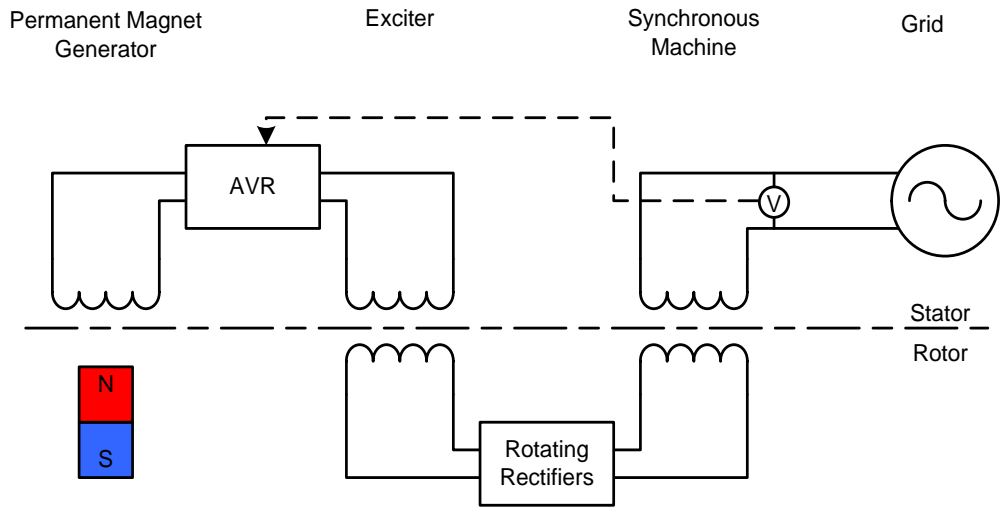


Figure 108 : Topological Diagram of the excitation system on a typical synchronous generator

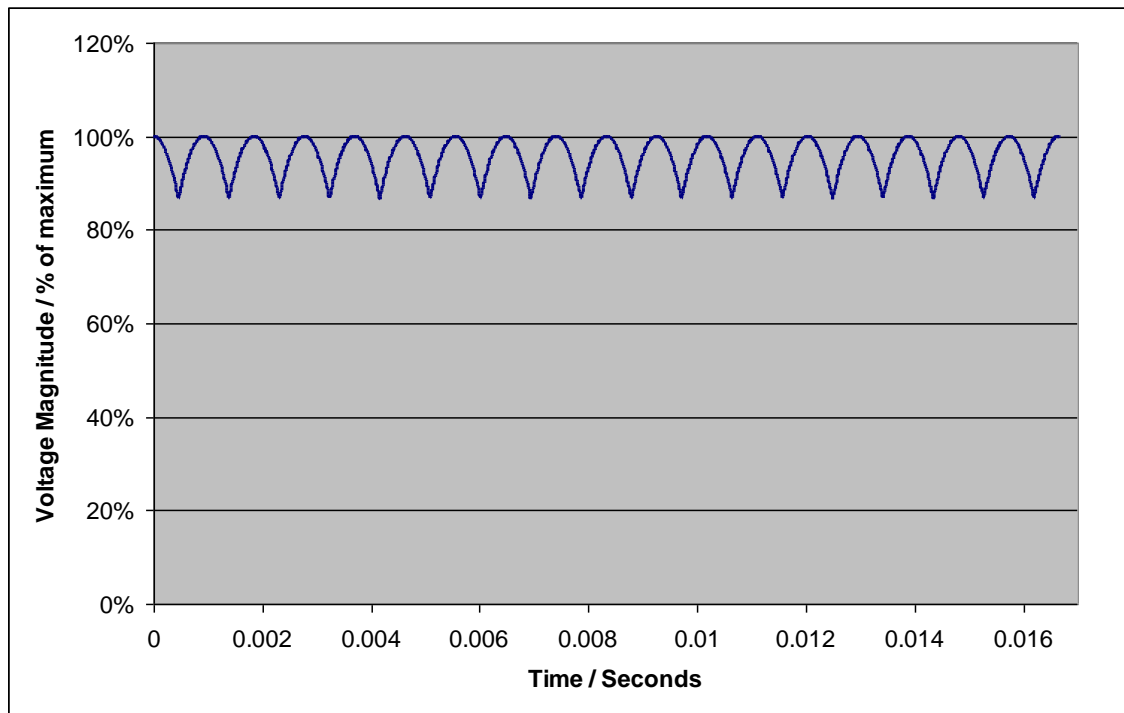


Figure 109 : 18 pulse exciter voltage waveform over 1 period

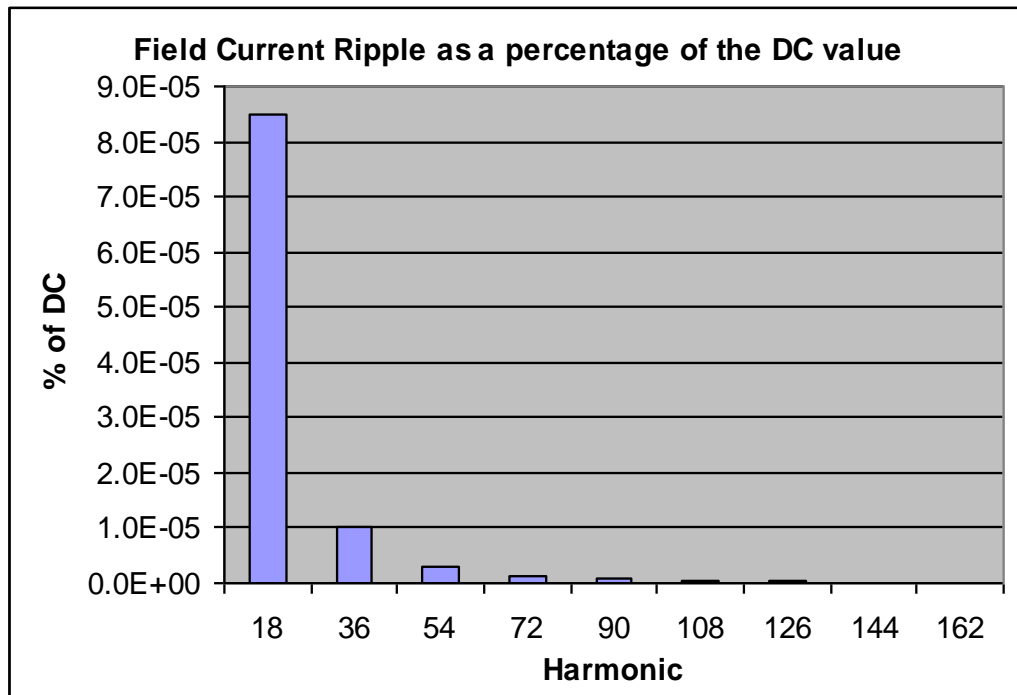


Figure 110 : Field Current harmonics due to machine exciter and rotating rectifier diodes.

From Figure 110 it is seen that the 18th harmonic has the largest effect upon the field ripple, however it should be noted that the harmonic magnitude is only about 0.00008%, corresponding to current in the micro amp range. This current is assumed negligible, demonstrating that the effect can be ignored.

6.4. Voltage Distortion Parameters

There are several different parameters that different customers require when quantifying the open circuit voltage distortion. The parameters are used by different qualification authorities and each is calculated in a slightly different manner. They are all calculated from the magnitudes of the harmonics, with or without weighting factors. Four frequently quoted factors are:

- T.H.D. - Total Harmonic Distortion
- T.H.F. - Telephonic Harmonic Factor
- T.I.F. - Telephonic Interference Factor
- H.V.F. - Harmonic Voltage Factor

Total Harmonic Distortion (T.H.D.) is the most commonly requested parameter, as it is specified in the most recent IEEE generator standards[31] and is the de facto industry standard. It is calculated as a summation of the squared non fundamental harmonics as a percentage of the fundamental, as shown in equation (6.9).

$$THD = \frac{\sqrt{\sum_{n=2}^{\infty} V_n^2}}{V_1} \quad \dots \quad (6.9)$$

Telephonic Harmonic Factor (T.H.F.) is the predecessor to T.H.D., as specified in the British Standard [43]. Although technically superseded, occasionally customers request this factor. This factor originates from when all telephone communication was analogue and hence any electromagnetic noise created on electricity lines near telephone lines had a catastrophic interfering effect if it was of a similar frequency to the bulk of the telephone traffic. Therefore the calculation is weighted such that harmonics that cause the most interference have a higher factor. The equation for calculating T.H.F. is shown in equation (6.10) and the harmonic weighting factors are listed in detail in Appendix J. T.H.F. is usually expressed as a percentage.

$$THF = \frac{\sqrt{\sum_{n=1,2,3\dots} V_n^2 \lambda_n^2}}{V_1} \quad \dots \quad (6.10)$$

where

V_n = Line r.m.s. Voltage of the n^{th} harmonic

λ_n = T.H.F. weighting factor of the n^{th} harmonic

Similarly to T.H.F., Telephonic Interference Factor (T.I.F.) is calculated using a weighted array of harmonic values. This again originates from the telephone interference but this standard is specific to 60Hz systems and hence the majority of customers are American in origin. This IEEE standard [44] has too been superseded for generators but it is very common for US customer to specify T.I.F. instead of T.H.D. The equation for calculating T.I.F. is shown in equation (6.10) and the harmonics weighting factors are listed in detail in Appendix J.

$$TIF = \sqrt{\sum_{n=1,2,3\dots} \left(\frac{V_n W_n}{V_t} \right)^2} \quad \dots (6.11)$$

where

V_t = Total line r.m.s. Voltage

V_n = Line r.m.s. Voltage of the n^{th} harmonic

λ_n = T.H.F. weighting factor of the n^{th} harmonic

Finally, Harmonic Voltage Factor (H.V.F.) is occasionally specified by customers as the testing standard. Although typically used in motor characterisation it can be applied to generators. This measurement of distortion is specified in the IEC standard [35]

$$HVF = \sqrt{\sum_{n=2}^{13} \frac{V_n^2}{n}} \quad \dots (6.12)$$

where

V_n = Line r.m.s. Voltage of the n^{th} harmonic

n = The order of the harmonic from 2 to 13

6.5. Comparison Of Total Harmonic Distortion

The total harmonic distortion of eight machines is calculated using equation (6.9) and shown in Figure 111. The factory test results are compared with both FE simulation methods and an existing analytical design tool documented in [38], based upon work within [36]. Machines A - D are four pole, 72 stator slot machines, with ratings from 5 to 10 MVA, whilst machines E - H are four pole, 60 stator slot generators with ratings of 12 to 20 MVA.

From Figure 111 it can be seen that all methods of prediction follow the correct trend and are never more than 20% different to the test results. Both FE methods are on average significantly more accurate than the existing analytical tool. From Figure 112 the two FE methods can be seen to reduce the error in prediction by around a half, with the proposed method being the better of the two. For only two out of eight machines is the analytical tool more accurate, and on machine C the improvement is small enough to be insignificant. Machines B and H show large errors compared to the test results. The

Finite element methods show harmonious correlation and are almost identical throughout. The proposed method can be seen to be a marginal improvement on the fully rotating method, with a mean average percentage error of 6.44%, compared to 7.59%.

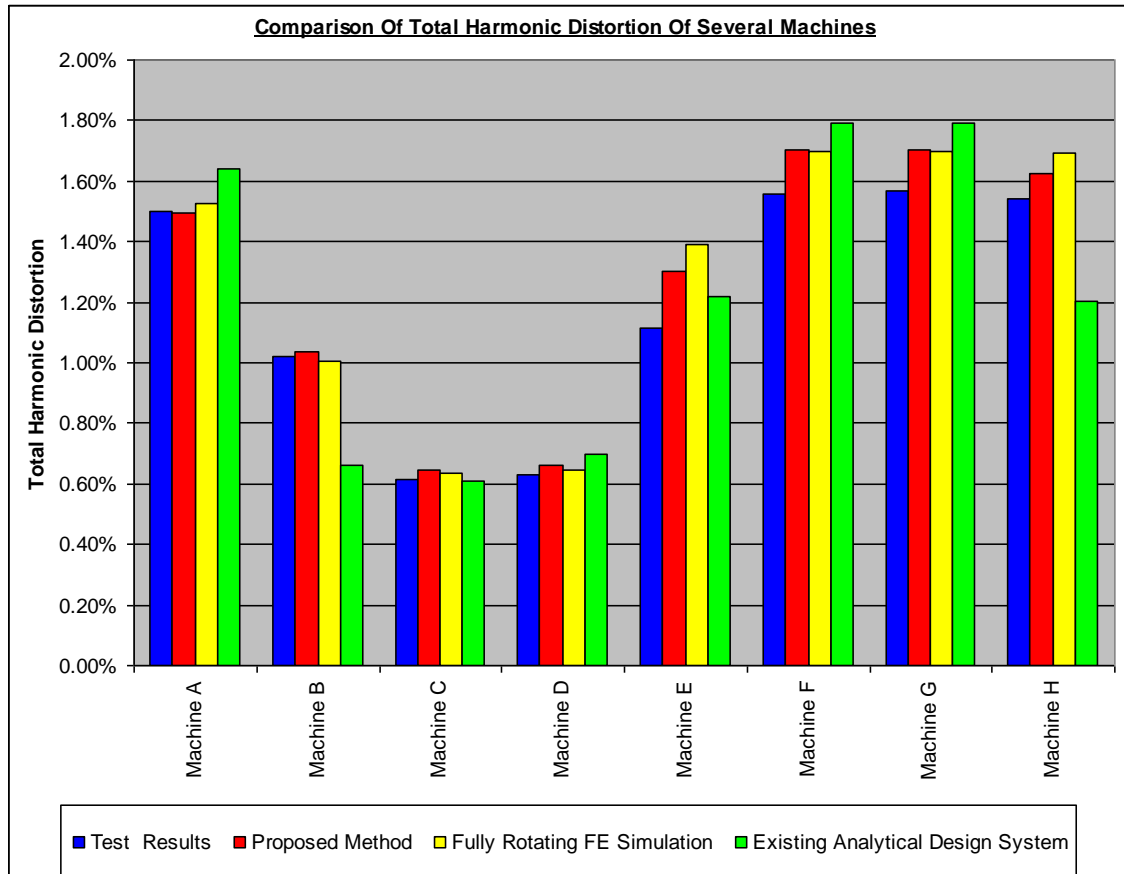


Figure 111 : Comparison of the Total Harmonic Distortion of several generators

	Mean average percentile error (MAPE) [45] vs. Test Results
Proposed Method	6.46%
Fully Rotating FE Simulation	7.59%
Existing Analytical Design System	14.67%

Figure 112 : Table showing Mean average percentile error (MAPE) vs. Test Results for 3 differing methods

All calculations were performed on a desktop PC with Intel Xeon 5130 CPU running at 2 GHz, with 8 GB of RAM, running Windows XP Professional x64 Edition. The calculations applying the proposed method were about 25 times faster than the fully rotating FE simulations performed for comparison.

6.6. The Effect of Damper Bars within Synchronous Machines

The validated pseudo rotating superposition method has allowed rapid simulation of several hundred unique synchronous machines and the effect of damper bars to be investigated. The positioning of damper bars upon the rotor pole face can be used to attenuate or magnify T.H.D. harmonics. Walker's work [36], shows that for machines with an even number of stator slots the harmonics are attenuated when damper bars are offset by 0.25 of a stator slot pitch in the opposite direction on each pole. This will place any induced harmonics associated with the damper bars in antiphase, so that the net harmonic effect of the damper bars is zero. The work also states that ideally the rotor pole should cover a whole number of stator slot pitches, so that as the rotor moves it will maintain a constant reluctance path, thus keeping perturbations to a minimum. (See sections 6.3 and 6.5.) Similarly the damper bar cage pitch should equal the stator slot pitch, so that during synchronous rotation a constant flux, due to the constant reluctance, is linked within the damper bars, resulting in zero induced current.

In Figure 113 the effect of varying both Damper bar pitch and offset is investigated for Saxi Batique - a typical 4 pole generator. The damper offset creates two distinct minima across the chart at 0.25 and 0.75 of a slot pitch. The 0.25 minimum corresponds to the predicted minima and the 0.75 minimum is simply the same antiphase effect, but with an additional period of separation. The two minima show slight migration to a higher offset as the damper bar pitch increases.

Conventional expectations are that minimum T.H.D. occurs when the damper bar slot pitch is equal to the stator slot pitch, since at that pitch there should be no slotting harmonics induced in the damper bars. In practice, Figure 113 indicates that in general the smaller the pitch, the lower the T.H.D. It is suggested that this is caused because the number of damper bars is held constant, and so as the bar pitch reduces then the coverage of the cage is reduced, along with the overall influence of the cage. If the cage had extra bars added then it would cover a similar quantity of the pole face, but the removal of magnetic material would lead to a reduction in overall terminal volts.

From Figure 114 it can be seen that combined effects of damper bar offset and pole shoe width produce a more complicated effect. The results of Figure 113 support the commonly held belief that the damper bars should be offset on adjacent poles by ± 0.25 of a slot pitch. However, Figure 114 shows that in reality this is also a function of the pole shoe arc. As the pole shoe arc reduces from 10.74 slots to 9.95 slots the minimum T.H.D. moves from 0.25 and 0.75 slot pitch offsets to 0.5 slot pitches.

Simple calculations predict that when the pole shoe spans an integer number of slot pitches then the field circuit reluctance should be independent of rotor position, resulting in the minimum total harmonic distortion. However, Figure 114 indicates that the true situation is much more complex, with a global minimum occurring at a pole shoe span of 10.34 with a damper bar pitch of 0.3. This discrepancy can be partially explained by the fringing of flux from the edges of the pole shoe. The assumption of radial flux is too simple - in reality the fringing flux makes the pole shoe seem magnetically wider than it is. For this reason the when the minima at 10.34 occurs the flux is fringing and covering 11 slots. This fringing effect is extenuated by the air gap shape, which is not constant. To create a more sinusoidal MMF the pole shoe is shaped such that the radial air gap at the pole tip is approximately 1.5 times the air gap at the centre of the pole.

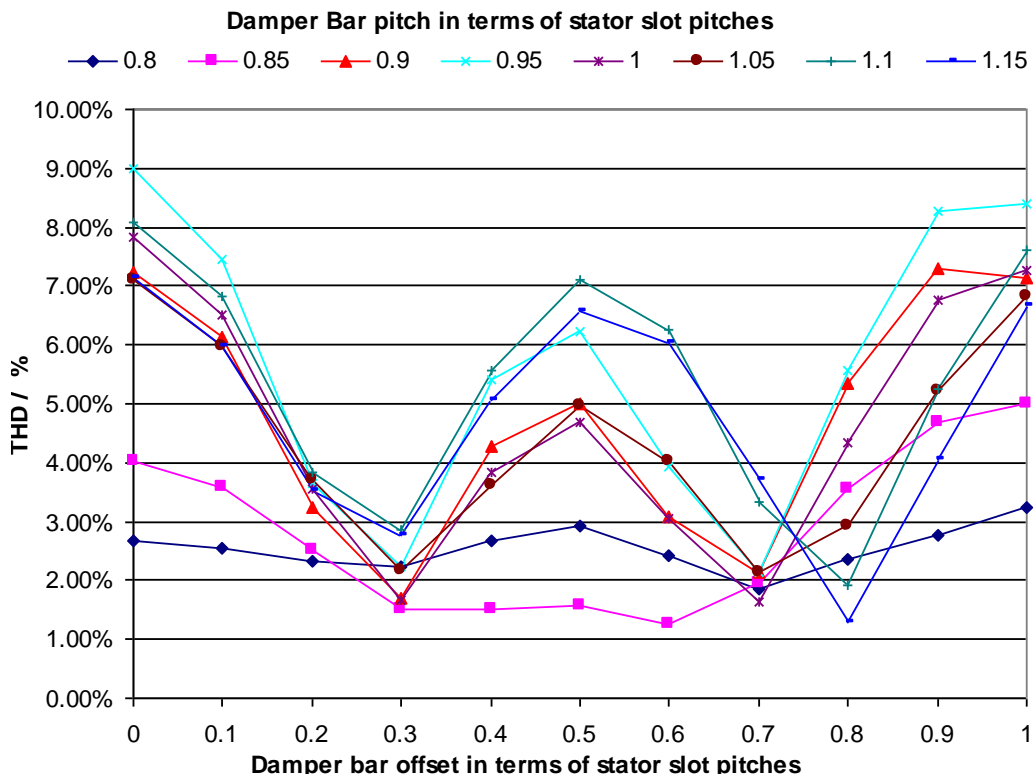
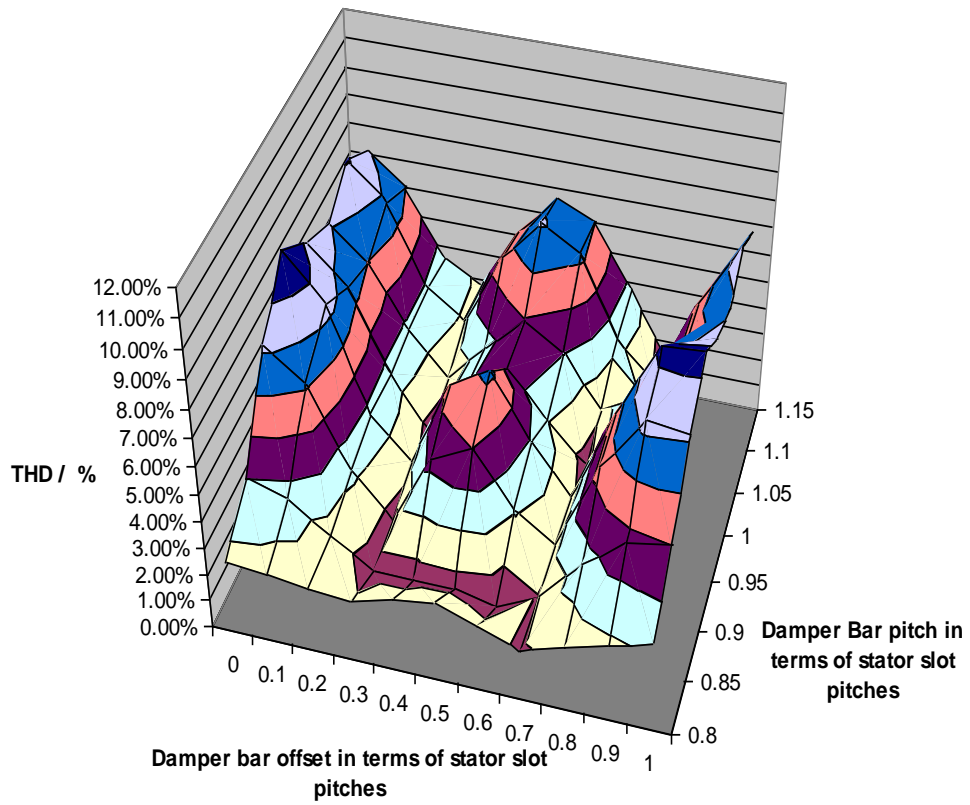


Figure 113 : The Effect of varying Damper bar pitch and offset upon the T.H.D. of a machine.

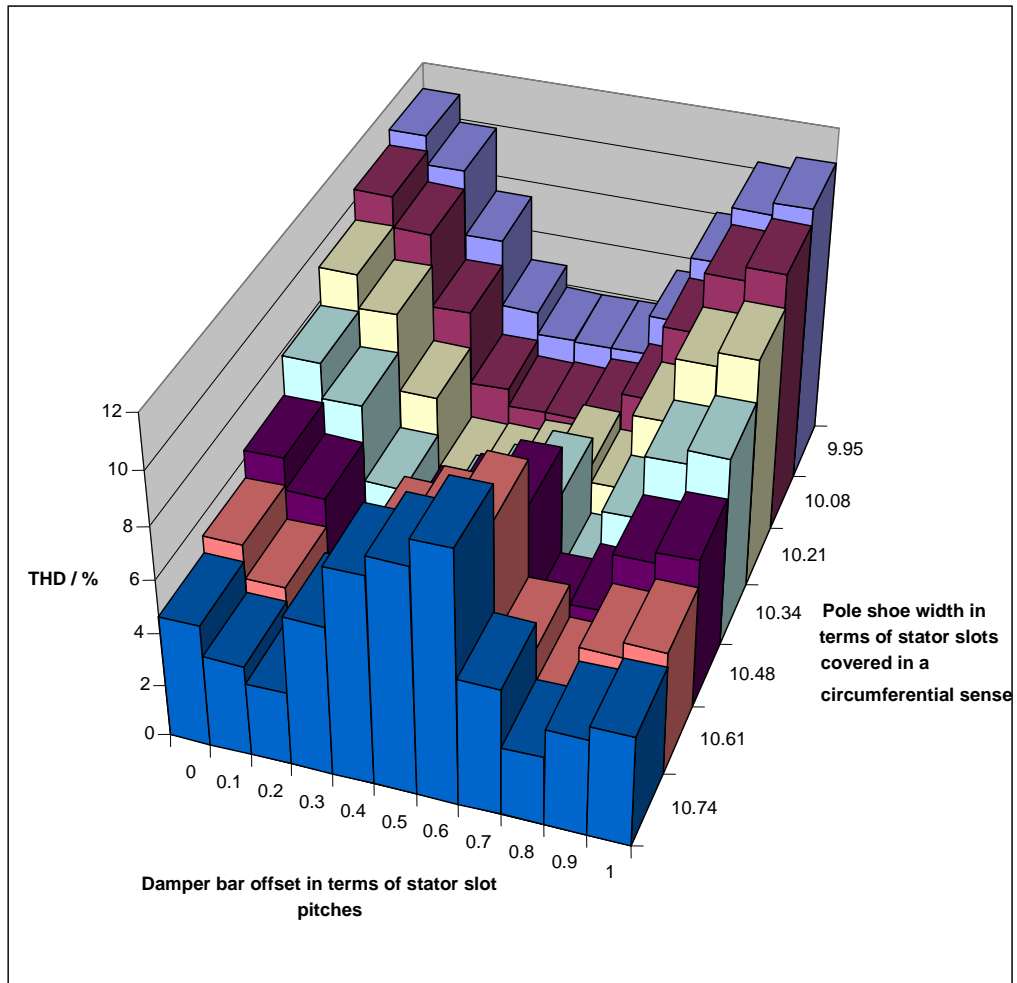


Figure 114 : The Effect of varying pole shoe width and Damper Bar Offset upon the T.H.D. of Saxis Batuque.

6.7. Automated Damper Bar Optimisation

Given that the created system accurately predicts the harmonic content of the open circuit waveform, a module which automatically optimises the position of the damper bars would be of value. For this reason the harmonic module has been programmed with an optimiser. For initial testing a generic genetic algorithm optimising routine has been used in MATLAB, which calls the finite element module with various parameters, and the THD is calculated as an output. The genetic algorithm works by populating a generation of solutions with a varying range of parameters or genes. Once a generation is complete the members of the population with the best characteristics are kept and chosen to breed. The best characteristic are determined by a fitness function - in this case the lowest THD. The chosen members have children: hence their genes are used to create members for the new generation which will be similar to their parents and hence

even more optimal. This process is repeated for several generations until either a tolerance is reached or a generational limit is reached. The genes are limited to practical machines that can be constructed hence: for example, the span of the damper bars is limited to the pole arc, the pitch of the bars must be large enough that they do not overlap etc.

As the optimising system was expected to be fairly slow it was programmed and set to run over a week when the processing PC was not in use. However the results had failed to converge because the system had too many parameters to vary. The program had been allowed to change any harmonic or damper bar related variable so it could modify:

- Damper bar pitch,
- Damper bar offset,
- Damper bar diameter,
- Damper bar depth (the depth of the bar under the pole face)
- Damper bar slot width (the width of the bar slot opening)
- The number of closed damper bar slots (usually one at each end)
- Rotor pitch circle diameter (the radius which creates the pole face shape)
- Rotor pole tip radius (radius of the round on the pole tip corner)
- The pole shoe width

This was clearly too many and, even after a week, the algorithm hadn't had enough time to find any optimised solutions.

To remove this obstacle the genes were simply limited to 2 - damper bar pitch and damper bar offset, whilst keeping the overall damper bar span roughly constant (hence the number of bars must be adjusted). This created a problem in the third run. Although the system did reach a solution, the algorithm had simply removed all the damper bars, hence removing any rotor permeance variations and thus reducing the THD. This is not an optimised solution as the perturbation damping properties of the bars have been removed and hence the hunting of the machine would be very poor, leading to subtransient resonance. This highlighted the obvious limitation of the simple electromagnetic FE - the lack of integrated dynamic mechanical calculations.

The Fourth run limited the span, keeping a minimum of 4 bars. This did find a solution with an offset of 0.223 and a pitch of 1.13 with a THD of 3.026%. Looking at Figure

113 it is quite clear that this is not a global minimum. The reason for the algorithm finding a non-optimal solution is down to one of several issues:

- local minima - a local minimised turning point will fool an algorithm if there isn't sufficient genetic diversity. This is unlikely, as looking at Figure 113 the range forms valleys, rather than sink holes. Nevertheless it is still possible and could be solved by adding greater diversity to the algorithm parameters, although this general forces the system to take more generations to solve
- Not enough generations - Due to time constraints to solve within a week a limited number of generations was permitted (25). This may need to be higher to allow paradigm shifts to occur within the population and true minima to be found.

This fourth solution took a week to solve and had only 2 variables in its genes. The data in Figure 113 was created in around a day and has a lower 2 variable THD solution. Due to the speed of FE the choice of a genetic algorithm clearly wasn't optimal. The requirement to populate each generation is far too time consuming and given that an engineering estimate can get a very good approximate very quickly, the use of a genetic algorithm is limited until such a time that FE can solve in seconds. The idea of an optimiser is not a bad one but the choice of algorithm was. Hence further work in this area is suggested. Further discussion on this topic is picked up in Chapter 8.

6.8. Chapter Summary

This chapter presents a transient finite element model which can accurately predict the stator voltage waveforms in a salient pole synchronous machine, including total harmonic distortion resulting from damper windings in the rotor poles. Unlike earlier methods, it fully incorporates magnetic non-linearity and transiently models the damper bar currents. The main conclusions of the work are that:

- The model exploits geometrical symmetry in the machine so that the transient solution only needs to cover rotation over one slot pitch and gives a rapid, but accurate solution.
- The proposed method is found to reduce T.H.D. prediction error by 55%, compared to an existing analytical design software.

- The field excitation cannot be simply modelled as a perfect current source, otherwise slotting effects are not properly represented.
- The effect of the rotating rectifiers in the machines excitation system is found to be negligible upon D.C. field current ripple.
- The method can easily be incorporated into a design package.
- The method had been used to show the effect of varying damper bar properties upon total harmonic distortion.

Chapter 7. Iron Loss Calculation

7.1. Abstract

The accurate calculation of iron loss from finite element analysis in electrical machines is essential if optimal machines are to be designed. This chapter conducts a holistic review of the extensive literature before examining, in detail, several methods in order to recommend an optimum engineering solution. Both frequency domain and time domain methods are discussed, including the use of different orthogonal components as well as the relative merits of using all, or some, of the Eddy Current, Anomalous and Hysteresis loss components. A theoretical cubic meter of iron is simulated to quickly demonstrate the inaccuracies of Cartesian coordinate methods, before calculations on several manufactured machines are undertaken, showing the superior accuracies of major/minor loop calculation. Calculation undertaken using the radial/tangential orthogonal plane is shown to have less than 1% average difference to the major/minor loop, yet is over 6 times quicker. The peak percentage error in an individual element is shown to be less than 5%. Discussions are also made regarding the method of curve fitting to gain loss constants and any possible sources of inaccuracy, particularly during manufacture.

7.2. Introduction

In order to calculate the final nameplate rating of a machine it is very important for the designer to be able to calculate any losses incurred. A fast, accurate and reliable method for the calculation of losses is essential in order to avoid any design concessions and potential financial penalties in any completed products. The losses within machines can be attributed to several causes, such as resistive heating, friction and windage and iron loss. This chapter specifically looks at the calculation of iron loss from flux density within the iron circuit of the machine, which is calculated using Finite Element Analysis (FE). Any loss calculation must be capable of being integrated into an existing FE design system which is currently used to analyse synchronous generators in the multi-megawatt range and be suitable to be used within a manufacturing design office. To this end the method must be consistent, quick, accurate and integrated to allow rapid design iteration, leading to optimised designs. The calculation method must also take into

account any variances created by machine manufacturing or material handling processes.

Several different models for iron loss have been presented by various authors and the field of literature is extensive. This thesis proposes a comparative study of the various methods, weighing the merits and limitations of each. Bertotti et al [46][47] developed a frequency domain model which divides the loss down into 3 components - Eddy Current loss, Hysteresis loss and Anomalous (sometimes called Excess) loss. The losses originate from the dynamic losses of the Weiss domains under variable magnetic fields. The discontinuous movements within the block walls create fast Barkhausen jumps and then eddy currents [48]. The hysteresis loss is physically caused by localised, irreversible changes during the magnetisation process, making it only dependant upon peak induction [49]. Bertotti's equations are expressed in equations (7.1)-(7.4) and are typically summed for each harmonic of any magnetic fields, hence necessitating Fourier analysis.

$$P = P_e + P_h + P_a \quad \dots (7.1)$$

$$\text{Eddy Current Loss [W/kg]} = P_e = Ke \cdot \hat{B}^2 f^2 \quad \dots (7.2)$$

$$\text{Anomalous Loss [W/kg]} = P_a = Ka \cdot \hat{B}^{1.5} f^{1.5} \quad \dots (7.3)$$

$$\text{Hysteresis Loss [W/kg]} = P_h = Kh \cdot \hat{B}^\alpha f \quad \dots (7.4)$$

where Kh , Ka , Ke and α are material dependant constants

7.3. Continuous time and Discrete time.

Frequency domain equations are especially useful when the data regarding the magnetisation is presented in frequency terms and many authors have used these equations with success [49][50][51]. This is not the case when time stepping FE analysis has been undertaken and relies upon a Fourier analysis of the time domain data to create the correct peak sinusoidal data for equations (7.2)-(7.4). The use of a Fourier analysis adds an extra process and, as data is analysed on an element by element basis within the FE, it can create a slower technique. To counter this the equations can be transformed into the time domain, leading to equations (7.5)-(7.7) below. This mathematical transform is detailed in Appendix F.

$$\text{Eddy Current Loss [W/kg]} = Ke. \frac{1}{2\pi^2} \frac{1}{T} \int_0^T \left| \frac{dB}{dt} \right|^2 dt \quad \dots (7.5)$$

$$\text{Anomalous Loss [W/kg]} = Ka. \frac{1}{8.76} \frac{1}{T} \int_0^T \left| \frac{dB}{dt} \right|^{1.5} dt \quad \dots (7.6)$$

$$\text{HysteresisLoss [W/kg]} = Kh. \frac{1}{T} \hat{B}^\alpha \quad \dots (7.7)$$

The eddy current and anomalous loss is caused by the rate of cycling of the flux through the atomic structure and hence the equations within the time domain have derivatives. The hysteresis loss is highly dependant upon the magnitude of the peak flux and thus the saturation of the material. As a consequence equation (7.7) does not undergo a full averaging over a period when transformed: only the peak magnitude of the flux is desired [49]. Equations (7.5)-(7.7) are within the continuous time domain, transcribing them into the discrete time domain yields (7.8)-(7.10) which are the most useful set of loss equations when dealing with finite element data.

$$\text{Eddy Current Loss [W/kg]} = Ke. \frac{1}{2\pi^2} \frac{1}{N} \sum_{n=1}^{n=N} \left| \frac{B_{n-1} - B_n}{t_{n-1} - t_n} \right|^2 \quad \dots (7.8)$$

$$\text{Anomalous Loss [W/kg]} = Ka. \frac{1}{8.76} \frac{1}{N} \sum_{n=1}^{n=N} \left| \frac{B_{n-1} - B_n}{t_{n-1} - t_n} \right|^{1.5} \quad \dots (7.9)$$

$$\text{HysteresisLoss [W/kg]} = Kh. \frac{1}{T} \hat{B}^\alpha \quad \dots (7.10)$$

Equations (7.8)-(7.10) have been used by multiple authors to yield successful results[52][53][54][55].

7.4. Orthogonal Components

Equations (7.8)-(7.10) assume that all flux is in a single direction and consequently can be described as one dimensional (1D). The majority of electrical machines have constant axial shape and to a good approximation can be analysed in a two dimensional (2D) plane. This 2D nature allows rotation of flux vectors, creating oscillation in both orthogonal components, as shown in Figure 115. Most FE packages calculate magnetic

flux density into orthogonal X and Y components. These can be processed in several ways. Commonly calculations are processed in the B_x and B_y components and loss components are calculated and then added together separately [52][53][56]. Alternatively the magnitude of the flux density is used according to (7.11) and (7.12) [57].

$$B = B_x e_x + B_y e_y \quad \dots (7.11)$$

where e_x and e_y are unit vectors on the Cartesian plain

$$|B| = \sqrt{B_x^2 + B_y^2} \quad \dots (7.12)$$

It should be noted that many authors such as [58] do not mention orthogonal components. The reason for this can only be guessed, but it is suggested authors have either not used FE and therefore escape this problem or have neglected to investigate it. Supplementary work on the losses associated with a rotating flux vector has been carried out by Brailsford [59] who points to the source of the losses originating from the expansion of domains.

Additionally authors have chosen whether to use one of three different axis planes. As discussed The XY plane is often chosen because finite element software natively outputs data within this Cartesian plane. Alternatively Cartesian components are transformed using equation (7.13) into radial and tangential components and loss components calculated accordingly [60][63].

$$\begin{bmatrix} B_a \\ B_b \end{bmatrix} = \begin{bmatrix} \cos(\phi) & \sin(\phi) \\ \sin(\phi) & -\cos(\phi) \end{bmatrix} \begin{bmatrix} B_x \\ B_y \end{bmatrix} \quad \dots (7.13)$$

where ϕ is the angle of an element relative to the axis

The axis selection can be made using the calculated vector information. For this authors must extract a full loop of data for each element, inspect to find the angle at which the major axis rests relative to the axis and transform the element's data using equation

(7.13). This process can be time consuming due to the extra computational cycles. Figure 116 shows a diagrammatic representation of potential calculation axes.

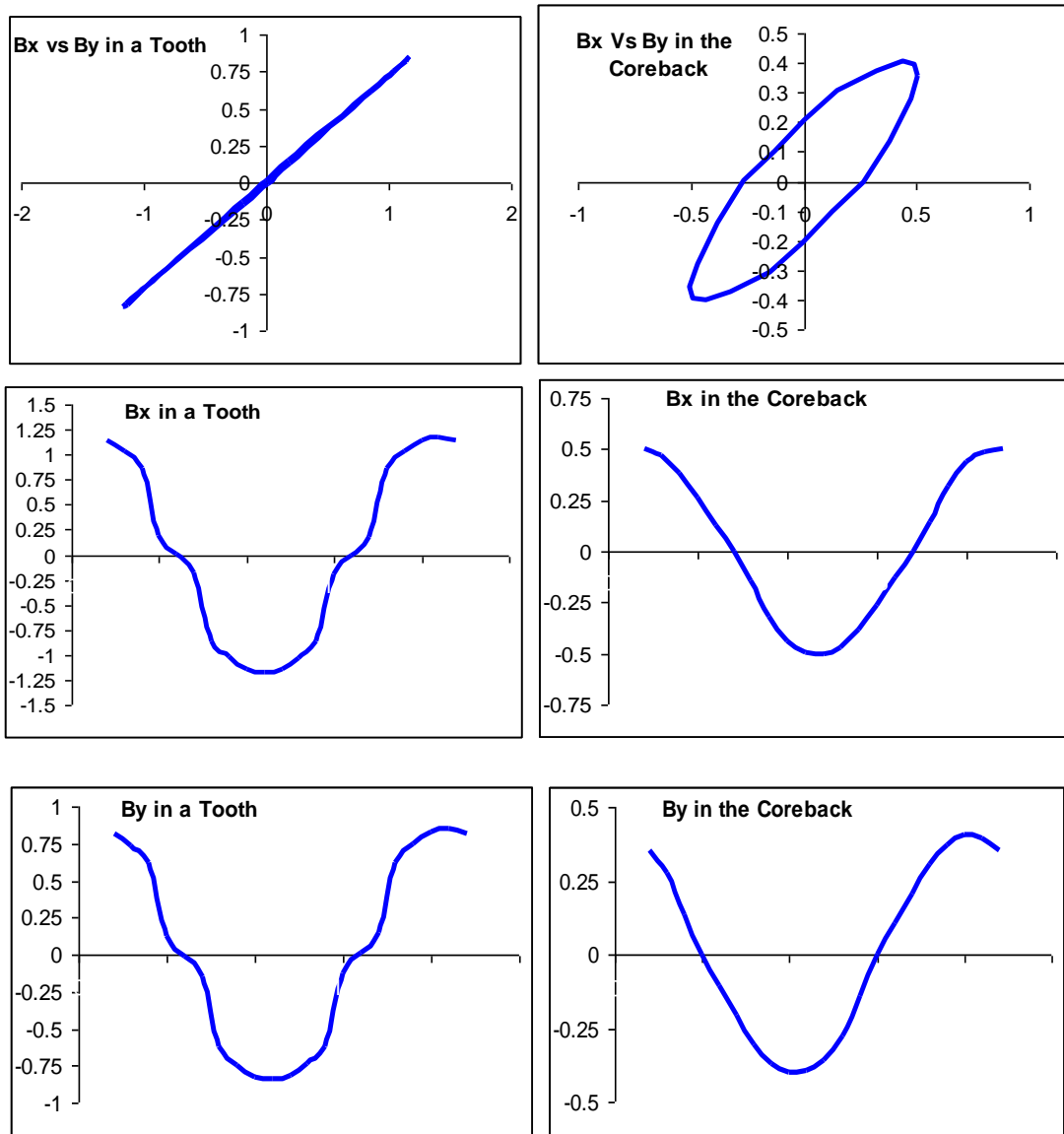


Figure 115- Flux graphs showing a 2D flux vector decomposed into Cartesian charts for both a point in the tooth and a point in the coreback of a machine. [All units in Tesla]

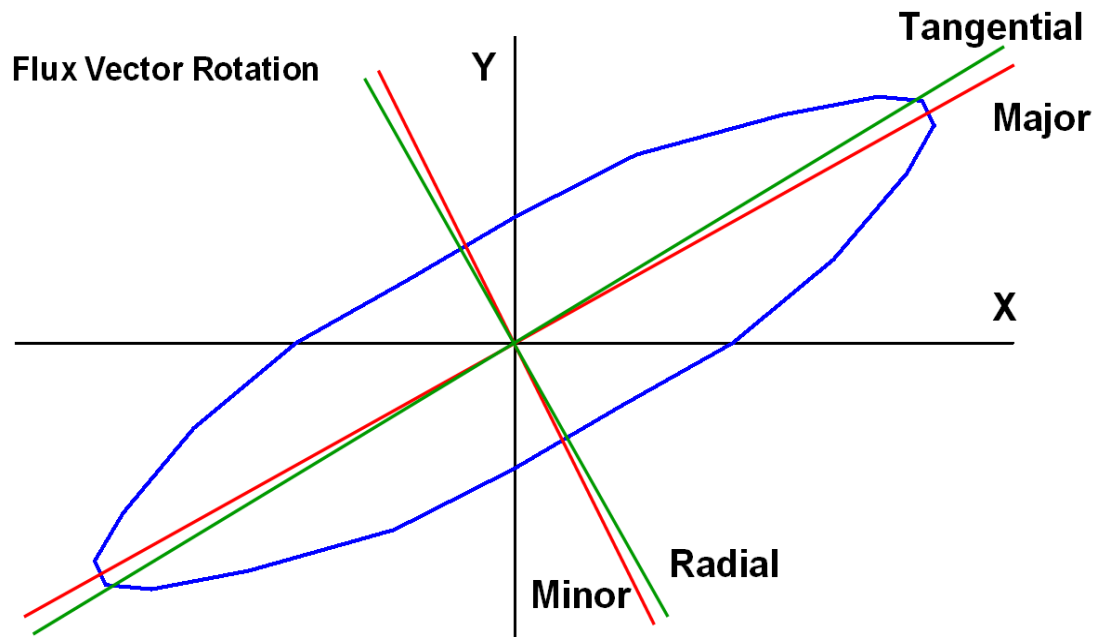


Figure 116- A diagrammatic representation of potential calculation axes

7.5. Alternative Calculations

Several authors have used variations on equations (7.1)-(7.10) for their loss calculations. Ma et al [60], Nam et al [51][61] and Smith et al [62] have used the frequency based approach in (7.1)-(7.4) but have neglected the anomalous loss term, P_a . Similarly Seo et al [63] use the same model within the time domain [equations (7.8) and (7.10)] but use functional fifth order polynomial coefficients for K_e and K_h and make $\alpha = 2$ in order to include the excess (anomalous) loss within the eddy current loss term. Additionally some authors include the effect of minor hysteresis loop magnetisation. This has not been investigated, as test plots at several locations have not shown the magnitude of any minor loops to be significant and the required finite element step size to investigate this phenomenon would render any method too slow for use within an industrial design environment.

7.6. Summary of Methods

Below is a table summarising the different methods authors have chosen to use for the calculation of Iron Loss.

		Eddy + Hysteresis + Anomalous		Eddy + Hysteresis	
		Frequency	Time	Frequency	Time
Orthogonal components	Sum Losses	[49]	[52][53][54][58]	[56][60] [62][63]	[64][63]
	Use $ B $			[57][65]	
	Unknown	[46][47][66]	[55][67]	[48][50] [51][61]	

7.7. Use of Pseudo Rotating Superposition (PRS)

The periodic symmetry of a machine around each slot has been used to allow rapid calculation of total harmonic distortion [68]. The PRS method can be used to create element by element flux waveforms for complete cycles, using simulations where rotation is over only a single slot, provided the mesh maintains rotational symmetry as shown in Figure 117. The elements in the first slot of a machine will have the same properties as the elements in the second slot when the rotor has rotated 1 slot. Very careful construction of the mesh must be addressed when the machine is drawn in order to guarantee the rotational symmetry of the mesh. For example, all the regions in Figure 117 have 4 sides and use a quadrilateral mesh generator, which results in a rotationally symmetric mesh. Even if the regions had 4 sides, but a polygonal or triangular meshing routine was used, the mesh would not have rotational symmetry and hence the nodal values used in the PRS method will not correspond. This would add an error into all calculations and completely invalidate the method. For example Figure 118 shows a triangular mesh that upon first inspection seems to be rotationally symmetrical, yet a closer analysis finds that the nodes move. The movement is accentuated the further

around the machine is inspected. Figure 119 shows the slot mesh detail of same machine where in two adjacent slots the mesh is completely different.

When using a regular mesh from a single static simulation of two poles a whole cycle of flux for any element can be created containing as many points as there are slots. By using a rotating machine solver within the FE many steps can be made over a single slot and hence the resolution of the waveform increased. This allows detailed waveforms to be created in relatively short periods of time. The PRS method could be used to find full waveforms and calculate Fourier series via equations (7.2)-(7.4). However this is slow and a more efficient method is to include equations (7.8)-(7.10) within the FE code and calculate total losses as a continual sum. As average losses are being considered in equations (7.8)-(7.10), the PRS method can be further simplified by solving over 1 slot and, rather than creating full waveforms for each element, summing all slots in a pole pair to yield the average for a single slot for a whole period. This negates having to manage data for all elements in all slots, manipulate the data and perform calculations on each elemental trace. It therefore ultimately makes the whole process easier and quicker, whilst maintaining the same level of accuracy.

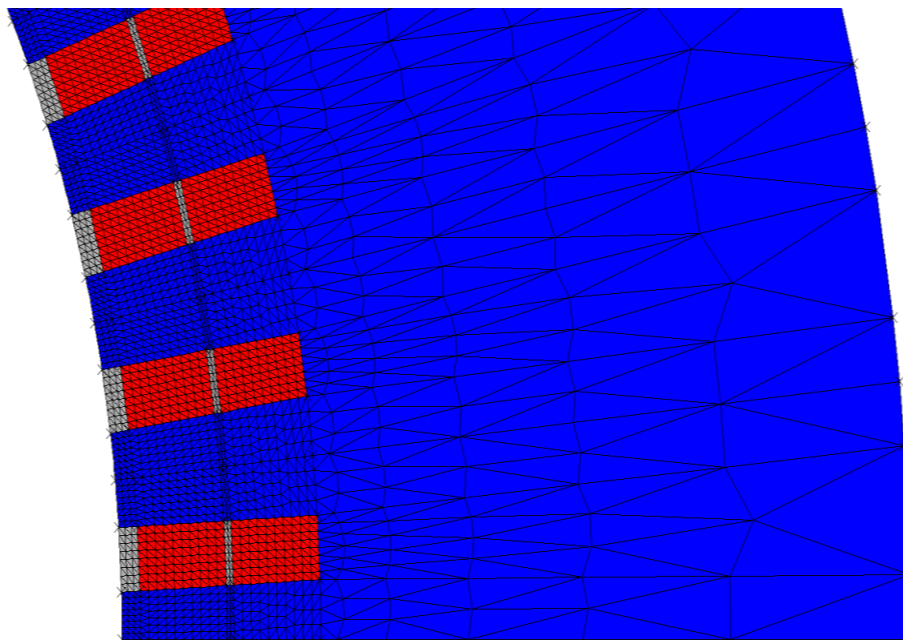


Figure 117 - A rotationally symmetrical mesh allows solution over a single slot to yield full machine data

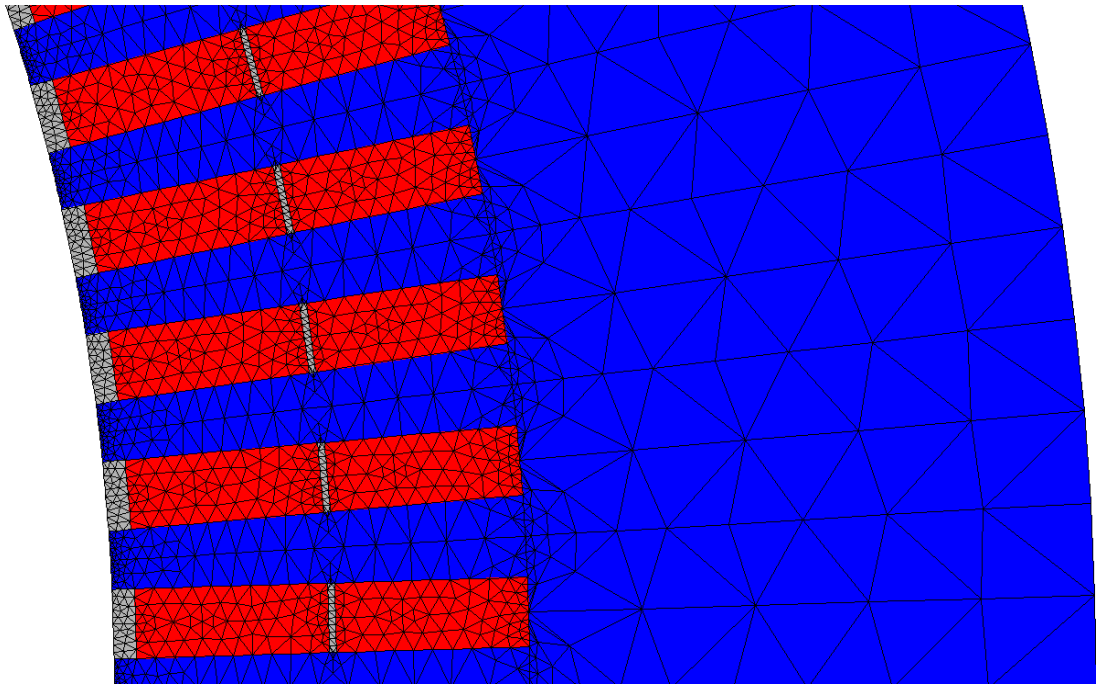


Figure 118 - A non-rotationally symmetric mesh.

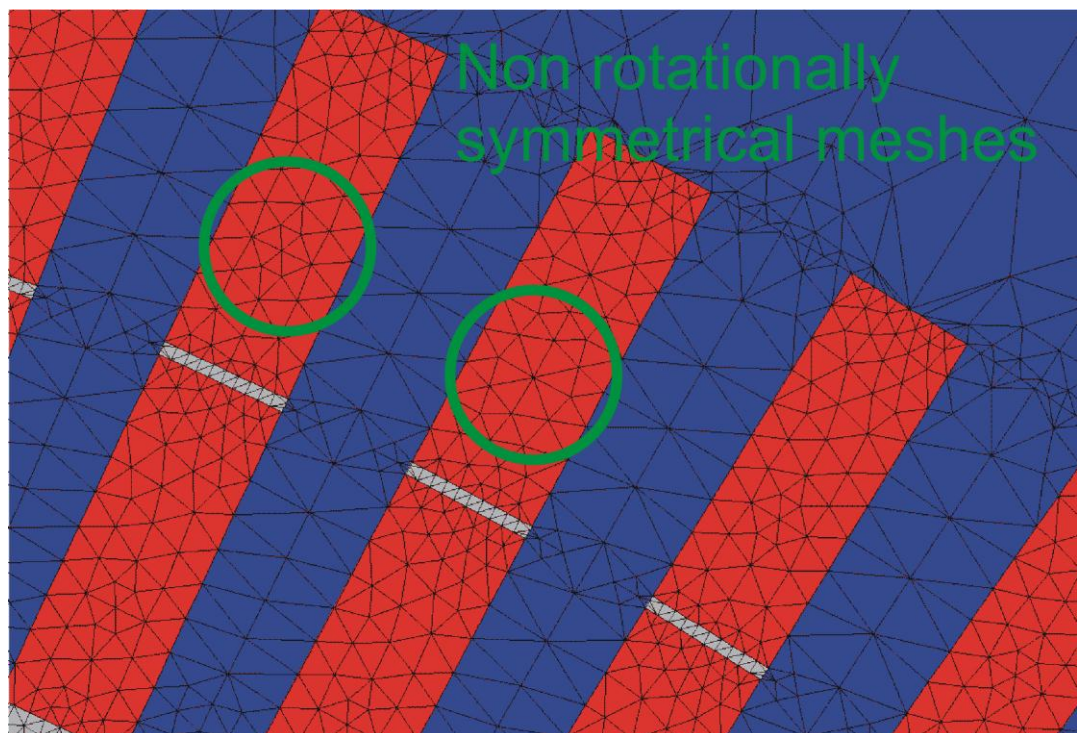


Figure 119 - Detail of the conductor mesh showing non-rotational uniformity

7.8. Determination of Constants

Loss curves for materials at various frequencies are often supplied by manufacturers [69]. These curves showing the losses at various frequencies and levels of magnetisation are used via a curve fitting method to find the various constants for the loss equations.

Equations (7.1)-(7.4) have been curve fit using a genetic algorithm (GA) with a fitness function based upon average coefficient of determination R^2 to gain the most accurate fit. The constant Ke can be approximated from the material properties, as defined in equation (7.14). This allows the curve fit to have either 3 or 4 variables. In the 3 variable case the variables for the curve fit are: the hysteresis loss constant (Kh) and the anomalous loss constants (Ka and α). The Eddy current loss (Ke) constant is calculated. In the 4 variable curve fit all of the constants Kh , Ka , α and Ke can be changed by the genetic algorithm. Figure 120 and Figure 121 show the curve fit data. Methods using alternate equations must have the loss curves fitted using their own characteristic equations in order to be valid and likewise can be fitted using GA and coefficient of determination. A summary of the coefficient of determination results can be seen in Figure 122. The table in Figure 123 give the calculated constant values

$$Ke = \frac{\gamma \pi^2 t^2}{6\delta} = 1.414 \times 10^{-4} \dots (7.14)$$

$$\text{where: } \gamma = \text{conductivity} = \frac{1}{3.8 \times 10^{-7}} \text{ S/m}$$

$$t = \text{lamination thickness} = 0.5 \text{ mm}$$

$$\delta = \text{density} = 7650 \text{ kg/m}^3$$

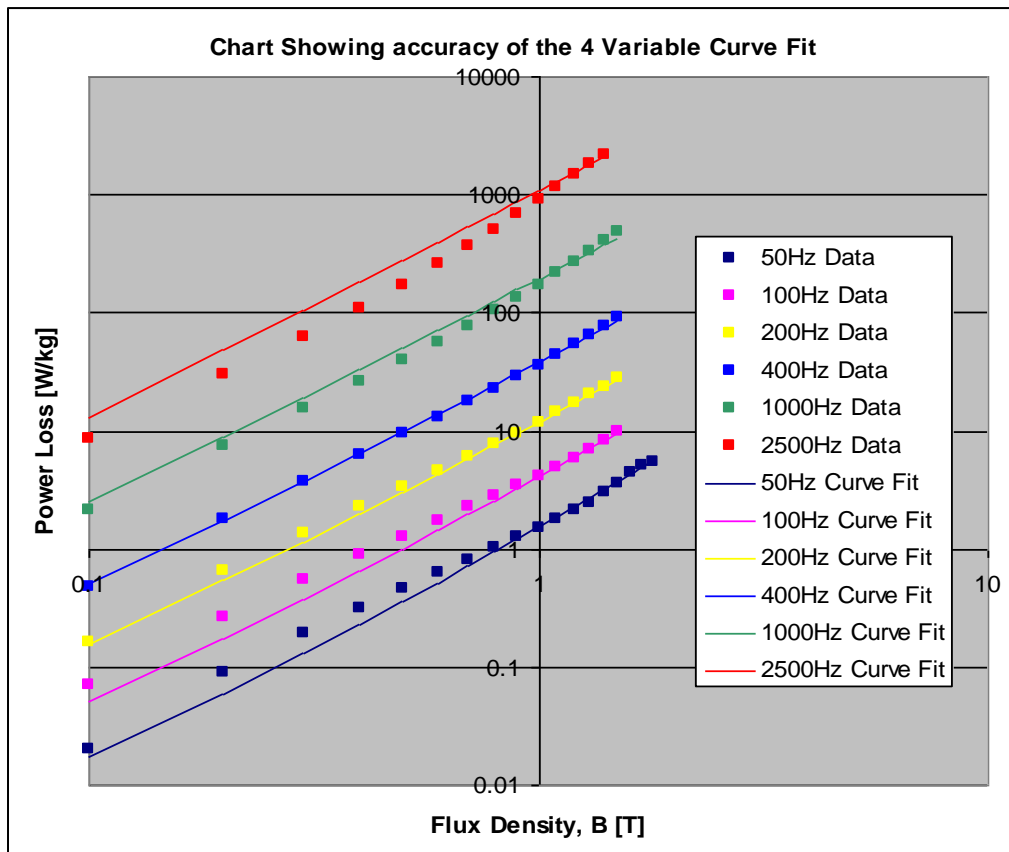


Figure 120 - Four Variable Curve fit for M400-50 grade material

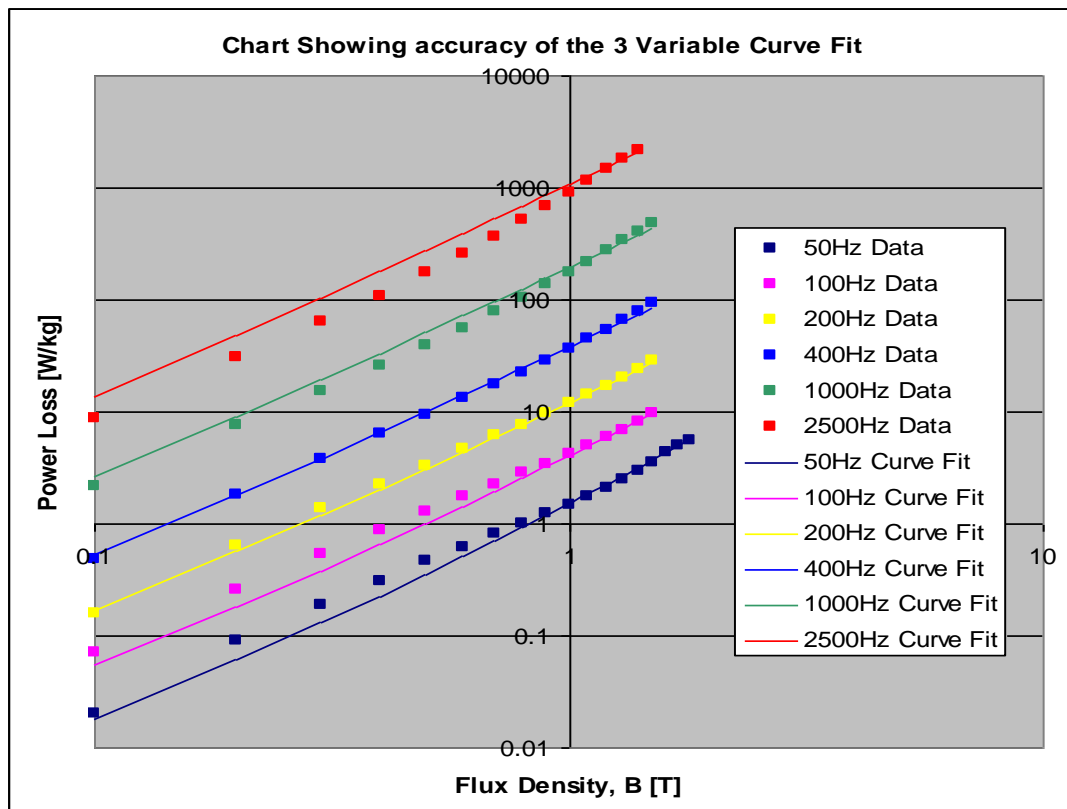


Figure 121 - Three Variable Curve fit for M400-50 grade material

	3 Variable	4 Variable
50hz	0.9952	0.9945
100hz	0.9959	0.9958
200hz	0.9988	0.9985
400hz	0.9942	0.9938
1000hz	0.9791	0.9794
2500hz	0.9710	0.9710
Average	0.9890	0.9888

Figure 122 - R squared Value Comparison for 3 and 4 variable curve fit.

	3 Variable	4 Variable
Ke	0.000141	0.000145
Ka	0.001165	0.000998
Kh	0.014763	0.016293
α	2.64688	2.529451

Figure 123 - Calculated Constant Values

7.9. The metre cube

Loss curves supplied by manufacturers [69] are measured with a standard method, which is used to define the grade of a material. The material grades as described in DIN EN 10106 describe the loss in a cubic metre of material when a uniaxial sinusoidal field is applied, which creates a flux density of peak value 1.5T at 50Hz. An electrical steel described as M400-50A will be 0.5mm thick and have 4W/kg loss under the test field conditions. These defined conditions allow a very quick and simple condition to be simulated and hence methods examined under a controlled situation. As a result the iron loss within an ideal 1m cube of iron has been calculated when all the elements within the block were experiencing the same alternating field, as depicted in Figure 124. The block is then rotated through 360 degrees around the z axis, keeping the field constant with respect to the block. The loss calculated using different orthogonal components at various positions throughout the rotation is plotted in Figure 125.

The Loss is found not to be constant when calculated using Cartesian components. This is a result of the anomalous loss term in each axis being raised to the power of 1.5 before being summed. With Eddy current losses the power raised is 2 and hence it is

immune to the rotation discrepancy. As Hysteresis losses are calculated from the peak induction [49] the maximum value, which is non axis dependant and does not suffer any rotational problems, is used. It is suggested that this discrepancy is the reason many people calculate loss without the anomalous component. Using major and minor loops the loss is constant and hence is a far more robust methodology to use in machines which are non-linear. The calculated loss using the major/minor loop axes is 3.78W/kg, which is below the maximum 4W/kg stated in the standard, indicating that the methods and curve fitting are correct.

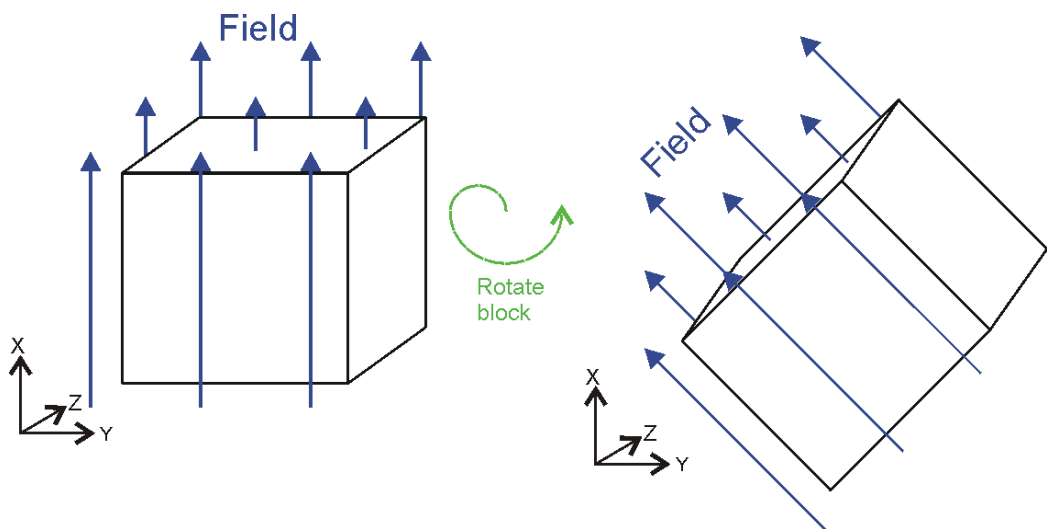


Figure 124 - Diagram showing the rotation of the 1m³ test sample

Losses Calculated Using Different Orthogonal Components

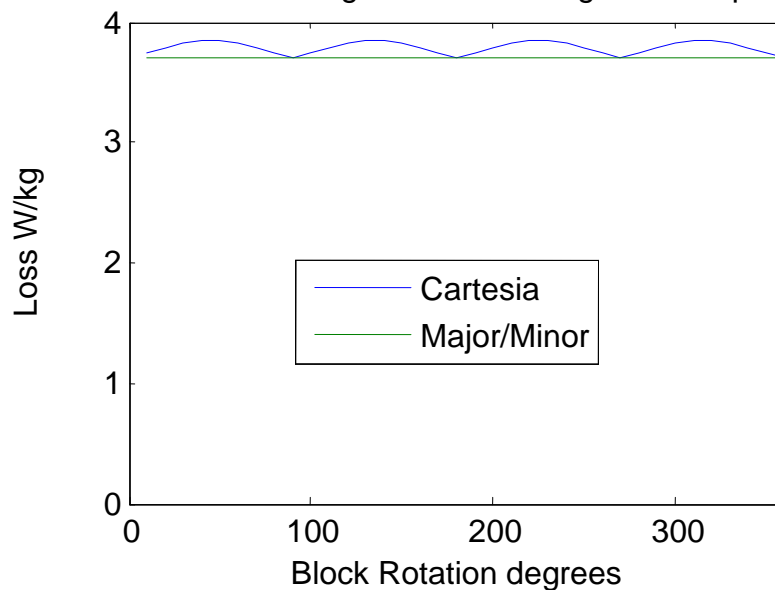


Figure 125 - Calculated losses in the 1m³ using different orthogonal components

7.10. The machine

Iron loss within a 17.5MVA synchronous generator has been calculated using several methods. The Major/Minor Loop and Radial/Tangential orthogonal axis systems have both been considered as well as methods with and without the anomalous loss components. From Figure 126, showing the loss calculated in the machine via different methods, it can be seen that methods do not vary widely. There is less than 1% average difference between methods, with peak elemental differences at just over 4%. This similarity can be easily attributed to the fact that the Major/Minor axes often lie in line with the Radial/Tangential ones. For example, within a tooth almost all flux is radial, where as in the core back the significant direction is tangential. The major discrepancies occur at the root of the teeth, where the flux is transitioning between the radial and tangential positions, hence placing the angle of the major axis somewhere in between the two. The error in this area can clearly be seen in Figure 127 where the elements have been shaded to show the difference between the Radial/Tangential and Major/Minor methods. In the core back and the tooth bodies the elements are mainly green showing near zero percentage difference. At the base of the teeth where it is expected there is a discrepancy the elements are blue showing almost -5% difference between the two methods.

Calculating the Loss using the finite element package can be divided into 3 procedures: pre-processing, solving and post-processing. The First two procedures are common to both methods and took in total 20 minutes. The time for the post-processing varies depending upon the method selected. Calculating the major/minor axis is computationally intense as it involves inspecting every element's complete vector locus to find the axis angle before applying the rotation transform. The radial/tangential method can have any transforms applied directly as the axis angle is found using the coordinates of the axis. For the examined machine the radial/tangential method took 6 minutes to calculate, whereas the major/minor loop calculation took 40 minutes. The excessive post processing time within the major/minor loop method yields an answer which is less than 1% different to the quicker radial/tangential method. This leads to the conclusion that within an integrated design package the use of the radial/tangential method is the better compromise.

Loss W/kg								% difference in Loss			
Major/Minor				Radial/Tangential							
Eddy + Hysteresis + Anomalous		Eddy + Hysteresis		Eddy + Hysteresis + Anomalous		Eddy + Hysteresis		Eddy + Hysteresis + Anomalous		Eddy + Hysteresis	
Core back	Tooth	Core back	Tooth	Core back	Tooth	Core back	Tooth	Core back	Tooth	Core back	Tooth
0.691	3.207	0.513	2.668	0.692	3.205	0.514	2.666	-0.135%	0.049%	-0.138%	0.075%

Figure 126 - Table showing the calculated loss in a 17.5MW machine using various methods.

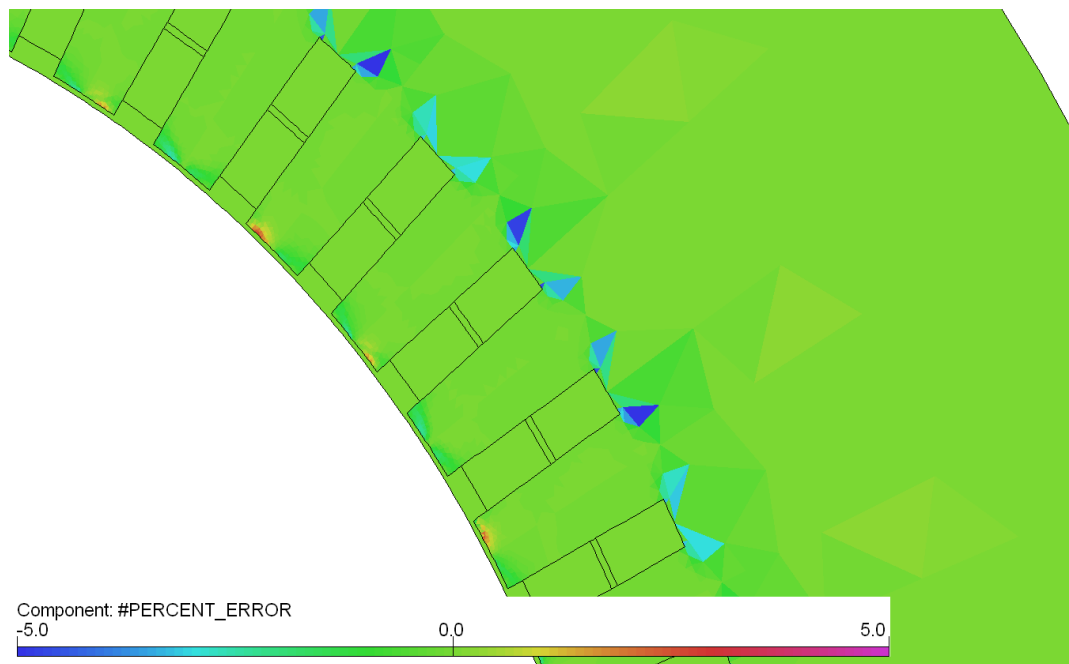


Figure 127 - Diagram showing the individual elemental percentage differences between the Radial/Tangential and the Major/Minor loop methods.

7.11. Comparison To Test Results

The radial/tangential method has been implemented within a design system to allow systematic simulation and comparison to test results of machines. Forty six synchronous generators, with rating of 5 to 20 MVA, have been compared to test results acquired during factory tests to IEEE STD 115-1995. The test setup involves measuring field and rotor voltages and currents on the test machine, as well as the driving motor, and running them under a variety of open and closed circuit conditions, allowing the iron loss to be found exclusive of any windage, friction or resistive losses. The machines are all four pole wound field synchronous generators, which are one of three different frame

sizes but are of various axial lengths. They are of a range of different ratings and of either 50Hz or 60Hz synchronous frequency. For each machine a design factor is calculated which is defined in equation (7.15). The results for the machines yield an average design factor of 1.71 and the series can be seen in Figure 128.

$$\text{Design Factor} = \frac{\text{Test Result}}{\text{Design Result}} \quad \dots (7.15)$$

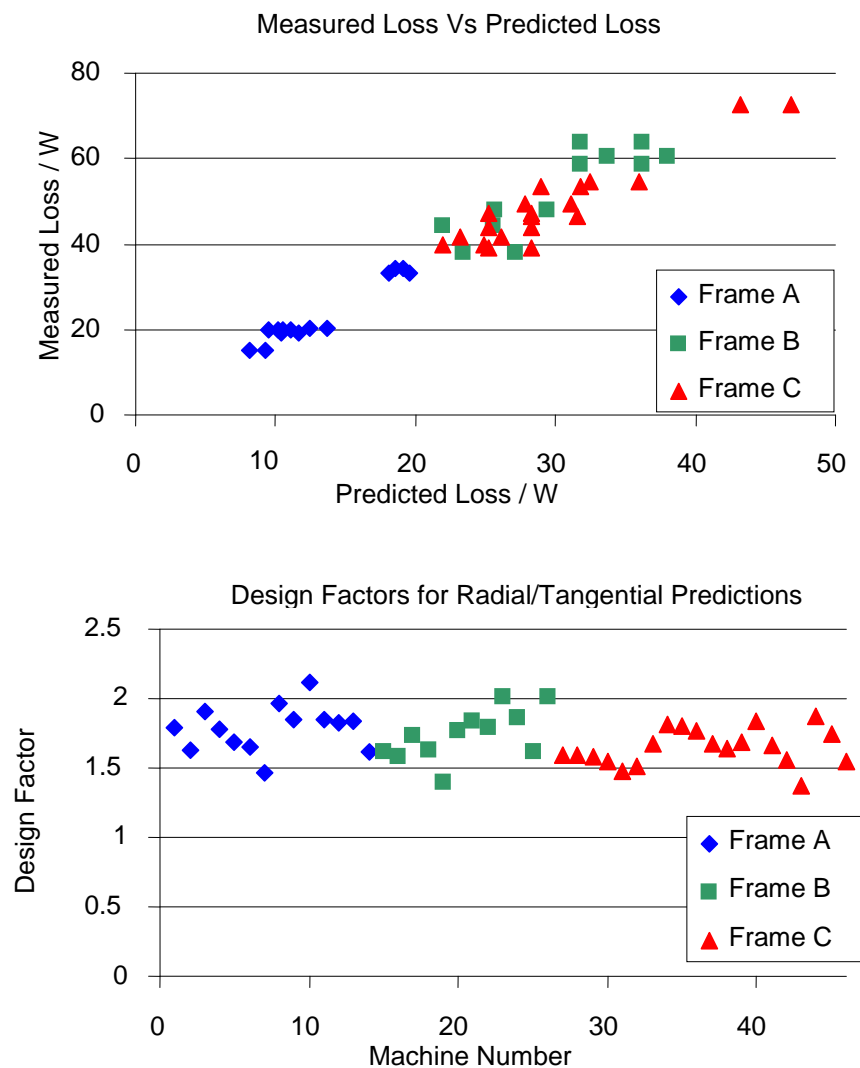


Figure 128 - Comparison of Test Results and Predictions.

It is accepted practise for large synchronous machines to have a design factor associated with them. The design factor exists as a method of accounting for the effect of a myriad of design and manufacturing processes, each of which adds unaccounted loss. Magnetic steel lamination manufacturers conduct Epstein tests upon steel before it has been

through the electrical machine factory manufacturing process, and consequently each process and material handling alters the laminations crystalline structure, increasing losses. The major sources of this process loss include the lamination stamping, where shear stress is elevated at edges, and brazing or welding which often occurs along the machine corebacks to maintain structural integrity (as can be seen in Figure 129). Additionally the Core undergoes Vacuum Pressure Impregnation (VPI) to coat the core and conductors in resin. After this process the stator core is cured in a large oven for several hours adding a thermal cycle to the steel. The design process uses a 2D analysis and assumes the machine is consistent along its axial length, whereas in reality machines are not constant. For example they have radial cooling ducts and end plates which will again alter the loss.



Figure 129- Several multi-megawatt generators at various stages of construction

The difference between individual machines is clearly highlighted in a series of three identical machines which were constructed in the same manner, to the same standard, yet the iron loss test results show a variance of 21%, with individual results of 47.2kW, 44.0kW and 38.9kW. This variance, although large at a macro level, is acceptable in comparison to the 15MVA full load rating of the machine. The size of the frame has little effect, with the each of the 3 frame sizes having respective averages of 1.78, 1.73 and 1.64. The smaller machines - Frame A - have the largest design factor and the larger machines of Frame C have lower design factors. As the stamping of laminations alters properties of the material close to the edges, the ratio of the edge area steel to non edge area steel will affect the design factor. Naturally this ratio will be higher in smaller machines, confirming the hypothesis that the more manufacturing the less accurate any predictions will be. This study only compares 3 frame sizes and shouldn't be extrapolated to machines of vastly different types without more study. However the general rule of "more manufacturing processes equals more iron loss" still holds weight.

7.12. Chapter Summary

This chapter compares several different methods of calculating iron loss from FE flux density plots. The chapter investigates both time and frequency methods and looks at the effects of alternate orthogonal component calculation methodology including: Cartesian, Radial/Tangential and Major/Minor Loop. By examining both an ideal 1m³ block, an actual synchronous generator and a series of forty six synchronous generators the main conclusions of the chapter are as follows:

- Loss Calculation in the Cartesian plane should not be used as it does not give geometry independent consistent solutions.
- The loss in accuracy in using a Radial/Tangential method compared to the Major/Minor Loop method, is typically less than 4%, yet the post processing calculation time was found to be around 6 times quicker. It is a good engineering compromise which can be easily incorporated into a design package.
- The capabilities of curve fitting routines, loss curves accuracies and material handling during manufacture can add larger inaccuracies than the method of loss calculations.

Chapter 8. Conclusions

The aim of this work has been to develop a fully integrated, simulation tool for synchronous generators. The tool is PC based and uses both Finite Element and arithmetic methods. It contains several sub modules allowing calculation of various parameters including saturation curves, voltage distortion, transient parameters and iron loss. Input is via a parametric data input allowing the tool to accommodate a range of machine sizes. The main software used is Vector Fields Opera 2D Finite Element software in conjunction with MALAB for data processing and handling.

The results have been compared to existing factory test results and compared to the existing design system, E.D.S. The results from this process have shown that across the board that the system is better than E.D.S. in terms of accuracy. Where the system has had limited success the deviation from the zero error is acceptable or below measurable tolerances. Initially machine saturation curves are created by using static finite element simulations and a Pseudo Rotating Superposition (PRS) system. Open circuit and zero power factor saturation curves are shown to be significantly more accurate than E.D.S. but E.D.S. has a better prediction of the short circuit curve. This is because EDS has been tuned to the unsaturated linear short circuit case whereas the FE methods are generic. The transient machine parameters are examined next and again use PRS as well as a separate rotating FE solution. The finite element methods employed are again an improvement on E.D.S. in terms of accuracy - in many cases being more than 35% more accurate. The FE struggles on its final parameter calculation - t''_d - because the actual numerical value is small, therefore a small absolute error gives a seemingly large percentage error.

To calculate the full load operating point both the Potier method and a novel FE optimisation routine are used. The Potier is more accurate because of the accurate saturation curves. The FE routine benefits from the use of static simulations and PRS, but it is the multivariable cluster optimisation that allows the method to be implemented within the desired time frame. All together these methods reduce the mean absolute percentile error from 6.68% for E.D.S. to just 1.97% for the FE system.

Open circuit waveform harmonics are predicted by using a rotating version of the PRS system. This allows the FE package to manage any induced currents and high order

harmonics to be validly found. The method is found to be about 25 times quicker than existing FE methods and 55% more accurate than E.D.S.

In the Final chapter Iron losses within a generator are investigated. A broad literature search finds many methods including ones using Eddy current, Hysteresis and the optional Anomalous Loss. The differences between Cartesian, Radial/Tangential and Major/Minor loops are discussed, as well as the method of summing the different axis losses. Through demonstration using a theoretical cubic meter of iron it is shown that Cartesian components mustn't be used. Calculations on several machines show that a design factor of 1.7 is required for this size of machine and that the Radial/Tangential method only loses 4% accuracy, yet is 6 times quicker. It is also discussed that the capabilities of curve fitting routines, loss curves accuracies and material handling during manufacture can add larger inaccuracies than the method of loss calculations

8.1. Summary of Errors

Throughout the methods created are compared to the existing design system - EDS. The proposed system is shown to be on average far more accurate than EDS. Below Figure 130 shows a summary table showing an overall comparison between the 2 systems.

	Mean Absolute Percentage Error Vs Factory Test Results	
	FE Method	EDS Method
Open Circuit Saturation Curve @ 1pu	2.22%	5.07%
Open Circuit Saturation Curve @ 0.5pu	3.82%	7.01%
Sustained Short Circuit Curve @ 1pu	1.28%	0.78%
Zero Power Factor @ 1pu	5.55%	8.32%
Transient Reactance X'_d	16.06%	27.30%
Subtransient Reactance X''_d	2.83%	8.10%
Transient Time Constant t'_d	17.49%	26.49%
Subtransient Time Constant t''_d	48.69%	29.65%
Full Load Field Current	1.97%	6.68%
Total Harmonic Distortion	6.46%	14.67%

Figure 130 - Table showing a summary of errors for the created FE methods and the existing EDS system

8.2. Contributions to Knowledge

This thesis has advanced knowledge in two significant areas. Firstly the introduction of novel modelling techniques and integration of methods to make a finite element based design program feasible. These methods include:

- The use of Pseudo Rotating Superposition from static models which minimises simulation times when calculating waveform fundamentals.
- Rotating Pseudo Rotating Superposition solved using a rotating solver over 1 stator slot which gives higher order harmonics including those influenced by induced damper bar and field winding currents.
- Use of axial simulations to calculate effective axial lengths
- Selective static boundary placement combined with rotating simulation to give transient parameters
- Integration of end winding calculations, B-H Dilution and several curve fitting techniques to reduce solution time and improve accuracy.

Secondly, knowledge has been gained as a consequence of the application of the above techniques. This knowledge includes:

- The positioning of individual conductors in slots is insignificant allowing the use of a single homogenous region when using FE simulations.
- The effective axial length is typical equal to axial length plus 2.3 to 2.5 times the radial air gap length per end. This is to account for axial flux fringing at the air gap.
- To minimise voltage distortion the placement of damper bars should be at the same pitch as stator teeth. The rotor pole width should be an integer number of stator slots wide when flux fringing is accounted for. Shaping of the pole face will create additional fringing complicating results.
- Rotating rectifiers add negligible ripple to the field current.
- Iron Loss can be calculated with FE but requires the correct plane of orientation. The Cartesian coordinate plane should not be used but the Radial/Tangential plane gives comparable results to the Major/Minor Loops with a significant reduction in calculation time.

-
- The stamping of laminations and mechanical handling creates significant loss often greater than the error associated with the method of loss calculation. This extra loss is often accounted for by use of a single design factor found for this size of synchronous machine to be 1.71

Additionally the extensive comparison between factory test results and the predicted results has also served as a highly valuable validation of the tools.

8.3. Limitations

The limitations of this work can be divided into two broad categories - Program Limitations and Fundamental Limitations. The program limitations concern the physical programming limitations of the system - the automated process handling and user interface. The Fundamental Limitations are to do with the theoretical limits imposed by the methods used. These limitations lead into some obvious areas that could be considered for further study.

8.3.1. Programming Limitations

The FE software used Cobham Vector Fields Opera 2D has 2 major limitations that could have potentially created a much better system:

- The lack of adaptive meshing has forced meshes to potentially be over complicated and hence slower to solve.
- The uneditable source code means that the direct on load FE solving method created by Brandl, Reichart and Voght could not be implemented.

The whole suite is coded in 2 different languages - MATLAB M-code and a code native to the FE software, a FORTRAN derivative. This leads to some very specific program limitations, for example the programming root folder cannot have spaces in any of the names, as the FE software code views a space as a phrase termination. Although minor, this caused many hours of problems with Windows based PCs and the default 'My Documents' folder. Additionally the FE software is non-case sensitive but MATLAB is. The FE software only allows variables to have up to 13 characters limiting naming conventions between programs. Finally the biggest limitation of the FE software is the

inability to use any form of array variables. This leads to variables which are given names with numbers such as `Id_01_01` and `Id_01_02` etc. This creates burdensome programming routines transferring lists of variables into MATLAB matrixes and back again. It is highly likely that these specific coding nuances could be solved by the adoption of a different FE software package.

The system is coded specifically for generators that follow a specific building convention, including and not limited to:

- The machines must have salient poles with wound fields.
- They must have 4 core studs and 2 core bars.
- The rotor pole faces must have a single face radius and a single corner radius.
- The stator must have a non fractionally wound winding that is of double layer lapped construction.
- The conductors must be rectangular in cross section and made of copper.

These program limitations shouldn't actually limit the processes and calculations that the system does. For example, if time was spent designing a new section of code that does 5 or 4 core studs the rest of the code would remain unaffected and should function perfectly. Some additional machines may be made to work without doing any re-coding and results would be approximately correct. For example, a solid pole (i.e. non-laminated) rotor could be simulated by putting an axial length in that is $\frac{1}{0.97}$ times longer to trick the B-H curve dilution routine to simulate using the correct, in effect unaltered, material curve. This incorrect additional length would alter several other variables and hence it is suggested this not undertaken.

8.3.2. Fundamental Limitations

The system is an electromagnetic system design tool and hence does not do any mechanical calculations. Although a fundamental limitation, it is arguable that mechanical calculations would be outside of the scope of this project. Similarly, calculation of thermal performance would be highly desirable.

One major limitation is the calculation of total losses. Chapter 7 deals with the calculation of Iron loss on no load or open circuit. To calculate efficiencies and overall system performance the losses for the rest of the machine must also be known. This would include:

- Stator copper loss
- Rotor copper loss
- Bearing losses
- Fan losses
- Iron loss on load
- Windage
- Exciter losses
- Damper bar copper loss

Several of these are mechanical losses and would require calculation, probably by use of a characteristic equation or look up table. The stator copper losses could be found using the machine's resistance calculated from copper dimensions and the current flowing whilst running on full load. An estimation of the length of the end windings, as calculated in Chapter 5, combined with the axial length should give a fairly accurate length of turn from which the I^2R loss could be found. The rotor field winding current and resistance are also known, so again the loss shouldn't pose problems. The damper bar copper loss currently isn't calculated and, although likely to be fairly small, it could be found by a couple of methods. The Finite Element software could be used to monitor the current in each bar and hence, from a calculated resistance, the loss could be found. Alternatively the bars could be given a conductivity and the loss calculated directly using the current density and the conductivity at every time step ($J^2\sigma$).

The calculation of iron loss on load currently is not done. This is probably the most complicated of the electromagnetic losses to be found. The loss on load will contain more harmonics because of the stator current that is flowing and therefore the loss is likely to be higher and hence is essential for efficiency calculations. The calculation is more complicated as it is probable than the axis that the flux rotates around will have varied from the radial/tangential axis. Also there will be additional induced harmonics in the rotor pole face creating additional flux perturbations and hence more iron loss. The axis will have moved because when on load the flux is skewed across from the D

axis towards the Q axis as the load angle increases. Hence the major/minor loop method must be used which is considerably slower. Also as the machine will have current flowing the slot current density magnitudes must change with the rotor position meaning the static simulations must each be excited individually - probably using a combination of Park and Clark transformations. The use of a loss calculation which includes the anomalous loss term complicates the calculation and as shown in section 7.6 some authors do not include this term. An investigation of the merit of removing the anomalous term in favour of a simpler system would be worth further study.

The thermal performance and temperature rises of windings is essential for a complete design. The designer must know the limit that the machine can be driven to before the windings overheat and suffer insulation breakdown. The lack of any temperature rise calculations means the system is effectively not closed loop. An engineer can get the performance of the machine but does not know whether the machine is efficiently using the materials or whether they can reduce the size of the machine.

8.4. Further work

The limitations of the work highlight the need for additional modules. Many of the additional modules are in parallel engineering disciplines and would need significant input from additional specialist engineers. This could potentially create a holistic design system which would need a lower skill but wider specialism engineer to operate. Supplementary modules could include:

- Mechanical losses: To calculate the drag of the fans, windage and bearing losses. Probably through a characteristic equation or look up table.
- Thermal module: To calculate the operating temperatures of the windings. This could either be a plug in thermal FE system or a nodal network fed by the losses calculated by electromagnetic FE.
- Computational Fluid Dynamics: calculation of the airflow circuit within the machine could be undertaken
- Mechanical: Lamination dimensions could be tweaked to reduce the quantity of steel but this in turn would require a mechanical stress analysis. Additionally the placement of damper bars alter the stress patterns

- Cost Estimation: A module that calculates quantities of steel, copper and the size of various structural support studs and bars would be invaluable during the tendering process.

The PRS system has been shown to be a useful tool for quickly identifying synchronous machine parameters, without having to complete a fully rotating FE simulation. This method could easily be developed into a system for other types of machines. Indeed, as this piece of work is drawn to a close, the sponsoring company has already started to develop the system into a Permanent Magnet Generator design system. Specifically the exact system used in Chapter 6 could be used for performing open circuit waveform analysis on a permanent magnet wind turbine generator for example.

Additionally it is postulated that the full load calculation from Chapter 5 could be easily transcribed to work for a permanent magnet generator. Potentially for a permanent magnet generator it would be an easier system as there is no field current to vary and therefore one less variable. Similarly, specifically for permanent magnet machines, the direct and quadrature reactances (X_d and X_q) are usually requested by the customer. Work calculating the D and Q axis reactances using FE simulations have been carried out [70][71]. Using static simulations at a single position yields results for machines with a high number of slots per pole but, as the number of slots decreases, a system such as used in Chapter 6 must be used. This is because the slotting harmonics become a higher order and add relatively larger errors to the fundamental. It is also speculated that the DQ parameters vary with rotor position (due to harmonics) if a single static simulation is used. Furthermore it is also suggested that for very low slots per phase (such as direct drive wind turbines) and when the machine is on load, the system may have to model the symmetry of a phase rather than of a slot. A full investigation of the DQ parameter calculations with a comparison to manufactured machine test results would be an excellent continuation of this work.

An investigation of the optimum design for solid pole synchronous rotors from a THD point of view may also be an interesting additional scheme of work. The same systems could be used as in this thesis but, as solid pole generators do not have damper bars, the rotor design could only be modified by changing the shape of the pole face. Additionally the pole shoe would have to be given a conductivity as the whole shoe, not

being laminated, acts as one large conductor. This in itself may prove complex as a non-electrical high tensile steel is often used and in such cases the steel manufacturer will not quote characteristic electrical properties. Solid pole rotor pole shoes are also bolted to the pole body, as shown in Figure 131. The position of holes and bolts is usually a mechanical consideration but the positioning of the holes and subsequent bolts must play a part in the electromagnetic circuit. The positioning will affect the BH curve dilution used and potentially the performance under transients. The solid pole machines can be used for line start synchronous motors. In this case the machine is brought to synchronisation by using the pole face as an induction machine at high slip, before transferring to a synchronous machine at lower slip levels. The induced currents cause I^2R heating in the pole face, which can lead to cracking of the steel. An investigation into the optimised positioning of the bolts to reduce pole face stress could also be undertaken. These studies area are potentially an area where 3D modelling both electrically, mechanically and thermally may be required, as the machine is not consistent down the axial length.

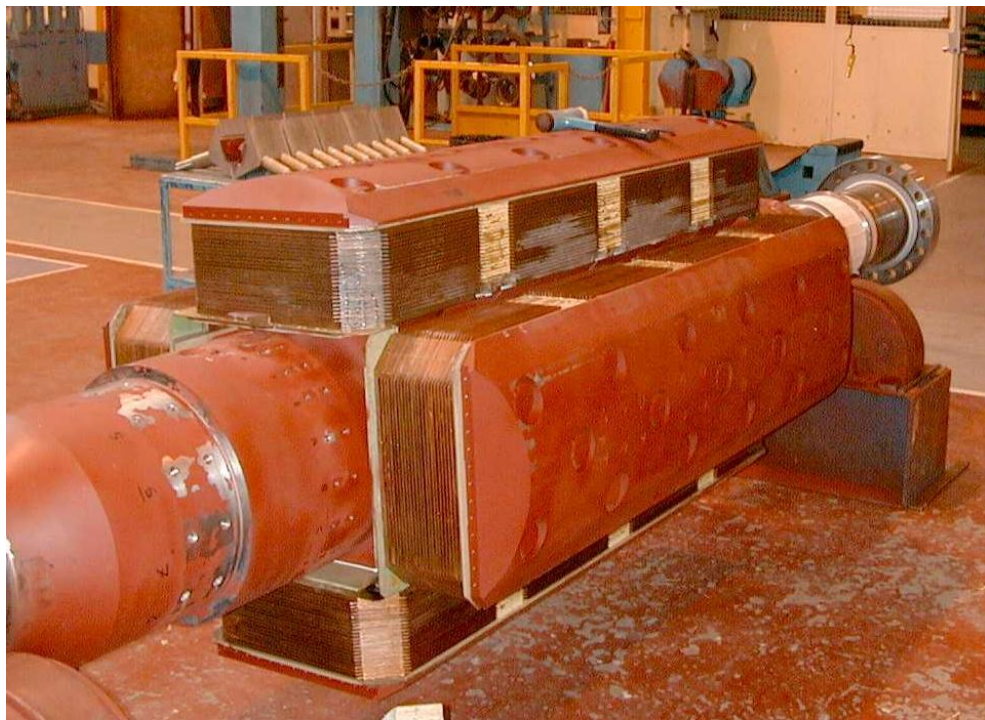


Figure 131 - A Solid pole rotor. Note the positioning of the pole face bolts

An interesting addition to the design system would be to have a closed loop machine optimiser. A system such as this could automatically take a start point from an existing design and then adapt various geometries to find a new design. This would be the best

in terms of machine optimisation but, as found in Section 6.7, this is likely to be a highly time consuming process. A highly adaptive intelligent routine would be required and would no doubt move the project into the realms of computer science rather than machine design. As a complement to the above optimisation it would also be desirable to see the system transcoded onto a cloud based computing topology. This would allow a much greater processing power and remove the need for a local high spec PC for every user. A cloud based system may also help in optimisation as certain clouds have the ability to solve many machines in parallel.

Appendix Index

A.	Open Circuit Voltage Results - 1 pu	II
B.	Open Circuit Voltage Results - 0.5 pu	III
C.	Short Circuit Current Results	IV
D.	Zero Power Factor Results	V
E.	Calculation of the End Winding Length	VI
F.	Calculation of R^2	VIII
G.	Frequency to Time Domain Transform.....	IX
H.	Graphical User Interface	XII
I.	Transferring Impedances across an Ideal transformer	XVIII
J.	T.H.F. and T.I.F. Weighting Factors.....	XIX

A. Open Circuit Voltage Results - 1 pu

Project ID	Field Current for 1pu Open Circuit Voltage			Percentage Error Vs Test	
	FE	EDS	Factory Test	FE	EDS
A145y4-P141239	109.5	109.5	105.5	3.81%	3.83%
A145a4-P141177	96.9	103.8	96.0	0.94%	8.16%
A145y4-P141179	122.9	125.0	124.0	-0.88%	0.81%
A145y4-P141203	121.1	124.7	119.0	1.80%	4.79%
A145y4-P141205	121.1	124.7	117.5	3.10%	6.13%
A145y4-P141228	101.6	102.6	102.0	-0.42%	0.59%
A145y4-P141245	109.5	109.5	113.0	-3.08%	-3.06%
A145y4-P141251	105.7	106.5	109.0	-3.05%	-2.29%
A145w4-P141230	104.4	104.1	102.3	2.09%	1.76%
A160a4-P141218	78.1	78.0	78.5	-0.51%	-0.64%
A160w4-P141224	93.7	93.4	96.1	-2.49%	-2.81%
A160b4-P141255	102.8	99.4	102.1	0.71%	-2.64%
A160c4-P141259	83.4	84.4	84.8	-1.64%	-0.47%
A160a4-P141273	83.9	84.5	84.0	-0.06%	0.60%
A160a4-P141275	100.6	100.6	101.3	-0.72%	-0.69%
A160a4-P141247 A	90.6	90.4	92.1	-1.65%	-1.88%
A160a4-P141247 B	90.6	90.4	92.4	-1.88%	-2.12%
A160a4-P141247 C	90.6	90.4	92.8	-2.32%	-2.56%
A160a4-P141249	78.6	78.3	79.4	-0.98%	-1.39%
A160a4-P141271	83.7	83.8	83.8	-0.15%	0.00%
A160e4-P141284	88.4	84.3	83.8	5.50%	0.58%
A160a4-P141139	78.8	79.1	74.4	5.95%	6.32%
A160a4-P141143	94.6	92.3	95.5	-0.96%	-3.35%
A160w4-P141145	89.1	89.6	86.3	3.30%	3.87%
A160a4-P141207	78.6	78.0	76.9	2.24%	1.43%
A132a4-P141267	91.1	97.5	94.7	-3.78%	2.96%
A132y4-P141253	90.3	97.0	92.6	-2.52%	4.75%
A132x4-P141233	102.6	109.2	106.1	-3.27%	2.92%
A132z4-P141222	90.8	96.7	88.9	2.08%	8.77%
A118u4-P141241	90.1	93.6	92.6	-2.69%	1.08%
A118u4-P141269	95.6	103.0	98.5	-2.93%	4.57%
A118q4-P141226	107.4	109.3	102.4	4.92%	6.74%
A118s4-P141183	92.9	98.6	95.2	-2.37%	3.57%
A145a4-P141181	103.6	103.5	103.2	0.35%	0.29%
A132y4-P141167	92.8	104.3	90.1	2.96%	15.76%
A118s4-P141185	97.8	105.9	98.0	-0.19%	8.07%
A118v4-P141152	113.8	128.6	111.0	2.50%	15.86%
A118t4-P141154	75.2	77.8	77.1	-2.41%	0.91%
A132y4-P141171	98.2	110.6	96.7	1.58%	14.37%
A145x4-P141132	104.4	107.1	104.6	-0.22%	2.39%
A118q4-P141134	104.2	116.4	102.8	1.36%	13.23%
T145b4-P140954	85.3	103.0	92.6	-7.87%	11.27%
A145a4-P140945	78.8	88.2	79.0	-0.30%	11.65%
S118q4-P140909.	89.2	97.0	91.8	-2.82%	5.67%
O118p4-P140911	98.4	110.6	95.9	2.63%	15.33%
S118q4-P140919	94.1	102.1	96.7	-2.65%	5.58%
O118q4-P140879	110.0	125.4	106.6	3.21%	17.64%
O118x4-P140765	98.3	105.7	98.8	-0.49%	6.98%

B. Open Circuit Voltage Results - 0.5 pu

Project ID	Field Current for 0.5 pu Open Circuit Voltage			Percentage Error Vs Test	
	FE	EDS	Factory Test	FE	EDS
A145y4-P141239	45.7	46.9	43.0	6.31%	9.16%
A145a4-P141177	43.5	45.0	43.5	0.11%	3.45%
A145y4-P141179	46.9	48.0	45.0	4.18%	6.67%
A145y4-P141203	46.9	48.0	45.0	4.14%	6.67%
A145y4-P141205	46.9	48.0	45.0	4.14%	6.67%
A145y4-P141228	45.8	47.0	46.0	-0.49%	2.17%
A145y4-P141245	45.7	46.9	44.5	2.72%	5.48%
A145y4-P141251	44.8	46.0	42.0	6.69%	9.52%
A145w4-P141230	46.6	47.8	42.5	9.70%	12.33%
A160a4-P141218	34.5	36.4	34.1	1.12%	6.73%
A160w4-P141224	39.3	41.7	36.6	7.26%	13.88%
A160b4-P141255	38.7	41.0	37.9	2.00%	7.99%
A160c4-P141259	37.1	39.4	35.8	3.57%	10.14%
A160a4-P141273	37.1	39.6	36.2	2.49%	9.49%
A160a4-P141275	40.1	42.8	38.4	4.45%	11.39%
A160a4-P141247 A	38.7	41.1	38.0	1.78%	8.07%
A160a4-P141247 B	38.7	41.1	38.7	-0.03%	6.16%
A160a4-P141247 C	38.7	41.1	40.4	-4.31%	1.61%
A160a4-P141249	34.7	36.9	33.8	2.87%	9.13%
A160a4-P141271	37.1	39.4	36.5	1.52%	7.93%
A160e4-P141284	38.3	38.2	34.1	12.49%	12.05%
A160a4-P141139	35.4	37.7	34.6	2.37%	8.93%
A160a4-P141143	38.8	41.2	39.3	-1.30%	4.78%
A160w4-P141145	37.9	40.4	40.4	-6.22%	0.00%
A160a4-P141207	34.7	37.0	33.9	2.56%	9.24%
A132a4-P141267	41.8	43.1	39.4	5.99%	9.23%
A132y4-P141253	41.5	43.0	40.4	2.89%	6.61%
A132x4-P141233	45.6	47.1	42.4	7.52%	11.09%
A132z4-P141222	41.7	43.0	38.9	7.25%	10.55%
A118u4-P141241	39.6	40.8	38.9	1.87%	5.00%
A118u4-P141269	40.7	42.1	40.7	-0.04%	3.43%
A118q4-P141226	41.6	43.5	42.4	-2.09%	2.48%
A118s4-P141183	39.7	41.3	46.3	-14.31%	-10.86%
A145a4-P141181	47.5	48.3	43.9	8.09%	9.99%
A132y4-P141167	41.6	43.2	37.0	12.38%	16.82%
A118s4-P141185	41.2	42.6	41.9	-1.69%	1.81%
A118v4-P141152	43.8	45.3	44.0	-0.57%	2.87%
A118t4-P141154	35.7	37.1	36.2	-1.61%	2.29%
A132y4-P141171	42.4	44.0	No Data	-	-
A145x4-P141132	46.1	47.6	43.5	6.05%	9.51%
A118q4-P141134	41.2	43.2	41.5	-0.67%	4.05%
T145b4-P140954	36.9	41.0	37.1	-0.66%	10.41%
A145a4-P140945	34.7	35.9	32.3	7.65%	11.41%
S118q4-P140909.	38.7	41.0	39.5	-1.92%	3.84%
O118p4-P140911	38.8	41.9	39.8	-2.46%	5.25%
S118q4-P140919	39.4	41.7	40.4	-2.46%	3.22%
O118q4-P140879	42.5	44.9	42.4	0.34%	5.95%
O118x4-P140765	41.6	43.3	No Data	-	-

C. Short Circuit Current Results

Project ID	Field Current for 1pu Short Circuit Current			Percentage Error Vs Test	
	FE	EDS	Factory Test	FE	EDS
A145y4-P141239	224.7	224.1	224.5	0.07%	-0.18%
A145a4-P141177	239.5	238.9	244.3	-1.98%	-2.23%
A145y4-P141179	185.4	184.8	185.2	0.10%	-0.21%
A145y4-P141203	185.4	184.8	184.7	0.34%	0.03%
A145y4-P141205	181.0	184.8	180.5	0.24%	2.37%
A145y4-P141228	250.5	254.5	260.9	-4.00%	-2.47%
A145y4-P141245	224.7	224.1	228.3	-1.56%	-1.80%
A145y4-P141251	224.0	224.6	230.4	-2.76%	-2.50%
A145w4-P141230	224.1	224.3	224.3	-0.08%	0.00%
A160a4-P141218	170.7	178.0	177.9	-4.05%	0.06%
A160w4-P141224	201.3	201.3	201.3	-0.02%	0.00%
A160b4-P141255	160.1	160.8	160.8	-0.41%	0.00%
A160c4-P141259	190.1	190.9	190.9	-0.40%	0.00%
A160a4-P141273	190.1	191.8	190.2	-0.04%	0.84%
A160a4-P141275	147.0	147.0	144.5	1.73%	1.73%
A160a4-P141247 A	149.7	152.6	151.0	-0.89%	1.06%
A160a4-P141247 B	149.7	152.6	153.0	-2.18%	-0.26%
A160a4-P141247 C	149.7	152.6	153.0	-2.18%	-0.26%
A160a4-P141249	186.5	189.9	190.2	-1.92%	-0.16%
A160a4-P141271	173.8	177.0	177.8	-2.26%	-0.44%
A160e4-P141284	187.6	188.0	186.0	0.89%	1.08%
A160a4-P141139	156.8	159.6	158.0	-0.74%	1.01%
A160a4-P141143	142.2	144.8	145.8	-2.44%	-0.69%
A160w4-P141145	185.1	186.5	183.7	0.74%	1.52%
A160a4-P141207	197.8	201.0	202.0	-2.06%	-0.50%
A132a4-P141267	219.7	220.1	217.7	0.91%	1.10%
A132y4-P141253	183.2	182.9	183.2	-0.03%	-0.16%
A132x4-P141233	160.5	162.9	160.0	0.28%	1.81%
A132z4-P141222	214.8	213.1	211.0	1.82%	1.00%
A118u4-P141241	172.6	174.9	174.1	-0.88%	0.46%
A118u4-P141269	225.3	227.3	229.0	-1.61%	-0.74%
A118q4-P141226	157.1	158.7	158.5	-0.88%	0.13%
A118s4-P141183	226.0	229.4	229.7	-1.60%	-0.13%
A145a4-P141181	235.7	236.2	231.6	1.78%	1.99%
A132y4-P141167	183.1	182.8	182.4	0.40%	0.22%
A118s4-P141185	223.5	223.0	225.0	-0.66%	-0.89%
A118v4-P141152	190.9	191.0	193.0	-1.08%	-1.04%
A118t4-P141154	185.5	186.6	188.1	-1.38%	-0.80%
A132y4-P141171	177.7	179.2	177.9	-0.12%	0.73%
A145x4-P141132	204.9	208.0	206.0	-0.55%	0.97%
A118q4-P141134	180.8	184.5	184.3	-1.89%	0.11%
T145b4-P140954	154.7	151.0	149.0	3.83%	1.34%
A145a4-P140945	168.5	167.9	167.9	0.34%	0.00%
S118q4-P140909.	211.7	216.0	214.0	-1.07%	0.93%
O118p4-P140911	246.5	248.0	249.0	-1.01%	-0.40%
S118q4-P140919	210.6	212.0	213.7	-1.43%	-0.80%
O118q4-P140879	239.7	240.6	240.4	-0.31%	0.08%
O118x4-P140765	148.6	154.6	154.2	-3.65%	0.26%

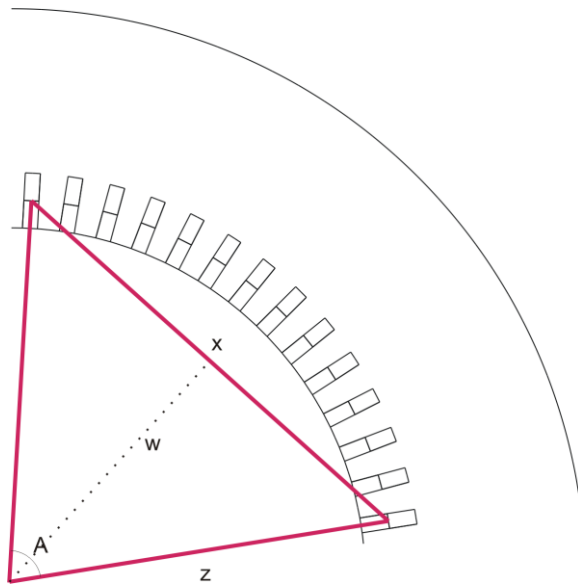
D. Zero Power Factor Results

Project ID	Field Current for 1pu Voltage at Zero Power Factor			Percentage Error Vs Test	
	FE	EDS	Factory Test	FE	EDS
A145y4-P141239	423.8	507.1	433.0	-2.12%	17.11%
A145a4-P141177	412.5	513.1	441.0	-6.47%	16.35%
A145y4-P141179	409.7	521.0	416.0	-1.51%	25.24%
A145y4-P141203	406.6	520.0	403.0	0.90%	29.03%
A145y4-P141205	397.5	520.0	395.0	0.63%	31.65%
A145y4-P141228	421.9	518.0	480.0	-12.11%	7.92%
A145y4-P141245	423.8	507.0	468.0	-9.44%	8.33%
A145y4-P141251	420.2	549.2	484.0	-13.18%	13.47%
A145w4-P141230	389.6	409.3	405.6	-3.94%	0.91%
A160a4-P141218	290.3	304.0	326.4	-11.05%	-6.86%
A160w4-P141224	383.8	460.1	427.2	-10.15%	7.70%
A160b4-P141255	384.7	475.4	394.9	-2.57%	20.38%
A160c4-P141259	326.7	358.6	353.7	-7.62%	1.39%
A160a4-P141273	328.6	356.0	355.0	-7.45%	0.28%
A160a4-P141275	320.5	409.6	346.1	-7.41%	18.35%
A160a4-P141247 A	286.0	300.6	312.6	-8.50%	-3.83%
A160a4-P141247 B	286.0	300.6	311.6	-8.20%	-3.52%
A160a4-P141247 C	286.0	300.6	319.8	-10.58%	-6.01%
A160a4-P141249	314.1	330.9	349.2	-10.06%	-5.24%
A160a4-P141271	301.9	312.5	323.5	-6.66%	-3.40%
A160e4-P141284	339.5	382.0	358.0	-5.18%	6.70%
A160a4-P141139	267.7	265.2	271.3	-1.33%	-2.25%
A160a4-P141143	280.6	289.9	285.7	-1.78%	1.47%
A160w4-P141145	329.7	351.0	355.0	-7.11%	-1.13%
A160a4-P141207	331.4	361.0	357.0	-7.16%	1.12%
A132a4-P141267	339.3	361.2	355.2	-4.46%	1.69%
A132y4-P141253	296.0	311.7	308.6	-4.08%	1.00%
A132x4-P141233	293.4	311.7	316.5	-7.31%	-1.52%
A132z4-P141222	333.9	350.0	335.8	-0.57%	4.23%
A118u4-P141241	287.1	308.0	299.3	-4.06%	2.91%
A118u4-P141269	366.3	414.1	382.2	-4.17%	8.35%
A118q4-P141226	301.3	318.3	300.2	0.37%	6.03%
A118s4-P141183	362.0	406.2	377.4	-4.09%	7.63%
A145a4-P141181	406.4	432.0	404.0	0.58%	6.93%
A132y4-P141167	300.4	327.5	308.0	-2.46%	6.33%
A118s4-P141185	372.3	415.0	386.0	-3.56%	7.51%
A118v4-P141152	353.7	420.0	366.3	-3.44%	14.66%
A118t4-P141154	282.0	283.1	293.4	-3.88%	-3.51%
A132y4-P141171	296.8	333.2	306.0	-3.02%	8.89%
A145x4-P141132	361.9	403.0	391.1	-7.47%	3.04%
A118q4-P141134	323.9	384.5	340.1	-4.77%	13.05%
T145b4-P140954	273.3	313.0	288.0	-5.10%	8.68%
A145a4-P140945	272.9	302.2	286.1	-4.60%	5.63%
S118q4-P140909.	340.6	318.0	360.2	-5.44%	-11.71%
O118p4-P140911	407.7	495.0	457.4	-10.88%	8.22%
S118q4-P140919	346.3	393.6	360.3	-3.88%	9.24%
O118q4-P140879	414.4	523.9	468.7	-11.59%	11.78%
O118x4-P140765	274.9	304.9	285.1	-3.59%	6.94%

E. Calculation of the End Winding Length

The end winding of a diamond coil actually forms a very complicated 3D involute shape this is simplified into an approximate triangle. The length of the end winding (l_{le}) is calculated by assuming that the coils produce an isosceles triangle that joins at 90 degrees. The base of the triangle is assumed to come out of the core half way down the slot. Additionally the length of the endplate, as it is not part of the active axial length that carries flux, must be added to each side.

First the length between 2 slots, X , is calculated



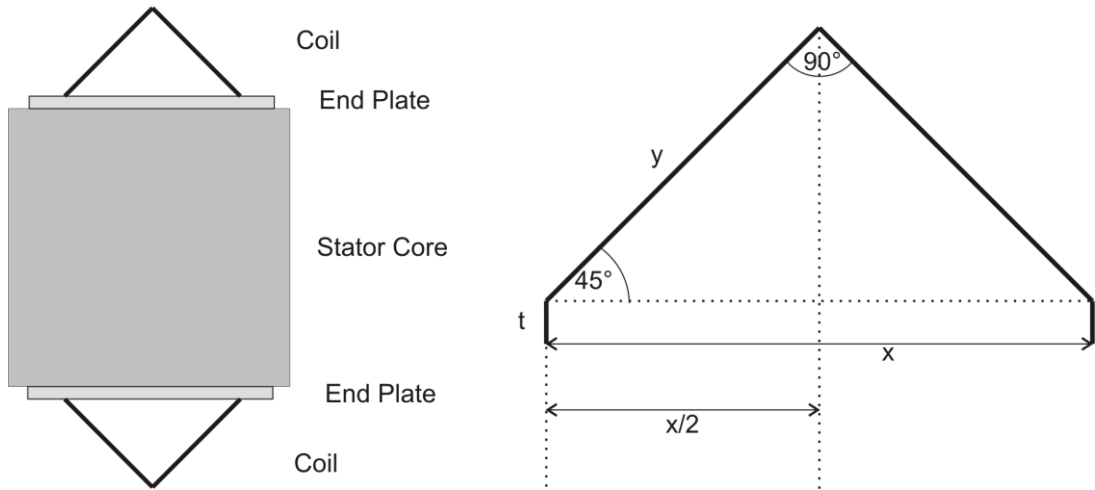
$$\text{Angle } A = \frac{360}{\text{Number of Slots}} \times \text{Chording}$$

$$Z = \text{Stator Bore} + \frac{\text{Slot Depth}}{2}$$

$$X = 2Z \sin\left(\frac{A}{2}\right)$$

Secondly the length of the end winding is calculated

Top Down View of a Single Coil



Length of 1 end winding:

$$l_{1e} = 2 \times \text{End Plate Thickness} + 2 \times y$$

$$l_{1e} = 2t + 2 \times \frac{X/2}{\cos(45)}$$

$$l_{1e} = 2t + \frac{X}{1/\sqrt{2}}$$

$$l_{1e} = 2t + X\sqrt{2}$$

F. Calculation of R²

The Coefficient of Determination is often used to show the accuracy of fit of a model when applied to a set of data. The value of R² ranges for 0 to 1 where 1 is a perfect fit.

Take a set of data y_i and associated model predictions f_i

First the mean of the data set is calculated:

$$\bar{y} = \frac{1}{n} \sum_i^n y_i$$

Next the total sum of squares is calculated i.e. each value has the mean subtracted from it before being squared and summed.

$$SS_{tot} = \sum_i (y_i - \bar{y})^2$$

Similarly the residual sum of squares is calculated i.e. each value has the corresponding value predicted by the model subtracted from it before being squared and summed.

$$SS_{err} = \sum_i (y_i - f_i)^2$$

Finally the coefficient of determination can be calculated

$$R^2 = 1 - \frac{SS_{err}}{SS_{tot}}$$

G. Frequency to Time Domain Transform

Classical Eddy Current Loss

Almost always defined in the frequency domain

Involves a loss constant which is calculated from material data

$$\text{Loss [W/kg]} = K_e f^2 B^2 \quad (\text{A1})[46]$$

$$\text{where } K_e = \frac{\gamma \pi^2 t^2}{6\rho} \quad (\text{A2})[46]$$

Substituting (A2) in (A1) therefore gives

$$\text{Loss [W/kg]} = \frac{\gamma \pi^2 t^2 f^2 B^2}{6\rho} \quad (\text{A3})$$

Typically a time based solution is preferred therefore if

$$B = \hat{B} \sin(\omega t) \quad (\text{A4})$$

Then rearranging and differentiating gives:

$$B = \hat{B} \sin(2\pi f t) \quad (\text{A5})$$

$$\frac{dB}{dt} = \hat{B} 2\pi f \cos(2\pi f t) \quad (\text{A6})$$

Squaring both sides gives:

$$\left(\frac{dB}{dt}\right)^2 = \hat{B}^2 4\pi^2 f^2 \cos^2(2\pi f t) \quad (\text{A7})$$

Finding the average over a period

$$\text{average} \left(\frac{dB}{dt}\right)^2 = \frac{1}{2\pi} \int_0^{2\pi} \hat{B}^2 4\pi^2 f^2 \cos^2(2\pi f t) d\omega t \quad (\text{A8})$$

$$\text{average}\left(\frac{dB}{dt}\right)^2 = \frac{\hat{B}^2 4\pi^2 f^2}{2\pi} \int_0^{2\pi} \cos^2(2\pi ft) dwt \quad (\text{A9})$$

given that

$$\cos^2(x) = \frac{(1 + \cos(2x))}{2} \quad \text{and} \quad wt = \theta \quad (\text{A10})\&(\text{A11})$$

Substituting (A10)&(A11) in (A9) gives

$$\text{average}\left(\frac{dB}{dt}\right)^2 = \frac{\hat{B}^2 4\pi^2 f^2}{2\pi} \int_0^{2\pi} \frac{(1 + \cos(2 \cdot \theta))}{2} d\theta \quad (\text{A12})$$

Rearranging

$$\text{average}\left(\frac{dB}{dt}\right)^2 = \frac{\hat{B}^2 4\pi^2 f^2}{2 \cdot 2\pi} \int_0^{2\pi} (1 + \cos(2 \cdot \theta)) d\theta \quad (\text{A13})$$

$$\text{average}\left(\frac{dB}{dt}\right)^2 = \frac{\hat{B}^2 4\pi^2 f^2}{2 \cdot 2\pi} \left[\theta + \frac{\sin(2 \cdot \theta)}{2} \right]_0^{2\pi} \quad (\text{A14})$$

$$\text{average}\left(\frac{dB}{dt}\right)^2 = \frac{\hat{B}^2 4\pi^2 f^2}{2 \cdot 2\pi} \left[2\pi + \frac{\sin(2 \cdot 2\pi)}{2} - 0 + \frac{\sin(2 \cdot 0)}{2} \right] \quad (\text{A15})$$

$$\text{average}\left(\frac{dB}{dt}\right)^2 = \frac{\hat{B}^2 4\pi^2 f^2}{2 \cdot 2\pi} [2\pi] \quad (\text{A16})$$

$$\text{average}\left(\frac{dB}{dt}\right)^2 = 2\hat{B}^2 f^2 \pi^2 \quad (\text{A17})$$

Therefore from (A17)

$$\text{average}\left(\frac{dB}{dt}\right)^2 = \int \left| \frac{dB}{dt} \right|^2 dt = 2\hat{B}^2 f^2 \pi^2 \quad (\text{A18})$$

Rearrange (A18)

$$\frac{1}{2\pi^2} \int \left| \frac{dB}{dt} \right|^2 dt = \hat{B}^2 f^2 \quad (\text{A19})$$

Substitute in (A19) in (A3)

$$\text{Loss [W/kg]} = \frac{\gamma \pi^2 t^2}{6\rho} \frac{1}{2\pi^2} \int \left| \frac{dB}{dt} \right|^2 dt \quad (\text{A20})$$

Simplify leaving Eddy current loss as a time domain function.

$$\text{Loss [W/kg]} = \frac{\gamma t^2}{12\rho} \int \left| \frac{dB}{dt} \right|^2 dt \quad (\text{A21})$$

H. Graphical User Interface

An easy to use graphical user interface has been created to allow the users to maintain high levels of productivity without a high number of hours devoted to training. This use of a graphical user interface is of up most importance to many users as the companies existing system is entirely command line text based making usage somewhat cumbersome. The GUI has been coded in MATLAB and is based around a set of core screens which allows the user to input data as either a single machine or a series of machines based upon data input files. Figure 132 shows the order that the GUI flows.

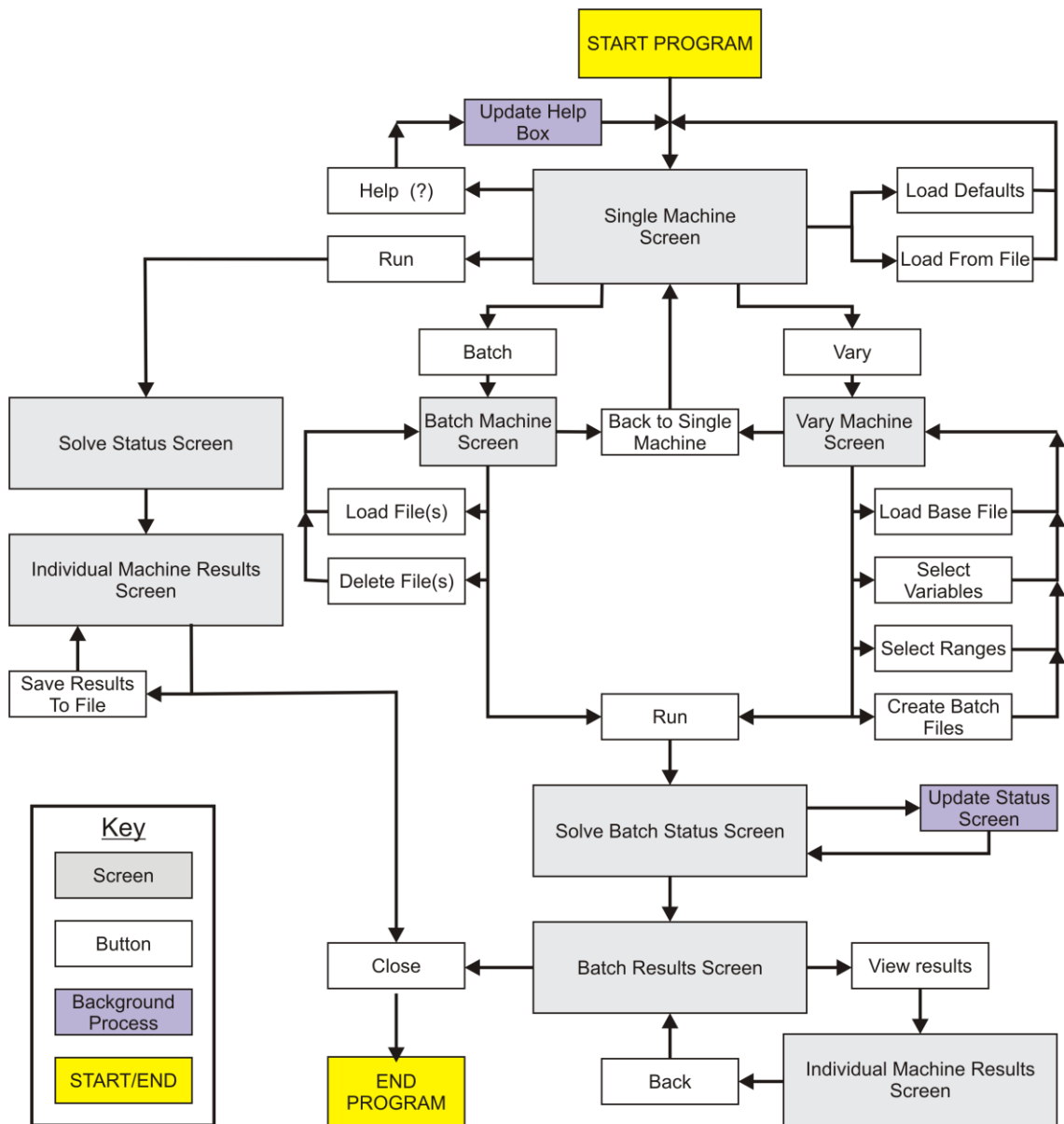


Figure 132 - Chart showing how flow of the GUI

Single Run

The basic single machine screen (Figure 133) allows manual input of all the relevant data values into each of the value boxes to allow rapid individual simulation. The value boxes automatically determine if the data input is of the correct numerical type and display any errors in the help box. Clicking the help button [?] next to each value displays a picture and text in the help box relevant to that value. Users can also load a series of default typical values for certain machine sizes or load a full machine design from a text file by using the appropriate buttons. From this screen the users must then select which solving routines they wish to be run before clicking 'Run' which then progresses the GUI to the status screen whilst the package solves the design. The 'Batch' and 'Vary' buttons move switch to their respective screens whilst the close button exits before and processing has occurred

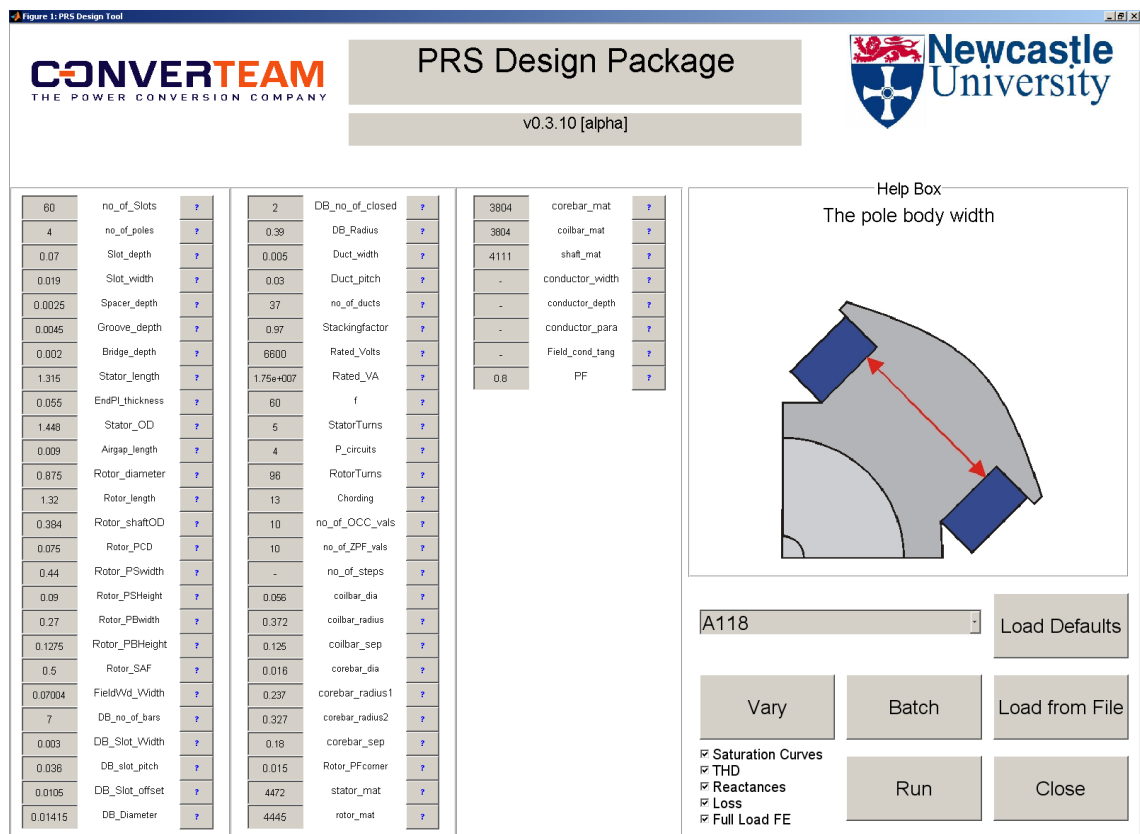


Figure 133 - Single Machine Screen

Batch

The Batch screen (Figure 134) allows the user to select several text files containing different machines and process them one after another. The Batch program runs the same solution options for all machines.

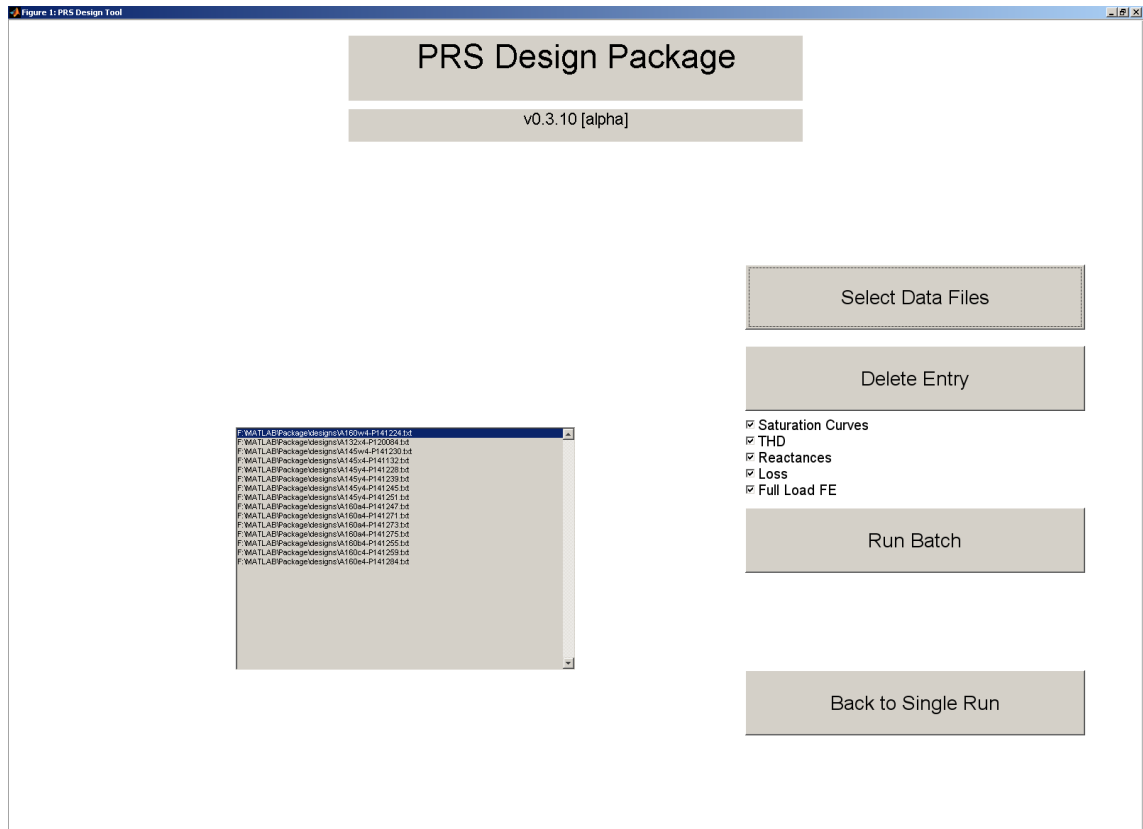


Figure 134 - Batch Machine Screen

Vary

The Vary screen (Figure 135) allows the user to pick a single text file input but then vary 1 or 2 parameters over a range. For example a designer may wish to change the spacing of the damper bars and pitch of the damper bars over several values and monitor the T.H.D.. This would be very time consuming if the user were to manually enter the values where as Vary can achieve this automatically. The values which are varied can be changed over a linearly spaced range or at set input values. The 'Run Pre check' button estimates the time for solution and creates input text files based on the data supplied so the user has an archive of their solution data.

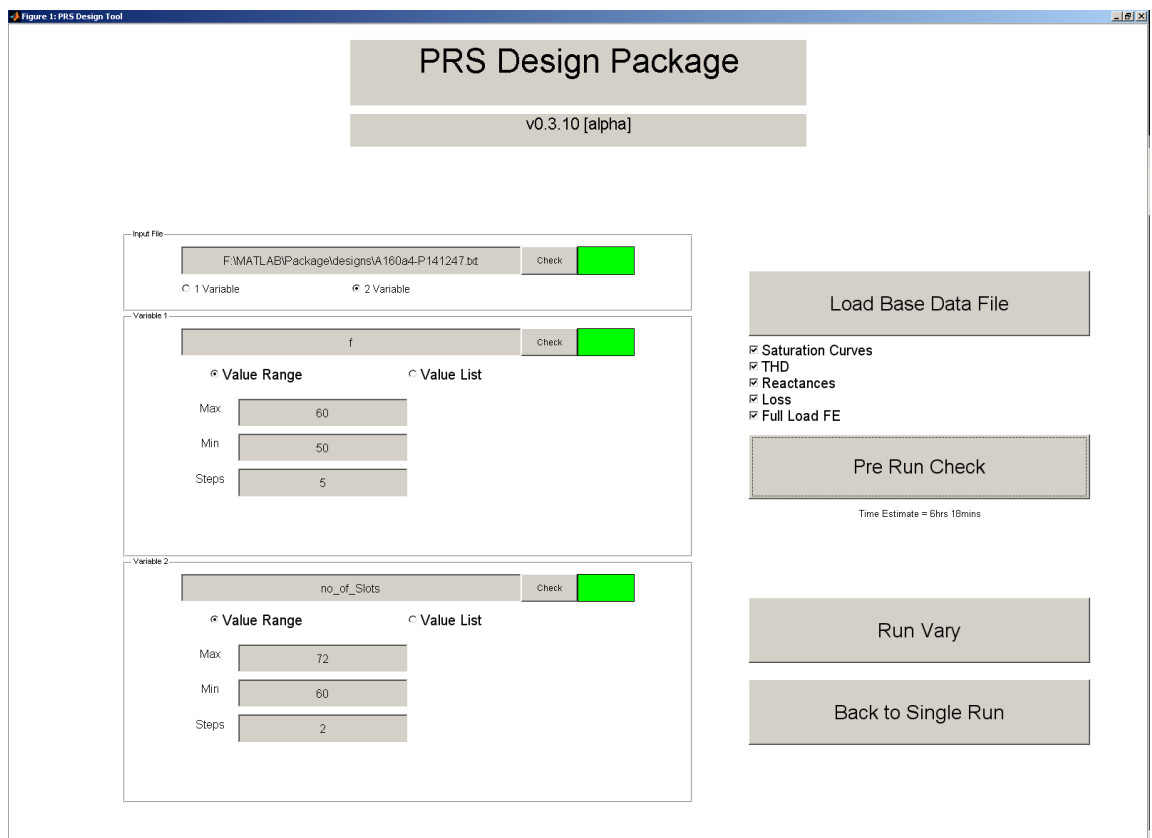


Figure 135 - Vary Machine Screen

Status and Results Screens

The Status and Results Screens (Figure 136 and Figure 137) give the user some feedback about how long the simulations are taking and what the results are. when more than on machine is solved a status indicator shows which machine is being solved for example stating 'Solving Machine 3 of 30'. Likewise the Batch results screen allows the user to select the machine they wish to see the results for before displaying the individual results screen. Batch and Vary routine automatically save each machines results as a .mat file where as with single machines the user must manually do this.

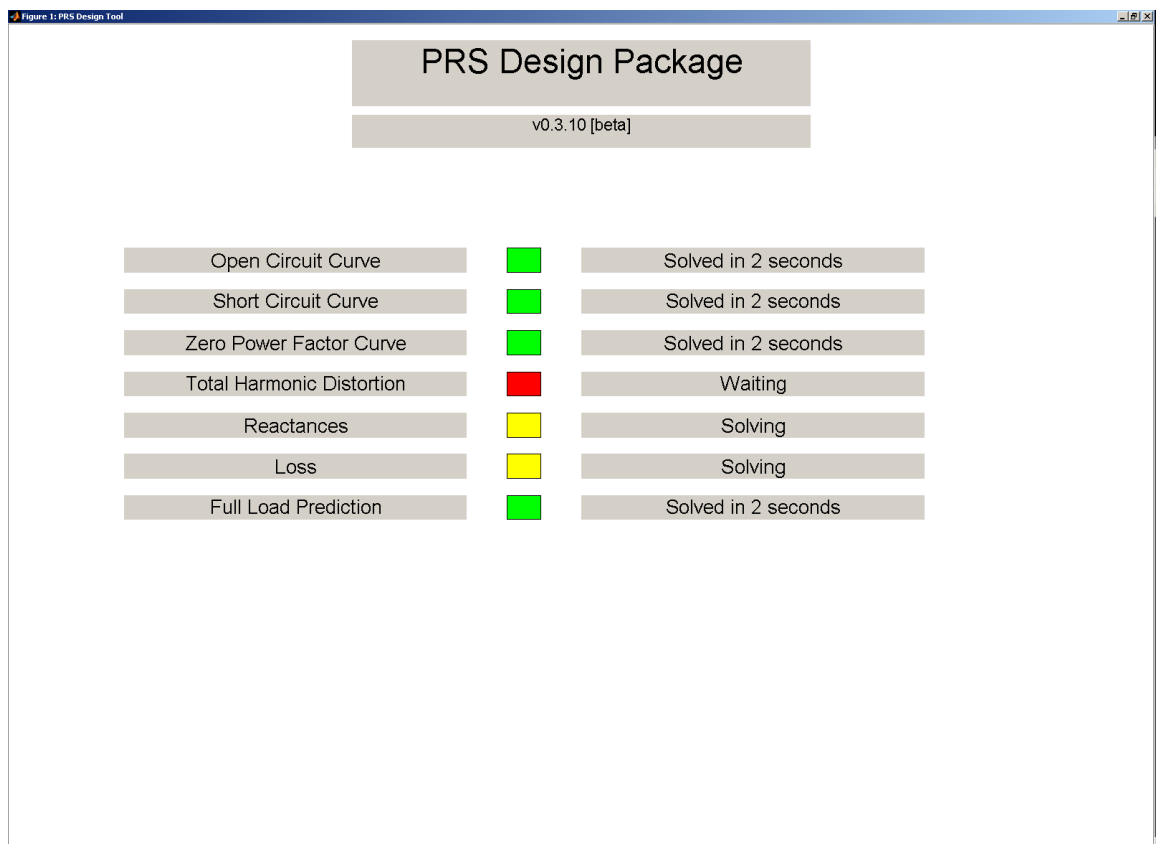


Figure 136 - Solve Status Screen

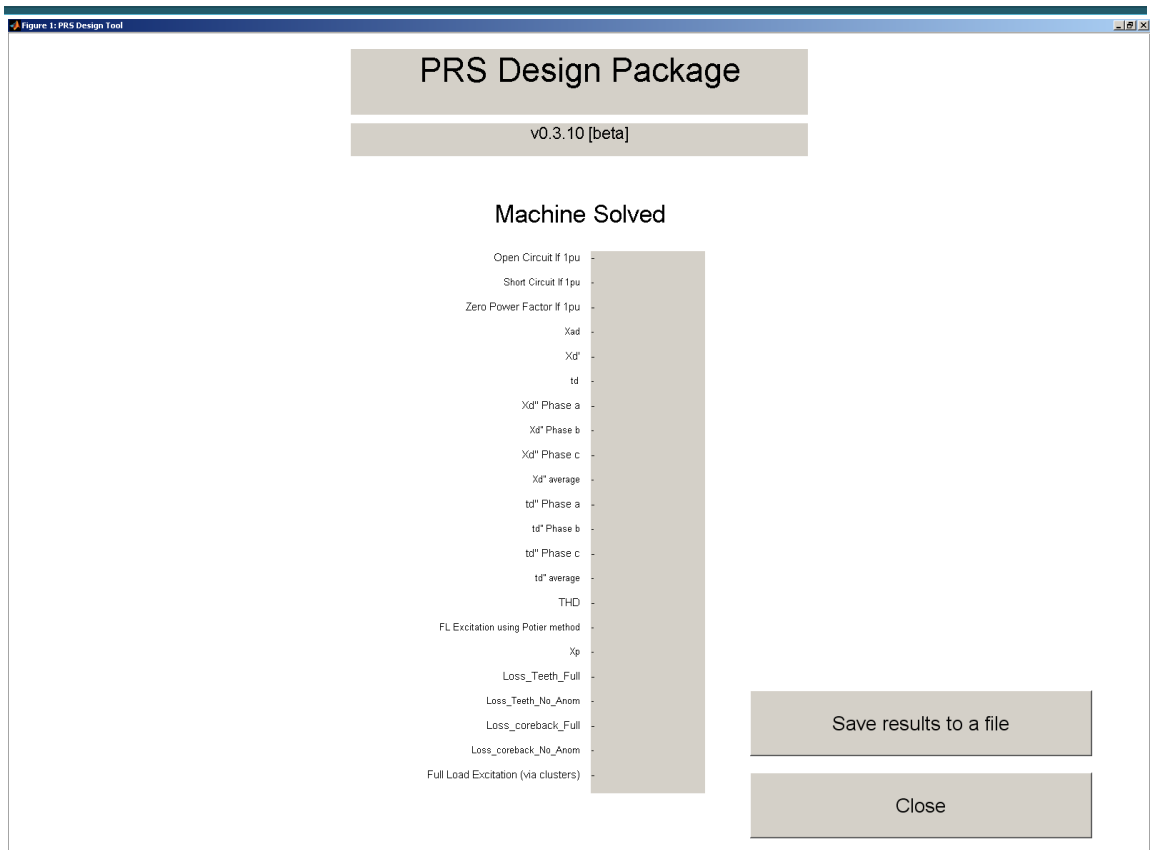
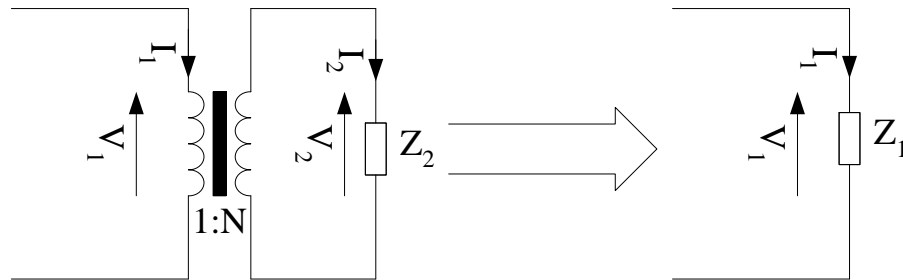


Figure 137 - Individual Machine Results Screen

I. Transferring Impedances across an Ideal transformer

Consider the Ideal transformer below:



The load can be described as:

$$Z_2 = \frac{V_2}{I_2} \quad (\text{C1})$$

Given that:

$$I_2 = NI_1 \quad (\text{C2})$$

$$V_2 = \frac{V_1}{N} \quad (\text{C3})$$

the load can be redescribed as

$$Z_2 = \frac{V_1}{N^2 I_1} \quad (\text{C4})$$

A primary side impedance is:

$$Z_1 = \frac{V_1}{I_1} \quad (\text{C5})$$

Hence the transferred impedance can be described as:

$$Z_1 = N^2 Z_2 \quad (\text{C6})$$

J. T.H.F. and T.I.F. Weighting Factors

Telephonic Harmonic Factor

Below is a list of weighting constants Telephonic Harmonic Factor calculation according to BS4999[43]. The factors, stated for 50Hz, must be interpolated for a machine running at 60Hz.

$$THF = \frac{\sqrt{\sum_{n=1,2,3\dots} V_n^2 \lambda_n^2}}{V_1}$$

where

V_n = Line r.m.s. Voltage of the n^{th} harmonic

λ_n = T.H.F. weighting factor of the n^{th} harmonic

<u>Harmonic</u>	<u>Frequency</u>	<u>Weighting factor, λ_n</u>
1	50	4.44E-05
2	100	0.00112
3	150	0.00665
4	200	0.0223
5	250	0.0556
6	300	0.111
7	350	0.165
8	400	0.242
9	450	0.327
10	500	0.414
11	550	0.505
12	600	0.595
13	650	0.691
14	700	0.79
15	750	0.895
16	800	1
17	850	1.1
18	900	1.21
19	950	1.32
20	1000	1.4
21	1050	1.46
22	1100	1.47
23	1150	1.49
24	1200	1.5
25	1250	1.53
26	1300	1.55
27	1350	1.57

28	1400	1.58
29	1450	1.6
30	1500	1.61
31	1550	1.63
32	1600	1.65
33	1650	1.66
34	1700	1.68
35	1750	1.7
36	1800	1.71
37	1850	1.72
38	1900	1.74
39	1950	1.75
40	2000	1.77
41	2050	1.79
42	2100	1.81
43	2150	1.82
44	2200	1.84
45	2250	1.86
46	2300	1.87
47	2350	1.89
48	2400	1.9
49	2450	1.91
50	2500	1.93
51	2550	1.93
52	2600	1.94
53	2650	1.95
54	2700	1.96
55	2750	1.96
56	2800	1.97
57	2850	1.97
58	2900	1.97
59	2950	1.97
60	3000	1.97
62	3100	1.94
64	3200	1.89
66	3300	1.83
68	3400	1.75
70	3500	1.65
72	3600	1.51
74	3700	1.35
76	3800	1.19
78	3900	1.04
80	4000	0.89
82	4100	0.74
84	4200	0.61
86	4300	0.496
88	4400	0.398
90	4500	0.316
92	4600	0.252

94	4700	0.199
96	4800	0.158
98	4900	0.125
100	5000	0.1

Telephonic Interference Factor

Below is a list of weighting constants Telephonic Interference Factor calculation according to IEEE Std 519-1992[44].

$$TIF = \sqrt{\sum_{n=1,2,3\dots} \left(\frac{V_n W_n}{V_t} \right)^2}$$

where

V_t = Total line r.m.s. Voltage

V_n = Line r.m.s. Voltage of the n^{th} harmonic

W_n = T.I.F. weighting factor of the n^{th} harmonic

Harmonic	Frequency	T.I.F. Weighting factor, W_n
1	60	0.5
3	180	30
5	300	225
6	360	400
8	480	650
9	540	1320
11	660	2260
12	720	2760
13	780	3360
15	900	4350
17	1020	5100
18	1080	5400
19	1140	5630
21	1260	6050
23	1380	6370
24	1440	6560
25	1500	6680
27	1620	6970
29	1740	7320
30	1800	7570
31	1860	7820
33	1980	8330

35	2100	8330
36	2160	9080
37	2220	9330
39	2340	9840
41	2460	10340
43	2580	10600
47	2820	10210
49	2940	9820
50	3000	9670
53	3180	8740
55	3300	8090
59	3540	6730
61	3660	6130
65	3900	4400
67	4020	3700
71	4260	2750
73	4380	2190

References

-
- [1] B. Mecrow and A. Jack, "Efficiency trends in electric machines and drives," *Energy Policy*, vol. 36, Dec. 2008, pp. 4336-4341.
- [2] 2009 data set from World Bank Development Data accessed through <http://www.google.co.uk/publicdata/directory> [Aug 2011]
- [3] M.K. Hubbert, "Nuclear energy and the fossil fuel," *Drilling and production practice*, 1956.
- [4] Phrase first was coined by Lewis Strauss [Chairman of the United States Atomic Energy Commission] in a 1954 speech to the National Association of Science Writers
- [5] J.H. Walker "Large Synchronous Machines: Design, Manufacture and Operation", Oxford University Press, page 9, 1981
- [6]<http://www.speedlab.co.uk/> - Mission statement. Retrieved October 2011
- [7] R.L. Courant, "Variational methods for the solution of problems of equilibrium and vibration", *Bull. Am Math Soc.*, 49: 1-61, 1943
- [8] J.L. Synge, "The Hypercircle in Mathematical Physics", *American Institute of Physics*, October 1957, page 45, ISBN 0031-9228
- [9] R.J. Duffin, "Distributed and Lumped Networks," *Journal of Mathematics and Mechanics*, 8, 1959, pp. 793-826.
- [10] S. Ahmed and P. Daly, "Waveguide solutions by the finite-element method," *Radio and Electronic Engineer*, vol. 38, 1969, p. 217.
- [11] P.L. Arlett, A.K. Bahrani, O.C. Zienkiewicz, "Application of finite elements to the solution of Helmholtz's equation". *Proceedings of the IEE* 1968; 1762–1766
- [12] P Silvester, "Finite-Element Solution of Homogeneous-Waveguide Problems", *Alta Frequenza*, 38, 1969, pp.313-317
- [13] G.E. Moore, "Cramming more components onto integrated circuits". *Electronics Magazine*. pp. 4. 1965. ftp://download.intel.com/museum/Moores_Law/Articles-Press_Releases/Gordon_Moore_1965_Article.pdf.
- [14] J.C. Maxwell, "On Physical Lines of Force", *Philosophical Magazine*, 1861, http://en.wikisource.org/wiki/On_Physical_Lines_of_Force
- [15] <http://www.ansys.com/>
- [16] <http://www.infolytica.com/>
- [17] <http://www.cobham.com/>
-

-
- [18] E Loh, "The Ideal HPC Programming Language". *Queue (Association of Computing Machines)* 8 (6) June 2010. <http://queue.acm.org/detail.cfm?id=1820518>.
- [19]<http://www.quickfield.com/>
- [20] <http://jmag-international.com/>
- [21] Opera Vector Fields V12.027
- [22] R.H. Park, "Two-reaction theory of synchronous machines generalized method of analysis-part I," *Transactions of the American Institute of Electrical Engineers*, vol. 48, Jul. 1929, pp. 716-727.
- [23] J.F. Gieras, M. Wing. *Appendix A: Leakage Inductance of A.C. Motors*, Permanent Magnet Motor Technology.
- [24] F.W. Carter, "Note on Airgap and Interpolar Induction" *Journal of the Institute of Electrical Engineers*, vol. XXIX 1899-1900, pp925-p33
- [25] Pohl. *Volume 52 Journal Institute of Electrical Engineers, 1914*
- [26] P.L. Dandeno, H.C. Karmaker, C. Azuaje, M. Glinkowski, I. Kamwa, S.J. Salon, R.M. Saunders, and S. Umans, "Experience with standstill frequency response (SSFR) testing and analysis of salient pole synchronous machines," *IEEE Transactions on Energy Conversion*, vol. 14, 1999, pp. 1209-1217.
- [27] P.L. Dandeno, A.T. Poray: 'Development of detailed turbogenerator equivalent circuits from standstill frequency response measurements', *IEEE Trans., 1981, PAS-100*, (4). pp. 1646 - 1654
- [28] A G. Jack, T.J. Bedford, "An analysis of the results from the computation of transients in synchronous generators using frequency domain methods," *IEEE Transactions on Energy Conversion*, vol. 3, Jun. 1988, pp. 375-383.
- [29] M.G. Say, "Alternating Current Machines", *Longman Scientific & Technical, 5th Edition, 1983*
- [30] R.W. Wieseman, "Graphical Determination of Magnetic Fields Practical Applications to Salient-Pole Synchronous Machine Design," *American Institute of Electrical Engineers, Transactions of the*, vol. 46, 1927, p. 141-154.
- [31] IEEE, "IEEE: Std 115-1995 Guide: Test Procedures for Synchronous Machines," vol. 1995, 1996.
- [32] IEC Definition retrieved from <http://www.electropedia.org/>
- [33] P. Brandl, K. Reichart, W.Voght, "Simulation of turbogenerators and steady state load", *Brown Boveri Review Volume 9 - 75*, Page 444-449, 1975
-

-
- [34] Jeffrey C. Lagarias, James A. Reeds, Margaret H. Wright, Paul E. Wright, "Convergence Properties of the Nelder-Mead Simplex Method in Low Dimensions", *SIAM Journal of Optimization*, p.112-147, 1998. within fminsearch.m Copyright 1984-2007 The MathWorks, Inc. Revision: 1.21.4.15 Date: 2007/06/14 05:08:40
- [35] International Electrotechnical Commission "IEC 60034-1 Rotating electrical machines – Part 1: Rating and performance", ed 11, (April 2004)
- [36] J. H. Walker, "Slot Ripples in Alternator E.M.F. Waves", *Journal I.E.E.*, Pt. 2, (Feb 1949)
- [37] E. J. J. Rocha Jr., M. K. Uemori, A. De Arruda Penteado, "The Damper Winding Influence Upon Salient Pole Synchronous Generator Electromotive Force", *IEEE International- Electric Machines and Drives Conference Record*, (1997).
- [38] P. E. Clark, G. D. LeFlem, C. J. Thoday, S. L. Richards, "Designs for the 90's", *Fourth International Conference on Electrical Machines and Drives*, p 1-5.
- [39] J. Matsuki, T. Katagi, T. Okada, "Slot Ripples in the Damper Windings of a Salient-Pole Synchronous Generator", *IEEE Transactions on Energy Conversion*, Vol. 9, No. 1, (March 1994)
- [40] A. M. Knight, H. Karmaker, K. Weeber, "Use of a Permeance Model to Predict Force Harmonics components and Damper Winding Effects in Salient Pole Synchronous Machines", *IEEE Transactions on Energy Conversion*, Vol. 17 No. 4, (December 2002)
- [41] S. Keller, M. T. Xuan, J. J. Simond, "Computation of the No-Load Voltage Waveforms of Laminated Salient-Pole Synchronous Generators", *IEEE Transactions on Industry Applications*", Vol. 42 No. 3, (May/June 2006)
- [42] C. E. Shannon, "Communication in the presence of noise", *Proc. Institute of Radio Engineers*, Vol. 37, no. 1, pp. 10–21, (Jan. 1949)
- [43] British Standard BS 4999: Part 101 1987: General requirements for rotating electrical machines. Specification for rating and performance.
- [44] IEEE Standard 519-1992 - IEEE Recommended Practices and Requirements for Harmonic Control in Electrical Power Systems.
- [45] R. Hyndman, A Koehler, "Another look at measures of forecast accuracy", *International Journal of Forecasting*, Vol 22, Issue 4, (2006)
- [46] G. Bertotti, "General properties of power losses in soft ferromagnetic materials," *IEEE Transactions on magnetics*, vol. 24, 1988, p. 621–630.
-

-
- [47] G. Bertotti, a. Boglietti, M. Chiampi, D. Chiarabaglio, F. Fiorillo, and M. Lazzari, "An improved estimation of iron losses in rotating electrical machines," *IEEE Transactions on Magnetics*, vol. 27, 1991, pp. 5007-5009.
- [48] M. Barcaro and N. Bianchi, "Air-Gap Flux Density Distortion and Iron Losses in Anisotropic Synchronous Motors," *IEEE Transactions on Magnetics*, vol. 46, 2010, pp. 121-126.
- [49] K. Atallah, Z. Zhu, and D. Howe, "An improved method for predicting iron losses in brushless permanent magnet DC drives," *IEEE Transactions on Magnetics*, vol. 28, 1992, pp. 2997-2999.
- [50] P. Rafajdus and J. Mihok, "Core Loss Analysis Of The Reluctance Synchronous Motor With Barrier Rotors," *Journal of Electrical Engineering*, vol. 55, 2004, pp. 273-276.
- [51] H. Nam, K. Ha, and J. Lee, "A study on iron loss analysis method considering the harmonics of the flux density waveform using iron loss curves tested on Epstein samples," *IEEE Transactions on Magnetics*, vol. 39, 2003, pp. 1472-1475.
- [52] C. McClay, "The influence of rotor skew on cage motor losses," *Eighth International Conference on Electrical Machines and Drives*, 1997, pp. 263-267.
- [53] C. McClay and S. Williamson, "Influence of rotor skew on cage motor losses," *IEE Proceedings - Electric Power Applications*, vol. 145, 1998, p. 414.
- [54] M. Mueller, S. Williamson, T. Flack, and K. Atallah, "Calculation of iron losses from time-stepped finite-element models of cage induction machines," *Electrical Machines and Drives, 1995. Seventh International Conference on (Conf. Publ. No. 412)*, 1995, pp. 88-92.
- [55] A. Knight and Y. Zhan, "Identification of flux density harmonics and resulting iron losses in induction machines with nonsinusoidal supplies," *IEEE Transactions on Magnetics*, vol. 44, 2008, p. 1562-1565.
- [56] P. Rafajdus, J. Mihok, P. Hudak, and J. Milhok, "Core Loss Analysis Of The Reluctance Synchronous Motor With Barrier Rotors," *Journal of Electrical Enigneering*, vol. 55, 2004, pp. 273-276.
- [57] A. Belahcen and A. Arkkio, "Comprehensive dynamic loss model of electrical steel applied to FE simulation of electrical machines," *IEEE Transactions on Magnetics*, vol. 44, 2008, p. 886-889.
-

-
- [58] C.A Hernandez-Aramburo, T.C Green, and S. Smith. "Assessment of power losses of an inverter-driven induction machine with its experimental validation." *IEEE Transactions on Industry Applications* 39, no. 4 (July 2003): 994-1004.
- [59] Brailsford, F.; Mazza, V.R.; , "The alternating magnetic flux distribution in right-angled corners of transformer laminations. An experimental investigation," *Proceedings of the IEE - Part A: Power Engineering* , vol.109, no.44, pp.173-180, April 1962
- [60] L. Ma, M. Sanada, S. Morimoto, and Y. Takeda, "Prediction of iron loss in rotating machines with rotational loss included," *IEEE Transactions on Magnetics*, vol. 39, 2003, p. 2036–2041.
- [61] H. Nam, J. Lee, K. Chang, J. Hong, and J. Lee, "Iron loss analysis method considering harmonics of magnetic flux density waveforms," *Electrical Machines and Systems, 2003. ICEMS 2003. Sixth International Conference on*, vol. 2, 2003, p. 736.
- [62] A. Smith and G. Phipson, "Iron losses in cage induction motors," *Conference on (Conf. Publ. No. 341)*, 1991, pp. 255-259.
- [63] J. Seo, T. Chung, C. Lee, S. Jung, and H. Jung, "Harmonic Iron Loss Analysis of Electrical Machines for High-Speed Operation Considering Driving Condition," *IEEE Transactions on Magnetics*, vol. 45, 2009, pp. 4656-4659.
- [64] J. Hu, Y. Luo, M. Liu, and X. Liu, "Analysis of the iron loss of line start permanent magnet synchronous motor using time-stepping finite element method," *International Conference on Electrical Machines and Systems, 2008. ICEMS 2008*, 2008, p. 3237–3240.
- [65] Cobham Ltd, "Iron Loss Calculation in Opera-2D", Opera 2D,
- [66] X. Yao, A. Moses, J. Sagarduy, and F. Anayi, "Influence of Switching Frequency on Eddy-Current Losses in a Three-Phase, Three-Limb Transformer Core Subjected to PWM Voltage Excitation," *International Conference on Power Engineering, Energy and Electrical Drives, 2007. POWERENG 2007*, 2007, p. 324–329.
- [67] Z. Zhu, K. Ng, and D. Howe, "Analytical prediction of stator flux density waveforms and iron losses in brushless DC machines, accounting for load condition," *ICEMS'2001. Proceedings of the Fifth International Conference on Electrical Machines and Systems (IEEE Cat. No.01EX501)*, vol. 2, pp. 814-817.
- [68] P. Hargreaves, B. Mecrow, and R. Hall, "Open circuit voltage distortion in salient pole synchronous generators with damper windings," *5th IET International Conference on Power Electronics, Machines and Drives (PEMD 2010)*, 2010, pp. MO431-MO431.
-

-
- [69] [http://www.sura.se/Sura/hp_products.nsf/vOpendocument/03A8B2433FAE16C4C1256AA8002280E6/\\$FILE/400-50.pdf?OpenElement](http://www.sura.se/Sura/hp_products.nsf/vOpendocument/03A8B2433FAE16C4C1256AA8002280E6/$FILE/400-50.pdf?OpenElement)
- [70] Y.S. Chen, Z.Q. Zhu, S. Member, and D. Howe, "Calculation of d - and q -Axis Inductances of PM Brushless ac Machines Accounting for Skew," *October*, vol. 41, 2005, pp. 3940-3942.
- [71] F. Libert, J. Souldard, and J. Engström, "Design of a 4-pole Line Start Permanent Magnet Synchronous Motor," *ITTF AB*, vol. cedrat.com, pp. 4-9.